A Sponsored Supplement to *Science*

Unlocking Alzheimer's mysteries: Deciphering the pathways to neurodegeneration

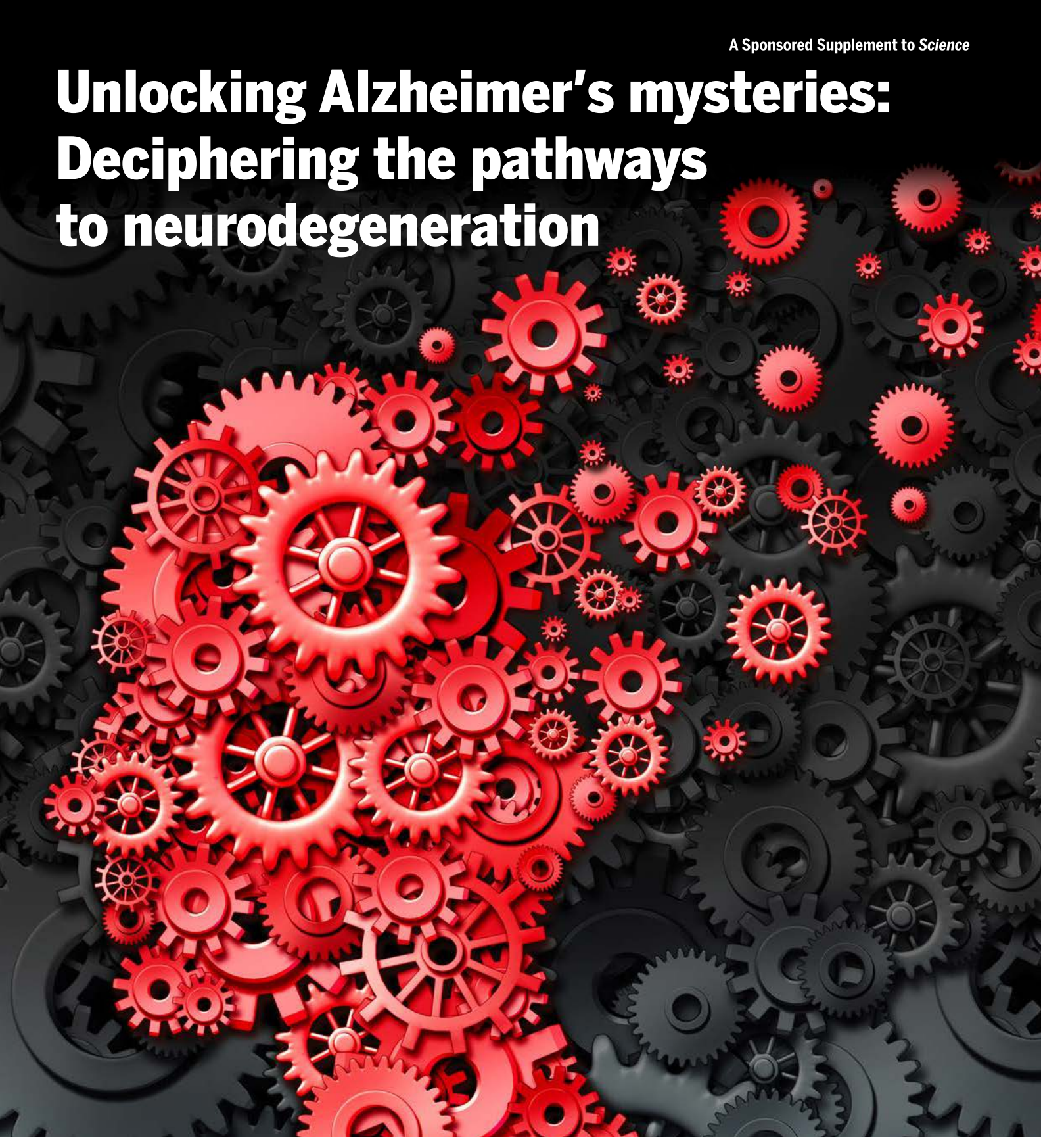

Sponsored by

sartorius

Produced by the *Science*/AAAS Custom Publishing Office

Science | AAAS

Table of Contents

This booklet was produced by the *Science*/AAAS Custom Publishing Office and sponsored by Sartorius.

White papers that appear in this supplement have not been peer-reviewed nor have they been assessed by *Science*.

Editor: Sean Sanders, Ph.D.
Proofreader/Copyeditor: Bob French
Designer: JD Huntsinger

ROGER GONCALVES,
ASSOCIATE SALES DIRECTOR
Custom Publishing
Europe, Middle East, and India
rgoncalves@science-int.co.uk
+41-43-243-1358

4 October 2019

Introductions

Research Articles

White Papers

Q&A

Neurodegenerative diseases ... chip away at this most fundamental part of us, slowly stealing our essential humanity.

Toward a brighter future for Alzheimer's disease treatment

Our brain is the seat of our personality, ambitions, dreams, and desires. It defines who we are as human beings, how we see the world—and sometimes how the world sees us. Neurodegenerative diseases—including Alzheimer's disease (AD)—are among the most devastating to the patient and to their family, in large part because they chip away at this most fundamental part of us, slowly stealing our essential humanity.

As the average age of populations across the globe continues to increase, the incidence of AD has been rising. It is estimated that 50 million people were living with dementia in 2017, a number that is predicted to grow to over 131 million by 2050.[1] In the United States alone, an estimated 5.8 million people over age 65 are currently living with the effects of AD; this number is expected to more than double in the next 30 years to 13.8 million.[2] Concomitantly, the cost of caring for and treating these patients is also rising. Costs for health care and long-term care for persons with AD in the U.S. totaled an estimated USD 290 billion in 2019. Add to this an almost equal amount, estimated at USD 234 billion, in unpaid caregiving from friends and family, and the financial toll of this disease is significant.[2]

From a research perspective, AD is being attacked on many fronts. In this supplement we have collected four important articles published in the *Science* family of journals that provide a sampling of the breadth of research into different aspects of AD. The opening 2016 review from Ransohoff (p. 4) gives a cogent summary of the potential role of neuroinflammation in a range of neurodegenerative disorders including AD, Parkinson's disease, and amyotrophic lateral sclerosis, with a particular focus on specialized cells in the brain known as microglia that are on the frontlines of active immune defense in the central nervous system.

Next, Ryan et al. (p. 10), having overcome some of the considerable challenges of in vitro microglia culture, describe a new model system that "recapitulated key aspects of microglia phenotype and function," enabling experiments that both elucidate microglia activity and test therapeutic interventions for neurodegenerative disorders.

In the third article, Wegmann et al. (p. 22) discuss their use of a more standard in vivo mouse model system that can track the spread of tau protein through different brain regions as test animals age, challenging the notion that single molecules of misfolded tau consistently trigger a cascade of tau misfolding and aggregation.

Finally, a recent paper from Dominy et al. (p. 31) investigates the intriguing connection between the presence of bacterium-derived proteases in the brain and the incidence of AD, pointing to a potential new pathway for AD treatment.

The supplement ends with two informative white papers from the booklet sponsor, Sartorius, which provide the reader with useful pointers for live-cell analysis of microglia and neurons that could advance their research, as well as a fascinating interview with Dr. Beth Stevens from Boston Children's Hospital in Massachusetts, where she lays out the current state of AD research and offers insights into some exciting new areas of investigation involving microglial cells.

While there is clearly much work to be done, many inroads are being made in better understanding AD in all its complexity, giving patients new hope that this devastating disease will eventually be defeated.

Sean Sanders, Ph.D.
Director and Senior Editor, Custom Publishing
Science/AAAS

Footnotes
[1]www.alz.co.uk/research/statistics
[2]www.alz.org/media/documents/alzheimers-facts-and-figures-2019-r.pdf

The importance of the interplay between the nervous and immune systems has become ever more apparent in recent years, and neuroimmunology has the potential to offer great opportunities for novel therapeutics.

Insights into neurodegeneration

The field of neuroscience is benefiting from an increased social spotlight and research interest. An aging population, combined with significant difficulties in identifying effective treatments for neurodegenerative disorders, has intensified the focus on age-related neuropathy research.

Alzheimer's disease (AD) is a form of dementia with neurodegeneration as the underlying cause. Alterations in synaptic structure and function can be observed in AD, but elucidation of the underlying mechanisms of disease progression has been limited by the lack of biologically relevant model systems. To advance our understanding of neurodegeneration pathways and the impact of potential therapeutic interventions, we need appropriate in vitro assays that better represent disease conditions, along with improved analytical approaches.

The neuroscience field has traditionally depended on the study of tumor cell lines, rodent primary brain regions, and human postmortem tissue. These approaches are limited by their inability to fully represent the brain's extraordinary complexity and plasticity, rendering the translational value of these models questionable. Recent advances in induced pluripotent stem cell (iPSC) development offer the potential for easy access to healthy human, patient-, and disease-specific cells, yielding more representative assays. This, in turn, may reduce the reliance on subpar animal models.

Maximizing the value of the iPSC revolution for neurodegenerative research requires the introduction of complex workflows involving cultured cell differentiation (e.g., maturation of iPSC-derived neurons) and transduction (e.g., CRISPR/Cas9 modification) prior to carrying out a phenotypic assay. Live-cell analysis, defined as the continuous or semicontinuous image-based measurement of cells without perturbation, is ideally suited to add quantitative monitoring. This enables informed decision-making throughout the experiment and lowers the risk of downstream failures. Live-cell assays allow for long-term recordings that can yield valuable information on plastic changes such as neurite outgrowth and neuronal activity. Importantly, these assays are compatible with and complementary to currently employed techniques—which allows for monitored live-cell cultures to be readily evaluated using methods such as high-content imaging, electrophysiological recording, or flow cytometry.

In addition, the importance of the interplay between the nervous and immune systems has become ever more apparent in recent years, and neuroimmunology has the potential to offer great opportunities for novel therapeutics. However, the challenges already outlined for developing translational phenotypic models are even more prevalent in these increasingly complex experimental paradigms. The integration of data from a variety of methodologies will be essential to replicate the intricacies of the nervous system.

Finally, the field of artificial intelligence has the potential to spawn further advances by aligning vast and diverse datasets. Application of this exciting new technology to the complexity of neuroscience data may reveal previously unrecognized insights.

Combining long-term continuous investigation of relevant live-cell models with novel research workflows and integrated analysis will yield significant breakthroughs that will benefit our aging society.

Susana L. Alcantara
Neuroscience Program Leader, Essen BioScience (Sartorius)

REVIEW

How neuroinflammation contributes to neurodegeneration

Richard M. Ransohoff

Neurodegenerative diseases such as Alzheimer's disease, Parkinson's disease, amyotrophic lateral sclerosis, and frontotemporal lobar dementia are among the most pressing problems of developed societies with aging populations. Neurons carry out essential functions such as signal transmission and network integration in the central nervous system and are the main targets of neurodegenerative disease. In this Review, I address how the neuron's environment also contributes to neurodegeneration. Maintaining an optimal milieu for neuronal function rests with supportive cells termed glia and the blood-brain barrier. Accumulating evidence suggests that neurodegeneration occurs in part because the environment is affected during disease in a cascade of processes collectively termed neuroinflammation. These observations indicate that therapies targeting glial cells might provide benefit for those afflicted by neurodegenerative disorders.

The human central nervous system (CNS) might represent the most complex entity in existence, although conclusive evidence to support or falsify that hypothesis will probably forever be elusive. Nonetheless, the CNS is beyond question the most elaborate system of which we have daily experience. CNS disorders alter and often degrade the structure and function of this intricate organ. Neurodegeneration is a common (but not invariable) component of CNS disorders and includes processes by which previously established CNS functions such as mobility, memory and learning, judgment, and coordination are progressively lost. Neurodegenerative diseases primarily occur in the later stages of life, positioning time as an essential cofactor in pathogenesis of the major neurodegenerative disorders in a mechanism driven fashion (*1*–*3*). The achievements of medicine and public health efforts in reducing early- and midlife mortality from certain cancers, infectious diseases, and cardiovascular disorders mean that a larger number of individuals are aging and therefore susceptible to neurodegenerative disease by virtue of their survival. The large cohort of aging people in the developed world threatens society with a substantial burden of care for those afflicted with neurodegeneration (*4*). Moreover and most poignantly, these diseases rob affected persons of those attributes that make long lives worth living: thinking, feeling, remembering, deciding, and moving. Here I consider neuroinflammation in neurodegeneration, a topic that comprises most of the nonneuronal contributors to the cause and progression of neurodegenerative disease. The study of this topic is animated by our hope that meaningful action, in the form of novel treatments, will follow understanding.

What is neurodegeneration?

Neurons are the primary cells of the CNS and endow it with its distinctive functions. Connections between neurons are enacted at synapses, where neurotransmitters are released in quanta to deliver an excitatory or inhibitory signal to the synaptic-target neuron. Cell processes that deliver these signals are termed axons, whereas dendrites receive synaptic inputs. Each of the ~10^{11} neurons in the human brain integrates many synaptic inputs from other neurons and, for each input received, may or may not initiate an axonal action potential and thereby provide synaptic input to its target neuron—a system comprising 10^{15} connections in all.

Neurodegeneration by definition disturbs the properties of the CNS and therefore affects neuronal function, as well as the structure or survival of neurons. Unlike primary cells from skin, the liver, or muscle, neuronal cells of the CNS do not regenerate after damage by disease, ischemia (deprivation of oxygen, glucose, or blood flow), or physical trauma. Because the complexity of the human CNS is so great, neurodegenerative disorders that derange its function have been challenging to understand and treat: No therapeutics ameliorate the natural course of neurodegenerative disease.

Major neurodegenerative diseases include Alzheimer's disease (AD), frontotemporal lobar dementia (FTLD), Parkinson's disease (PD), and amyotrophic lateral sclerosis (ALS). Individuals diagnosed with multiple sclerosis (MS) are also at risk of developing a neurodegenerative course, typically at later stages of the disease; such cases are termed progressive MS (P-MS). One might consider that AD, PD, and ALS are primary neurodegenerative diseases, in which the initial signs of pathology affect neurons. By comparison, neurodegeneration in P-MS appears to be secondary to the initiating events, which target CNS myelin.

"Neuroinflammation has been famously difficult to define in relation to neurodegenerative disease."

Those studying neurodegenerative conditions rely on a shared set of research tools. Among many others, neurodegeneration researchers draw from neuropathology (analysis of affected tissue), genetics, and model systems. Most neurodegenerative disorders directly affect only the nervous system and specifically the CNS (brain, spinal cord, and optic nerve), as distinguished from the peripheral nervous system (PNS), which encompasses the nerves and muscles of the body and its internal organs. Over many decades of dedicated study, neuropathologists have found that discrete populations of neurons are lost or impaired in each of these diseases—for example, pigmented dopamine neurons in PD and neurons of the motor system in ALS. Additionally, AD, ALS, FTLD, and PD feature characteristic protein aggregates within neurons; representative instances are neurofibrillary tangles in AD and Lewy bodies in PD. A distinctive tissue change termed amyloidosis, in which extracellular proteins are arrayed in beta-pleated sheets, typifies the cortex and hippocampus in AD and in PD with dementia (PDD) (Table 1). In both AD and PDD, N-terminal fragments of amyloid precursor protein (APP) are the major constituents of the extracellular amyloid deposits. Discovering the neurons targeted by each disease and identifying disease-selective pathological protein aggregates has enabled substantial progress in understanding these disorders.

Table 1. Protein aggregates in neurodegenerative diseases. A-β, N-terminal amyloidogenic fragments of APP; MAPT, microtubule-associated protein tau; TDP-43, 43-kDa TAR DNA-binding protein.

Composition of aggregate	Associated disorders	Physiological localization	Localization in disease
A-β	AD, PDD	Membrane	Extracellular
MAPT	AD, FTLD-tau	Axonal	Cytoplasmic
α-synuclein	PD, PDD	Synaptic	Cytoplasmic
TDP-43	ALS, FTLD-TDP	Nuclear	Cytoplasmic

Biogen, 225 Binney Street, Cambridge, MA 02142, USA.
Email: richard.ransohoff@biogen.com

A small minority (<5%) of patients affected by AD, PD, ALS, or FTLD demonstrate Mendelian inheritance of their disease. Furthermore, for each disorder and each major constituent of the characteristic protein aggregate, rare mutations of the encoding genes validate a causal relation between mutant proteins and disease (*5*–*7*). For the most part, disease manifestations of the Mendelian forms of neurodegeneration phenocopy those of the sporadic cases, save only for earlier onset in the case of the former. For this reason, it is considered highly likely that a pathogenic relationship also holds between protein aggregates and disease for sporadic cases. Given their importance for categorizing distinct disorders, the protein aggregates are used in a new molecular nosology that includes synucleinopathies, tauopathies, and amyloidoses. Researchers have accumulated substantial evidence favoring the interlinked hypotheses that relate protein aggregates to sporadic neurodegenerative disease. Nonetheless, only successful therapeutic trials targeting protein aggregates, their upstream causes, or their downstream effects will confirm that these devastating diseases are indeed caused by processes related to protein aggregates.

The current paradigm for these major primary neurodegenerative diseases includes additional commonalities. First, neurodegenerative diseases including PD, AD, and FTLD demonstrate a predictable temporospatial pathological evolution, involving one brain region followed by another and then another. It has been proposed that this mode of progression is mediated at least in part by the transfer of pathogenic protein forms between adjacent cells (*8, 9*). It is important, however, to emphasize that this intra-individual spreading of pathogenic protein, although reminiscent of prion disease, is not proposed to be associated with risk of exposure to affected persons or their tissues (*10*). Furthermore, although cell-to-cell spread of fibrillar forms of pathogenic proteins can be demonstrated experimentally, its role in disease progression is not a matter of universal agreement. It remains plausible instead that pathology occurs serially in vulnerable neuronal populations, which are proposed to have increasing regionally restricted frequency in the aging brain (*11*). Second, it is hypothesized that protein aggregates, although visually striking when viewed in tissue sections, may not in all cases represent the crucial pathogenic alteration, but rather that their fibrillar or oligomeric precursors may have direct neurotoxicity (*11*). Third, it is widely held that defects in mitochondrial function and turnover (termed mitophagy), autophagy, and management of oxidative stress are involved in various ways in each of these disorders (*12*).

What is neuroinflammation?

Neuroinflammation has been famously difficult to define in relation to neurodegenerative disease. In contrast, neuroinflammation in multiple sclerosis (MS) is unambiguous, comprising often florid infiltration of the CNS parenchyma by blood-derived lymphocytes and monocyte-derived macrophages, accompanied by frank impairment of blood-brain barrier (BBB) function and intense glial reaction. Neuroinflammation in diseases such as AD, PD, and ALS is typified instead by a reactive morphology of glial cells, including both astrocytes and microglia (Fig. 1), accompanied by low to moderate levels of inflammatory mediators in the parenchyma. This reaction, both cellular and molecular, is not distinguishable between one disease and another or from other conditions such as stroke or traumatic injury. Given this lack of specificity, it is easy to conclude that the glial reaction is secondary to neuronal death or dysfunction and is accordingly unlikely to provide useful targets for therapeutic intervention or topics for intensive investigation.

It has been several decades since the detection of inflammatory mediators in AD and PD autopsy brain sections led to the proposal that neuroinflammation might promote progression of these disorders (*13, 14*). Additional support came from a population-based prospective study that used pharmacological records and showed a dose-related negative correlation between the use of nonsteroidal anti-inflammatory drugs (NSAIDs) during midlife and the likelihood of later developing AD (*15*). However, subsequent AD treatment trials using NSAIDs, glucocorticosteroids, or selective cyclooxygenase-2 inhibitors failed to provide evidence for efficacy and imposed considerable adverse effects (*16*), leaving inflammation's part in neurodegenerative disease in doubt through the early years of the 21st century.

In this regard, it could until recently be argued that neurodegeneration was mainly a cell-autonomous process affecting neurons. Neurodegenerative disease research advanced the understanding of molecular pathogenesis by identifying selective neuron populations that are affected in each disease. Moreover, there was a potent prima facie plausibility relating the affect-

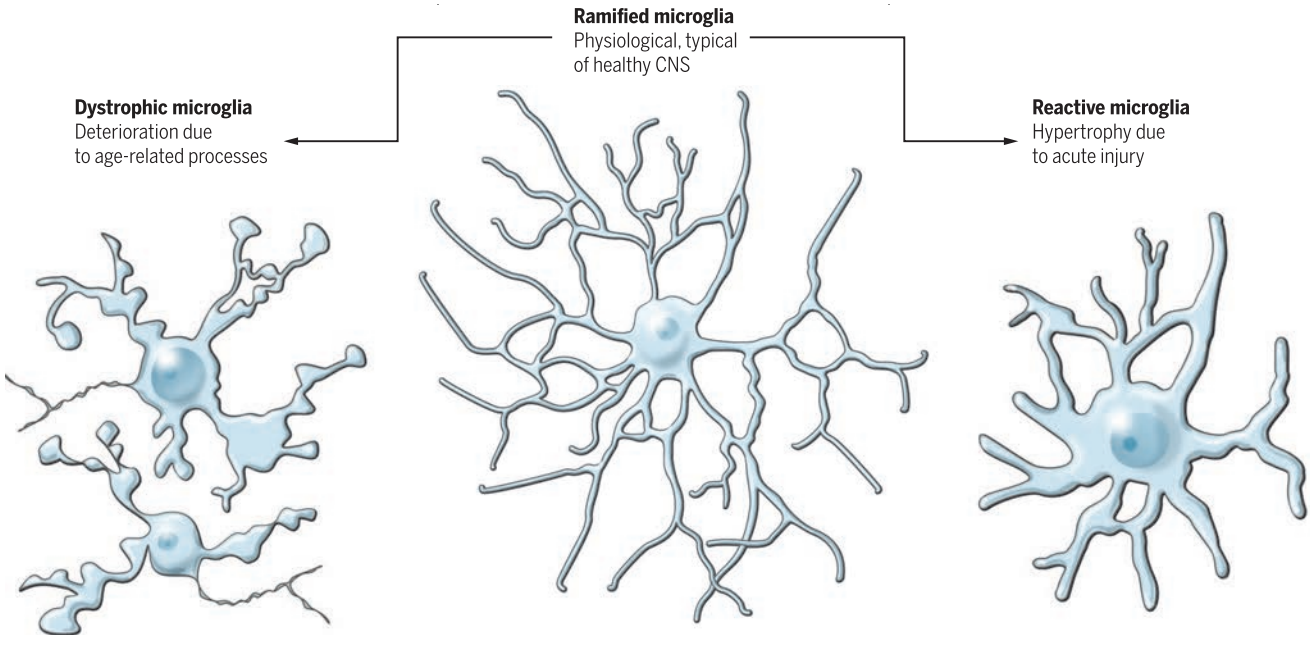

Fig. 1. Morphology of ramified (healthy CNS), reactive, and dystrophic microglia. Microglia reflect their response to the environment in part through their morphology. Morphology does not reliably reflect function, dysfunction, or RNA expression profile phenotype but only demonstrates that the cell is responding to altered homeostasis (*76*). The cartoon depicts three states of microglial morphology: ramified (physiological) microglia, typical of those observed in the healthy CNS; reactive microglia, characteristic of those seen after acute injury; and dystrophic microglia, as observed in the aging brain, particularly in the context of neurodegeneration.

Table 2. Selected elements of the CNS neuroinflammatory system.

Name	Category	Peripheral counterpart	Peripheral function	CNS function
Microglia	Myeloid cell	Circulating monocyte or tissue macrophage	Host defense, wound repair	Synapse formation (*58*), refinement (*59*), monitoring (*60*), and maintenance; inflammatory response; adult neurogenesis modulation (*61*, *62*)
Astrocyte	Glial cell	None	Not applicable	Glutamate reuptake, ionic buffering, water balance, energy substrate for neurons, BBB maintenance (*63*), inflammatory response (*64*, *65*)
Oligodendrocyte	Glial cell	Schwann cell	Myelination of peripheral axons	Myelination of CNS axons, trophic support for myelinated axons (*66*)
$NG2^+$ glia	Glial cell	None	Not applicable	Precursor to adult oligodendroglia (*67*, *68*), inflammatory response (*69*)
CX3CR1	Chemokine receptor	Same as CNS	Monocytes patrolling vessel walls, inflammatory response	Neuron-glia interactions (*50*, *70*, *71*)
C1q, C3, C4, CR3	Complement components	Same as CNS	Host defense	Synaptic pruning (*72*)
TNF-α	Cytokine	Same as CNS	Host defense, inflammation	Synaptic scaling (*73*), neuroprotection (*74*, *75*)

ed cell population with signs and symptoms of the disease, as with neuronal death in the motor system in ALS, in which patients suffer muscle atrophy and weakness. Incisive PD studies using in vitro systems, including the use of somatic cells reprogrammed to become (for example) dopamine neurons, provided support for this hypothesis (*17*).

Demonstrating a non–cell-autonomous neurodegenerative process would open new prospects for understanding how neurodegeneration might be promoted by local CNS inflammation, but it was unclear how to proceed until genetic bases for the Mendelian forms of neurodegeneration were identified and then used to develop in vivo disease models. Dramatic findings came from studying a mouse model of ALS in which the gene encoding mutant superoxide dismutase-1 (mSOD1) was expressed using a ubiquitous pro-moter, yielding a severe phenotype of motor neuron death with weakness and shortened life span, as observed in humans carrying the same gene variant (*18*). The question was deceptively simple: Did it matter whether the *mSOD1* transgene was expressed in cells other than neurons? Modifying this model to enable inducible deletion of *mSOD1* from all myeloid cells (represented in the CNS by microglia) produced an unexpected prolongation of life span without altering the timing of disease onset (*19*). A comparable effect was obtained by conditionally deleting *mSOD1* from astrocytes (*20*), and this manipulation also suppressed microglial acquisition of reactive morphology, suggesting a pathogenic scheme by which astrocyte-microglial interactions promoted mSOD1-related neurodegeneration (*21*, *22*). These results showed unequivocally that lack of transgene expression by glia altered the course in the mSOD1 model. Additional positive support for non–cell-autonomous neuronal degeneration came from expression of a mutant α-synuclein transgene selectively in astrocytes, which produced PD-like pathology and behavioral deficits in mice (*23*, *24*). Simultaneously, reports emerged that autopsy tissue sections from cases of PD, PDD, and other diseases associated with aggregated α-synuclein (collectively termed synucleinopathies) featured distinctive aggregates in astrocytes and oligodendrocytes, as well as neuronal Lewy bodies (*25*, *26*).

Unlike neurons, microglia and astrocytes are challenging to study in vitro, partially because they adopt a reactive nonphysiological phenotype upon explant culture, showing a gene expression profile that is markedly different from that of glia when isolated and analyzed immediately ex vivo (*27*). Additionally, the intrinsic functions of glia are exerted in support of neurons within a complex three-dimensional matrix, so that meaningful glial properties cannot be modeled in two-dimensional cultures (*28*). Given this difficulty of using reductionist experimental approaches to evaluate glial neuroinflammatory properties, and in view of the nonspecific nature of cardinal inflammatory changes in glia during neurodegenerative disease, it seems reasonable to propose an all-purpose definition of neuroinflammation in neurodegeneration: contributions by glial cells, elements of the BBB, or systemic inflammatory processes that are harmful or beneficial to the severity of neurodegenerative disease. This broad definition acknowledges the primacy of neurons in brain function and disease and further recognizes that the glial reaction to neuronal injury, dysfunction, or death may be helpful or harmful (or neutral). Additionally, it is proposed that neurodegeneration can progress in a fashion that is non–cell-autonomous with respect to neurons, suggesting that glial biology, the BBB, or the systemic environment all could offer legitimate targets for therapeutic intervention. Moreover, there is no implied similarity to peripheral inflammatory reactions, as demonstrated (for example) by skin or gut macrophages in response to pathogens, because applications of knowledge gleaned from studying peripheral host defense and wound repair have been misleading when applied incautiously to CNS glia (*29*).

Genetic clues associate neurodegeneration with neuroinflammation

Progress in every domain of biological science has been propelled by genome-level data, and neuroinflammation is no exception. CNS cells involved in neuroinflammatory reactions (microglia, astrocytes, and proteoglycan-$NG2^+$ glia; Table 2) were first identified by their altered morphologies, a descriptive analysis that was unavailing for deciphering whether the cellular reaction was advantageous or deleterious or whether the reaction made any meaningful contribution to pathogenesis. It was therefore a substantial advance to associate Nasu-Hakola disease with homozygous null mutations of *TREM2* (*30*), a gene expressed only by microglia among CNS cells. Despite the extreme rarity of this neurodegenerative disorder, its CNS manifestations of early midlife dementia were unambiguously referable to microglial dysfunction and represented the first evidence that intact microglial activities were essential for brain homeostasis. Relatively subtle *TREM2* genetic variants have now been associated with AD, FTLD, and possibly PD (*31*). Notwithstanding the wealth of *TREM2* coding variants with clinical phenotypes that we can investigate, a mechanistic under-standing of why *TREM2* plays such a major role in the risk for neurodegeneration remains contentious and unresolved (*32*)(Fig. 2). Nonetheless, *TREM2* genetics have shown unmistakably that dysfunction of microglia or infiltrating myeloid cells could make a primary rather than a reactive contribution to neurodegeneration and thereby galvanized this field of research.

The most salient effects have been found in AD research, where genome-wide association studies (GWAS), supplemented by examination of rare variants and identification of expression quantitative trait loci in microglia, have identified about 20 well-validated genes harboring risk alleles, of which about half are predominantly or only expressed in microglia (*33*). For example, *APOE*, the dominant risk-associated gene, is mainly expressed in astrocytes and reactive microglia (*34*). The availability of convenient, searchable, brain cell–specific databases of RNA-sequencing and microarray expression profiles enables the pursuit of this research direction (*34*–*36*).

In P-MS, inflammation begets neurodegeneration—but how?

MS is relatively common (prevalence of 1:1000) among susceptible populations. Onset occurs at about age 30, with two-thirds of affected individuals being women. Life is only modestly shortened by MS; the disease course is about 45 years. In its early phases of clinical presentation, MS is distinctive, which led to its characterization as a discrete disease entity more than 150 years ago. Patients experience abrupt (minutes to hours) or subacute (days to weeks) alterations in neurological function, termed attacks or relapses. In its early phase, MS remains a disturbing but not disabling disease for many patients, about 85% of whom present with the relapsing form of the disease. Relapses occur from time to time, with substantial or complete resolution, and attacks leading to permanent disability are more the exception than the rule. MS patients exhibiting this disease pattern are said to have relapsing-remitting MS (RR-MS). Importantly, neurological function, as experienced by patients and assessed by neurologists, remains stable between relapses. Among all CNS diseases [except for neuromyelitis optica (NMO), an autoimmune astrocytopathy], MS is distinctive by virtue of its recurrent (multiphasic) and regionally diverse (multifocal) symptoms, punctuated by periods of symptomatic quiescence. The recurrent nature of MS is most likely due to cellular autoimmunity to myelin that drives the disease.

After a variable period of RR-MS, the disease appears to change its behavior. Attacks become much less common and may cease altogether, to be replaced by a progressive phase during which patients slowly and often relentlessly worsen, without periods of symptom reversal or improvement. This pattern of symptom evolution is designated secondary P-MS. In about 10% of cases, MS presents with progression from the onset, lacking the earlier phase of attacks and remissions. It seems most likely that this symptom pattern, termed primary P-MS, represents the sequelae of typical MS lesions that were clinically silent during the inflammatory phase of disease (*37, 38*). However, recurrent longstanding neuroinflammation does not inevitably lead to neurodegeneration: In NMO, the other major inflammatory disease of the human CNS, which is caused by autoantibody-mediated astrocytopathy directed at aquaporin-4, there is no progressive phase for the vast majority of patients.

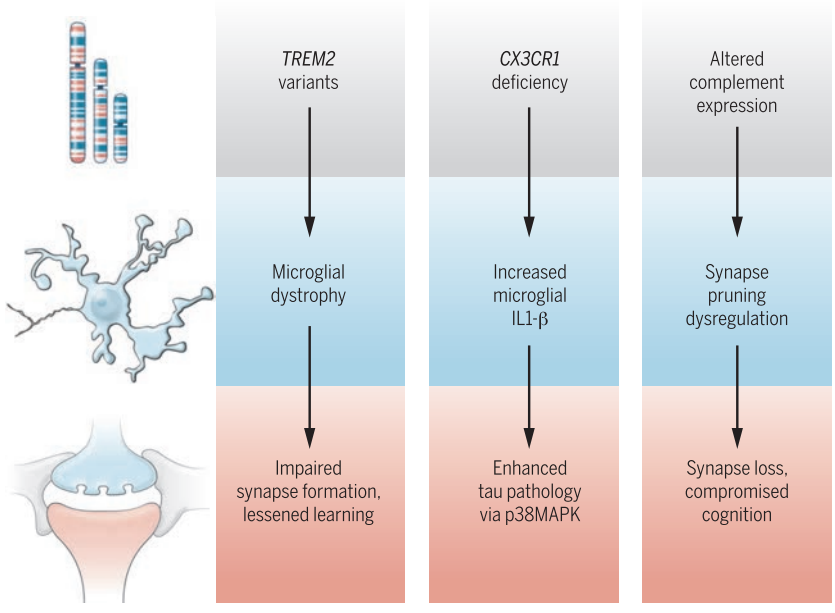

Fig. 2. Pathways from microglial gene variants or altered gene expression to neurodegeneration. *TREM2* variants (*31*), targeted deletion of *CX3CR1* (*70*), and altered complement expression (*77*) have all been associated with neurodegenerative phenotypes in the clinic or in animal models (top row). The middle and bottom rows show the downstream effects. The TREM2 phenotype of microglial dystrophy was studied by means of targeted gene deletion in mice (*78*); the behavioral effect, namely, cognitive deficit in heterozygous *TREM2* haploinsufficiency, was defined clinically (left column) (*79*). Also shown are the neurodegenerative effects of *CX3CR1* deficiency in hTau mice (middle column) (*70*) and complement dysregulation in a model of amyloid pathology (right column) (*77*).

There is a coherent hypothesis to account for neurodegeneration after inflammatory demyelination in MS (Fig. 3). In this view, the sequelae of acute demyelination can lead to progressive loss of axons and neurons unless robust remyelination occurs, which happens in a subset of MS cases (*39, 40*). In addition to these cellular sequelae of demyelination that produce neurodegeneration in MS, meningeal inflammatory infiltrates are established at the earliest stages of disease (*41, 42*) and continue to be detectable during clinical progression (*43*), remaining readily observable at autopsy (*44*). Tissue studies (*41, 44*) and magnetic resonance imaging–pathological correlations (*43*) support the likelihood that these intrathecal inflammatory foci drive ongoing demyelination of underlying cortical tissue.

Which neuroinflammatory treatment target for which disease?

The study of the neuroinflammatory aspects of neurodegeneration is now in a "good news–bad news" situation. Genetic, epidemiological, and descriptive research using brain tissue from patients—as well as results from model systems including genetically modified mice, zebrafish, flies, worms, and induced pluripotent stem cells (iPSCs), which harbor disease-associated genetic variants in the native genomic context—forcefully implicate inflammation in the neurodegenerative process. As one example, mice lacking progranulin, which is encoded by *Grn* and expressed predominantly in the microglia of both humans (*34*) and mice (*36*), showed substantial dysregulation of microglial complement gene expression and of lysosome maturation. These findings were associated with evidence of unexpectedly selective and regionally restricted loss of inhibitory vesicular GABA (γ-aminobutyric acid) transporter–labeled synapses of parvalbuminpositive neurons in the ventral thalamus, where complement deposition was observed on both excitatory and inhibitory synapses. In turn, aged $Grn^{-/-}$ mice exhibited altered thalamic excitability and excessive grooming. The relationship to complement gene expression was established by showing substantial phenotypic rescue in $Grn^{-/-}$::$C1qa^{-/-}$ mice (*45*). These findings are exciting because of the demonstration that a specific neuronal circuit can be functionally derailed through complement- and microglial-mediated synapse removal. At the same time, several issues were not addressed, including the relation of the phenotype to loss of progranulin as opposed to loss of granulin peptides (derived by proteolysis from progranulin); how complement dysregulation leads to selective synapse loss, given that deposition does not discriminate excitatory from inhibitory synapses; the role (if any) of lysosomal trafficking in the phenotype; and signaling pathways underlying altered microglial gene expression (*45*). Overall, this study advances our understanding of progranulin deficiency while standing in continuity with other studies showing that specific neuroinflammatory genes or pathways are plausibly associated with AD, PD, and ALS. Nonetheless, no therapeutics have emerged from this line of re-

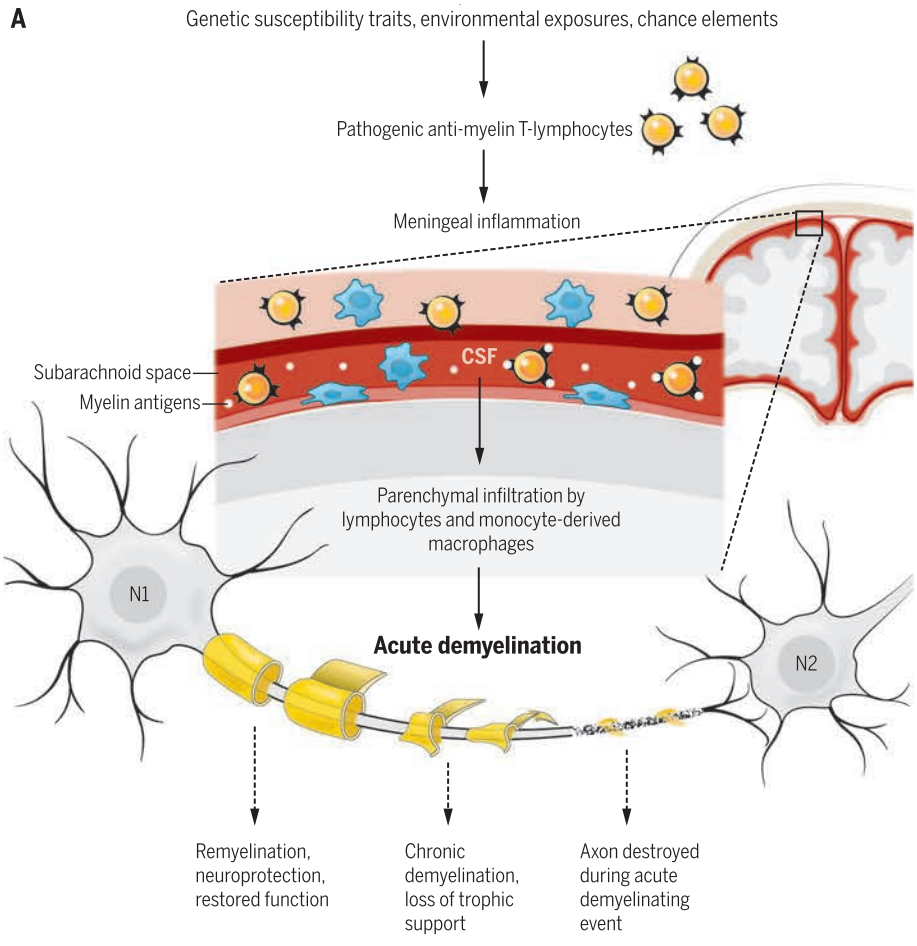

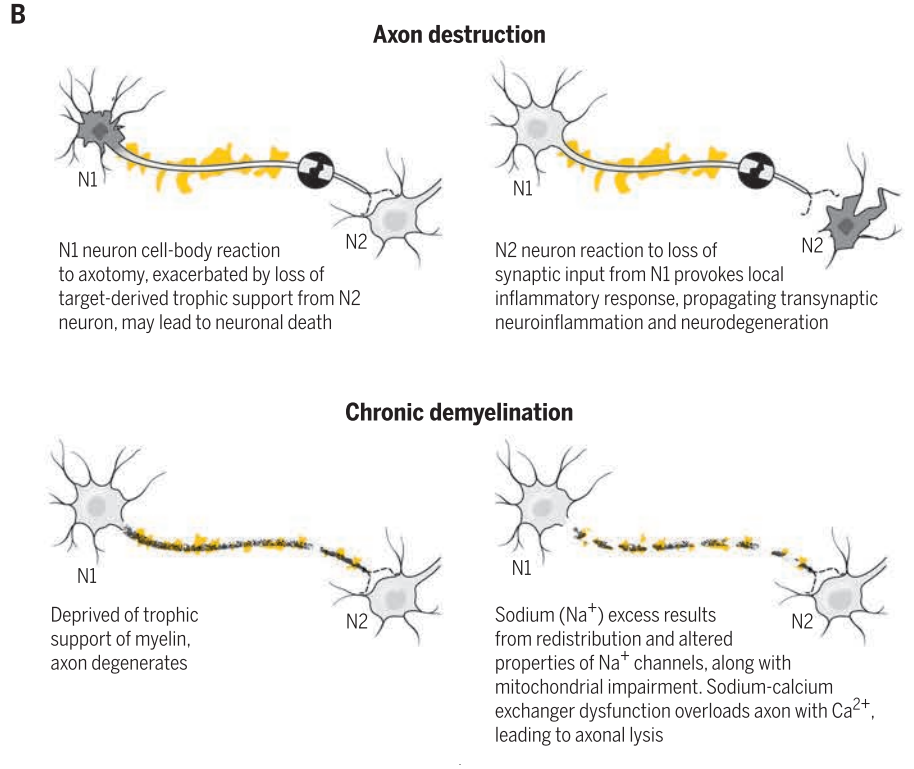

Fig. 3. Pathogenesis of neurodegeneration in P-MS. (**A**) Pathogenesis and short-term outcomes of acute demyelination. N1 is a neuron, shown extending an axon to synapse with neuron N2. The axon is myelinated (yellow shapes). In MS, generation of pathogenic antimyelin T cells results from gene-environment interactions, supplemented by yet-to-be-identified chance elements (*80*–*82*). Pathogenic T cells traffic through cerebrospinal fluid (CSF) and can be restimulated by myelin antigens in the subarachnoid space (*83*) to initiate meningeal inflammation (*41*); this is followed by parenchymal invasion by T cells and monocyte-derived macrophages, which mediate demyelination. Potential alternative outcomes of acute demyelination are shown at the bottom. (**B**) Outcomes of acute axotomy during demyelination and of chronic demyelination. Acute axotomy (top) causes a stereotyped cell-body reaction for neuron N1. Contingent on the proximity of the axotomy to the neuron cell body and the loss of trophic support from N2, this reaction may lead to the death of the N1 neuron. Additionally, removal of synaptic input can produce an intense local inflammatory reaction around the N2 target neuron (*84*) as glia sense the change in neuronal function. Chronic demyelination (bottom) deprives axons of essential trophic support, threatening their viability and producing susceptibility to axon degeneration (*85*). Furthermore, chronic demyelination causes redistribution of sodium (Na^+) channels away from nodes of Ranvier into the demyelinated segment, as well as altered channel expression (*86*), worsening the risk of Na^+ overload. Axonal conduction produces a Na^+ influx that is poorly balanced by Na^+- and K^+-dependent adenosine triphosphatase, which is impaired as a result of mitochondrial dysfunction (*87*). Sustained Na^+ overload reverses the Na^+-Ca^{2+} antiporter, and the resulting Ca^{2+} influx activates calcium-dependent enzymes, lysing the axon.

search. There are reasonable explanations for this circumstance, including the inherent complexity of neurodegenerative disease, challenges related to clinical trial design, and lack of actionable high-througput screening platforms (particularly as regards cultured glial cells), among others. For now, the following strategic formulations to address these issues may be useful.

Genetics are key

Target identification based on human-disease genetic validation enhances prospects for success. GWAS loci have proven to be robustly reproducible, and the initial threshold for genome-wide significance appears durable (*46*). Proceeding from loci to genes to pathways remains challenging, but methods for confirming "hits" are highly promising. Systems biology can make additional contributions to target prosecution.

Remain unbiased even after the omics are done

Confronted with an uncertain comprehension of neurodegenerative disease, it is tempting to rely on dogma. Deciphering inflammation has

"...neurodegeneration can progress in a fashion that is non–cell-autonomous with respect to neurons, suggesting that glial biology, the BBB, or the systemic environment all could offer legitimate targets for therapeutic intervention."

been challenging, even in the familiar context of adaptive-immune disorders such as rheumatoid arthritis. Innate immunity in the CNS is an unfamiliar landscape in which well-known actors and their properties may be upended. One example comes from considering neuroprotective properties of TNF-α (tumor necrosis factor–α) and the associated NF-κB (nuclear factor κB) signaling pathway (Table 2).

New models will be needed

In vitro cultures of glial cells have been poorly predictive of relevant activities and phenotypes in vivo (*28*). Novel systems including organotypic brain-slice cultures (*47*), zebrafish (*48*), and iPSCs (for astrocytes) (*49*) are required.

Consider the periphery

Glial cell phenotypes are modulated profoundly by peripheral inflammatory stimuli (*50*), including dysbiosis due to altered gut microbiota (*51, 52*), findings which have been confirmed in clinical studies (*53*). Compared with direct manipulation of CNS cells or factors, manipulating the peripheral environment to modulate neurodegenerative disease would be manifestly less encumbered by concerns about safety, biomarker selection, or off-target effects. This consideration also pertains directly to the potential role of the BBB in neurodegeneration (*54, 55*), which was highlighted by the finding that access of blood-borne pathogens to the CNS in the context of a compromised BBB might stimulate amyloid deposition (*56*).

Conclusions and future prospects

The study of neuroinflammation as a major contributor to neurodegeneration is, in some ways, fewer than two decades old, dating from the demonstration that altered microglia produce a neurodegenerative phenotype in humans (*57*). This line of research encompasses disease-related alterations in the environment in which neurons exist, including those coming from glial reaction to the disorder, as well as intra-CNS effects of peripheral inflammatory stimuli and the degradation of homeostasis caused by an impaired BBB. Available research resources such as genomic and epigenetic data sets, model organisms, and iPSC-derived cells enable an unprecedented scope of research attack. Given these circumstances, neuroinflammation researchers should be cognizant of the task's complexity and previous defeats, while approaching with cautious optimism the prospect of therapeutic success against these severe diseases.

REFERENCES AND NOTES

1. R. Madabhushi, L.Pan, L. H.Tsai, *Neuron* **83**, 266–282 (2014).
2. R. Lardenoije *et al.*, *Prog. Neurobiol.* **131**, 21–64 (2015).
3. G. G. Kovacs *et al.*, *Neuroscience* **269**, 152–172 (2014).
4. H. Leicht *et al.*, *PLOS ONE* **8**, e70018 (2013).
5. M. Goedert *et al.*, *Philos. Trans. R. Soc. Lond. B Biol. Sci.* **356**, 213–227 (2001).
6. S. Ajroud-Driss, T. Siddique, *Biochim. Biophys. Acta* **1852**, 679–684 (2015).
7. V. Chouraki, S. Seshadri, *Adv. Genet.* **87**, 245–294 (2014).
8. M. Jucker, L. C. Walker, *Nature* **501**, 45–51 (2013).
9. L. C. Walker, M. I. Diamond, K. E. Duff, B. T. Hyman, *JAMA Neurol.* **70**, 304–310 (2013).
10. J. Brettschneider, K. Del Tredici, V. M.-Y. Lee, J. Q. Trojanowski, *Nat. Rev. Neurosci.* **16**, 109–120 (2015).
11. D. J. Selkoe, J. Hardy, *EMBO Mol. Med.* **8**, 595–608 (2016).
12. M. Redmann, V. Darley-Usmar, J. Zhang, *Aging Dis.* **7**, 150–162 (2016).
13. P. L. McGeer, S. Itagaki, B. E. Boyes, E. G. McGeer, *Neurology* **38**, 1285–1291 (1988).
14. J. Rogers *et al.*, *Neurobiol. Aging* **17**, 681–686 (1996).
15. B. A. in 't Veld *et al.*, *N. Engl. J. Med.* **345**, 1515–1521 (2001).
16. D. Jaturapatporn, M. G. Isaac, J. McCleery, N. Tabet, *Cochrane Database Syst. Rev.* **2**, CD006378 (2012).
17. L. Qiang, R. Fujita, A. Abeliovich, *Neuron* **78**, 957–969 (2013).
18. D. L. Price *et al.*, *Ann. N. Y. Acad. Sci.* **920**, 179–191 (2000).
19. S. Boillée *et al.*, *Science* **312**, 1389–1392 (2006).
20. K. Yamanaka *et al.*, *Nat. Neurosci.* **11**, 251–253 (2008).
21. S. Boillée, C. Vande Velde, D. W. Cleveland, *Neuron* **52**, 39–59 (2006).
22. C. S. Lobsiger, D. W. Cleveland, *Nat. Neurosci.* **10**, 1355–1360 (2007).
23. X. L. Gu *et al.*, *Mol. Brain* **3**, 12 (2010).
24. J. C. McGann, D. T. Lioy, G. Mandel, *Curr. Opin. Neurobiol.* **22**, 850–858 (2012).
25. D. Brück, G. K. Wenning, N. Stefanova, L. Fellner, *Neurobiol. Dis.* **85,** 262–274 (2016).
26. L. Fellner, K. A. Jellinger, G. K. Wenning, N. Stefanova, *Acta Neuropathol.* **121**, 675–693 (2011).
27. O. Butovsky *et al.*, *Nat. Neurosci.* **17**, 131–143 (2014).
28. R. M. Ransohoff, V. H. Perry, *Annu. Rev. Immunol.* **27**, 119–145 (2009).
29. R. M. Ransohoff, *Nat. Neurosci.* **19**, 987–991 (2016).
30. M. M. Bianchin *et al.*, *Cell. Mol. Neurobiol.* **24**, 1–24 (2004).
31. J. Walter, *J. Biol. Chem.* **291**, 4334–4341 (2016).
32. R. E. Tanzi, *N. Engl. J. Med.* **372**, 2564–2565 (2015).
33. C. Villegas-Llerena, A. Phillips, P. Garcia-Reitboeck, J. Hardy, J. M. Pocock, *Curr. Opin. Neurobiol.* **36**, 74–81 (2016).
34. M. L. Bennett *et al.*, *Proc. Natl. Acad. Sci. U.S.A.* **113**, E1738–E1746 (2016).
35. I. R. Holtman *et al.*, *Glia* **63**, 1495–1506 (2015).
36. Y. Zhang *et al.*, *J. Neurosci.* **34**, 11929–11947 (2014).
37. O. H. Kantarci *et al.*, *Ann. Neurol.* **79**, 288–294 (2016).
38. B. A. Cree, *Handb. Clin. Neurol.* **122**, 211–230 (2014).
39. P. Patrikios *et al.*, *Brain* **129**, 3165–3172 (2006).
40. B. Kornek *et al.*, *Am. J. Pathol.* **157**, 267–276 (2000).
41. C. F. Lucchinetti *et al.*, *N. Engl. J. Med.* **365**, 2188–2197 (2011).
42. B. Obermeier *et al.*, *Nat. Med.* **14**, 688–693 (2008).
43. M. Absinta *et al.*, *Neurology* **85**, 18–28 (2015).
44. R. Magliozzi *et al.*, *Ann. Neurol.* **68**, 477–493 (2010).
45. H. Lui *et al.*, *Cell* **165**, 921–935 (2016).
46. J. R. Wendland, M. D. Ehlers, *Biol. Psychiatry* **79**, 650–656 (2016).
47. A. Masuch *et al.*, *Glia* **64**, 1285–1297 (2016).
48. D. A. Lyons, W. S. Talbot, *Cold Spring Harb. Perspect. Biol.* **7**, a020586 (2015).
49. P. W. Zhang *et al.*, *Glia* **64**, 63–75 (2016).
50. A. E. Cardona *et al.*, *Nat. Neurosci.* **9**, 917–924 (2006).
51. D. Erny *et al.*, *Nat. Neurosci.* **18**, 965–977 (2015).
52. V. Rothhammer *et al.*, *Nat. Med.* **22**, 586–597 (2016).
53. C. Holmes *et al.*, *Neurology* **73**, 768–774 (2009).
54. Z. Zhao, A. R. Nelson, C. Betsholtz, B. V. Zlokovic, *Cell* **163,** 1064–1078 (2015).
55. R. D. Bell *et al.*, *Neuron* **68**, 409–427 (2010).
56. D. K. Kumar *et al.*, *Sci. Transl. Med.* **8**, 340ra72 (2016).
57. H. H. Klünemann *et al.*, *Neurology* **64**, 1502–1507 (2005).
58. C. N. Parkhurst *et al.*, *Cell* **155**, 1596–1609 (2013).
59. D. P. Schafer *et al.*, *Neuron* **74**, 691–705 (2012).
60. M. E. Tremblay, R. L. Lowery, A. K. Majewska, *PLOS Biol.* **8**, e1000527 (2010).
61. L. Fourgeaud *et al.*, *Nature* **532**, 240–244 (2016).
62. R. M. Ransohoff, *Nature* **532**, 185–186 (2016).
63. B. Obermeier, A. Verma, R. M. Ransohoff, *Handb. Clin. Neurol.* **133**, 39–59 (2016).
64. M. Pekny *et al.*, *Acta Neuropathol.* **131**, 323–345 (2016).
65. M. V. Sofroniew, *Nat. Rev. Neurosci.* **16**, 249–263 (2015).
66. K. A. Nave, *Nature* **468**, 244–252 (2010).
67. M. O'Rourke, R. Gasperini, K. M. Young, *Neural Regen. Res.* **9**, 1261–1264 (2014).
68. A. Nishiyama, L. Boshans, C. M. Goncalves, J. Wegrzyn, K. D. Patel, *Brain Res.* **1638**, 116–128 (2016).
69. Z. Kang *et al.*, *Nat. Neurosci.* **16**, 1401–1408 (2013).
70. K. Bhaskar *et al.*, *Neuron* **68**, 19–31 (2010).
71. R. M. Ransohoff, A. E. Cardona, *Nature* **468**, 253–262 (2010).
72. A. H. Stephan, B. A. Barres, B. Stevens, *Annu. Rev. Neurosci.* **35**, 369–389 (2012).
73. D. Stellwagen, R. C. Malenka, *Nature* **440**, 1054–1059 (2006).
74. O. Watters, J. J. O'Connor, *J. Neuroinflammation* **8**, 87 (2011).
75. L. Marchetti, M. Klein, K. Schlett, K. Pfizenmaier, U. L. Eisel, *J. Biol. Chem.* **279**, 32869–32881 (2004).
76. V. H. Perry, *Acta Neuropathol.* **120**, 277–286 (2010).
77. S. Hong *et al.*, *Science* **352**, 712–716 (2016).
78. P. L. Poliani *et al.*, *J. Clin. Invest.* **125**, 2161–2170 (2015).
79. L. Montalbetti *et al.*, *Funct. Neurol.* **20**, 71–75 (2005).
80. S. Sawcer *et al.*, *Nature* **476**, 214–219 (2011).
81. R. M. Ransohoff, *Nat. Immunol.* **11**, 570–572 (2010).
82. K. L. Munger, A. Ascherio, *Expert Rev. Clin. Immunol.* **3**, 739–748 (2007).
83. R. M. Ransohoff, B. Engelhardt, *Nat. Rev. Immunol.* **12**, 623–635 (2012).
84. R. B. Banati *et al.*, *Brain* **123**, 2321–2337 (2000).
85. K. A. Nave, *Nat. Rev. Neurosci.* **11**, 275–283 (2010).
86. S. G. Waxman, *Trends Mol. Med.* **12**, 192–195 (2006).
87. R. J. Franklin, C. ffrench-Constant, J. M. Edgar, K. J. Smith, *Neurology* **8**, 624–634 (2012).

NEURODEGENERATION

A human microglia-like cellular model for assessing the effects of neurodegenerative disease gene variants

Katie J. Ryan,[1,2,3,4] Charles C. White,[1,2,4] Kruti Patel,[1,2,3,4] Jishu Xu,[1,2,4] Marta Olah,[4,5] Joseph M. Replogle,[1,2,3,4]* Michael Frangieh,[1,2,4] Maria Cimpean,[1,2,4]† Phoebe Winn,[1,2,4] Allison McHenry,[1,2,4] Belinda J. Kaskow,[1,2,3,4] Gail Chan,[1,2,3,4] Nicole Cuerdon,[1,2,3,4] David A. Bennett,[6] Justin D. Boyd,[1,3] Jaime Imitola,[7] Wassim Elyaman,[4,5] Philip L. De Jager,[4,5] Elizabeth M. Bradshaw[4,5]‡

Microglia are emerging as a key cell type in neurodegenerative diseases, yet human microglia are challenging to study in vitro. We developed an in vitro cell model system composed of human monocyte-derived microglia-like (MDMi) cells that recapitulated key aspects of microglia phenotype and function. We then used this model system to perform an expression quantitative trait locus (eQTL) study examining 94 genes from loci associated with Alzheimer's disease, Parkinson's disease, and multiple sclerosis. We found six loci (*CD33*, *PILRB*, *NUP160*, *LRRK2*, *RGS1*, and *METTL21B*) in which the risk haplotype drives the association with both disease susceptibility and altered expression of a nearby gene (cis-eQTL). In the *PILRB* and *LRRK2* loci, the cis-eQTL was found in the MDMi cells but not in human peripheral blood monocytes, suggesting that differentiation of monocytes into microglia-like cells led to the acquisition of a cellular state that could reveal the functional consequences of certain genetic variants. We further validated the effect of risk haplotypes at the protein level for *PILRB* and *CD33*, and we confirmed that the *CD33* risk haplotype altered phagocytosis by the MDMi cells. We propose that increased *LRRK2* gene expression by MDMi cells could be a functional outcome of *rs76904798*, a single-nucleotide polymorphism in the *LRKK2* locus that is associated with Parkinson's disease.

INTRODUCTION

Genome-wide association studies (GWAS) and sequencing studies have implicated the innate immune system in neurodegenerative diseases, specifically Alzheimer's disease (AD), Parkinson's disease (PD), and multiple sclerosis (MS). An increasing number of disease-specific genetic loci that contain innate immune-specific genes are being identified. For example, *CD33* is known to play a role in AD as shown by our group and others (*1*–*3*), and *TREM2* has been implicated in frontotemporal dementia, PD, and amyotrophic lateral sclerosis in addition to AD (*4*–*9*). To leverage GWAS findings for therapeutic targeting, the GWAS associations must first be translated into functional outcomes, as has been done for *CD33*. We have demonstrated that the *CD33* risk allele leads to increased CD33 expression on the surface of monocytes and to diminished internalization of amyloid-β 42 peptide, supporting a genotype-to-phenotype association for this AD single-nucleotide polymorphism (SNP) (*1*). Mapping gene expression as a quantitative trait [expression quantitative trait locus (eQTL) analysis] can identify which genes in a locus modulate their expression in response to a SNP; then, one can relate the direction of the association with expression to the direction of association with other traits, such as disease susceptibility. Because the number of these eQTL studies has increased, it has become clear that many eQTLs are dependent on cell type, activation state, or environment. This observation reflects the fact that epigenomic features that are specific to a differentiation state, for example, influence access to the sequence variant and hence influence the transcriptional output of the locus (*10*–*12*).

We have previously reported a number of monocyte-specific eQTL associations for MS, AD, and PD susceptibility variants (*13*). Given that MS, AD, and PD are all diseases of the central nervous system (CNS), we wanted to further examine these susceptibility loci in innate immune cells in the context of the CNS environment. Microglia are the resident innate immune cells of the CNS, and they are critical regulators of CNS homeostasis in health and of inflammatory responses in disease (*14*–*16*). There is also strong evidence that in diseases such as stroke, brain trauma (*17*), AD (*18*, *19*), PD (*20*, *21*), and MS (*22*), peripheral leukocytes, including monocytes, infiltrate the brain and differentiate into effector cells such as macrophages that are found at the site of pathology. Therefore, for genetic studies, we would ideally isolate these resident microglia and infiltrating macrophages from a large number of subjects. However, because of the difficulty in acquiring these cells from the human brain, alternative methods of obtaining these cells are needed. In one approach, patient-derived cells can be reprogrammed into human induced pluripotent stem cells (hiPSCs) and then differentiated into neurons or certain glial cells (*23*–*25*). The differentiation of hiPSCs into microglia, however, remains technically challenging, takes several months (*26*), and is currently not performed on the scale needed for genetic studies.

The investigation of genetically-driven changes in gene expression inmicroglia and infiltrating macrophages from patients with neurodegenerative diseases is limited by lack of access to these cells

[1]Ann Romney Center for Neurologic Diseases, Brigham and Women's Hospital, Harvard Medical School, Boston, MA 02115, USA. [2]Program in Translational NeuroPsychiatric Genomics, Institute for the Neurosciences, Departments of Neurology and Psychiatry, Brigham and Women's Hospital, 77 Avenue Louis Pasteur, NRB168, Boston, MA 02115, USA. [3]Harvard Medical School, Boston, MA 02115, USA. [4]Program in Medical and Population Genetics, Broad Institute, 7 Cambridge Center, Cambridge, MA 02142, USA. [5]Center for Translational and Computational Neuroimmunology, Department of Neurology, Columbia University Medical Center, 630 West 168th Street, New York, NY 10032, USA. [6]Rush Alzheimer's Disease Center, Rush University Medical Center, Chicago, IL 60612, USA. [7]Laboratory of Neural Stem Cells and Functional Neurogenetics, Departments of Neurology and Neuroscience, The Ohio State University College of Medicine, 333 West 10th Avenue, Columbus, OH 43210, USA.
*Present address: Medical Scientist Training Program, University of California, San Francisco, San Francisco, CA 94143, USA.
†Present address: Division of Biology and Biomedical Sciences, Graduate Program in Immunology, Washington University in St. Louis, One Brookings Drive, St. Louis, MO 63130, USA.
‡Corresponding author. Email: emb2280@cumc.columbia.edu

from the number of subjects required to perform well-powered genomic and functional analyses. However, a number of protocols do exist to differentiate human monocytes toward a microglia-like phenotype (*27*–*32*). These protocols have leveraged the plasticity of immune cells to direct human primary bone marrow–derived monocytes toward a microglia-like phenotype through coculture with astrocytes or astrocyte-conditioned medium, or via stimulation with recombinant human cytokines. These differentiated cells have been shown to have a ramified morphology, a phagocytic ability including engulfing synapses, and a $CX3CR1^{high}/CCR2^{low}$ phenotype (*27*, *29*, *32*). They also express the proteins P2RY12 and TMEM119 (*32*). Because these cells do not share the embryonic origin of the vast majority of resident microglia in the nondiseased brain (*33*), it is possible that they are more similar to infiltrating macrophages that have taken up residence in the CNS. There is currently no robust marker capable of distinguishing these two cell types in humans. A study by Etemad *et al.* (*27*) generated these cells by culturing ex vivo human monocytes in the presence of macrophage colony-stimulating factor (M-CSF), granulocyte-macrophage colony-stimulating factor (GM-CSF), nerve growth factor–β (NGF-β), and chemokine ligand 2 (CCL2), all of which are important for microglia development and survival (*33*–*37*). In addition, Ohgidani *et al.* (*29*) developed ramified microglia-like cells from human monocytes using a combination of GM-CSF and interleukin-34 (IL-34). IL-34 shares a receptor (CSF-1R) with M-CSF and is known to be important for directing the differentiation of microglia (*38*). These studies have shown that inducible microglia/macrophages display features observed in CNS resident microglia and that they are optimal for high-throughput studies to enable genetic analyses. Because the protocols use recombinant cytokines and serum-free media, potential batch-to-batch variation, which could arise from astrocytes or astrocyte conditioned media, is reduced.

Here, we used an in vitro model system composed of human monocytes differentiated using CNS cytokines that are known to be critical for the microglia microenvironment in vivo. We refer to these cells as human monocyte-derived microglia-like (MDMi) cells. We leveraged the capacity of this system to be deployed on a moderate scale to perform a genetic study of genes associated with susceptibility to several neurodegenerative diseases. To validate this in vitro system, we compared our human MDMi to human embryonic and induced pluripotent stem cell–derived microglia (ESC/iPSC) (*26*), ex vivo–derived human microglia (*39*), and murine microglia (*40*). Protocols that in vitro polarize microglia and macrophages toward proinflammatory "M1" and anti-inflammatory "M2" phenotypes allowed us to study molecular mechanisms that may help to distinguish microglia from other myeloid cells. It has been shown that the M1 phenotype of human microglia is distinct from the M1 phenotype of monocyte-derived macrophages (MDMs) (*41*), which has allowed us to characterize our inducible microglia/macrophages. With the generation of a detailed transcriptomic reference and an understanding of the characteristics of our model system in hand, we have evaluated the effect of common genetic variation on the expression of genes found in susceptibility loci for MS, PD, and AD.

RESULTS

Differentiation of monocytes into MDMi cells

We first identified the genes that are more highly expressed in our MDMi model system when compared to a tissue-level profile from human dorsolateral prefrontal cortex (DLPFC). Specifically, human peripheral monocytes from five young healthy individuals were stimulated with GM-CSF, M-CSF, CCL2, NGF-β, and IL-34 for 10 days and analyzed for gene expression using RNA-sequencing (RNA-seq). We then compared RNA-seq data from the MDMi model system to the RNA-seq data from the DLPFC of 238 individuals without a pathological diagnosis of AD. We then assembled a list of 368 genes with a threefold difference in expression in this analysis (fold-change genes) (table S1). These fold-change genes were then compared to published lists of microglia-enriched genes in ESC/iPSC-derived microglia (pMGL) (*26*), in ex vivo murine microglia (P60MG) (*40*), and in ex vivo human microglia isolated from resected brain tumor tissue or epileptic foci after surgery (HuMG) (*39*). There was more overlap in these gene lists among the three human models compared to the gene list for mouse microglia. We found that MDMi and pMGL shared 203 genes (55%) of the MDMi differentially expressed genes (Fig. 1A). Further, MDMi cells had 118 genes (32%) of the fold-change genes, in common with enriched genes in microglia from surgically resected human brain tissue (HuMG), whereas HuMG shared 100 genes (29%) of the pMGL-enriched genes. In comparison, MDMi cells only shared 24 genes (6.5%) with the enriched genes in murine p60 microglia (*40*). Similarly, the pMGL cells shared 19 genes (5.5%) and the brain tissue–derived microglia shared 34 genes (5.4%) with the enriched genes in murine p60 microglia.

The comparison of the data sets clearly demonstrated inter-mammalian differences in microglia gene expression; however, we also examined specific genes that have been reported to be key for microglial function in the murine system. For example, we found up-regulation of genes such as *TGFBR1* ($P < 0.0001$), *PROS1* ($P = 0.0005$), *P2RX7* ($P = 0.0058$), and *C1QB* ($P = 0.0007$) (Fig. 1B) in our MDMi cell model system relative to ex vivo human peripheral blood monocytes and MDMs. Notably, *P2RY12* and *TMEM119*, other murine microglia signature genes, were not up-regulated compared to ex vivo monocytes, although *P2RY12* mRNA was up-regulated in MDMi cells compared to MDMs (fig. S1A). Therefore, we examined the proteins encoded by these genes and determined that both TMEM119 and P2RY12 were highly expressed in MDMi cells compared to monocytes from the same individuals (Fig. 1C and fig. S1, B to D). Microglia are thought to be long-lived cells, whereas monocytes and MDMs are thought to be more transient. To explore this, we kept the MDMi cells and the MDM cells in culture for 30 days and found that the apoptotic activator gene BAX was highly expressed in ex vivo monocytes and MDM cells cultured for 30 days, but not in MDMi cells (fig. S2).

We also evaluated the function of MDMi cells and demonstrated that, like primary human microglia, MDMi cells differed from peripheral myeloid cells with respect to their response to environmental stimuli (*41*). Under conditions driving an M1 but not an M2 phenotype, *IL10* expression was significantly higher ($P = 0.0018$) in MDMi cells compared to macrophages from the same individuals (Fig. 1D), which is concordant with a published report (*41*).

Functional consequences of genetic variants in human peripheral blood monocytes and MDMi cells

Using a Fluidigm high-throughput quantitative polymerase chain reaction (qPCR) chip, we measured 94 genes found in loci associated with one of three neurodegenerative diseases (AD, MS, or PD) in MDMi cells from 95 young, healthy subjects of European ancestry with genome-wide genotype data. From this mRNA data set, we

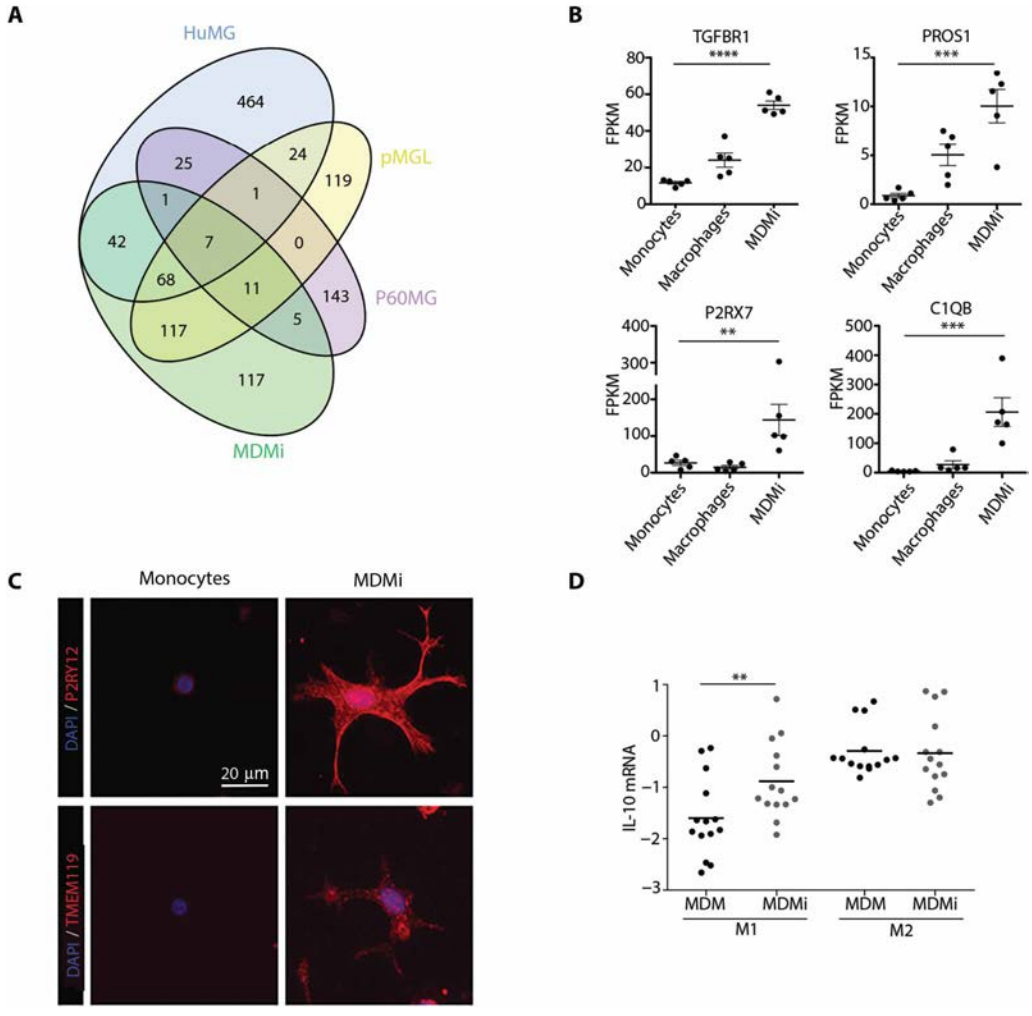

Fig. 1. Differentiation of human peripheral blood monocytes into MDMi cells induces a microglial gene expression and functional phenotype. Human peripheral blood monocytes from young, healthy subjects were incubated with cytokines and differentiated into monocyte-derived microglia-like (MDMi) cells. (**A**) The cell type–specific enriched gene expression for MDMi cells, ex vivo human microglia (HuMG), ex vivo murine microglia (P60MG), and human embryonic and induced pluripotent stem cell–derived microglia (ESC/iPSC)–derived microglia (pMGL) were compared. (**B**) Four genes defined as being microglia-specific in mice were significantly up-regulated in MDMi cells (TGFβR1: ****P < 0.0001; PROS1: ***P = 0.0005; C1QB: ***P = 0.0007; P2RX7: **P = 0.0058) at day 10 of differentiation compared to freshly isolated monocytes and MDM cells from the same five individuals. Gene expression was quantified using RNA sequencing and expressed as fragments per kilobase of transcript per million (FPKM). One-way analysis of variance (ANOVA) with Tukey's post hoc test. (**C**) P2RY12 and TMEM119 proteins were more highly expressed in MDMi cells compared to monocytes. (**D**) MDMi cells functionally mimicked human microglia in response to conditions that led to either an M1 or M2 phenotype. Under M1 conditions, MDMi cells expressed significantly more interleukin-10 (IL-10) mRNA (**P < 0.01) compared to MDM cells from the same individuals. Student's t test, n = 14. For (B) and (D), each dot represents a biological replicate. Horizontal line denotes the mean. DAPI, 4′,6-diamidino-2-phenylindole.

performed an eQTL study to identify genotype-driven effects on the expression of nearby genes in MDMi cells [cis-eQTL analysis (cis-eQTL)] (Fig. 2A). Specifically, for each gene measured, we evaluated whether SNPs found within 1 Mb of the transcription start site of the measured gene were associated with the gene's expression. At a false discovery rate (FDR) < 0.05, we identified cis-eQTL associations for 35 genes in MDMi cells (table S2). After linkage disequilibrium (LD) pruning of the list of SNPs with an MDMi eQTL (eliminating those SNPs with $R^2 > 0.2$, with the top SNP in a locus), 141 SNPs with a cis-eQTL remained. We compared our MDMi eQTLs to our previously published human peripheral blood monocyte eQTL data derived from 211 young, healthy subjects of European ancestry (*13*). We found that 82 (58.1%) of these SNPs were also cis-eQTLs in human monocytes (global FDR < 0.05) (table S3). Of those eQTLs that were shared, 100% (82 of 82) shared the same direction of effect in MDMi cells and monocytes, showing that differentiation did not affect the function of these variants. Correlations of the effect size (ρ) of the SNPs in each gene (MDMi ρ versus monocytes ρ) were plotted for each lead SNP (fig. S3).

Figure 2B shows that of the best eQTL SNPs for each gene in the MDMi cells, some were shared with human peripheral blood monocytes (for example, *NUP160*), whereas others were only found in the MDMi cells (for example, *CD37*) (Fig. 2B, left); this was also found for the top eQTL SNPs in the human monocytes (for example, *CD40*) (Fig. 2B, right). In Fig. 2C, regional plots of *CD37* and *CR1* illustrate the fact that certain haplotypes influenced gene expression very differently in monocytes and MDMi cells, with clear peaks of associations in MDMi cells and no effect in our larger sample of subjects with monocytes that underwent transcriptional profiling.

Association of disease-specific SNPs with gene expression in MDMi cells

To provide mechanistic insights into the effect of GWAS-derived SNPs on disease susceptibility, we merged our cis-eQTL results with a list of disease-associated SNPs influencing AD (*42*, *43*), PD (*44*), and MS (*45*). Of the 70 disease-associated SNPs within 1 Mb of our genes of interest, we found seven eQTL associations at a secondary, targeted FDR of 0.05 (Table 1). The SNP/gene expression associations of *rs10838725*/*NUP160*, *rs701006*/*METTL21B*, and *rs1323292*/*RGS1* were also found in human peripheral blood monocytes (*13*); the associations for *rs1476679*/*PILRB* and *rs76904798*/*LRRK2* appeared to be unique to MDMi cells (Table 1). Figure 3A (top) shows the cis-eQTL shared between monocytes and MDMi cells, where the association for *RGS1* and the MS SNP *rs1323292* was similar in both

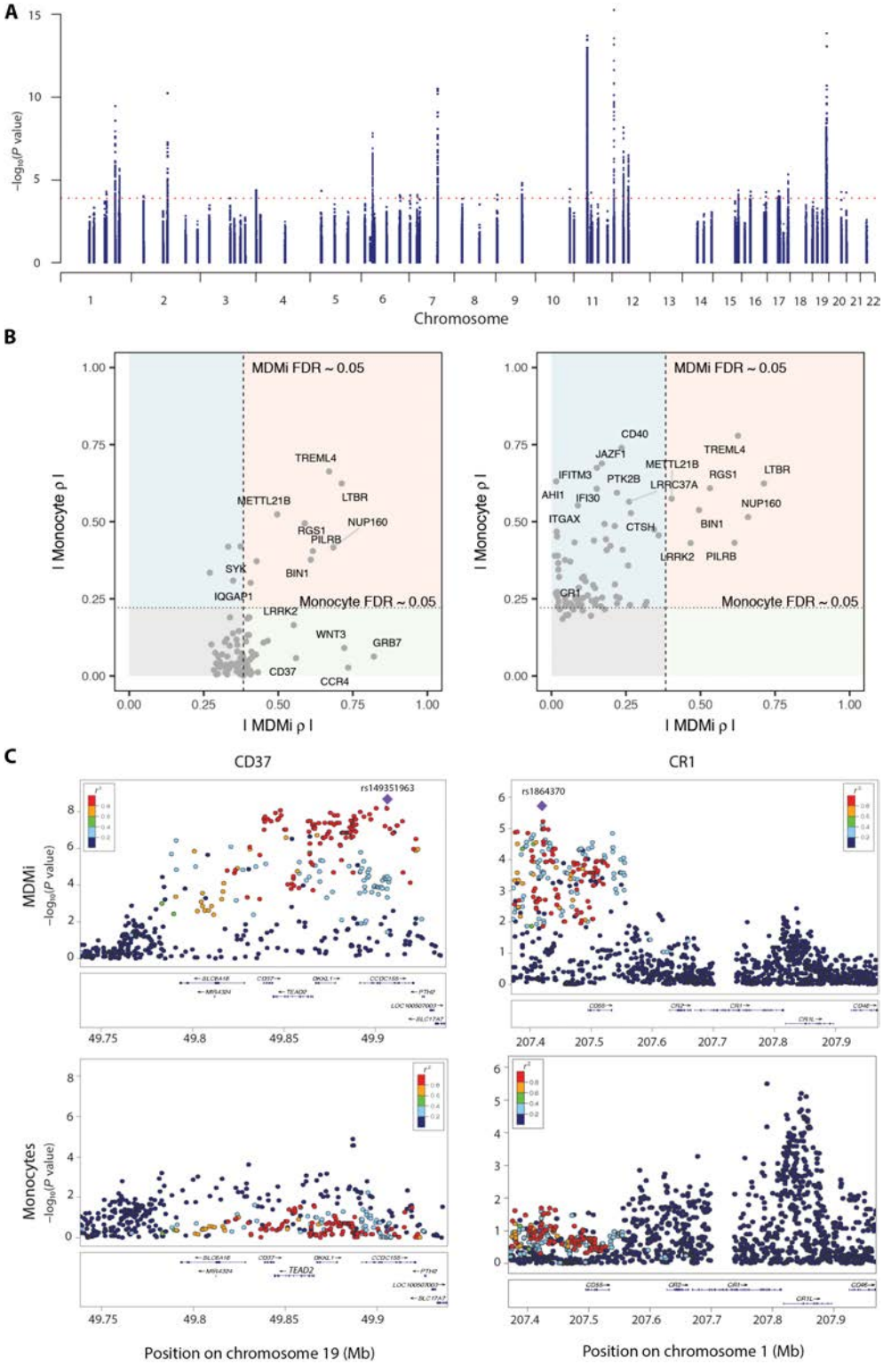

Fig. 2. Genotype-induced differential gene expression is different in MDMi cells compared to monocytes. Using a Fluidigm high-throughput quantitative polymerase chain reaction (qPCR) chip, we measured the expression of 94 genes found in loci associated with susceptibility to Alzheimer's disease (AD), multiple sclerosis (MS), or Parkinson's disease (PD) in MDMi cells differentiated from the peripheral blood monocytes of 95 young, healthy subjects of European ancestry with genome-wide genotype data available. (**A**) Manhattan plot of expression quantitative trait locus (eQTL) results for the 94 genes measured in MDMi cells. n = 95 biological replicates per gene. Each dot represents one single-nucleotide polymorphism (SNP); selected SNPs include all of those found within 1 Mb of the transcription start site of the profiled gene. The x axis denotes the physical position of the SNP, and the y axis reports the significance of the SNP's association with the expression of the nearby gene (eQTL result). The red line highlights the threshold of significance in our analysis. (**B**) We compared our MDMi eQTL results to those of our previously published monocyte eQTL results derived from n = 211 young, healthy subjects of European ancestry (*13*). Left: We plotted the top eQTL SNP for each gene in the MDMi data; the x axis reports the absolute value of the effect size (ρ) of the SNP in MDMi cells; the ρ in the monocyte data is presented on the y axis. The threshold of significance [false discovery rate (FDR) < 0.05] is shown by dotted lines in each dimension. The light-red quadrant contains those loci with consistent effects in both cell types, whereas the light-green quadrant contains those loci that had a significant association only in MDMi cells. The light-blue quadrant contains those loci with an effect in monocytes that was not significant in our current MDMi analysis. Right: The best SNP for each locus in the monocyte data. (**C**) Locus zoom plots highlight the regional distribution of associations in two loci, *CD37* and *CR1*, which have very different eQTL associations in MDMi cells compared to monocytes. Each dot is one SNP in these figures, with the physical position captured on the x axis and the eQTL significance on the y axis. The location of genes in this locus is shown below the SNPs. The top eQTL SNP for the MDMi data is shown as a purple diamond, and the other SNPs are colored by the extent of linkage disequilibrium (r^2) with the lead SNP. In the monocyte plots, the SNP colors are defined by the lead MDMi SNP, highlighting the fact that the haplotype driving association in MDMi cells does not have a strong effect in monocytes. MDMi cells n = 95 biological replicates, monocytes n = 211 biological replicates.

cell types. Figure 3A (bottom) shows an example of a differentiation state–specific cis-eQTL in which *PTK2B* and its respective disease-associated SNP *rs28834970* was observed in the monocyte data set but not in the MDMi Fluidigm data set. On the other hand, significant associations were found in MDMi cells for the *PILRB* gene (thought to be an activating immune receptor) and the AD SNP *rs1476679*

Table 1. Disease-associated cis-eQTLs in MDMi cells.

SNP	Gene	Chromosome	MDMi	MDMi *P* value	Monocyte	Monocyte *P* value	Disease	MDMi-targeted FDR
rs3865444	CD33_SHORT	19	−0.688	1.39×10^{-14}	−0.254*	1.96×10^{-14}*	AD	1.38×10^{-12}
	CD33_LONG		0.339	7.91×10^{-4}				1.30×10^{-2}
rs1476679	PILRB	7	−0.337	8.42×10^{-4}	−0.09	1.90×10^{-1}	AD	1.30×10^{-2}
rs10838725	NUP160	11	−0.383	1.29×10^{-4}	−0.241	4.08×10^{-4}	AD	3.22×10^{-3}
rs76904798	LRRK2	12	−0.479	8.92×10^{-7}	−0.163	1.77×10^{-2}	PD	2.96×10^{-5}
rs1323292	RGS1	1	0.516	8.62×10^{-8}	0.486	6.33×10^{-14}	MS	4.30×10^{-6}
rs701006	METTL21B	12	0.335	9.14×10^{-4}	0.413	4.18×10^{-10}	MS	1.30×10^{-2}

*Total CD33 (includes CD33_Long and CD33_Short).

that were not seen in the human peripheral blood monocyte data set. Specifically, the *rs1476679*^{T} risk allele was associated with increased *PILRB* expression in MDMi cells (P = 0.00084) but not in monocytes (P = 0.19) (Fig. 3B, top). These results were replicated via PCR in a smaller study examining an independent set of individuals from whom we assessed both monocytes and MDMi cells (Fig. 3B, middle). PILRB protein expression mirrored the mRNA expression data in both monocytes and MDMi cells (Fig. 3B, bottom). In MDMi cells, a one-way analysis of variance (ANOVA) revealed a significant effect of genotype on *PILRB* mRNA [$F_{(2, 34)}$ = 6.78, P = 0.0034] and protein [$F_{(2, 31)}$ = 5.15, P = 0.0112] expression that was not present in monocytes [mRNA: $F_{(2, 34)}$ = 1.67, P = 0.2037; protein: $F_{(2, 31)}$ = 2.14, P = 0.1346].

Of particular interest, we examined the GWAS SNP for PD at the *LRRK2* locus (*44*). The role of LRRK2 in PD has been of great interest because dominant mutations in the gene have been associated with familial PD (*46*). The PD GWAS *rs76904798*^{T} risk allele was associated with increased *LRRK2* expression in MDMi cells (P = 8.92×10^{-7}), whereas there was a nonsignificant trend (P = 0.0177) in monocytes (Fig. 4A). Thus, the differentiation of the monocytes to MDMi cells appeared to enhance the magnitude of the correlation between the PD SNP *rs76904798* and *LRRK2*; the effect size of the SNP was significantly different between the two cell types (P < 0.05). Critically, using the colocalization method (which assesses whether two association signals are consistent with a shared causal variant) (*47*), we found that the PD association and the eQTL SNP colocalized in MDMi cells (posterior probability eQTL and PD associations driven by a shared causal variant = 0.90) but not in monocytes (Fig. 4B). This suggested that the disease SNP regulated gene expression in the in vitro MDMi cell model only and not in human monocytes.

Differential expression of CD33 isoforms in MDMi cells

CD33 is a cell surface protein expressed by myeloid cells, and higher CD33 expression in the brain has been associated with more advanced cognitive decline and AD (*2*, *48*). We recently demonstrated that individuals with the *rs3865444*^{CC} risk genotype have increased CD33 on the surface of their monocytes compared to those with the *rs3865444*^{AA} protective genotype (*1*). Furthermore, alternative splicing of *CD33* generates two isoforms of the protein: full-length CD33^{M} and truncated CD33^{m}, which lacks the immunoglobulin V-set domain encoded by exon 2 (*49*). The AD SNP *rs3865444* or a SNP in high LD leads to alternative splicing of exon 2, which is the primary mechanism of the genetically driven differential expression of CD33 (*3*, *13*). Here, we found a significant effect of genotype on CD33 expression. There was an increase in full-length *CD33*^{M} mRNA expression [$F_{(2, 75)}$ = 7.74, P = 0.0009] and a decrease in *CD33*^{m} mRNA expression [$F_{(2, 75)}$ = 42, P < 0.0001] in MDMi cells from subjects with the *rs3865444*^{CC} risk genotype; the changes in gene expression were dose-dependent (Table 1) (Fig. 5A). Similar findings were observed for the CD33 protein (Fig. 5B). Densitometry analysis of the Western blot revealed a significant effect of genotype on CD33^{M} protein expression in monocytes (P = 0.034) and MDMi cells (P = 0.009) from the same individuals. The effect of genotype on CD33^{m} protein expression was only observed in MDMi cells (P = 0.016) and not in monocytes (P = 0.124) [as we had previously reported (*13*)]. The genotype-dependent difference in CD33 surface expression was further confirmed in MDMi cells using high content imaging (P = 0.001; Fig. 5C). Myeloid cells, such as infiltrating macrophages or microglia, are thought to be involved in AD through phagocytosis of amyloid-β that accumulates in neuritic amyloid plaques, a neuropathological feature of AD (*50*). Thus, we tested whether MDMi cells from subjects with the *rs3865444*^{C} *CD33* risk allele showed reduced activation of microglia and, therefore, a reduced phagocytic ability compared to MDMi cells from subjects with the protective allele. We found reduced phagocytic uptake of fluorescently labeled dextran in MDMi cells bearing the *rs3865444*^{CC} risk allele (P = 0.047; Fig. 5D), similar to what we had previously reported for monocytes (*1*).

DISCUSSION

The recent identification of microglia-specific gene signatures has enabled us to examine the phenotype of MDMi cells through gene expression changes rather than subtle shifts in mean fluorescence intensity representing the expression of specific surface markers or changes in morphology. Here, we show that monocytes cultured for 10 days in the presence of specific cytokines up-regulate expression of microglia-specific genes, including the key microglial gene *TGFBR1*, compared to monocytes not treated with cytokines (*51*). Other genes highly expressed by MDMi cells include *C1QB*, a critical mediator of synaptic refinement and plasticity (*52*), and *PROS1*, which directs microglia to phagocytose apoptotic cells (*53*). A role for *P2RX7*, another highly expressed MDMi gene, has been described by Monif *et al.* (*54*), who found that *P2RX7* drives microglia activation and proliferation. Thus, MDMi cells express many genes that are important for microglia function.

There is no single functional assay that defines microglia. Several groups have used the ability to phagocytose material as a functional

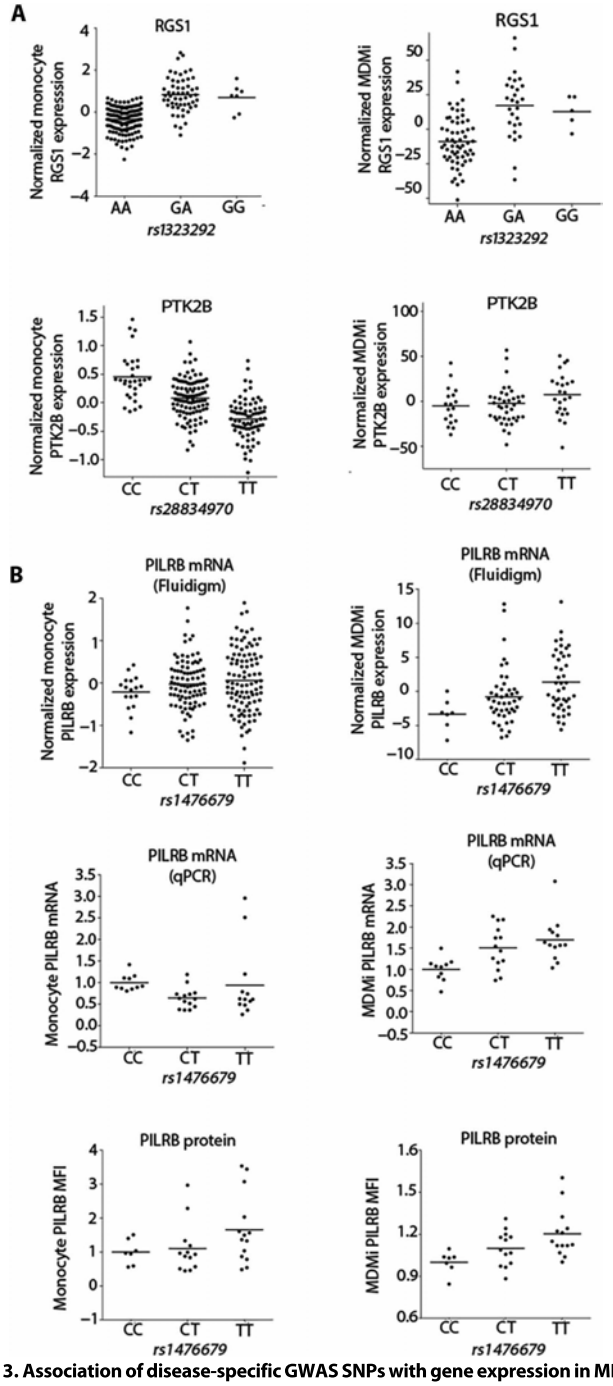

Fig. 3. Association of disease-specific GWAS SNPs with gene expression in MDMi cells differs from that in monocytes. Each gene selected for the Fluidigm experiment was in a locus associated with AD, PD, or MS. (**A**) Example of a cis-eQTL shared between monocytes and MDMi cells (top). The association of *RGS1* expression with the MS risk allele *rs1323292*^{G} was similar in both cell types. With *PTK2B* (bottom), the AD-associated rs28834970^{C} risk allele had an effect in monocytes but not in MDMi cells. n = 95 (MDMi), n = 211 (monocytes). (**B**) A significant eQTL was found in MDMi cells for the *PILRB* gene (P = 0.00084), illustrated with the AD SNP rs1476679; this was not seen in the monocyte data set (P = 0.19) (top). n = 95 (MDMi cells), n = 211 (monocytes). This finding was replicated in an independent set of 37 individuals for RNA expression (P = 0.0034) using TaqMan PCR (middle row) and 34 individuals for protein expression (P = 0.0112) (bottom row). One-way ANOVA with Tukey's post hoc test. Each dot represents a biological replicate. Horizontal line denotes the mean. GWAS, genome-wide association studies. Mean fluorescence intensity, MFI.

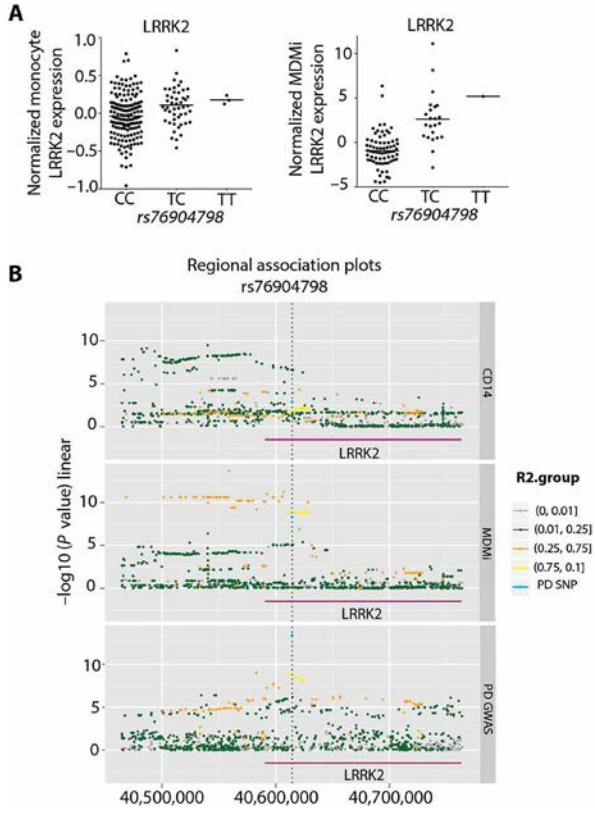

Fig. 4. Significant association in MDMi cells between *LRRK2* gene expression and the PD SNP *rs7690479*. (**A**) The PD GWAS *rs76904798*^{T} risk allele was associated with increased *LRRK2* expression in MDMi cells (right) ($P < 8.92 \times 10^{-7}$); there was a nonsignificant trend in the monocyte data (left) ($P < 1.77 \times 10^{-2}$). (**B**) Three regional association plots illustrate the colocalization of the PD susceptibility haplotype, tagged by *rs76904798*, and the eQTL haplotype in MDMi cells but not in monocytes. Top: Data from monocytes: Each dot is one SNP and is colored in relation to the extent of linkage disequilibrium (r^2) with the lead PD SNP (*rs76904798*). The color key is presented to the right of the panels. The x axis presents the physical position of the SNP, and the y axis presents the association between the SNP and the amount of LRRK2 expression. Middle: The same set of SNPs is presented; here, the association P value is derived from the relation of each SNP to LRRK2 expression in MDMi cells. Bottom: The results of the published PD GWAS (*44*) are presented for the same set of SNPs.

readout; however, other myeloid cells, including monocytes and macrophages, share this ability. Synaptic pruning is another characteristic function, but this is difficult to model in vitro. We leveraged a recent study (*41*) that characterized the functional properties of human microglia in vitro by assessing cytokine production when they were driven toward an M1 or M2 inflammatory phenotype. Consistent with this study, we demonstrate here that, under M1 conditions, MDMi cells produced more IL-10 compared to MDM cells; no difference was seen between MDMi cells and MDM cells under M2 conditions. We also found that the MDMi cells survived for up to 30 days in culture without up-regulating the proapoptotic gene *BAX* in contrast to MDM cells, which did up-regulate *BAX* and showed increased cell death. These findings highlight the functional differences between MDMi cells and MDM cells.

It is difficult to differentiate human microglia and CNS-infiltrating blood-derived macrophages; the role of infiltrating blood-derived macrophages in the brain remains poorly understood but may be related to disease. In AD, inflammation and microglial activation have

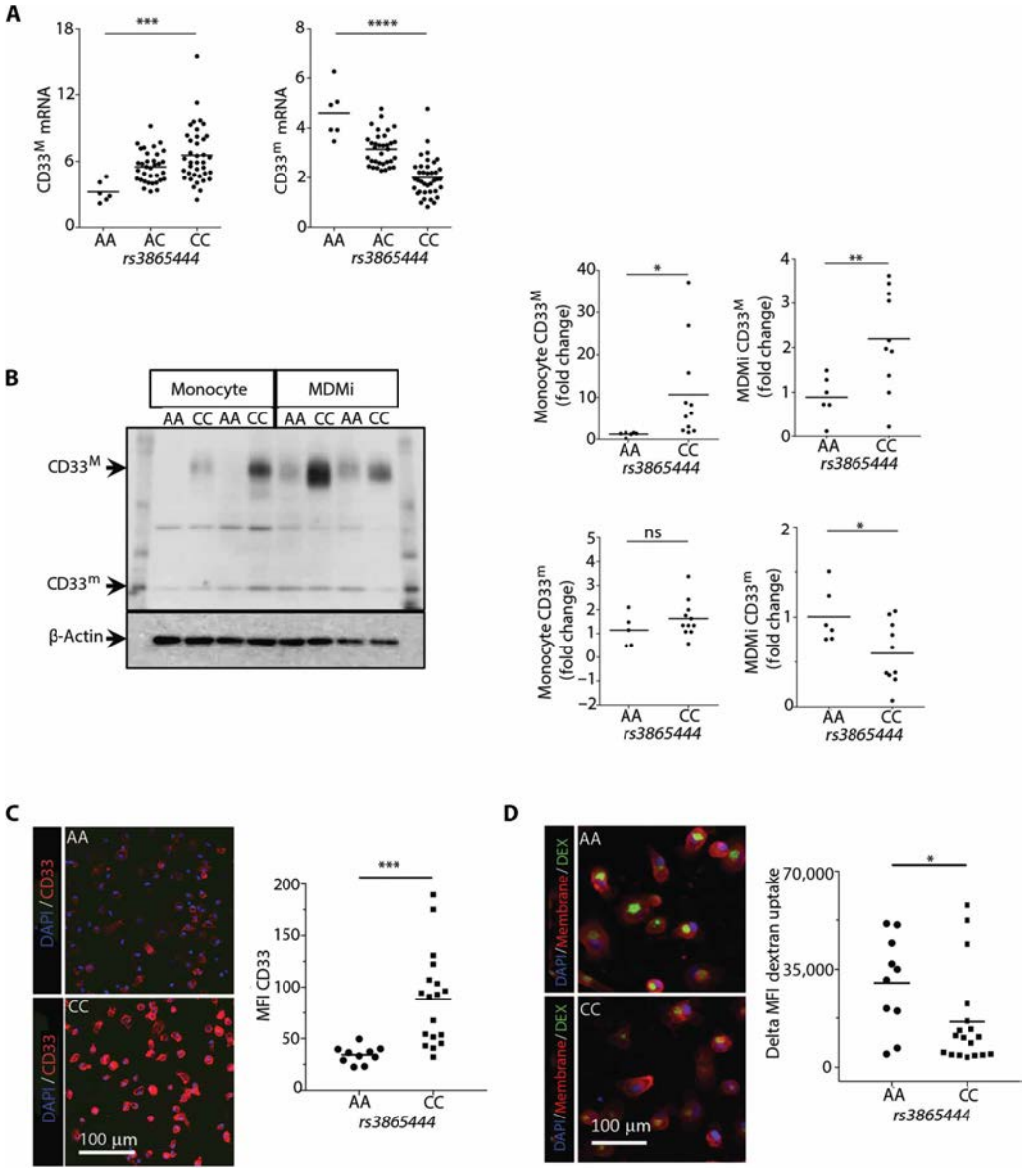

Fig. 5. Differential expression of CD33 isoforms in MDMi cells. (**A**) In our model system, we found a significant effect of genotype on CD33 expression. We observed an increase in full-length *CD33*^{M} mRNA expression (***$P = 0.0009$) and a decrease in truncated *CD33*^{m} mRNA expression (****$P < 0.0001$) in MDMi cells in a dose-dependent fashion relative to the *rs3865444*^{C} risk allele in the Fluidigm data set. One-way ANOVA with Tukey's post hoc test, $n = 95$. (**B**) Western blot analysis showed a significant effect of genotype on CD33^{M} protein expression in monocytes (*$P = 0.034$) and MDMi cells (**$P = 0.009$) from a second set of individuals ($n = 16$). However, a significant effect of genotype on CD33^{m} protein expression was only observed for MDMi cells (*$P = 0.016$) and not for monocytes ($P = 0.124$). A representative Western blot displays the data from four subjects, with each subject's sample run in a separate lane. The genotype of the subject is included at the top of each lane. (**C**) The genotype-dependent difference in CD33 surface expression ($P = 0.001$) and (**D**) fluorescein isothiocyanate–dextran (DEX) uptake ($P = 0.047$) were further confirmed in MDMi cells using high content imaging. Each dot represents a biological replicate. Student's *t* test was performed for (B) to (D). ns, not significant.

been extensively studied, but the contribution of blood-derived immune cells remains unclear. Recent data suggest that blood-derived monocytes may play a role in amyloid-β clearance. For example, more perivascular amyloid-β was observed in CCR2-deficient Tg2576 AD mice, which show reduced early recruitment of monocytes (*35*), compared to Tg2576 mice expressing CCR2. In support of this protective role, increasing monocyte recruitment has been reported to delay the progression of AD (*55*, *56*). On the other hand, infiltrating monocytes may enhance tissue damage in MS. For example, MDMs were found to initiate demyelination in the experimental autoimmune encephalomyelitis (EAE) rodent model of MS (*57*). Furthermore, blocking monocyte recruitment to the CNS blocked EAE progression, suggesting that these infiltrating cells may be required for disease progression in MS (*58*). An argument could be made that our MDMi cell model system more likely represents blood-derived macrophages that infiltrate the CNS rather than embryonically derived microglia, but we need more knowledge about these two cell types before we can decide which cell type our model more faithfully recapitulates.

GWAS studies have identified new loci associated with disease susceptibility. In determining the mechanistic outcomes of these genetic variants, it has been demonstrated that eQTLs are context-dependent, existing only in certain cell types and activation states (*12*, *13*). To extend our understanding of the modulation of gene expression by genetic variants in our in vitro model of microglia, we associated MDMi RNA expression with SNPs. We examined the expression of 94 genes in loci associated with increased risk of developing AD, MS, or PD in MDMi cells from 95 young, healthy individuals and compared their expression to microarray data from peripheral blood monocytes from 211 individuals generated in an earlier study (*13*). The expression of many of these genes was affected by genetic variation in the MDMi cells. For a number of genes, genetic regulation of gene expression was determined by completely different SNPs in the MDMi cells compared to the monocytes (Fig. 2). This demonstrates that the genotype-driven gene expression differences between monocytes and MDMi cells can be context-specific and highlights the importance of examining

genotype-induced gene expression differences in CNS-relevant cell types.

A striking example of a cell type–specific cis-eQTL was found in the *PILRB* gene. We found an association in MDMi cells between *PILRB* gene expression and the AD SNP *rs1476679* that was not seen in the monocyte eQTL data set. On the basis of a Bayesian colocalization analysis (*47*) that sought to determine whether our MDMi eQTL and the International Genomics of Alzheimer's Project stage 1 (*42*) AD susceptibility GWAS effects were driven by a shared causal variant, it appeared more likely that the eQTL and AD GWAS effects were not driven by a shared variant (posterior probability eQTL and AD associations driven by a shared causal variant = 0.04). This result suggested that whereas the AD SNP displayed some association with *PILRB* expression, the effect of the *rs1476679* SNP was probably mediated by another mechanism, and the association may be the result of partial LD between the AD and eQTL causal variants.

Activation of monocytes has been shown to highlight different eQTL associations (*12*). We found that the differentiation of MDMi cells identified additional associations (for example, with the *PILRB* gene) and enhanced some associations that were weakly seen in monocytes (for example, as observed for *LRRK2*). Pathogenic mutations in *LRRK2* are the most common genetic cause of familial PD (*59*, *60*). High LRRK2 expression has been discovered recently in myeloid cells, but not in T cells, suggesting a functional role for *LRRK2* in the innate immune system (*61*). In addition, LRRK2 is expressed in microglia where it modulates the proinflammatory response in these cells (*62*). In our data, the monocyte eQTL SNP *rs10784428* (*56*) was associated with LRRK2 expression in both monocytes and MDMi cells, whereas the PD-associated SNP *rs76904798* was associated with LRRK2 expression only in MDMi cells (Fig. 4). This suggested that *LRRK2* may have a context-specific role that may also vary with disease state. These results highlight the potential use of MDMi cells for studying the functional role of the *LRRK2* variant in microglia.

On the basis of the expression of CD33 in human microglia (*1*) and our recent characterization of the AD risk gene *CD33* in monocytes where we found increased CD33 surface protein in individuals carrying the *CD33 rs3865444*^{CC} risk genotype, we explored whether this was also the situation in MDMi cells. We found that MDMi cells recapitulated the previously described expression and functional effects of the risk allele, but we also observed differential protein expression of the truncated CD33^{m} in MDMi cells that was not seen in monocytes (*63*). Notably, whereas the *CD33* locus has been associated with AD at a threshold of genome-wide significance (*64*), it fell below that threshold in a recent analysis (*42*). Further evaluation of these data and additional replication data supporting the role of CD33 in non-European populations (*65*–*67*) and AD-related endophenotypes (*1*) support its association with AD. Functional studies also link CD33 to TREM2 (*68*), complementing these genetic findings. Regardless of the association with AD, the CD33 variant has an important functional effect on myeloid cells. The differential effect of the CD33 variant in MDMi cells compared to monocytes suggests that the disease-associated effect of *rs3865444* may differ subtly between microglia and monocytes. To confirm this, future work should investigate whether the isoform-specific pattern we observed is also seen in postmortem primary human microglia from genotyped individuals.

Our study presents the detailed characterization of an in vitro cellular model system that can be used to investigate the effects of genetic variants associated with neurodegenerative diseases on human innate immune cells. The characterization of eQTL effects using MDMi cells illustrates the utility of the model system for moderate-throughput experiments in which 95 different subjects were examined in parallel. MDMi cells may offer an important tool for translational studies that could complement data from biopsy-derived or autopsy-derived microglia and macrophages.

However, there are some limitations to our study that should be considered. First, MDMi cells were derived from peripheral blood monocytes and may be different from microglia derived from the yolk sac, especially in terms of epigenetic changes that occur over a lifetime. Despite this, our data suggest that MDMi cells may enable the study of cells that share many features with microglia, for example, brain macrophages that differentiate from infiltrating monocytes exposed to the CNS cytokine milieu. As we continue to use this cellular system to model human microglia and macrophages, we will identify additional strengths and limitations of this model system, as has been the case for monocyte-derived dendritic cells, which are routinely used to model in vivo dendritic cells (*69*).

A second limitation is that monolayers of MDMi cells do not resemble the three-dimensional (3D) spatial arrangement of microglia in the CNS, and stiff plastic culture dishes do not resemble the physical environment of the brain. Therefore, a recently described 3D culture system using a collagen construct may enable the study of these MDMi cells in a more relevant tissue-like microenvironment (*70*). In addition, because of unknown reasons, we found that in about 10% of our subjects, their monocytes did not survive the differentiation process. This may have implications in studies where the sample size is small. To control for this, we excluded subjects from analysis who had poorly differentiated MDMi cells based on visual observations of morphology.

Notably, the MDMi cells in the present study were derived from frozen peripheral blood mononuclear cells (PBMCs). It should be possible to collect many PBMC samples and bank them for use in large-scale studies, such as the eQTL analyses presented here, that are performed in a single batch, thus minimizing the effect of experimental variation. In addition, the use of a well-defined set of recombinant cytokines to generate MDMi cells will further reduce variability compared to approaches involving astrocyte-conditioned medium, for example.

In terms of understanding the functional outcomes of GWAS SNPs, it is now clear that they must be examined in the correct cell type and context. Because of the limitations of acquiring human microglia in sufficient quantity from large numbers of human subjects (as is needed for genetic association studies) and a lack of a cell line that adequately mimics human microglia, we suggest that the MDMi cell model system could overcome this challenge. In addition to genetic studies, MDMi cells may be useful in drug screening where biochemical or functional changes in response to drugs could be monitored when microglia are thought to be the target cell type. Additional potential applications of MDMi cells may include the exploration of various biological behaviors of human microglia in neurodegenerative disorders. Coculturing MDMi cells with human neurons and astrocytes would enable the modeling of innate immune dysfunction in a more complex system where the target cell is interacting with other relevant cell types. Finally, given that the differentiation protocol takes just 10 days, one could envisage that in the future, MDMi cells derived from a patient's monocytes could be rapidly characterized to help with drug selection and disease management (*71*). In conclusion, we propose that our in vitro translational

tool for generating microglia-like cells quickly and easily from adult blood could be useful for exploring microglia function and dysfunction.

MATERIALS AND METHODS

Study design

The overall aim of the study was to characterize and refine a translational research tool in which microglia-like cells were generated from human peripheral blood monocytes in the presence of specific cytokines. We refer to these cells as MDMi. The objective of the first portion of the study was to determine whether MDMi cells expressed known microglia genes and whether they had a functional phenotype that was similar to microglia. To do this, we derived MDMi cells from the peripheral venous blood of healthy control volunteers from the PhenoGenetic Project. This is a living tissue bank that consists of healthy subjects who are recontactable and can therefore be recalled based on their genotype. A total of 1753 healthy subjects >18 years of age have been recruited from the general population of Boston. Subjects were free of chronic inflammatory, infectious, and metabolic diseases and are of diverse ethnicities (29% are non-Caucasian), and 62.7% are women. The median age was 24 years. The objective of the second portion of the study was to extend our understanding of the genetic modulation of gene expression in our in vitro MDMi cell model. To do this, we associated MDMi RNA expression with SNPs. We used this model system to perform an eQTL study examining the expression of 94 genes in loci associated with increased risk of developing AD, MS, or PD in MDMi cells from 95 young, healthy individuals from the PhenoGenetic Project. We compared the expression of these genes in MDMi cells to microarray data from monocytes from 211 individuals (also from the PhenoGenetic Project) generated in an earlier study (*13*). For the eQTL analysis in monocytes ($n = 211$), which included only Caucasians, the median age was 25 years and 56.9% were women. For the eQTL analysis in MDMi cells ($n = 95$), also from Caucasian subjects only, the median age was 29 years and 67.4% were women. Informed consent was obtained from all human subjects. All blood draws and data analyses were done in compliance with protocols approved by the institutional review boards of each institution.

Induction of MDMi and MDM

PBMCs were separated by Lymphoprep gradient centrifugation (StemCell Technologies). PBMCs were frozen at a concentration of 1×10^7 to 3×10^7 cells ml^{-1} in 10% dimethyl sulfoxide (DMSO; Sigma-Aldrich) or 90% (v/v) fetal bovine serum (FBS; Corning). Before each study, aliquots of frozen PBMCs from the PhenoGenetic cohort were thawed and washed in 10 ml of phosphate-buffered saline. Monocytes were positively selected from whole PBMCs using anti-$CD14^+$ microbeads (Miltenyi Biotec) and plated at the following densities per well: 1×10^5 cells (96-well plate), 3×10^5 cells (24-well plate), and 1×10^6 cells (6-well plate). To induce the differentiation of MDMi, we incubated monocytes under serum-free conditions using RPMI-1640 Glutamax (Life Technologies) with 1% penicillin/streptomycin (Lonza) and Fungizone (2.5 μg/ml; Life Technologies) and a mixture of the following human recombinant cytokines: M-CSF (10 ng/ml; BioLegend, 574806), GM-CSF (10 ng/ml; R&D Systems, 215-GM-010/CF), NGF-β (10 ng/ml; R&D Systems, 256-GF-100), CCL2 (100 ng/ml; BioLegend, 571404), and IL-34 (100 ng/ml; R&D Systems, 5265-IL-010/CF) under standard humidified culture conditions (37°C, 5% CO_2) for up to 15 days. MDMs were generated by incubating monocytes with M-CSF (20 ng/ml) in RMPI plus 10% FBS. The cells were used for experiments and characterization at different time points as indicated. For the 30-day culture, both MDM and MDMi cells were moved on day 15 to unconditioned RPMI media until day 30.

Statistical analyses

Statistical analyses for Figs. 1 (A and D) and 5 (B to D) were performed using Prism 5 (GraphPad Software). Comparisons of protein and mRNA expression data across groups were analyzed by Student's *t* test or one-way ANOVA as appropriate, and significant differences were deconvoluted using Tukey's multiple comparison test. Probability values of <0.05 were considered to represent statistically significant differences.

SUPPLEMENTARY MATERIALS

www.sciencetranslationalmedicine.org/cgi/content/full/9/421/eaai7635/DC1

Materials and Methods

Fig. S1. Higher expression of P2RY12 and TMEM119 in MDMi cells compared to monocytes.

Fig. S2. The proapoptotic gene *BAX* is increased in monocytes and MDM cells compared to MDMi cells.

Fig. S3. Many SNPs have differential eQTLs in MDMi cells compared to monocytes.

Table S1. Differentially expressed genes in MDMi cells compared to bulk brain tissue.

Table S2. Cis-eQTLs in MDMi cells.

Table S3. LD-pruned list of cis-eQTLs in MDMi cells.

References (*72*–*77*)

REFERENCES AND NOTES

1. E. M. Bradshaw, L. B. Chibnik, B. T. Keenan, L. Ottoboni, T. Raj, A. Tang, L. L. Rosenkrantz, S. Imboywa, M. Lee, A. Von Korff; The Alzheimer Disease Neuroimaging Initiative, M. C. Morris, D. A. Evans, K. Johnson, R. A. Sperling, J. A. Schneider, D. A. Bennett, P. L. De Jager, *CD33* Alzheimer's disease locus: Altered monocyte function and amyloid biology. *Nat. Neurosci.* **16**, 848–850 (2013).
2. A. Griciuc, A. Serrano-Pozo, A. R. Parrado, A. N. Lesinski, C. N. Asselin, K. Mullin, B. Hooli, S. H. Choi, B. T. Hyman, R. E. Tanzi, Alzheimer's disease risk gene *CD33* inhibits microglial uptake of amyloid beta. *Neuron* **78**, 631–643 (2013).
3. M. Malik, J. F. Simpson, I. Parikh, B. R. Wilfred, D. W. Fardo, P. T. Nelson, S. Estus, CD33 Alzheimer's risk-altering polymorphism, CD33 expression, and exon 2 splicing. *J. Neurosci.* **33**, 13320–13325 (2013).
4. R. J. Guerreiro, E. Lohmann, J. M. Bras, J. R. Gibbs, J. D. Rohrer, N. Gurunlian, B. Dursun, B. Bilgic, H. Hanagasi, H. Gurvit, M. Emre, A. Singleton, J. Hardy, Using exome sequencing to reveal mutations in *TREM2* presenting as a frontotemporal dementia-like syndrome without bone involvement. *JAMA Neurol.* **70**, 78–84 (2013).
5. R. Guerreiro, A. Wojtas, J. Bras, M. Carrasquillo, E. Rogaeva, E. Majounie, C. Cruchaga, C. Sassi, J. S. Kauwe, S. Younkin, L. Hazrati, J. Collinge, J. Pocock, T. Lashley, J. Williams, J.-C. Lambert, P. Amouyel, A. Goate, R. Rademakers, K. Morgan, J. Powell, P. St George-Hyslop, A. Singleton, J. Hardy, *TREM2* variants in Alzheimer's disease. *N. Engl. J. Med.* **368**, 117–127 (2013).
6. T. Jonsson, H. Stefansson, S. Steinberg, I. Jonsdottir, P. V. Jonsson, J. Snaedal, S. Bjornsson, J. Huttenlocher, A. I. Levey, J. J. Lah, D. Rujescu, H. Hampel, I. Giegling, O. A. Andreassen, K. Engedal, I. Ulstein, S. Djurovic, C. Ibrahim-Verbaas, A. Hofman, M. A. Ikram, C. M. van Duijn, U. Thorsteinsdottir, A. Kong, K. Stefansson, Variant of *TREM2* associated with the risk of Alzheimer's disease. *N. Engl. J. Med.* **368**, 107–116 (2013).
7. J. Cady, E. D. Koval, B. A. Benitez, C. Zaidman, J. Jockel-Balsarotti, P. Allred, R. H. Baloh, J. Ravits, E. Simpson, S. H. Appel, A. Pestronk, A. M. Goate, T. M. Miller, C. Cruchaga, M. B. Harms, *TREM2* variant p.R47H as a risk factor for sporadic amyotrophic lateral sclerosis. *JAMA Neurol.* **71**, 449–453 (2014).
8. S. Rayaprolu, B. Mullen, M. Baker, T. Lynch, E. Finger, W. W. Seeley, K. J. Hatanpaa, C. Lomen-Hoerth, A. Kertesz, E. H. Bigio, C. Lippa, K. A. Josephs, D. S. Knopman, C. L. White III, R. Caselli, I. R. Mackenzie, B. L. Miller, M. Boczarska-Jedynak, G. Opala, A. Krygowska-Wajs, M. Barcikowska, S. G. Younkin, R. C. Petersen, N. Ertekin-Taner, R. J. Uitti, J. F. Meschia, K. B. Boylan, B. F. Boeve, N. R. Graff-Radford, Z. K. Wszolek, D. W. Dickson, R. Rademakers, O. A. Ross, TREM2 in neurodegeneration: Evidence for association of the p.R47H variant with frontotemporal dementia and Parkinson's disease. *Mol. Neurodegener.* **8**, 19 (2013).
9. G. Liu, Y. Liu, Q. Jiang, Y. Jiang, R. Feng, L. Zhang, Z. Chen, K. Li, J. Liu, Convergent genetic and expression datasets highlight TREM2 in Parkinson's disease susceptibility. *Mol. Neurobiol.* **53**, 4931–4938 (2016).

10. M. N. Lee, C. Ye, A.-C. Villani, T. Raj, W. Li, T. M. Eisenhaure, S. H. Imboywa, P. I. Chipendo, F. A. Ran, K. Slowikowski, L. D. Ward, K. Raddassi, C. McCabe, M. H. Lee, I. Y. Frohlich, D. A. Hafler, M. Kellis, S. Raychaudhuri, F. Zhang, B. E. Stranger, C. O. Benoist, P. L. De Jager, A. Regev, N. Hacohen, Common genetic variants modulate pathogen-sensing responses in human dendritic cells. *Science* **343**, 1246980 (2014).
11. C. J. Ye, T. Feng, H.-K. Kwon, T. Raj, M. T. Wilson, N. Asinovski, C. McCabe, M. H. Lee, I. Frohlich, H.-i. Paik, N. Zaitlen, N. Hacohen, B. Stranger, P. De Jager, D. Mathis, A. Regev, C. Benoist, Intersection of population variation and autoimmunity genetics in human T cell activation. *Science* **345**, 1254665 (2014).
12. B. P. Fairfax, P. Humburg, S. Makino, V. Naranbhai, D. Wong, E. Lau, L. Jostins, K. Plant, R. Andrews, C. McGee, J. C. Knight, Innate immune activity conditions the effect of regulatory variants upon monocyte gene expression. *Science* **343**, 1246949 (2014).
13. T. Raj, K. Rothamel, S. Mostafavi, C. Ye, M. N. Lee, J. M. Replogle, T. Feng, M. Lee, N. Asinovski, I. Frohlich, S. Imboywa, A. Von Korff, Y. Okada, N. A. Patsopoulos, S. Davis, C. McCabe, H.-i. Paik, G. P. Srivastava, S. Raychaudhuri, D. A. Hafler, D. Koller, A. Regev, N. Hacohen, D. Mathis, C. Benoist, B. E. Stranger, P. L. De Jager, Polarization of the effects of autoimmune and neurodegenerative risk alleles in leukocytes. *Science* **344**, 519–523 (2014).
14. J. W. Pollard, Trophic macrophages in development and disease. *Nat. Rev. Immunol.* **9**, 259–270 (2009).
15. M.-È. Tremblay, B. Stevens, A. Sierra, H. Wake, A. Bessis, A. Nimmerjahn, The role of microglia in the healthy brain. *J. Neurosci.* **31**, 16064–16069 (2011).
16. J. Vinet, H. R. J. van Weering, A. Heinrich, R. E. Kälin, A. Wegner, N. Brouwer, F. L. Heppner, N. van Rooijen, H. W. G. M. Boddeke, K. Biber, Neuroprotective function for ramified microglia in hippocampal excitotoxicity. *J. Neuroinflammation* **9**, 27 (2012).
17. J. Priller, A. Flügel, T. Wehner, M. Boentert, C. A. Haas, M. Prinz, F. Fernández-Klett, K. Prass, I. Bechmann, B. A. de Boer, M. Frotscher, G. W. Kreutzberg, D. A. Persons, U. Dirnagl, Targeting gene-modified hematopoietic cells to the central nervous system: Use of green fluorescent protein uncovers microglial engraftment. *Nat. Med.* **7**, 1356–1361 (2001).
18. O. Butovsky, M. Koronyo-Hamaoui, G. Kunis, E. Ophir, G. Landa, H. Cohen, M. Schwartz, Glatiramer acetate fights against Alzheimer's disease by inducing dendritic-like microglia expressing insulin-like growth factor 1. *Proc. Natl. Acad. Sci. U.S.A.* **103**, 11784–11789 (2006).
19. M. Fiala, Q. N. Liu, J. Sayre, V. Pop, V. Brahmandam, M. C. Graves, H. V. Vinters, Cyclooxygenase-2-positive macrophages infiltrate the Alzheimer's disease brain and damage the blood–brain barrier. *Eur. J. Clin. Invest.* **32**, 360–371 (2002).
20. I. Rektor, D. Goldemund, K. Sheardová, I. Rektorova, Z. Michalková, M. Dufek, Vascular pathology in patients with idiopathic Parkinson's disease. *Parkinsonism Relat. Disord.* **15**, 24–29 (2009).
21. I.-U. Song, Y.-D. Kim, H.-J. Cho, S.-W. Chung, The effects of silent cerebral ischemic lesions on the prognosis of idiopathic Parkinson's disease. *Parkinsonism Relat. Disord.* **19**, 761–763 (2013).
22. S. P. Cramer, H. Simonsen, J. L. Frederiksen, E. Rostrup, H. B. W. Larsson, Abnormal blood–brain barrier permeability in normal appearing white matter in multiple sclerosis investigated by MRI. *Neuroimage Clin.* **4**, 182–189 (2014).
23. S. E. Sullivan, T. L. Young-Pearse, Induced pluripotent stem cells as a discovery tool for Alzheimer's disease. *Brain Res.* **1656**, 98–106 (2017).
24. P.-W. Zhang, A. M. Haidet-Phillips, J. T. Pham, Y. Lee, Y. Huo, P. J. Tienari, N. J. Maragakis, R. Sattler, J. D. Rothstein, Generation of GFAP::GFP astrocyte reporter lines from human adult fibroblast-derived iPS cells using zinc-finger nuclease technology. *Glia* **64**, 63–75 (2016).
25. M. C. Liao, C. R. Muratore, T. M. Gierahn, S. E. Sullivan, P. Srikanth, P. L. De Jager, J. C. Love, T. L. Young-Pearse, Single-cell detection of secreted Aβ and sAPPα from human IPSC-derived neurons and astrocytes. *J. Neurosci.* **36**, 1730–1746 (2016).
26. J. Muffat, Y. Li, B. Yuan, M. Mitalipova, A. Omer, S. Corcoran, G. Bakiasi, L.-H. Tsai, P. Aubourg, R. M. Ransohoff, R. Jaenisch, Efficient derivation of microglia-like cells from human pluripotent stem cells. *Nat. Med.* **22**, 1358–1367 (2016).
27. S. Etemad, R. M. Zamin, M. J. Ruitenberg, L. Filgueira, A novel *in vitro* human *microglia* model: Characterization of human monocyte-derived microglia. *J. Neurosci. Methods* **209**, 79–89 (2012).
28. C. Leone, G. Le Pavec, W. Même, F. Porcheray, B. Samah, D. Dormont, G. Gras, Characterization of human monocyte-derived microglia-like cells. *Glia* **54**, 183–192 (2006).
29. M. Ohgidani, T. A. Kato, D. Setoyama, N. Sagata, R. Hashimoto, K. Shigenobu, T. Yoshida, K. Hayakawa, N. Shimokawa, D. Miura, H. Utsumi, S. Kanba, Direct induction of ramified microglia-like cells from human monocytes: Dynamic microglial dysfunction in Nasu-Hakola disease. *Sci. Rep.* **4**, 4957 (2014).
30. D. Noto, H. Sakuma, K. Takahashi, R. Saika, R. Saga, M. Yamada, T. Yamamura, S. Miyake, Development of a culture system to induce microglia-like cells from haematopoietic cells. *Neuropathol. Appl. Neurobiol.* **40**, 697–713 (2014).
31. J. Sievers, R. Parwaresch, H.-U. Wottge, Blood monocytes and spleen macrophages differentiate into microglia-like cells on monolayers of astrocytes: Morphology. *Glia* **12**, 245–258 (1994).
32. C. M. Sellgren, S. D. Sheridan, J. Gracias, D. Xuan, T. Fu, R. H. Perlis, Patient-specific models of microglia-mediated engulfment of synapses and neural progenitors. *Mol. Psychiatry* **22**, 170–177 (2017).
33. F. Ginhoux, M. Greter, M. Leboeuf, S. Nandi, P. See, S. Gokhan, M. F. Mehler, S. J. Conway, L. G. Ng, E. R. Stanley, I. M. Samokhvalov, M. Merad, Fate mapping analysis reveals that adult microglia derive from primitive macrophages. *Science* **330**, 841–845 (2010).
34. R. De Simone, E. Ambrosini, D. Carnevale, M. A. Ajmone-Cat, L. Minghetti, NGF promotes microglial migration through the activation of its high affinity receptor: Modulation by TGF-β. *J. Neuroimmunol.* **190**, 53–60 (2007).
35. J. El Khoury, M. Toft, S. E. Hickman, T. K. Means, K. Terada, C. Geula, A. D. Luster, Ccr2 deficiency impairs microglial accumulation and accelerates progression of Alzheimer-like disease. *Nat. Med.* **13**, 432–438 (2007).
36. N. Esen, T. Kielian, Effects of low dose GM-CSF on microglial inflammatory profiles to diverse pathogen-associated molecular patterns (PAMPs). *J. Neuroinflammation* **4**, 10 (2007).
37. T. Schilling, R. Nitsch, U. Heinemann, D. Haas, C. Eder, Astrocyte-released cytokines induce ramification and outward K^+ channel expression in microglia via distinct signalling pathways. *Eur. J. Neurosci.* **14**, 463–473 (2001).
38. Y. Wang, K. J. Szretter, W. Vermi, S. Gilfillan, C. Rossini, M. Cella, A. D. Barrow, M. S. Diamond, M. Colonna, IL-34 is a tissue-restricted ligand of CSF1R required for the development of Langerhans cells and microglia. *Nat. Immunol.* **13**, 753–760 (2012).
39. Y. Zhang, S. A. Sloan, L. E. Clarke, C. Caneda, C. A. Plaza, P. D. Blumenthal, H. Vogel, G. K. Steinberg, M. S. B. Edwards, G. Li, J. A. Duncan III, S. H. Cheshier, L. M. Shuer, E. F. Chang, G. A. Grant, M. G. H. Gephart, B. A. Barres, Purification and characterization of progenitor and mature human astrocytes reveals transcriptional and functional differences with mouse. *Neuron* **89**, 37–53 (2016).
40. M. L. Bennett, F. C. Bennett, S. A. Liddelow, B. Ajami, J. L. Zamanian, N. B. Fernhoff, S. B. Mulinyawe, C. J. Bohlen, A. Adil, A. Tucker, I. L. Weissman, E. F. Chang, G. Li, G. A. Grant, M. G. H. Gephart, B. A. Barres, New tools for studying microglia in the mouse and human CNS. *Proc. Natl. Acad. Sci. U.S.A.* **113**, E1738–E1746 (2016).
41. B. A. Durafourt, C. S. Moore, D. A. Zammit, T. A. Johnson, F. Zaguia, M.-C. Guiot, A. Bar-Or, J. P. Antel, Comparison of polarization properties of human adult microglia and blood-derived macrophages. *Glia* **60**, 717–727 (2012).
42. J. C. Lambert, C. A. Ibrahim-Verbaas, D. Harold, A. C. Naj, R. Sims, C. Bellenguez, A. L. DeStafano, J. C. Bis, G. W. Beecham, B. Grenier-Boley, G. Russo, T. A. Thorton-Wells, N. Jones, A. V. Smith, V. Chouraki, C. Thomas, M. A. Ikram, D. Zelenika, B. N. Vardarajan, Y. Kamatani, C. F. Lin, A. Gerrish, H. Schmidt, B. Kunkle, M. L. Dunstan, A. Ruiz, M. T. Bihoreau, S. H. Choi, C. Reitz, F. Pasquier, C. Cruchaga, D. Craig, N. Amin, C. Berr, O. L. Lopez, P. L. De Jager, V. Deramecourt, J. A. Johnston, D. Evans, S. Lovestone, L. Letenneur, F. J. Morón, D. C. Rubinsztein, G. Eiriksdottir, K. Sleegers, A. M. Goate, N. Fiévet, M. W. Huentelman, M. Gill, K. Brown, M. I. Kamboh, L. Keller, P. Barberger-Gateau, B. McGuiness, E. B. Larson, R. Green, A. J. Myers, C. Dufouil, S. Todd, D. Wallon, S. Love, E. Rogaeva, J. Gallacher, P. St George-Hyslop, J. Clarimon, A. Lleo, A. Bayer, D. W. Tsuang, L. Yu, M. Tsolaki, P. Bossù, G. Spalletta, P. Proitsi, J. Collinge, S. Sorbi, F. Sanchez-Garcia, N. C. Fox, J. Hardy, M. C. Deniz Naranjo, P. Bosco, R. Clarke, C. Brayne, D. Galimberti, M. Mancuso, F. Matthews; European Alzheimer's Disease Initiative (EADI); Genetic and Environmental Risk in Alzheimer's Disease; Alzheimer's Disease Genetic Consortium; Cohorts for Heart and Aging Research in Genomic Epidemiology, S. Moebus, P. Mecocci, M. Del Zompo, W. Maier, H. Hampel, A. Pilotto, M. Bullido, F. Panza, P. Caffarra, B. Nacmias, J. R. Gilbert, M. Mayhaus, L. Lannefelt, H. Hakonarson, S. Pichler, M. M. Carrasquillo, M. Ingelsson, D. Beekly, V. Alvarez, F. Zou, O. Valladares, S. G. Younkin, E. Coto, K. L. Hamilton-Nelson, W. Gu, C. Razquin, P. Pastor, I. Mateo, M. J. Owen, K. M. Faber, P. V. Jonsson, O. Combarros, M. C. O'Donovan, L. B. Cantwell, H. Soininen, D. Blacker, S. Mead, T. H. Mosley Jr., D. A. Bennett, T. B. Harris, L. Fratiglioni, C. Holmes, R. F. de Bruijn, P. Passmore, T. J. Montine, K. J. I. R. Bettens, A. Brice, K. Morgan, T. M. Foroud, W. A. Kukull, D. Hannequin, J. F. Powell, M. A. Nalls, K. Ritchie, K. L. Lunetta, J. S. Kauwe, E. Boerwinkle, M. Riemenschneider, M. Boada, M. Hiltuenen, E. R. Martin, R. Schmidt, D. Rujescu, L. S. Wang, J. F. Dartigues, R. Mayeux, C. Tzourio, A. Hofman, M. M. Nöthen, C. Graff, B. M. Psaty, L. Jones, J. L. Haines, P. A. Holmans, M. Lathrop, M. A. Pericak-Vance, L. J. Launer, L. A. Farrer, C. M. van Duijn, C. Van Broeckhoven, V. Moskvina, S. Seshadri, J. Williams, G. D. Schellenberg, P. Amouyel, Meta-analysis of 74,046 individuals identifies 11 new susceptibility loci for Alzheimer's disease. *Nat. Genet.* **45**, 1452–1458 (2013).
43. J. M. Replogle, G. Chan, C. C. White, T. Raj, P. A. Winn, D. A. Evans, R. A. Sperling, L. B. Chibnik, E. M. Bradshaw, J. A. Schneider, D. A. Bennett, P. L. De Jager, A TREM1 variant alters the accumulation of Alzheimer-related amyloid pathology. *Ann. Neurol.* **77**, 469–477 (2015).
44. M. A. Nalls, N. Pankratz, C. M. Lill, C. B. Do, D. G. Hernandez, M. Saad, A. L. DeStefano, E. Kara, J. Bras, M. Sharma, C. Schulte, M. F. Keller, S. Arepalli, C. Letson, C. Edsall,

H. Stefansson, X. Liu, H. Pliner, J. H. Lee, R. ChengInternational Parkinson's Disease Genomics Consortium (IPDGC); Parkinson's Study Group (PSG) Parkinson's Research: The Organized GENetics Initiative (PROGENI); 23andMe; GenePD; NeuroGenetics Research Consortium (NGRC); Hussman Institute of Human Genomics (HIHG); Ashkenazi Jewish Dataset Investigator; Cohorts for Health and Aging Research in Genetic Epidemiology (CHARGE); North American Brain Expression Consortium (NABEC); United Kingdom Brain Expression Consortium (UKBEC); Greek Parkinson's Disease Consortium; Alzheimer Genetic Analysis Group, M. A. Ikram, J. P. A. Ioannidis, G. M. Hadjigeorgiou, J. C. Bis, M. Martinez, J. S. Perlmutter, A. Goate, K. Marder, B. Fiske, M. Sutherland, G. Xiromerisiou, R. H. Myers, L. N. Clark, K. Stefansson, J. A. Hardy, P. Heutink, H. Chen, N. W. Wood, H. Houlden, H. Payami, A. Brice, W. K. Scott, T. Gasser, L. Bertram, N. Eriksson, T. Foroud, A. B. Singleton, Large-scale meta-analysis of genome-wide association data identifies six new risk loci for Parkinson's disease. *Nat. Genet.* **46**, 989–993 (2014).

45. International Multiple Sclerosis Genetics Consortium (IMSGC), A. H. Beecham, N. A. Patsopoulos, D. K. Xifara, M. F. Davis, A. Kemppinen, C. Cotsapas, T. S. Shah, C. Spencer, D. Booth, A. Goris, A. Oturai, J. Saarela, B. Fontaine, B. Hemmer, C. Martin, F. Zipp, S. D'Alfonso, F. Martinelli-Boneschi, B. Taylor, H. F. Harbo, I. Kockum, J. Hillert, T. Olsson, M. Ban, J. R. Oksenberg, R. Hintzen, L. F. Barcellos; Wellcome Trust Case Control Consortium 2 (WTCCC2); International IBD Genetics Consortium (IIBDGC), C. Agliardi, L. Alfredsson, M. Alizadeh, C. Anderson, R. Andrews, H. B. Søndergaard, A. Baker, G. Band, S. E. Baranzini, N. Barizzone, J. Barrett, C. Bellenguez, L. Bergamaschi, L. Bernardinelli, A. Berthele, V. Biberacher, T. M. C. Binder, H. Blackburn, I. L. Bomfim, P. Brambilla, S. Broadley, B. Brochet, L. Brundin, D. Buck, H. Butzkueven, S. J. Caillier, W. Camu, W. Carpentier, P. Cavalla, E. G. Celius, I. Coman, G. Comi, L. Corrado, L. Cosemans, I. Cournu-Rebeix, B. A. C. Cree, D. Cusi, V. Damotte, G. Defer, S. R. Delgado, P. Deloukas, A. di Sapio, A. T. Dilthey, P. Donnelly, B. Dubois, M. Duddy, S. Edkins, I. Elovaara, F. Esposito, N. Evangelou, B. Fiddes, J. Field, A. Franke, C. Freeman, I. Y. Frohlich, D. Galimberti, C. Gieger, P.-A. Gourraud, C. Graetz, A. Graham, V. Grummel, C. Guaschino, A. Hadjixenofontos, H. Hakonarson, C. Halfpenny, G. Hall, P. Hall, A. Hamsten, J. Harley, T. Harrower, C. Hawkins, G. Hellenthal, C. Hillier, J. Hobart, M. Hoshi, S. E. Hunt, M. Jagodic, I. Jelčić, A. Jochim, B. Kendall, A. Kermode, T. Kilpatrick, K. Koivisto, I. Konidari, T. Korn, H. Kronsbein, C. Langford, M. Larsson, M. Lathrop, C. Lebrun-Frenay, J. Lechner-Scott, M. H. Lee, M. A. Leone, V. Leppä, G. Liberatore, B. A. Lie, C. M. Lill, M. Lindén, J. Link, F. Luessi, J. Lycke, F. Macciardi, S. Männistö, C. P. Manrique, R. Martin, V. Martinelli, D. Mason, G. Mazibrada, C. McCabe, I.-L. Mero, J. Mescheriakova, L. Moutsianas, K. M. Myhr, G. Nagels, R. Nicholas, P. Nilsson, F. Piehl, M. Pirinen, S. E. Price, H. Quach, M. Reunanen, W. Robberecht, N. P. Robertson, M. Rodegher, D. Rog, M. Salvetti, N. C. Schnetz-Boutaud, F. Sellebjerg, R. C. Selter, C. Schaefer, S. Shaunak, L. Shen, S. Shields, V. Siffrin, M. Slee, P. S. Sorensen, M. Sorosina, M. Sospedra, A. Spurkland, A. Strange, E. Sundqvist, V. Thijs, J. Thorpe, A. Ticca, P. Tienari, C. van Duijn, E. M. Visser, S. Vucic, H. Westerlind, J. S. Wiley, A. Wilkins, J. F. Wilson, J. Winkelmann, J. Zajicek, E. Zindler, J. L. Haines, M. A. Pericak-Vance, A. J. Ivinson, G. Stewart, D. Hafler, S. L. Hauser, A. Compston, G. McVean, P. De Jager, S. J. Sawcer, J. L. McCauley, Analysis of immune-related loci identifies 48 new susceptibility variants for multiple sclerosis. *Nat. Genet.* **45**, 1353–1360 (2013).
46. D. G. Healy, M. Falchi, S. S. O'Sullivan, V. Bonifati, A. Durr, S. Bressman, A. Brice, J. Aasly, C. P. Zabetian, S. Goldwurm, J. J. Ferreira, E. Tolosa, D. M. Kay, C. Klein, D. R. Williams, C. Marras, A. E. Lang, Z. K. Wszolek, J. Berciano, A. H. V. Schapira, T. Lynch, K. P. Bhatia, T. Gasser, A. J. Lees, N. W. Wood; International LRRK2 Consortium, Phenotype, genotype, and worldwide genetic penetrance of *LRRK2*-associated Parkinson's disease: A case-control study. **7**, 583–590 (2008).
47. C. Giambartolomei, D. Vukcevic, E. E. Schadt, L. Franke, A. D. Hingorani, C. Wallace, V. Plagnol, Bayesian test for colocalisation between pairs of genetic association studies using summary statistics. *PLOS Genet.* **10**, e1004383 (2014).
48. C. M. Karch, A. T. Jeng, P. Nowotny, J. Cady, C. Cruchaga, A. M. Goate, Expression of novel Alzheimer's disease risk genes in control and Alzheimer's disease brains. *PLOS ONE* **7**, e50976 (2012).
49. T. Hernández-Caselles, M. Martínez-Esparza, A. B. Pérez-Oliva, A. M. Quintanilla-Cecconi, A. García-Alonso, D. M. R. Alvarez-López, P. Garcia-Peñarrubia, A study of CD33 (SIGLEC-3) antigen expression and function on activated human T and NK cells: Two isoforms of CD33 are generated by alternative splicing. *J. Leukoc. Biol.* **79**, 46–58 (2006).
50. M. Fiala, D. H. Cribbs, M. Rosenthal, G. Bernard, Phagocytosis of amyloid-β and inflammation: Two faces of innate immunity in Alzheimer's disease. *J. Alzheimers Dis.* **11**, 457–463 (2007).
51. O. Butovsky, M. P. Jedrychowski, C. S. Moore, R. Cialic, A. J. Lanser, G. Gabriely, T. Koeglsperger, B. Dake, P. M. Wu, C. E. Doykan, Z. Fanek, L. Liu, Z. Chen, J. D. Rothstein, R. M. Ransohoff, S. P. Gygi, J. P. Antel, H. L. Weiner, Identification of a unique TGF-β–dependent molecular and functional signature in microglia. *Nat. Neurosci.* **17**, 131–143 (2014).
52. A. R. Bialas, B. Stevens, TGF-β signaling regulates neuronal C1q expression and developmental synaptic refinement. *Nat. Neurosci.* **16**, 1773–1782 (2013).
53. L. Fourgeaud, P. G. Través, Y. Tufail, H. Leal-Bailey, E. D. Lew, P. G. Burrola, P. Callaway, A. Zagórska, C. V. Rothlin, A. Nimmerjahn, G. Lemke, TAM receptors regulate multiple features of microglial physiology. *Nature* **532**, 240–244 (2016).
54. M. Monif, C. A. Reid, K. L. Powell, M. L. Smart, D. A. Williams, The P2X7 receptor drives microglial activation and proliferation: A trophic role for P2X7R pore. *J. Neurosci.* **29**, 3781–3791 (2009).
55. T. Town, Y. Laouar, C. Pittenger, T. Mori, C. A. Szekely, J. Tan, R. S. Duman, R. A. Flavell, Blocking TGF-β-Smad2/3 innate immune signaling mitigates Alzheimer-like pathology. *Nat. Med.* **14**, 681–687 (2008).
56. S. S. Shaftel, S. Kyrkanides, J. A. Olschowka, J.-n. Miller, R. E. Johnson, M. K. O'Banion, Sustained hippocampal IL-1β overexpression mediates chronic neuroinflammation and ameliorates Alzheimer plaque pathology. *J. Clin. Invest.* **117**, 1595–1604 (2007).
57. R. Yamasaki, H. Lu, O. Butovsky, N. Ohno, A. M. Rietsch, R. Cialic, P. M. Wu, C. E. Doykan, J. Lin, A. C. Cotleur, G. Kidd, M. M. Zorlu, N. Sun, W. Hu, L. Liu, J.-C. Lee, S. E. Taylor, L. Uehlein, D. Dixon, J. Gu, C. M. Floruta, M. Zhu, I. F. Charo, H. L. Weiner, R. M. Ransohoff, Differential roles of microglia and monocytes in the inflamed central nervous system. *J. Exp. Med.* **211**, 1533–1549 (2014).
58. B. Ajami, J. L. Bennett, C. Krieger, K. M. McNagny, F. M. V. Rossi, Infiltrating monocytes trigger EAE progression, but do not contribute to the resident microglia pool. *Nat. Neurosci.* **14**, 1142–1149 (2011).
59. C. Paisán-Ruíz, S. Jain, E. W. Evans, W. P. Gilks, J. Simón, M. van der Brug, A. López de Munain, S. Aparicio, A. M. Gil, N. Khan, J. Johnson, J. R. Martinez, D. Nicholl, I. M. Carrera, A. S. Peña, R. de Silva, A. Lees, J. F. Martí-Massó, J. Pérez-Tur, N. W. Wood, A. B. Singleton, Cloning of the gene containing mutations that cause *PARK8*-linked Parkinson's disease. *Neuron* **44**, 595–600 (2004).
60. A. Zimprich, S. Biskup, P. Leitner, P. Lichtner, M. Farrer, S. Lincoln, J. Kachergus, M. Hulihan, R. J. Uitti, D. B. Calne, A. J. Stoessl, R. F. Pfeiffer, N. Patenge, I. C. Carbajal, P. Vieregge, F. Asmus, B. Müller-Myhsok, D. W. Dickson, T. Meitinger, T. M. Strom, Z. K. Wszolek, T. Gasser, Mutations in *LRRK2* cause autosomal-dominant Parkinsonism with pleomorphic pathology. *Neuron* **44**, 601–607 (2004).
61. J. Thévenet, R. Pescini Gobert, R. Hooft van Huijsduijnen, C. Wiessner, Y. J. Sagot, Regulation of LRRK2 expression points to a functional role in human monocyte maturation. *PLOS ONE* **6**, e21519 (2011).
62. M. S. Moehle, P. J. Webber, T. Tse, N. Sukar, D. G. Standaert, T. M. DeSilva, R. M. Cowell, A. B. West, LRRK2 inhibition attenuates microglial inflammatory responses. *J. Neurosci.* **32**, 1602–1611 (2012).
63. T. Raj, K. J. Ryan, J. M. Replogle, L. B. Chibnik, L. Rosenkrantz, A. Tang, K. Rothamel, B. E. Stranger, D. A. Bennett, D. A. Evans, P. L. De Jager, E. M. Bradshaw, CD33: Increased inclusion of exon 2 implicates the Ig V-set domain in Alzheimer's disease susceptibility. *Hum. Mol. Genet.* **23**, 2729–2736 (2014).
64. A. C. Naj, G. Jun, G. W. Beecham, L.-S. Wang, B. N. Vardarajan, J. Buros, P. J. Gallins, J. D. Buxbaum, G. P. Jarvik, P. K. Crane, E. B. Larson, T. D. Bird, B. F. Boeve, N. R. Graff-Radford, P. L. De Jager, D. Evans, J. A. Schneider, M. M. Carrasquillo, N. Ertekin-Taner, S. G. Younkin, C. Cruchaga, J. S. K. Kauwe, P. Nowotny, P. Kramer, J. Hardy, M. J. Huentelman, A. J. Myers, M. M. Barmada, F. Y. Demirci, C. T. Baldwin, R. C. Green, E. Rogaeva, P. St George-Hyslop, S. E. Arnold, R. Barber, T. Beach, E. H. Bigio, J. D. Bowen, A. Boxer, J. R. Burke, N. J. Cairns, C. S. Carlson, R. M. Carney, S. L. Carroll, H. C. Chui, D. G. Clark, J. Corneveaux, C. W. Cotman, J. L. Cummings, C. DeCarli, S. T. DeKosky, R. Diaz-Arrastia, M. Dick, D. W. Dickson, W. G. Ellis, K. M. Faber, K. B. Fallon, M. R. Farlow, S. Ferris, M. P. Frosch, D. R. Galasko, M. Ganguli, M. Gearing, D. H. Geschwind, B. Ghetti, J. R. Gilbert, S. Gilman, B. Giordani, J. D. Glass, J. H. Growdon, R. L. Hamilton, L. E. Harrell, E. Head, L. S. Honig, C. M. Hulette, B. T. Hyman, G. A. Jicha, L.-W. Jin, N. Johnson, J. Karlawish, A. Karydas, J. A. Kaye, R. Kim, E. H. Koo, N. W. Kowall, J. J. Lah, A. I. Levey, A. P. Lieberman, O. L. Lopez, W. J. Mack, D. C. Marson, F. Martiniuk, D. C. Mash, E. Masliah, W. C. McCormick, S. M. McCurry, A. N. McDavid, A. C. McKee, M. Mesulam, B. L. Miller, C. A. Miller, J. W. Miller, J. E. Parisi, D. P. Perl, E. Peskind, R. C. Petersen, W. W. Poon, J. F. Quinn, R. A. Rajbhandary, M. Raskind, B. Reisberg, J. M. Ringman, E. D. Roberson, R. N. Rosenberg, M. Sano, L. S. Schneider, W. Seeley, M. L. Shelanski, M. A. Slifer, C. D. Smith, J. A. Sonnen, S. Spina, R. A. Stern, R. E. Tanzi, J. Q. Trojanowski, J. C. Troncoso, V. M. Van Deerlin, H. V. Vinters, J. P. Vonsattel, S. Weintraub, K. A. Welsh-Bohmer, J. Williamson, R. L. Woltjer, L. B. Cantwell, B. A. Dombroski, D. Beekly, K. L. Lunetta, E. R. Martin, M. I. Kamboh, A. J. Saykin, E. M. Reiman, D. A. Bennett, J. C. Morris, T. J. Montine, A. M. Goate, D. Blacker, D. W. Tsuang, H. Hakonarson, W. A. Kukull, T. M. Foroud, J. L. Haines, R. Mayeux, M. A. Pericak-Vance, L. A. Farrer, G. D. Schellenberg, Common variants at *MS4A4/MS4A6E*, *CD2AP*, *CD33* and *EPHA1* are associated with late-onset Alzheimer's disease. *Nat. Genet.* **43**, 436–441 (2011).
65. Y.-F. Mao, Z.-Y. Guo, J.-L. Pu, Y.-X. Chen, B.-R. Zhang, Association of *CD33* and *MS4A* cluster variants with Alzheimer's disease in East Asian populations. *Neurosci. Lett.* **609**, 235–239 (2015).
66. C. Reitz, G. Jun, A. Naj, R. Rajbhandary, B. N. Vardarajan, L.-S. Wang, O. Valladares, C.-F. Lin, E. B. Larson, N. R. Graff-Radford, D. Evans, P. L. De Jager, P. K. Crane, J. D. Buxbaum, J. R. Murrell, T. Raj, N. Ertekin-Taner, M. Logue, C. T. Baldwin, R. C. Green, L. L. Barnes,

L. B. Cantwell, M. D. Fallin, R. C. P. Go, P. Griffith, T. O. Obisesan, J. J. Manly, K. L. Lunetta, M. I. Kamboh, O. L. Lopez, D. A. Bennett, H. Hendrie, K. S. Hall, A. M. Goate, G. S. Byrd, W. A. Kukull, T. M. Foroud, J. L. Haines, L. A. Farrer, M. A. Pericak-Vance, G. D. Schellenberg, R. Mayeux; Alzheimer Disease Genetics Consortium, Variants in the ATP-binding cassette transporter (*ABCA7*), apolipoprotein E ϵ4, and the risk of late-onset Alzheimer disease in African Americans. *JAMA* **309**, 1483–1492 (2013).

67. M. M. Carrasquillo, O. Belbin, T. A. Hunter, L. Ma, G. D. Bisceglio, F. Zou, J. E. Crook, V. S. Pankratz, S. B. Sando, J. O. Aasly, M. Barcikowska, Z. K. Wszolek, D. W. Dickson, N. R. Graff-Radford, R. C. Petersen, P. Passmore, K. Morgan; Alzheimer's Research UK (ARUK) consortium, S. G. Younkin, Replication of *EPHA1* and *CD33* associations with late-onset Alzheimer's disease: A multi-centre case-control study. *Mol. Neurodegener.* **6**, 54 (2011).
68. G. Chan, C. C. White, P. A. Winn, M. Cimpean, J. M. Replogle, L. R. Glick, N. E. Cuerdon, K. J. Ryan, K. A. Johnson, J. A. Schneider, D. A. Bennett, L. B. Chibnik, R. A. Sperling, E. M. Bradshaw, P. L. De Jager, CD33 modulates TREM2: Convergence of Alzheimer loci. *Nat. Neurosci.* **18**, 1556–1558 (2015).
69. P. Sachamitr, S. Hackett, P. J. Fairchild. Induced pluripotent stem cells: Challenges and opportunities for cancer immunotherapy. *Front. Immunol.* **5**, 176 (2014).
70. R. T. Y. Haw, C. K. Tong, A. Yew, H. C. Lee, J. B. Phillips, S. Vidyadaran, A three-dimensional collagen construct to model lipopolysaccharide-induced activation of BV2 microglia. *J. Neuroinflammation* **11**, 134 (2014).
71. M. Ohgidani, T. A. Kato, S. Kanba, Introducing directly induced microglia-like (iMG) cells from fresh human monocytes: A novel translational research tool for psychiatric disorders. *Front. Cell. Neurosci.* **9**, 184 (2015).
72. B. J. Haas, A. Papanicolaou, M. Yassour, M. Grabherr, P. D. Blood, J. Bowden, M. B. Couger, D. Eccles, B. Li, M. Lieber, M. D. Macmanes, M. Ott, J. Orvis, N. Pochet, F. Strozzi, N. Weeks, R. Westerman, T. William, C. N. Dewey, R. Henschel, R. D. LeDuc, N. Friedman, A. Regev, De novo transcript sequence reconstruction from RNA-seq using the Trinity platform for reference generation and analysis. *Nat. Protoc.* **8**, 1494–1512 (2013).
73. B. Li, C. N. Dewey, RSEM: Accurate transcript quantification from RNA-Seq data with or without a reference genome. *BMC Bioinformatics* **12**, 323 (2011).
74. M. Leidi, E. Gotti, L. Bologna, E. Miranda, M. Rimoldi, A. Sica, M. Roncalli, G. A. Palumbo, M. Introna, J. Golay, M2 macrophages phagocytose rituximab-opsonized leukemic targets more efficiently than m1 cells in vitro. *J. Immunol.* **182**, 4415–4422 (2009).
75. A. S. P. Lim, G. P. Srivastava, L. Yu, L. B. Chibnik, J. Xu, A. S. Buchman, J. A. Schneider, A. J. Myers, D. A. Bennett, P. L. De Jager, 24-hour rhythms of DNA methylation and their relation with rhythms of RNA expression in the human dorsolateral prefrontal cortex. *PLOS Genet.* **10**, e1004792 (2014).
76. D. A. Bennett, J. A. Schneider, A. S. Buchman, L. L. Barnes, P. A. Boyle, R. S. Wilson, Overview and findings from the Rush Memory and Aging Project. *Curr. Alzheimer Res.* **9**, 646–663 (2012).
77. D. A. Bennett, J. A. Schneider, Z. Arvanitakis, R. S. Wilson, Overview and findings from the religious orders study. *Curr. Alzheimer Res.* **9**, 628–645 (2012).

Acknowledgments: We thank the participants of the PhenoGenetic Project for their time and the specimens that they contributed. **Funding:** This work was supported by the NIH grants R01 AG043617, R01 NS089674, and R01 AG048015 and the Alzheimer's Association grant DVT-14-321148. **Author contributions:** K.J.R., P.L.D.J., and E.M.B. designed and implemented the study and wrote the manuscript. K.J.R. conducted the RNA-seq, real-time gene expression, cis-eQTL, M1/M2 IL-10 expression, and flow cytometry experiments with technical assistance from K.P., M.F., M.C., P.W., A.M., M.O., B.J.K., G.C., J.I., and W.E. K.P., M.C., and M.O. performed the staining experiments for P2RY12 and TMEM119 and the 30-day culture experiment. D.A.B. generated data for the comparison of MDMi to human brain microglia. J.D.B. assisted with high content imaging of MDMi. C.C.W., J.M.R., and J.X. performed the statistical analyses and assisted with the interpretation of the results. P.L.D.J. and N.C. coordinated the collection of blood from the PhenoGenetic Project. **Competing interests:** E.M.B. is a consultant for Pfizer. P.L.D.J. is a consultant for Sanofi Genzyme, Roche, and Celgene. J.I. is a consultant for Biogen and performs editorial duties for the *Journal of Neuroimmunology*. All the other authors declare that they have no competing interests. **Data and materials availability:** The total brain RNA-seq data originating from the DLPFC is available at Synapse (www.synapse.org/#!Synapse:syn3219045). The MDMi RNA-seq data set is also available at Synapse (www.synapse.org/#!Synapse:syn3607404). Biospecimens are available under a material transfer agreement (details are at www.radc.rush.edu).

Submitted 8 August 2016
Resubmitted 12 April 2017
Accepted 18 August 2017
Published 20 December 2017
10.1126/scitranslmed.aai7635

Citation: K. J. Ryan, C. C. White, K. Patel, J. Xu, M. Olah, J. M. Replogle, M. Frangieh, M. Cimpean, P. Winn, A. McHenry, B. J. Kaskow, G. Chan, N. Cuerdon, D. A. Bennett, J. D. Boyd, J. Imitola, W. Elyaman, P. L. De Jager, E. M. Bradshaw, A human microglia-like cellular model for assessing the effects of neurodegenerative disease gene variants. *Sci. Transl. Med.* **9**, eaai7635 (2017).

DISEASES AND DISORDERS

Experimental evidence for the age dependence of tau protein spread in the brain

Susanne Wegmann[1,2*†], Rachel E. Bennett[2*], Louis Delorme[2], Ashley B. Robbins[2], Miwei Hu[2], Danny McKenzie[2], Molly J. Kirk[2], Julia Schiantarelli[2], Nahel Tunio[2], Ana C. Amaral[2], Zhanyun Fan[2], Samantha Nicholls[2], Eloise Hudry[2], Bradley T. Hyman[2†]

The incidence of Alzheimer's disease (AD), which is characterized by progressive cognitive decline that correlates with the spread of tau protein aggregation in the cortical mantle, is strongly age-related. It could be that age predisposes the brain for tau misfolding and supports the propagation of tau pathology. We tested this hypothesis using an experimental setup that allowed for exploration of age-related factors of tau spread and regional vulnerability. We virally expressed human tau locally in entorhinal cortex (EC) neurons of young or old mice and monitored the cell-to-cell tau protein spread by immunolabeling. Old animals showed more tau spreading in the hippocampus and adjacent cortical areas and accumulated more misfolded tau in EC neurons. No misfolding, at any age, was observed in the striatum, a brain region mostly unaffected by tangles. Age and brain region dependent tau spreading and misfolding likely contribute to the profound age-related risk for sporadic AD.

INTRODUCTION

Alzheimer's disease (AD) is a progressive dementia typically starting with memory impairments and progressing to profound cognitive impairments. The incidence of AD is strongly age-related, with rare cases diagnosed before age 50 and with the number of cases doubling every 10 years until more than half of the population is affected by age 90 (*1*). The cognitive symptoms are largely attributed to the intraneuronal aggregation of tau (*2*) that appears first in entorhinal and hippocampal projection neurons and over time spreads to other limbic areas, neocortical association areas, and ultimately to primary sensory cortices (*3*, *4*).

In the past years, the idea that tau protein can spread from one anatomical region to the next has been supported in experiments using transgenic mice, by viral constructs for a spatially restricted expression of mutant human tau in the brain (*5*, *6*), or by direct injections of pathological tau protein isolated from transgenic mice or human AD brain into transgenic tau mice (*7*–*11*). We reasoned that, if age played a role for the propagation and aggregation of tau in the human brain, then this would also be reflected in animal models of tau propagation. We therefore developed a method to assess the effect of (i) the age of the animal, (ii) the specific brain region, or (iii) the aggregation/misfolding state of tau on the propagation of tau in the living mouse brain.

RESULTS

Adeno-associated viruses to visualize tau protein spread between neurons

We constructed adeno-associated viruses (AAVs) that allowed us to reliably distinguish between neurons that express human tau versus neurons that receive human tau through transmissive reception of human tau protein (huTau): The AAVs are coding one mRNA, green fluorescent protein (GFP)–2a-huTau (monocistronic), but produce an equimolar ratio of two individual proteins, GFP and huTau (Fig. 1A). The short 2a peptide sequence catalyzes a self-cleavage reaction that separates GFP and huTau during translation at the ribosome (*12*). As a result, neurons that are transduced with the virus (or received the mRNA via less common mechanisms such as episomal or exosome-associated RNA transfer) produce GFP and huTau as individual proteins. In contrast, neurons that receive huTau through cell-to-cell spreading of tau protein have huTau but no GFP. Such neurons can be identified in neuronal cultures or in brain sections by coimmunofluorescence labeling of huTau and GFP (fig. S1A). In our AAV constructs, we purposefully chose the location of GFP upstream of huTau because of the following reasons: In the case of dysfunctional 2a peptide cleavage, a cell would produce the fusion protein GFP-2a-huTau, which could, in principle, also travel between cells. However, the presence of GFP would classify donor and recipient cells of GFP-2a-huTau as GFP^+ and therefore reject them from the group of tau recipient neurons. This diminishes the false positives in the system and increases the stringency of our analysis; we may, as a consequence, underestimate the amount of tau recipient neurons.

First, we verified the function of the viral constructs in vitro [fig. S1, B and C; (*13*)]. As predicted, if we express tau in a small fraction of neurons, some nontransduced murine neurons become human tau positive by receiving tau protein through cell-to-cell transmission during the first 7 days of transduction (detected by immunostaining and flow cytometry of GFP^+ and $huTau^+/GFP^-$ cells; fig. S1, B and C).

Tau protein spreads to adjacent and a few distal neurons in the mouse brain

The viral vectors were then used to explore the spreading of tau in neural circuits in vivo (Fig. 1, B to D, and fig. S2, A to D). Previous studies showed propagation of misfolded P301Ltau along a major neural pathway—from entorhinal cortex (EC) to dentate gyrus neurons—in transgenic mice after 15+ months (*5*, *6*, *14*). The propagation of pathological aggregated tau that is competent to seed tau aggregation in mutant tau transgenic mice occurs across connected brain

[1]German Center for Neurodegenerative Diseases (DZNE), 10117 Berlin, Germany. [2]Massachusetts General Hospital, Harvard Medical School, Boston, MA, USA.
*These authors contributed equally to this work.
†Corresponding author. Email: susanne.wegmann@dzne.de (S.W.); bhyman@mgh.harvard.edu (B.T.H.)

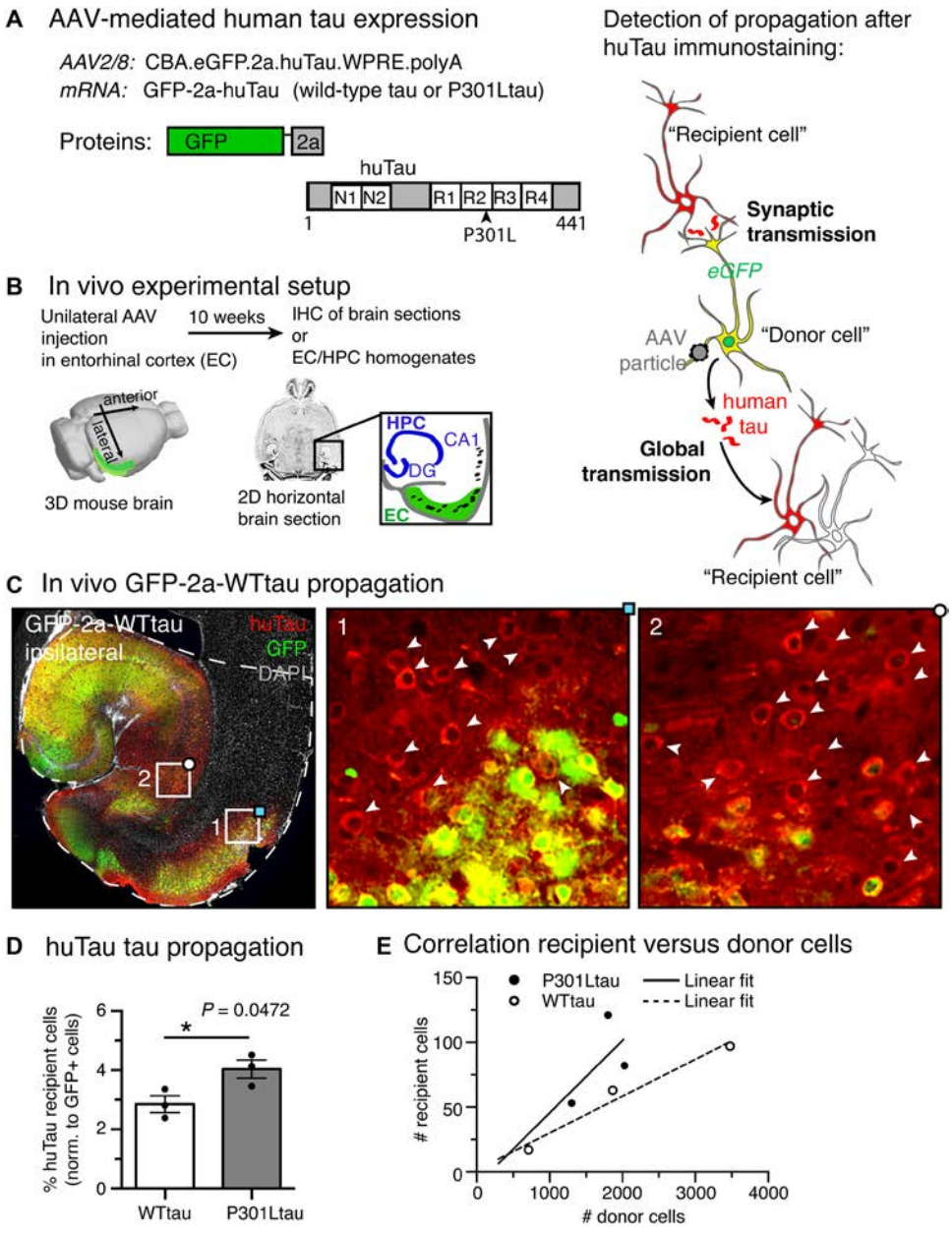

Fig. 1. Enhanced neuron-to-neuron propagation of mutant P301Ltau in vivo. (**A**) Schematic showing the AAV sequence, the mRNA, and the proteins encoded in AAV CBA.eGFP.2a.huTau (WTtau and P301Ltau), as well as the tau protein propagation principle and detection methodology. Using a self-cleaving 2a peptide, transduced "donor" neurons express both eGFP and human tau as individual proteins. The propagation of tau can be visualized by immunofluorescence labeling of postmortem brain sections or fixed neurons in culture: Human tau detected in "recipient" neurons that do not express the fluorescence transduction marker eGFP indicates the propagation of tau between cells. Thereby, the upstream location of the GFP transduction marker prevents the detection of false positives that could occur due to incomplete translation of the mRNA. (**B**) Schematic for the unilateral injection of AAV eGFP-2a-huTau into the EC (green) and the experimental work flow. The location of the EC, the HPC (and subregion CA1), and the dentate gyrus (DG) in horizontal mouse brain sections is indicated. (**C**) Example of the immunofluorescence labeling of human tau (red) and GFP (green) in a horizontal brain section of a GFP-2a-WTtau–injected mouse with many huTau recipient cells: [huTau$^+$/GFP$^-$] cells, which received tau by cell-to-cell propagation (white arrowheads in close-ups 1 and 2), can be seen adjacent to the EC injection side (1) and in synaptic connected area CA1 (2). Cells transduced with the AAV (GFP$^+$) can, in this specific case, be found in the EC and CA3. (**D**) Quantification of tau propagation (no. of recipient cells/no. of transduced cells) was done by counting all recipient (huTau$^+$, red) and donor neurons (GFP$^+$, green) in the entire ipsilateral EC and HPC formation (dashed white line). A higher propagation ($P = 0.0472$) was detected for P301Ltau compared to WTtau. (**E**) Scatterplot shows the average of recipient versus donor cells per mouse. Mean ± SEM, $n = 3$ animals per group and $n = 4$ to 5 brain sections per animal; single data points represent the mean per animal; unpaired two-tailed Student's t test with Welch's correction.

regions as well (*10*, *11*). We predicted that the spreading of tau proteins would respect anatomical pathways also when using our AAV approach and tested this idea by coinjecting AAV GFP-2a-P301Ltau with the established anterograde tracer, *Phaseolus vulgaris* leucoagglutinin (PHA-L), or the retrograde tracer cholera toxin B (CtB; fig. S3). As expected from previous reports, some recipient tau

neurons appear in areas downstream of entorhinal neurons expressing GFP-2a-tau (PHA-L$^+$) and in distal areas that are anatomically connected to the EC via long-distance projections; for example, the olfactory cortex and the contralateral EC and hippocampus (HPC) (fig. S4). However, many huTau recipient neurons were located adjacent to GFP-2a-tau donor neurons in the EC or in areas that seem to be retrogradely connected (CtB$^+$; Fig. 1C and fig. S3). This indicates that AAV-driven expression of soluble human tau in EC neurons leads to some synaptic long-distance spread and to strong local spreading of tau protein to neurons in adjacent brain areas. Notably, local spreading of tau protein could be synaptic because adjacent neurons are connected by many local recurrent collaterals; we have not yet conclusively tested this.

Enhanced spreading of soluble nonaggregated mutant tau

One of the working hypotheses states that the propagation of tau in the brain is coupled to tau misfolding. Frontotemporal dementia (FTD)–associated point mutations in the *MAPT* gene, for example, P301L, P301S, or ΔK280, enhance the misfolding and aggregation propensity of tau (*15*) and are therefore used to introduce aggregation and neurofibrillary tangle (NFT) formation in transgenic tauopathy animal models (*16*). Here, we directly compared the spreading of wild type (WT) and P301Ltau after viral expression of GFP-2a-WTtau or GFP-2a-P301Ltau in the EC and some hippocampal neurons of adult WT mice (8 to 10 months of age). Reliable detection of individual tau recipient neurons, using their immunoreactivity for huTau but not for GFP, requires a very careful evaluation of the immunolabeled brain sections, which is extremely time consuming. For simplification and experimental feasibility, we decided to count tau recipient neurons only in the hippocampal formation and adjacent cortical areas (outlined in Fig. 1C). When comparing the spreading of tau (number of recipient neurons [huTau$^+$/GFP$^-$] normalized to the number of transduced neurons [GFP$^+$] to account for animal-to-animal differences in transduction efficiency), we found more spreading for P301Ltau compared to WTtau after 8 weeks (WTtau: 2.85 ± 0.28%, n = 3; P301Ltau: 4.04 ± 0.31%, n = 3; P = 0.0472; Student's t test with Welch's correction; Fig. 1D); the number of recipient neurons varied between animals (on average 17 to 121 recipient neurons per brain section per mouse) and correlated with the number of transduced neurons, and this observation seemed somewhat independent of the amount of transduced neurons.

Next, we hypothesized that GFP-2a-P301Ltau–expressing mice would have more misfolded or aggregated tau than WTtau-expressing mice and, at the same time, tested whether tau misfolding would be necessary for tau propagation. When analyzing the aggregation state of tau in the injected mice using the Alz-50 antibody that recognizes a conformational tau epitope present in AD, P301L-expressing donor neurons in the EC were consistently immunoreactive for misfolded tau [fig. S5A; (*17*)] and showed aggregation seeding potential in a cell-based tau aggregation assay [fig. S5B; (*18*)]. In contrast, WTtau-expressing neurons showed Alz-50 reactivity only after prolonged expression (i.e., 40 weeks in fig. S5A). We did not observe obvious neuronal death even after long-term expression of the GFP-2a-P301Ltau (fig. S5C). Notably, even 40 weeks after transduction, no β sheet containing tau aggregates (positive for the tangle dye Thiazine Red) could be found in P301Ltau-expressing neurons (fig. S5D), suggesting that misfolded tau accumulations in the donor cells can persist but do not rapidly and inevitably progress into amyloid-like β sheet structures or lead to neuronal death. Alz-50$^+$ misfolded tau was not detected in recipient neurons in either P301Ltau- or WTtau-injected mice. These data suggest that misfolding of tau in the donor cells can enhance tau propagation, but tau misfolding/aggregation is not a prerequisite for propagation. These findings are further supported by work from the Buée laboratory showing the propagation of WT human tau after lentiviral expression in rat brain (*19*).

Enhanced P301Ltau spreading without changes in glial cell activation and proteostasis

In the brain, glial cells remove accumulating misfolded proteins including tau (*20*) and are part of the response to neurotoxic insults (*21*). Microglia may also be involved in tau propagation (*22*). Differences in microglia and astrocytes between WTtau- and P301Ltau-expressing mice could therefore explain the accumulation of misfolded tau and the elevated tau spreading in P301Ltau-expressing animals. By stereology, both WTtau- and P301Ltau-expressing mice had a similar increase of microglia (Iba1$^+$) in the HPC adjacent to the tau-expressing EC (WTtau: $1.63 \times 10^{-4} \pm 0.2 \times 10^{-4}$ cells/μm^2, n = 4; P301Ltau: $1.71 \times 10^{-4} \pm 0.43 \times 10^{-4}$ cells/μm^2, n = 3; P = 0.7460; unpaired Student's t test; fig. S6A). The amount of microglia was therefore not related to tau propagation in our model. By Western blot, increased astrocytic glial fibrillary acidic protein (GFAP) was detected in two of three P301Ltau-expressing ECs, although this failed to reach significance (fig. S6B). Together, we cannot rule out that differences in astrocyte activity contribute to the spread of tau in P301Ltau- versus WTtau-expressing mice, a phenomenon that has been reported elsewhere (*23*, *24*).

The intracellular misfolding of proteins can be triggered by deficits in proteostasis mechanisms; the amount of misfolded proteins increases upon decrease in chaperone activity, upon reduced protein degradation via the proteasome (which is activated upon ER stress followed by the unfolded protein response), or upon reduced autophagy (*25*). We tested whether these mechanisms contributed to the observed increase in P301Ltau protein misfolding and spreading, but found no obvious changes in autophagy (Lamp3) and proteasome (PSMD13) markers in the injected EC of P301Ltau compared to WTau-expressing mice (fig. S6C). P301Ltau-expressing mice seemed to have less chaperone activity (Hsp70) and less phospho-tau (sS396/pS404 and pS262/pS356; fig. S6D) compared to WTtau in the EC. These findings were somewhat surprising since we suspected that tau misfolding, which is enhanced for P301Ltau, would be associated with increased chaperone activity to compensate for the increase in misfolded proteins. However, the lower levels of misfolded tau in WTtau-expressing neurons could be a consequence of the higher Hsp70 levels in these mice, similar to what has been observed in a previous study (*26*). Tau misfolding is also coupled to tau hyperphosphorylation in the human AD brain. However, it may be that higher levels of phospho-tau, at least at the tested AD-relevant epitopes pS396/pS404 and pS262/pS356, are in fact more relevant for the Hsp70 chaperone response than tau misfolding.

Both WT tau hyperphosphorylation and tau misfolding are indicators of tau toxicity in the brain, which can manifest in synapse loss (*27*, *28*) or DNA damage (*29*). We did not find differences in synapse markers (PSD95 and synapsin 1) between WTtau-expressing ECs (higher phosphorylation) versus P301Ltau-expressing ECs (increased misfolding), but DNA damage (H2a.X) seemed to be increased in P301Ltau-expressing ECs (fig. S6, E and F). In summary, our findings suggest that the increased propagation of P301Ltau is likely not caused by higher intracellular tau levels because of decreased tau degradation or by changes in the total synaptic pool; instead, the

action of misfolded tau on the genomic DNA may contribute to the observed increased propagation.

Tau protein spreads faster in the old brain

Next, we explored the dependency of tau propagation and misfolding on age. Given the stronger spreading efficiency of P301Ltau, we focused on this construct. In transgenic mice, detectable P301Ltau propagation occurs in old animals (~18+ months) (*5*, *6*). It remains unclear though whether the molecular event of tau transfer between cells is too rare for an earlier detection, which therefore only becomes possible with extended time, or whether aged animals provide a neural system environment that is more permissive for tau propagation events. To answer this question, we injected young (3 months old) and old (22 to 24 months old) mice with AAV GFP-2a-P301Ltau in the EC and counted all individual huTau recipient neurons ($huTau^+/GFP^-$ neurons) and all donor neurons having GFP ($huTau^+/GFP^+$ neurons) in the entire hippocampal formation and adjacent cortical areas (Fig. 2A). Both young and old animals showed some recipient neurons after 12 weeks. Consistent with the hypothesis that the aged brain provides a milieu that is more permissive for tau spread than the young brain, the spreading rate (no. of recipient neurons/no. of transduced neurons) in old animals was about twofold higher than that in young animals (Fig. 2B; young: 0.41 ± 0.06%, $n = 4$; old: 1.01 ± 0.19%, $n = 5$; $P = 0.0322$; Student's t test with Welch's correction). The amount of transduced donor cells (GFP^+) in the EC was variable but similar in young and old mice and correlated with the number of recipient neurons (Fig. 2, C and D, and fig. S7A; on average 2.5 to 12 recipient neurons per brain section per mouse).

Neuronal death can lead to the bulk release of intracellular tau, which could boost the spreading of tau. However, young and old mice had similar numbers of neurons in the injected and noninjected EC (Fig. 2D), showing that no overt neuronal death occurred upon GFP-2a-P301Ltau expression in either group; we therefore exclude the possibility that the higher tau spreading in old mice resulted from neuronal death of transduced neurons in these animals. In fact, old mice had more recipient cells than young mice compared to the number of donor neurons (fig. S7A).

Differences in glial cell activation or deficits in proteostasis in old mice could lead to an accumulation of tau in the donor EC neurons and thereby promote the release and spreading of P301Ltau in older animals. We tested these ideas but did not find differences between young and old animals, in the amount of hippocampal microglia cells (Fig. 2E) and entorhinal astrocyte activation (GFAP in EC extracts; Fig. 2F), or in markers for autophagy (LC3B and p62) or ER stress (CCAAT/enhancer-binding protein-homologous protein, or CHOP, which is upstream of the unfolded protein response and proteasome activation; Fig. 2G and fig. S7B). A larger accumulation of tau in the donor neurons of old mice may, however, contribute to the enhanced spread, even in the absence of homeostasis changes. Other changes could also lead to an increase of tau spreading with age, for example, age-related changes in the extracellular matrix (*30*), which likely has a large influence on tau release and uptake; changes in unconventional protein secretion mediated by sulfated proteoglycans (*31*); or changes in gene transcription regulation (*32*, *33*). We also tested the level of DNA damage (H2a.X) but did not find an increase in old P301Ltau-expressing mice (fig. S7, B and C); in the future, more detailed investigations of these possibilities are needed.

To examine whether tau misfolding would also be enhanced in the old brain (the second part of our hypothesis), we compared the number of EC neurons having misfolded tau (Fig. 2H) in young versus old mice. Some old mice have ~3 times more Alz-50 immunoreactive neurons in the EC, although this did not reach statistical significance [Fig. 2I; young: $(2.65 \pm 1.4) \times 10^{-5}$ cells/µm^2, $n = 4$; old: $(4.97 \pm 2.87) \times 10^{-5}$ cells/µm^2, $n = 5$; $P = 0.1857$; Student's t test]. Considering our finding that old mice do not seem to have major deficits in protein homeostasis, it might be that some other unknown age-dependent factors are involved in the enhanced tau misfolding.

Misfolding of tau depends on the brain region

We were very intrigued to see that injections of AAV GFP-2a-P301Ltau into the striatal caudoputamen (CPu), a brain area that is not—or is very late—affected by NFT pathology in sporadic AD, did not yield P301Ltau misfolding in the same mice (Fig. 3), although both the EC and the CPu received the same amount of virus and showed similar levels of GFP-2a-P301Ltau expression in the injection sites (fig. S7D), as well as on a single-cell level (fig. S7E). Notably, in EC neurons, the level of GFP fluorescence (a proxy for P301Ltau expression level) did not correlate with tau misfolding (Fig. 3B; neurons with low GFP signal are positive for Alz-50), and neurons with similar GFP intensity were $Alz\text{-}50^+$ in the EC but not the CPu. These data suggest that tau misfolding in EC neurons is not only an effect of intracellular P301Ltau level. One possibility to explain this observation is an inherent difference between the two neuronal populations that allow (or promote) tau misfolding in EC neurons, but not in CPu neurons. These differences could be encoded in the physiology, the metabolism, the architecture, or the gene expression of other cellular pathways of the neuronal populations in different brain structures. For example, the levels of tau kinases and phosphatases seem to be different in the two brain structures (*34*), which may contribute to differential phosphorylation and misfolding.

DISCUSSION

We introduced a newly developed AAV tool, AAV GFP-2a-tau, that allows the detection of tau (or other) protein spread in the living brain in versatile ways and more efficiently than previous techniques. Notably, this model differs conceptually from models that investigate the propagation of tau pathology (tau hyperphosphorylation, aggregation, and NFT formation) in the brain upon injection of pathological tau material; those models have previously made great strides in proving the seeded aggregation of tau in different connected brain areas. In contrast, the tool we present in this study enables us to determine the spreading of tau proteins independent of their misfolding state and shows that the previously reported propagation of seeded tau aggregation may underestimate the degree of soluble nonaggregated tau spread in the brain. In addition, the viral GFP-2a-tau vectors allow us to gain experimental traction on the effect of age and brain region on neurodegeneration-related tau phenotypes in the mammalian brain: spreading, misfolding, and brain region selectivity. By injecting AAV GFP-2a-huTau into differently aged WT animals, and thereby dissociating age from the duration of transgene exposure, we showed that age has a profound effect on tau protein spreading efficiency. Given that tau spreading per se is a rare event, even in neural systems overexpressing proaggregant forms of tau in transgenic or AAV-injected mice, the ~2-fold

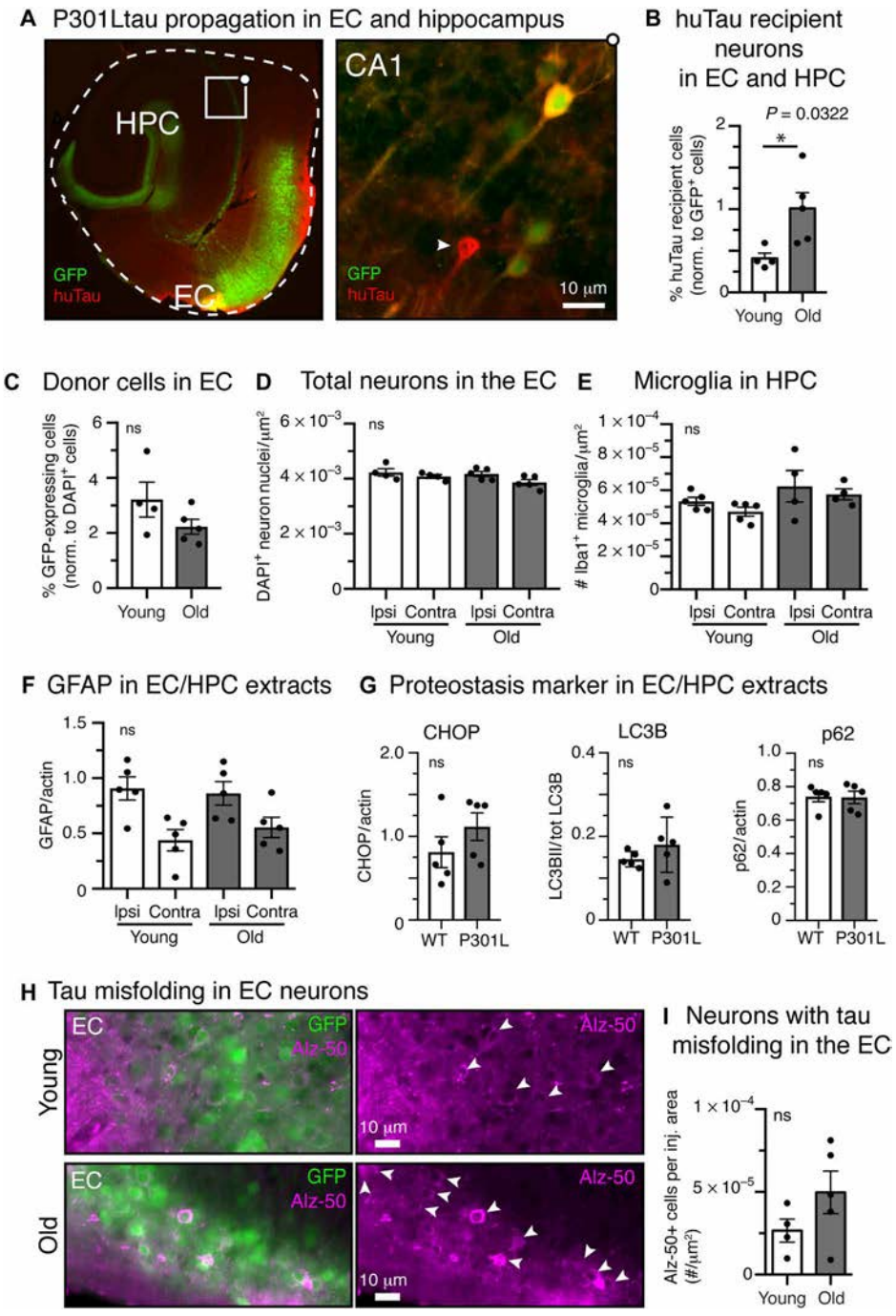

Fig. 2. Propagation and misfolding of tau are enhanced with age. (**A**) Representative images of human P301Ltau propagation after AAV GFP-2a-P301Ltau injection into the EC in young and old mice. For analysis, huTau recipient neurons (white arrowhead in CA1 close-up) were counted in the EC, the hippocampal formation, and the adjacent cortex (ROI outlined with dashed white line). (**B**) Tau propagation (no. of recipient cells/no. of transduced cells) in old animals was still small but threefold higher ($P = 0.0322$) compared to young adult animals (12 weeks after injection). (**C**) The amount of transduced GFP$^+$ neurons in the EC of young and old mice relative to the amount of total neurons (DAPI$^+$ neuronal nuclei) was determined by counting nuclei and GFP$^+$ cells in the same area of EC in parallel. (**D**) Number of neurons (large DAPI$^+$ nuclei; smaller glia nuclei were neglected) in the injected (ipsi) and noninjected (contra) EC of young and old mice reveals no difference in neuronal numbers. (**E**) Number of microglia (Iba1$^+$) in the HPC of the ipsilateral and contralateral hemisphere shows no difference between young and old mice. (**F**) GFAP levels in EC/HPC extracts from young and old mice (6 weeks after injection) suggest more activated astrocytes in the ipsilateral side of both young and old mice, compared to the contralateral side. (**G**) Western blot analysis of EC/HPC extracts from noninjected young and old mice reveals no general difference in proteostasis, in the ER stress marker CHOP, or in autophagy markers LC3B and p62. (**H**) Images showing transduced neurons (GFP$^+$, green) in the EC having misfolded tau (Alz-50$^+$, pink) in an old and a young animal. (**I**) The amount of Alz-50$^+$ neurons in the EC (normalized to area covered by transduced GFP$^+$ neurons) appears to be ~2-fold higher in old animals (ns, not significant; $P = 0.1531$). Data presented as mean ± SEM. For cell counts, $n = 4$ young and 5 old animals and $n = 3$ to 5 brain sections per animal; single data points represent the mean per animal. For brain lysates, $n = 5$ young and old animals. Two-tailed Student's *t* test with Welch's correction when comparing two groups, and one-way ANOVA with Sidak's correction when comparing multiple groups.

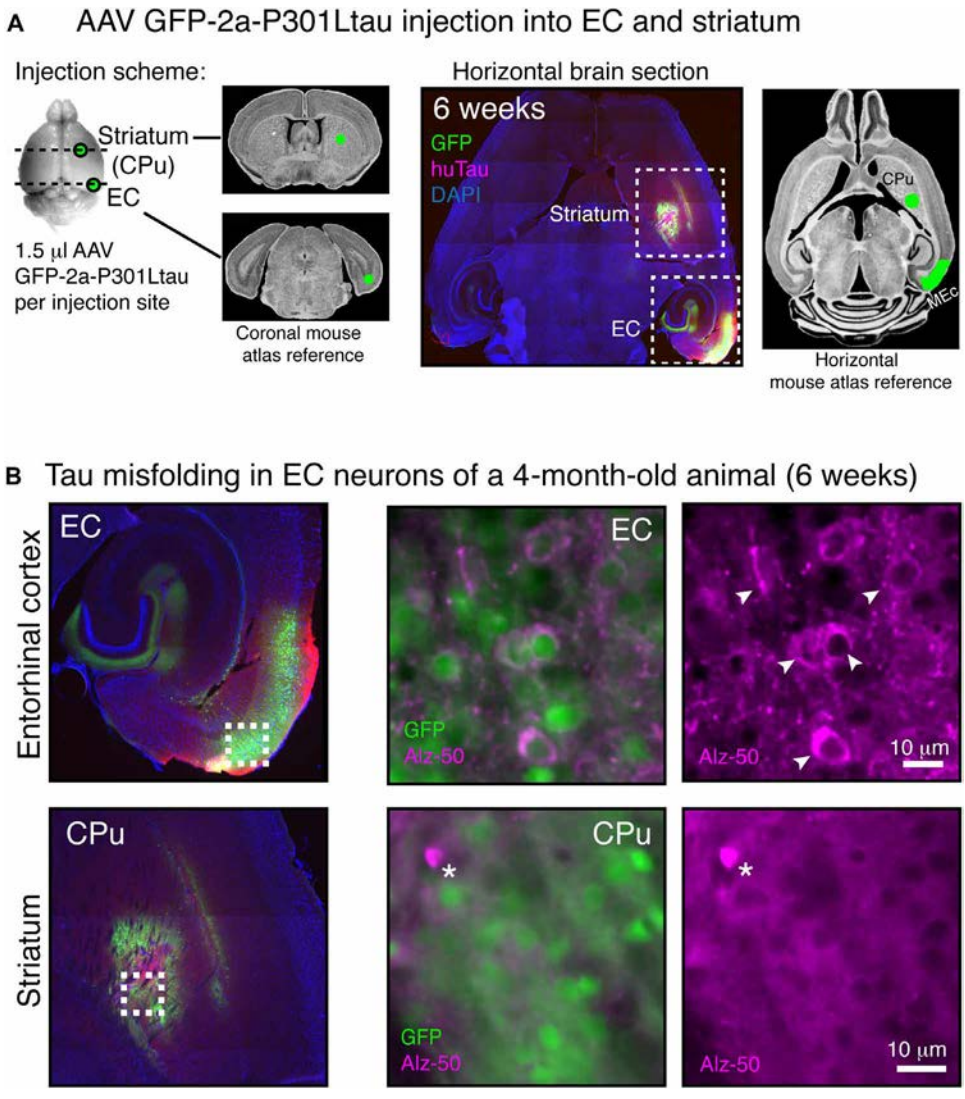

Fig. 3. P301Ltau misfolding in EC but not striatal neurons. (**A**) Injection schematic and representative immunofluorescently labeled horizontal brain section of mice that were injected in both the EC and the striatum (CPu). Reference images of brain sections (coronal and horizontal) were taken from the MBL mouse atlas (www.mbl.org/atlas232/atlas232_frame.html). (**B**) Brain sections and close-ups of P301Ltau-expressing neurons in the injection sites in the EC and the striatum. Neurons with misfolded tau (Alz-50$^+$) in the cell body can be found in the EC but not in the CPu, a region that, in most cases, does not develop tau pathology in AD. Notably, the amount of P301Ltau expression (approximated from GFP intensity) does not correlate with Alz-50 reactivity in the EC or CPu.

increased rate of spreading seen over just 12 weeks in aged mice could play a substantial role for the progression of tau pathology in older individuals.

Cell-to-cell protein transmission (in most cases) relies on the cellular release and uptake of proteins, and neuronal uptake of misfolded/aggregated tau relies on endocytosis, whereas uptake of soluble tau is additionally facilitated by macropinocytosis (*35*). Considering that we found most of the propagated tau (WT and P301L) to be soluble and not aggregated (neither Alz-50$^+$ nor Thiazine Red$^+$), this can explain the difference we observed in the tau spreading pattern (local soluble tau transmission) compared to studies that observed pathological tau aggregation/misfolding in downstream brain areas after injection or infusion of preaggregated tau into mice expressing aggregation-prone tau mutants (*9*–*11*); the propagation of soluble, nonaggregated tau has not been tested in these models. Our data indicate that the propagation of tau pathology in the brain not only could be facilitated by neuron-to-neuron transmission of misfolded seeding-competent tau but also may result from cell autonomous conditions (or cascades) that enable the misfolding of tau in certain brain areas. However, the number and the species of tau that travels across synapses remain unknown, mainly due to technical challenges.

The underlying reason for increased tau spreading in aging remains unclear. We did not find evidence of increased glial cell activation or deficits in proteostasis mechanisms, which could be expected to decrease during aging and thereby enlarge the pool of misfolded and aggregated proteins in the brain. Thus, there may be alternative drivers of tau propagation; we suspect that inherent cell autonomous conditions, which are specific for certain neuronal subpopulations in the brain, can predispose a cell for tau reception and misfolding. For example, changes in the gene transcription in individual cells, caused by DNA damage or altered heterochromatin organization, could play a role in this process. Activity dependence

of tau propagation has recently been shown in mice (*36*); however, at this point, we cannot comment on whether a related mechanism underlies the difference in tau propagation we detect in WTtau- versus P301Ltau-expressing mice, and in young versus old mice. Notably, in a recent study, we showed that both WTtau- and P301Ltau-expressing transgenic mice have a similar reduced neuronal baseline activity (*37*).

It is important to note that P301Ltau-expressing EC neurons, despite having misfolded tau (Alz-50$^+$), did not develop NFTs over a fairly extended time frame. Also important is the fact that tau recipient neurons did not develop Alz-50 reactivity. These findings suggest that the kinetics of tau spreading can be dissected from the kinetics of misfolding and aggregation at multiple points in the process: (i) Tau molecules can spread without being misfolded; (ii) tau misfolding or aggregation in donor neurons is not necessary for, but may enhance, tau spreading; and (iii) tau misfolding does not need to lead to NFT-like tau aggregation. These results challenge recent data, which suggest that even single molecules of misfolded tau are sufficient, in vitro, to initiate an irreversible cascade of tau misfolding and aggregation (*38*). It appears that under complex in vivo conditions, neurons seem to be capable of maintaining tau in a misfolded, nonaggregated state, which reinforces the possibility for a potential therapeutic window, in which one could stop the spread of tau pathology by targeting the propagation of tau regardless of its conformational state.

MATERIALS AND METHODS

Animals

All procedures were performed following the guidelines of the Institutional Animal Care and Use Committee and in compliance with the Animal Welfare Act, the *Guide for the Care and Use of Laboratory Animals*, the Office of Laboratory Animal Welfare, and the guidelines of Massachusetts General Hospital. The animals' living conditions, including housing, feeding, and nonmedical care, were maintained by the house internal animal facility (CCM). For the comparison between GFP-2a-WTtau– and GFP-2a-P301Ltau–expressing mice, 8- to 10-month-old male WT (C57BL/6, the Jackson Laboratory) mice were used. For the comparison of young (3 months old) versus old (22 to 24 months old) mice, male C57BL/6 WT mice of the respective ages were purchased from the National Institute of Aging (NIA).

Primary neuron cultures

Primary embryonic mouse neuron cultures were prepared from freshly dissected embryonic cortices, as described previously. Briefly, pregnant female CD-1 mice (Charles River) were euthanized at embryonic days 14 to 16, embryonic cortices were dissected and homogenized using a papain dissociation kit (Worthington Biochemical), and neurons were plated on culture dishes that were pretreated with poly-L-lysine. For tau propagation studies, neurons were transduced by the direct addition of AAV enhanced GFP (eGFP)–2a-WTtau or eGFP-2a-P301Ltau particles to the culture medium at 7 days in vitro (DIV), and neurons were fixed for immunostaining at 14 DIV or detached with StemPro Accutase Cell Dissociation Reagent (Thermo Fisher Scientific) from the culture dish for flow cytometry at 14 or 21 DIV.

AAV design, cloning, and production

The cloning of eGFP-2a-WTtau and eGFP-2a-P301Ltau under the ubiquitous chicken β actin (CBA) promotor was performed as described previously (*13*). The plasmid DNA of both eGFP-2a-huTau constructs and GFP were then tested for inverted terminal repeat integrity by digestion with the restriction enzyme Sma I, DNA of sufficient quality was packaged into an AAV2/8 [titers ~0.6×10^{13} virus particles/ml; Massachusetts Eye and Ear Institute vector core], and active AAV stock was aliquoted and stored at −80°C to prevent freeze-thaw cycles.

Intracranial injections

AAVs encoding eGFP, eGFP-2a-WTtau, or eGFP-2a-P301Ltau were injected unilaterally into the EC and/or striatum (CPu) of WT mice (per injection site: 3.0 μl of AAV into the EC for WTtau and P301Ltau comparison, and 1.0 μl of AAV for age and brain region comparison; three to five mice per group). Injections were performed as described previously under standard aseptic surgery conditions: Animals were anesthetized with isoflurane (3% induction and 2% maintenance), a midline incision of the skin was made above the injection sites, and burr holes were drilled through the skull at the selected coordinates [coordinates (from bregma) for EC injections: anterior/posterior (A/P): −4.7 mm, medial/lateral (M/L): ±3.3 mm, dorsal/ventral (D/V): −2.0 mm from brain surface; coordinates for striatum (CPu) injections: A/P: +0.2 mm, M/L: ±2.0 mm, D/V: −2.6 mm from brain surface]. After lowering the needle into the brain to the injection location, AAV solutions were injected at a flow rate of 0.2 μl/min. In the case of coinjections of AAV with neural tracers PHA-L (rhodamine-labeled PHA-L, Vector Laboratories) and CtB (Sigma-Aldrich), 1.0 μl of AAV solution was mixed with 1.0 μl of each tracer solution, and 3 μl of the mix was immediately injected as described. A 10-μl Hamilton syringe with a 30-gauge beveled needle that was coupled to an injector pump was used. The injector was attached to a stereotaxic frame, in which the mice were head-fixated. After finishing the injection, the needle was left in place for 2 min to allow the diffusion of the injected AAV solution. Afterward, the skin over the injection site was sutured, and the animals were allowed to recover from anesthesia on a 37°C warming pad before returning them into a clean home cage. For analgesia, all mice received a subcutaneous injection of buprenorphine (0.05 mg/kg) immediately after AAV injection and were treated with Tylenol (in drinking water) for 3 days after the surgery.

Brain tissue and lysates

For lysates of EC and HPC, mice were perfused with phosphate-buffered saline (PBS), and then we extracted the brain, dissected the EC and posterior HPC of the injected and noninjected hemisphere on ice, and snap-frozen the tissue in liquid nitrogen and stored it at −80°C. Tris-buffered saline (TBS) extracts were prepared by homogenizing the tissue in three times (v/w) TBS containing protease inhibitor (cOmplete Mini, Roche) manually with a handheld Eppendorf tube homogenizer (30 to 40 strokes on ice), followed by centrifugation at 10,000*g* for 10 min at 4°C, and the supernatant was taken as the cytosolic brain extract; this fraction was used for the human embryonic kidney (HEK) cell seeding assays and for Western blots. The total protein content of nuclear enriched fraction and of brain extracts was determined using a bicinchoninic acid assay (Pierce).

Immunofluorescence labeling

For immunofluorescence labeling of brain sections, injected mice were perfused with PBS containing 4% paraformaldehyde (PFA). The whole brains were extracted and postfixed in 4% PFA/PBS for 3 days at

4°C and then cryoprotected in 30% (w/v) sucrose in PBS for 3 days, cut horizontally into 40-μm-thick brain sections on a freezing microtome, and stored in PBS/50% glycerol at −20°C. For immunostaining, the floating brain sections were washed briefly in PBS and then permeabilized with 0.2% Triton X-100/TBS for 20 min at room temperature, blocked in 5% normal goat serum (NGS)/PBS for 1 hour at room temperature, and then incubated with primary antibodies diluted in 3% NGS/PBS overnight at 4°C: chicken anti-GFP (1:1000, Aves), mouse anti–human tau Tau13 (1:1000, BioLegend), rabbit anti–human tau TauY9 (1:1000, Enzo Life Sciences), mouse immunoglobulin M (IgM) anti-misfolded tau (1:500, Alz-50, provided by P. Davis), and goat anti-CtB (1:1000, Millipore). After washing three times with PBS, secondary antibodies were diluted in 3% NGS/PBS and applied for 1.5 hours at room temperature: Alexa 488 anti-chicken, Cy3 anti-mouse, Cy3 anti-rabbit, Alexa 647 anti-mouse IgM, and Alexa 647 anti-goat (1:1000, Thermo Fisher Scientific). After three washes in PBS, sections were mounted on microscope glass slides with mounting media containing 4′,6-diamidino-2-phenylindole (DAPI) (Southern Biotech).

Thiazine Red staining of tangles was done by applying 0.05% (w/v) Thiazine Red (Sigma-Aldrich) dissolved in PBS (GIBCO) to permeabilized brain sections for 20 min at room temperature, followed by extensive washing in PBS (four times for 10 min and once overnight) to remove unspecifically bound dye. Imaging of immunolabeled sections was done using 5×, 10×, or 20× objectives on a Zeiss Axiovert equipped with a QuickSnap camera or on an Olympus BX51.

For flow cytometry experiments, directly labeled Tau13–Alexa 647 was produced by incubating anti-human tau antibody (100 μg) Tau13 (BioLegend) with active *N*-hydroxysuccinimide–Alexa 647 (solved in dimethyl sulfoxide, Thermo Fisher Scientific) for 1 hour at room temperature in PBS (pH 7.5). Excess dye was removed by dialysis of the antibody/dye mix in dialysis cassettes (Slide-A-Lyzer, molecular weight cutoff, 3000; PIERCE) against 2 liters of PBS overnight at 4°C.

Western blot analysis of brain lysates

For Western blot analysis of various proteins in EC/HPC extracts, 10 to 20 μg of total protein per lane was loaded on 4 to 12% bis-tris SDS–polyacrylamide gel electrophoresis (SDS-PAGE) gels (Invitrogen) and separated by SDS-PAGE using MES or Mops running buffers (Invitrogen). After blotting on nitrocellulose membrane (Amersham), the membranes were blocked in PBS-based blocking buffer (LICOR) for 1 hour at room temperature and then incubated in primary antibody solutions overnight at 4°C. Antibodies in blocking buffer were as follows: mouse anti-human tau Tau13 (1:1000, BioLegend), chicken anti-GFP (1:1000, Aves), rabbit-anti GFAP (1:1000, Abcam ab7260), rat-anti Hsc70 (1:1000, Abcam ab19136), rabbit-anti Hsp70 (1:1000, Abcam ab79852), mouse-anti CHOP (alternative name DDTR1, 1:1000, Abcam ab11419), rabbit-anti PSMD13 (1:1000, Abcam ab229812), rabbit-anti Lamp3 (1:1000, ab83659), rabbit-anti LC3B (1:1000, Abcam ab51520), rabbit-anti p62 (1:1000, Abcam ab109012), mouse anti–phospho-tau PHF1 (1:1000, provided by P. Davis), mouse anti–phospho-tau 12e8 (1:1000, Prothena), goat anti-PSD95 (1:1000, Abcam ab12093), mouse anti–synapsin 1 (1:1000, Millipore MABN894), H2a.X (1:500, Abcam), and mouse anti-actin (1:1000, Millipore MAB1501R). After three washes in 0.02% Tween 20/TBS, the membranes were incubated with secondary antibodies in blocking buffer: goat anti-mouse/rabbit/rat-680 and donkey anti-mouse/rabbit/chicken/goat-800 (each 1:3000, LICOR, Rockland) for 2 hours at room temperature. Protein bands were visualized using a LICOR infrared scanner at wavelengths of 680 and 800 nm.

Stereological cell counts

The number of huTau donor cells, huTau recipient cells, Alz-50$^+$ neurons (misfolding), and DAPI$^+$ nuclei (to assess cell loss) in the EC, subiculum, and hippocampal formation of AAV-injected hemispheres was determined by counting all [GFP$^+$], [huTau$^+$/GFP$^-$], and [Alz-50$^+$] cells in the area of interest, which was outlined as region of interest (ROI) using the CAST software (Olympus). The cell numbers were counted in three to four brain sections per mouse and three to five mice per group. For DAPI$^+$ nuclei counting in the EC, we outlined layers 1, 2/3, and 4/5 of the EC and performed stereological counting of 20% of the nuclei in the ROI, followed by extrapolation to 100%. Counting was done on an Olympus BX51 light microscope equipped with a 20× objective.

Analysis of endogenous GFP fluorescence

Fixed brain sections were incubated with DAPI for 15 min and mounted on glass slides (without immunostaining), and images of whole brain sections were taken using a slide scanner with a 20× objective (VS120, Olympus). For analysis, areas with GFP fluorescence in EC and CPu were outlined in each brain section and the mean ± SD fluorescence intensity of the areas was measured using ImageJ. For single-cell fluorescence, individual cell bodies were outlined manually in the EC and CPu injection sites, and their fluorescence intensity was measured.

Flow cytometry of huTau recipient neurons

To gently detach primary neurons from culture dishes (six-well plates, Corning), each well was rinsed with 2 ml of sterile warm D-PBS$^{+/+}$ (GIBCO) and then incubated in 1 ml of prewarmed accutase (StemPro Accutase Cell Dissociation Reagent, Thermo Fisher Scientific) in the incubator for 1 hour. Using a 1-ml tip, the cell suspension was homogenized, transferred into a sterile 15-ml conical tube on ice, and centrifuged at 300*g* for 10 min at 4°C, and the cell pellet was resuspended in 2 ml of D-PBS$^{+/+}$ containing 0.5% BSA. After pelleting of the cells as before by centrifugation at 300*g*, cells were resuspended in 1 ml of D-PBS$^{+/+}$ with 0.5% BSA, and 2% PF/PBS (1 ml) was added for 10 min at room temperature to fix the cells. After washing the cells with PBS/0.5% BSA, cells were resuspended for permeabilization in 0.1% saponin (0.5 ml) in DPBS$^{+/+}$ with 0.5% BSA, and 1 μl of direct-labeled Tau13-Alexa 647 antibody was added for 30 min in the dark at 4°C. To remove excess antibody, cells were washed once in 2 ml of DPBS$^{+/+}$ with 0.5% BSA and finally resuspended in 1 ml of DPBS$^{+/+}$. Flow cytometry of huTau recipient neurons was performed on a MACSQuant VYB flow cytometer (Miltenyi Biotec). The gating for neurons having GFP and/or huTau-Alexa 647 was done using neuronal cultures transduced with AAV GFP for [GFP$^+$ and huTau$^-$] cells and with nontransduced neurons for background fluorescence. Cells were gated first on the basis of forward- and side-scatter to exclude debris and select for singlets. The proportion of Tau13$^+$ cells with and without GFP was then compared.

HEK cell tau aggregation assay

HEK293 cells that stably express CFP$^-$/YFP-TauRD-P301S (TauRD, repeat domain amino acids 244–372 of 2N4R human tau; P301S, FTD mutation) were maintained under usual cell culture conditions

in Opti-MEM (Gibco) supplemented with 5% FBS. For the experiments, cells were plated into eight-well glass-bottom dishes or 96-well plates at 50 to 60% cell density. Then the number of cells with aggregates was counted after treatment with [EC/HPC] extracts from mice injected into the EC. Tau seeding activity of TBS brain extracts was tested by applying 2.0 μg of total protein per well in a total of 200 μl of Opti-MEM containing 1% Lipofectamine 2000 (Invitrogen) in eight-well dishes and in a total of 50 μl of Opti-MEM with Lipofectamine in 96-well plates. After 30 hours, cells were washed with PBS, fixed with 4% PFA/PBS for 10 min at room temperature, and then imaged using a 20× objective on an Axiovert microscope.

Statistical analysis

To compare cell numbers and propagation rates, we determined the average cell number or cell percentage (no. of recipients/no. of donors) per mouse from three to four brain sections in three to five mice per group. For Western blots, three to five mice per group were analyzed for injected animals. Statistical analysis of differences between groups was performed using GraphPad Prism 6; groups were compared using unpaired two-tailed Student's *t* tests with Welch's correction, and confidence intervals of 95% were used. Comparison of more than two groups was done using one-way analysis of variance (ANOVA) with Sidak's or Tukey's test for multiple comparison. All values are given as mean ± SEM. Raw data are available online after publication of the manuscript.

SUPPLEMENTARY MATERIALS

Supplementary material for this article is available at http://advances.sciencemag.org/cgi/content/full/5/6/eaaw6404/DC1

Fig. S1. Detection of tau protein propagation using AAV GFP-2a-huTau.
Fig. S2. Unilateral expression of AAV GFP-2a-huTau in EC and HPC of the mouse brain.
Fig. S3. Labeling of areas connected to the AAV expression site in the EC.
Fig. S4. Tau propagates to distally connected areas after GFP-2a-WTtau expression in the EC.
Fig. S5. Enhanced misfolding in the absence of aggregation in P301Ltau-expressing EC neurons.
Fig. S6. Proteostasis, phospho-tau, and neurotoxicity markers in WTtau- and P301Ltau-expressing ECs.
Fig. S7. P301Ltau propagation, Western blots, and comparison of GFP-2a-P301Ltau expression in young and old mice.

REFERENCES AND NOTES

1. Alzheimer's Association, 2016 Alzheimer's disease facts and figures. *Alzheimers Dement.* **12**, 459–509 (2016).
2. P. V. Arriagada, J. H. Growdon, E. T. Hedley-Whyte, B. T. Hyman, Neurofibrillary tangles but not senile plaques parallel duration and severity of Alzheimer's disease. *Neurology* **42**, 631 (1992).
3. S. E. Arnold, B. T. Hyman, J. Flory, A. R. Damasio, G. W. Van Hoesen, The topographical and neuroanatomical distribution of neurofibrillary tangles and neuritic plaques in the cerebral cortex of patients with Alzheimer's disease. *Cereb. Cortex* **1**, 103–116 (1991).
4. H. Braak, E. Braak, Staging of Alzheimer's disease-related neurofibrillary changes. *Neurobiol. Aging* **16**, 271–278 (1995).
5. A. de Calignon, M. Polydoro, M. Suárez-Calvet, C. William, D. H. Adamowicz, K. J. Kopeikina, R. Pitstick, N. Sahara, K. H. Ashe, G. A. Carlson, T. L. Spires-Jones, B. T. Hyman, Propagation of Tau pathology in a model of early Alzheimer's disease. *Neuron* **73**, 685–697 (2012).
6. L. Liu, V. Drouet, J. W. Wu, M. P. Witter, S. A. Small, C. Clelland, K. Duff, Trans-synaptic spread of tau pathology in vivo. *PLoS One.* **7**, e31302 (2012).
7. F. Clavaguera, T. Bolmont, R. A. Crowther, D. Abramowski, S. Frank, A. Probst, G. Fraser, A. K. Stalder, M. Beibel, M. Staufenbiel, M. Jucker, M. Goedert, M. Tolnay, Transmission and spreading of tauopathy in transgenic mouse brain. *Nat. Cell Biol.* **11**, 909–913 (2009).
8. J. L. Guo, S. Narasimhan, L. Changolkar, Z. He, A. Stieber, B. Zhang, R. J. Gathagan, M. Iba, J. D. McBride, J. Q. Trojanowski, V. M. Y. Lee, Unique pathological tau conformers from Alzheimer's brains transmit tau pathology in nontransgenic mice. *J. Exp. Med.* **213**, 2635–2654 (2016).
9. M. Iba, J. L. Guo, J. D. McBride, B. Zhang, J. Q. Trojanowski, V. M.-Y. Lee, Synthetic tau fibrils mediate transmission of neurofibrillary tangles in a transgenic mouse model of Alzheimer's-like tauopathy. *J. Neurosci.* **33**, 1024–1037 (2013).
10. M. Iba, J. D. McBride, J. L. Guo, B. Zhang, J. Q. Trojanowski, V. M.-Y. Lee, Tau pathology spread in PS19 tau transgenic mice following locus coeruleus (LC) injections of synthetic tau fibrils is determined by the LC's afferent and efferent connections. *Acta Neuropathol.* **130**, 349–362 (2015).
11. Z. Ahmed, J. Cooper, T. K. Murray, K. Garn, E. McNaughton, H. Clarke, S. Parhizkar, M. A. Ward, A. Cavallini, S. Jackson, S. Bose, F. Clavaguera, M. Tolnay, I. Lavenir, M. Goedert, M. L. Hutton, M. J. O'Neill, A novel in vivo model of tau propagation with rapid and progressive neurofibrillary tangle pathology: The pattern of spread is determined by connectivity, not proximity. *Acta Neuropathol.* **127**, 667–683 (2014).
12. A. L. Szymczak, C. J. Workman, Y. Wang, K. M. Vignali, S. Dilioglou, E. F. Vanin, D. A. A. Vignali, Correction of multi-gene deficiency in vivo using a single 'self-cleaving' 2A peptide–based retroviral vector. *Nat. Biotechnol.* **22**, 589–594 (2004).
13. S. Wegmann, R. E. Bennett, A. S. Amaral, B. T. Hyman, Studying tau protein propagation and pathology in the mouse brain using adeno-associated viruses. *Methods Cell Biol.* **141**, 307–322 (2017).
14. S. Wegmann, E. A. Maury, M. J. Kirk, L. Saqran, A. Roe, S. L. DeVos, S. Nicholls, Z. Fan, S. Takeda, O. Cagsal-Getkin, C. M. William, T. L. Spires-Jones, R. Pitstick, G. A. Carlson, A. M. Pooler, B. T. Hyman, Removing endogenous tau does not prevent tau propagation yet reduces its neurotoxicity. *EMBO J.* **34**, 3028–3041 (2015).
15. M. von Bergen, S. Barghorn, L. Li, A. Marx, J. Biernat, E.-M. Mandelkow, E. Mandelkow, Mutations of tau protein in frontotemporal dementia promote aggregation of paired helical filaments by enhancing local β-structure. *J. Biol. Chem.* **276**, 48165–48174 (2001).
16. V. M.-Y. Lee, T. K. Kenyon, J. Q. Trojanowski, Transgenic animal models of tauopathies. *Biochim. Biophys. Acta* **1739**, 251–259 (2005).
17. G. Carmel, E. M. Mager, L. I. Binder, J. Kuret, The structural basis of monoclonal antibody Alz50's selectivity for Alzheimer's disease pathology. *J. Biol. Chem.* **271**, 32789–32795 (1996).
18. B. B. Holmes, J. L. Furman, T. E. Mahan, T. R. Yamasaki, H. Mirbaha, W. C. Eades, L. Belaygorod, N. J. Cairns, D. M. Holtzman, M. I. Diamond, Proteopathic tau seeding predicts tauopathy in vivo. *Proc. Natl. Acad. Sci. U.S.A.* **111**, E4376–E4385 (2014).
19. S. Dujardin, K. Lécolle, R. Caillierez, S. Bégard, N. Zommer, C. Lachaud, S. Carrier, N. Dufour, G. Aurégan, J. Winderickx, P. Hantraye, N. Déglon, M. Colin, L. Buée, Neuron-to-neuron wild-type Tau protein transfer through a trans-synaptic mechanism: Relevance to sporadic tauopathies. *Acta Neuropathol. Commun.* **2**, 14 (2014).
20. W. Luo, W. Liu, X. Hu, M. Hanna, A. Caravaca, S. M. Paul, Microglial internalization and degradation of pathological tau is enhanced by an anti-tau monoclonal antibody. *Sci. Rep.* **5**, 11161 (2015).
21. C. E. G. Leyns, D. M. Holtzman, Glial contributions to neurodegeneration in tauopathies. *Mol. Neurodegener.* **12**, 50 (2017).
22. H. Asai, S. Ikezu, S. Tsunoda, M. Medalla, J. Luebke, T. Haydar, B. Wolozin, O. Butovsky, S. Kügler, T. Ikezu, Depletion of microglia and inhibition of exosome synthesis halt tau propagation. *Nat. Neurosci.* **18**, 1584–1593 (2015).
23. R. Piacentini, D. D. Li Puma, M. Mainardi, G. Lazzarino, B. Tavazzi, O. Arancio, C. Grassi, Reduced gliotransmitter release from astrocytes mediates tau-induced synaptic dysfunction in cultured hippocampal neurons. *Glia* **65**, 1302–1316 (2017).
24. H. Martini-Stoica, A. L. Cole, D. B. Swartzlander, F. Chen, Y.-W. Wan, L. Bajaj, D. A. Bader, V. M. Y. Lee, J. Q. Trojanowski, Z. Liu, M. Sardiello, H. Zheng, TFEB enhances astroglial uptake of extracellular tau species and reduces tau spreading. *J. Exp. Med.* **215**, 2355–2377 (2018).
25. A. Ciechanover, Y. T. Kwon, Protein quality control by molecular chaperones in neurodegeneration. *Front. Neurosci.* **11**, 185 (2017).
26. F. Dou, W. J. Netzer, K. Tanemura, F. Li, F. U. Hartl, A. Takashima, G. K. Gouras, P. Greengard, H. Xu, Chaperones increase association of tau protein with microtubules. *Proc. Natl. Acad. Sci. U.S.A.* **100**, 721–726 (2003).
27. K. J. Kopeikina, S. Wegmann, R. Pitstick, G. A. Carlson, B. J. Bacskai, R. A. Betensky, B. T. Hyman, T. L. Spires-Jones, Tau causes synapse loss without disrupting calcium homeostasis in the rTg4510 model of tauopathy. *PLOS ONE* **8**, e80834 (2013).
28. S. Jadhav, V. Cubinkova, I. Zimova, V. Brezovakova, A. Madari, V. Cigankova, N. Zilka, Tau-mediated synaptic damage in Alzheimer's disease. *Transl. Neurosci.* **6**, 214–226 (2015).
29. B. Frost, M. Hemberg, J. Lewis, M. B. Feany, Tau promotes neurodegeneration through global chromatin relaxation. *Nat. Neurosci.* **17**, 357–366 (2014).
30. M. Morawski, M. Filippov, A. Tzinia, E. Tsilibary, L. Vargova, ECM in brain aging and dementia. *Prog. Brain Res.* **214**, 207–227 (2014).
31. T. Katsinelos, M. Zeitler, E. Dimou, A. Karakatsani, H.-M. Müller, E. Nachman, J. P. Steringer, C. Ruiz de Almodovar, W. Nickel, T. R. Jahn, Unconventional secretion mediates the trans-cellular spreading of tau. *Cell Rep.* **23**, 2039–2055 (2018).
32. H.-G. Fischer, M. Morawski, M. K. Brückner, A. Mittag, A. Tarnok, T. Arendt, Changes in neuronal DNA content variation in the human brain during aging. *Aging Cell* **11**, 628–633 (2012).
33. S. N. Saldanha, L. P. Watanabe, *Epigenetics and Dermatology* (Elsevier Science, 2015).
34. W. Hu, F. Wu, Y. Zhang, C.-X. Gong, K. Iqbal, F. Liu, Expression of tau pathology-related proteins in different brain regions: A molecular basis of tau pathogenesis. *Front. Aging Neurosci.* **9**, 311 (2017).

35. L. D. Evans, T. Wassmer, G. Fraser, J. Smith, M. Perkinton, A. Billinton, F. J. Livesey, Extracellular monomeric and aggregated tau efficiently enter human neurons through overlapping but distinct pathways. *Cell Rep.* **22**, 3612–3624 (2018).
36. J. W. Wu, S. A. Hussaini, I. M. Bastille, G. A. Rodriguez, A. Mrejeru, K. Rilett, D. W. Sanders, C. Cook, H. Fu, R. A. C. M. Boonen, M. Herman, E. Nahmani, S. Emrani, Y. H. Figueroa, M. I. Diamond, C. L. Clelland, S. Wray, K. E. Duff, Neuronal activity enhances tau propagation and tau pathology in vivo. *Nat. Neurosci.* **19**, 1085–1092 (2016).
37. M. A. Busche, S. Wegmann, S. Dujardin, C. Commins, J. Schiantarelli, N. Klickstein, T. V. Kamath, G. A. Carlson, I. Nelken, B. T. Hyman, Tau impairs neural circuits, dominating amyloid-β effects, in Alzheimer models in vivo. *Nat. Neurosci.* **22**, 57–64 (2019).
38. H. Mirbaha, D. Chen, O. A. Morazova, K. M. Ruff, A. M. Sharma, X. Liu, M. Goodarzi, R. V. Pappu, D. W. Colby, H. Mirzaei, L. A. Joachimiak, M. I. Diamond, Inert and seed-competent tau monomers suggest structural origins of aggregation. *eLife* **7**, e36584 (2018).

Acknowledgments
Funding: S.W., R.E.B., and B.T.H. received funding from the Ruth K. Broad Biomedical Research Foundation, BrightFocus Foundation, MGH, and the NIA. S.W. received additional funding from Deutsches Zentrum für Neurodegenerative Erkrankungen (DZNE) of the Helmholtz Foundation. B.T.H. received additional funding from the Tau Consortium and the Coins For Alzheimer's Research Trust (CART). **Author contributions:** S.W., R.E.B., and B.T.H. designed study concept and experiments. S.W. and R.E.B. performed most of the experiments. L.D., A.B.R., A.C.A., M.H., D.M., M.J.K., J.S., and N.T. helped with experiments. Z.F., S.N., and E.H. helped with AAV construct design and cloning. S.W., R.E.B., and B.T.H. discussed results and wrote the manuscript**. Competing interests:** The authors declare that they have no competing interests. **Data and materials availability:** All data needed to evaluate the conclusions in the paper are present in the paper and/or the Supplementary Materials. Additional data related to this paper may be requested from the authors. The plasmid encoding reporter 2A tau constructs can be provided by B.T.H. pending scientific review and a completed material transfer agreement. Requests for the material should be submitted to bhyman@mgh.harvard.edu. Additional data are available upon request from susanne.wegmann@dzne.de.

Submitted 11 January 2019
Accepted 16 May 2019
Published 26 June 2019
10.1126/sciadv.aaw6404

Citation: S. Wegmann, R. E. Bennett, L. Delorme, A. B. Robbins, M. Hu, D. McKenzie, M. J. Kirk, J. Schiantarelli, N. Tunio, A. C. Amaral, Z. Fan, S. Nicholls, E. Hudry, B. T. Hyman, Experimental evidence for the age dependence of tau protein spread in the brain. *Sci. Adv.* **5**, eaaw6404 (2019).

HEALTH AND MEDICINE

Porphyromonas gingivalis in Alzheimer's disease brains: Evidence for disease causation and treatment with small-molecule inhibitors

Stephen S. Dominy[1*†], Casey Lynch[1*], Florian Ermini[1], Malgorzata Benedyk[2,3], Agata Marczyk[2], Andrei Konradi[1], Mai Nguyen[1], Ursula Haditsch[1], Debasish Raha[1], Christina Griffin[1], Leslie J. Holsinger[1], Shirin Arastu-Kapur[1], Samer Kaba[1], Alexander Lee[1], Mark I. Ryder[4], Barbara Potempa[5], Piotr Mydel[2,6], Annelie Hellvard[3,6], Karina Adamowicz[2], Hatice Hasturk[7,8], Glenn D. Walker[9], Eric C. Reynolds[9], Richard L. M. Faull[10], Maurice A. Curtis[11,12], Mike Dragunow[11,13], Jan Potempa[2,5*]

Porphyromonas gingivalis, **the keystone pathogen in chronic periodontitis, was identified in the brain of Alzheimer's disease patients. Toxic proteases from the bacterium called gingipains were also identified in the brain of Alzheimer's patients, and levels correlated with tau and ubiquitin pathology. Oral *P. gingivalis* infection in mice resulted in brain colonization and increased production of $A\beta_{1-42}$, a component of amyloid plaques. Further, gingipains were neurotoxic in vivo and in vitro, exerting detrimental effects on tau, a protein needed for normal neuronal function. To block this neurotoxicity, we designed and synthesized small-molecule inhibitors targeting gingipains. Gingipain inhibition reduced the bacterial load of an established *P. gingivalis* brain infection, blocked $A\beta_{1-42}$ production, reduced neuroinflammation, and rescued neurons in the hippocampus. These data suggest that gingipain inhibitors could be valuable for treating *P. gingivalis* brain colonization and neurodegeneration in Alzheimer's disease.**

[1]Cortexyme, Inc., 269 East Grand Ave., South San Francisco, CA, USA. [2]Department of Microbiology, Faculty of Biochemistry, Biophysics and Biotechnology, Jagiellonian University, Krakow, Poland. [3]Malopolska Centre of Biotechnology, Jagiellonian University, Krakow, Poland. [4]Division of Periodontology, Department of Orofacial Sciences, University of California, San Francisco, San Francisco, CA, USA. [5]Department of Oral Immunology and Infectious Diseases, University of Louisville School of Dentistry, Louisville, KY, USA. [6]Broegelman Research Laboratory, Department of Clinical Science, University of Bergen, Bergen, Norway. [7]The Forsyth Institute, Cambridge, MA, USA. [8]Harvard University School of Dental Medicine, Boston, MA, USA. [9]Cooperative Research Centre for Oral Health Science, Melbourne Dental School and the Bio21 Institute of Molecular Science and Biotechnology, University of Melbourne, Melbourne, Victoria, Australia. [10]Department of Anatomy with Radiology, Centre for Brain Research and NeuroValida, Faculty of Medical and Health Sciences, University of Auckland, Auckland, New Zealand. [11]Centre for Brain Research and NeuroValida, Faculty of Medical and Health Sciences, University of Auckland, Auckland, New Zealand. [12]Department of Anatomy and Medical Imaging, Faculty of Medical and Health Sciences, University of Auckland, Auckland, New Zealand. [13]Department of Pharmacology, Faculty of Medical and Health Sciences, University of Auckland, Auckland, New Zealand.
*These authors contributed equally to this work as co-senior authors.
†Corresponding author. Email: sdominy@cortexyme.com

INTRODUCTION

Alzheimer's disease (AD) patients exhibit neuroinflammation consistent with infection, including microglial activation, inflammasome activation, complement activation, and altered cytokine profiles (*1*, *2*). Infectious agents have been found in the brain and postulated to be involved with AD, but robust evidence of causation has not been established (*3*). The recent characterization of amyloid-β (Aβ) as an antimicrobial peptide has renewed interest in identifying a possible infectious cause of AD (*4*–*6*).

Chronic periodontitis (CP) and infection with *Porphyromonas gingivalis*—a keystone pathogen in the development of CP (*7*)—have been identified as significant risk factors for developing Aβ plaques, dementia, and AD (*8*–*12*). A prospective observational study of AD patients with active CP reported a notable decline in cognition (Alzheimer's Disease Assessment Scale—Cognitive and Mini Mental State Examination scales) over a 6-month period compared to AD patients without active CP, raising questions about possible mechanisms underlying these findings (*13*). In *Apoe*$^{-/-}$ mice, oral infection with *P. gingivalis*, but not with two other oral bacteria, results in brain infection and activation of the complement pathway (*14*). In transgenic mice overexpressing mutated human amyloid precursor protein

(hAPP-J20), oral infection with *P. gingivalis* impairs cognitive function, increases the deposition of AD-like plaques, and results in alveolar bone loss compared to control hAPP-J20 mice (*15*). *P. gingivalis* lipopolysaccharide has been detected in human AD brains (*16*), promoting the hypothesis that *P. gingivalis* infection of the brain plays a role in AD pathogenesis (*17*).

P. gingivalis is mainly found during gingival and periodontal infections; however, it can also be found at low levels in 25% of healthy individuals with no oral disease (*18*). Transient bacteremia of *P. gingivalis* can occur during common activities such as brushing, flossing, and chewing, as well as during dental procedures (*19*), resulting in documented translocation to a variety of tissues including coronary arteries (*20*), placenta (*21*), and liver (*22*). A recent study found that 100% of patients with cardiovascular disease had *P. gingivalis* arterial colonization (*23*).

P. gingivalis is an asaccharolytic Gram-negative anaerobic bacterium that produces major virulence factors known as gingipains, which are cysteine proteases consisting of lysine-gingipain (Kgp), arginine-gingipain A (RgpA), and arginine-gingipain B (RgpB). Gingipains are secreted, transported to outer bacterial membrane surfaces, and partially released into the extracellular milieu in soluble and outer membrane vesicle (OMV)–associated forms (*24, 25*). Kgp and RgpA/B are essential for *P. gingivalis* survival and pathogenicity, playing critical roles in host colonization, inactivation of host defenses, iron and nutrient acquisition, and tissue destruction (*24, 26*). Gingipains have been shown to mediate the toxicity of *P. gingivalis* in endothelial cells, fibroblasts, and epithelial cells (*27–29*). Moreover, because treatment with broad-spectrum antibiotics rarely eradicates *P. gingivalis* and may lead to resistance (*30*), gingipains are implicated as narrow-spectrum virulence targets (*24, 31–33*). Blocking gingipain proteolytic activity with short peptide analogs reduces *P. gingivalis* virulence (*34*).

We hypothesized that *P. gingivalis* infection acts in AD pathogenesis through the secretion of gingipains to promote neuronal damage. We found that gingipain immunoreactivity (IR) in AD brains was significantly greater than in brains of non-AD control individuals. In addition, we identified *P. gingivalis* DNA in AD brains and the cerebrospinal fluid (CSF) of living subjects diagnosed with probable AD, suggesting that CSF *P. gingivalis* DNA may serve as a differential diagnostic marker. We developed and tested potent, selective, brain-penetrant, small-molecule gingipain inhibitors in vivo. Our results indicate that small-molecule inhibition of gingipains has the potential to be disease modifying in AD.

AD diagnosis correlates with gingipain load in brain

Tissue microarrays (TMAs) containing sex- and age-matched brain tissue cores from the middle temporal gyrus (MTG) of both AD patients and neurologically normal individuals were used for immunohistochemical (IHC) studies (tables S1 and S2). Gingipain-specific antibodies, CAB101 and CAB102, targeting RgpB and Kgp, respectively, were used to determine gingipain load in brain tissue cores. Tau load in the TMAs was measured using an antibody (DAKO A0024) that recognizes both nonphosphorylated and phosphorylated tau. RgpB and Kgp exhibited punctate intraneuronal staining in tissue from AD brains (Fig. 1, A and B, respectively). On the basis of threshold analysis (see Materials and Methods), 96% (51 of 53) of AD samples were positive for RgpB and 91% (49 of 54) of AD samples were positive for Kgp. The RgpB load was significantly higher in AD brains than in nondemented control brains (Fig. 1C), and similarly, the Kgp load was significantly higher in AD brains compared to nondemented control brains (Fig. 1D).

We next stained for tau and found a highly significant correlation between RgpB load and tau load (Fig. 1E) and Kgp load and tau load (Fig. 1F). Tau pathology has been shown to correlate with cognitive impairment in AD (*35*). We next stained the TMAs for ubiquitin, a small protein tag that marks damaged proteins for degradation by proteasomes (*36*) and accumulates in both tau tangles and Ab plaques (*37*). There was a significant correlation between RgpB load and ubiquitin load (Fig. 1G) and Kgp load and ubiquitin load (Fig. 1H) in the TMAs. Of note, in nondemented control tissues, RgpB staining was observed in 39% (18 of 46) of samples and Kgp staining was observed in 52% (26 of 50) of samples. The correlation analyses between the gingipain load and tau load (Fig. 1, E and F) and between the gingipain and ubiquitin load (Fig. 1, G and H) in the nondemented control samples revealed a continuum of gingipain and AD pathology already present in the controls. These findings are consistent with the concept of preclinical AD, i.e., the stage of disease when pathogenesis has begun, but clinical symptoms are not yet present (*38*).

To further validate the gingipain IHC in the TMAs, we performed a correlation analyses between the RgpB load and Kgp load and found a significant correlation between the two different antigens (Fig. 1I). As a further IHC control, brain TMAs from several different non-AD neurological diseases were probed with the CAB101 antibody. RgpB immunostaining on MTG TMAs of Parkinson's disease, Huntington's disease, and amyotrophic lateral sclerosis revealed no significant differences compared to controls (fig. S1). In summary, both RgpB and Kgp antigens in brain independently demonstrated a significant correlation with AD diagnosis, tau load, and ubiquitin load.

RgpB colocalizes with neurons, astrocytes, and pathology in AD hippocampus

In AD, the hippocampus is one of the first brain areas to be damaged. Using a different antibody for RgpB than CAB101 (18E6 monoclonal; see Materials and Methods), RgpB-IR was confirmed in neurons of the dentate gyrus and CA3, CA2, and CA1 of AD hippocampus with brightfield microscopy (Fig. 2A). IHC analysis of a series of brains from a university brain bank revealed a similar pattern of staining for RgpB (fig. S2). Using immunofluorescence, RgpB-IR (CAB101) colocalized primarily with neurons [microtubule-associated protein 2 (MAP2)] (Fig. 2C) as well as occasional astrocytes, but not with microglia (Iba1) (Fig. 2D). In addition, RgpB colocalized with pathology including tau tangles and intraneuronal Aβ (Fig. 2E).

Detection of Kgp in AD cerebral cortex

AD is also associated with atrophy of the gray matter of the cerebral cortex. Brain lysates from the cerebral cortex of three AD brains and six nondemented control brains were immunoprecipitated (IP) with CAB102 and run on a Western blot (WB) (Fig. 3B). The CAB102 polyclonal antibody recognizes amino acids 22 to 400 of Kgp, covering the propeptide and the N-terminal region of the catalytic domain (see Materials and Methods). The WB from all three AD brains revealed similar Kgp bands of molecular weights corresponding to the molecular weights of Kgp bands from bacterial lysates from *P. gingivalis* strains W83, ATCC33277, and FDC381 (Fig. 3A). Strain HG66, which contains a mutation affecting the retention of gingipains on its cell surface (*39*), demonstrated only a single Kgp band at the molecular weight of the Kgp catalytic domain (Fig. 3A). The Kgp catalytic domain was identified at the proper molecular weight (*40*) in all of the AD brain samples (Fig. 3B). In addition, five of the six nondemented control brains demonstrated Kgp banding patterns similar to the AD brains (Fig. 3B), consistent with our IHC data demonstrating a continuum of gingipain and AD pathology present in nondemented control brains (Fig. 1, D, F, and H). In the sixth nondemented control brain sample (C6), the Kgp bands were very faint, indicating near absence of Kgp (Fig. 3B).

Identification of the *P. gingivalis 16S rRNA* and *hmuY* genes in AD cerebral cortex

To further validate the Kgp protein detection data, we performed quantitative polymerase chain reaction (qPCR) analysis on DNA isolated from the same brain tissue used for the Kgp IP and WB analysis. qPCR analysis using *P. gingivalis 16S rRNA* primers revealed the presence of the *P. gingivalis 16S rRNA* gene in the AD brains and five of the six nondemented control brains (Fig. 3C). Control brain C6, which exhibited near absence of Kgp bands in Fig. 3B above, was negative by qPCR for the *P. gingivalis 16S rRNA* gene (Fig. 3C). To further validate the *16S rRNA* qPCR results, we performed PCR analysis using primers for the *hmuY* gene, a gene highly specific for *P. gingivalis* (*41*). All three AD brains and the five nondemented control brains that were positive for the *16S rRNA* gene were also positive for the *hmuY* gene, and sequencing of the *hmuY* PCR products confirmed the presence of *P. gingivalis* in brain DNA (fig. S3). Because we were using

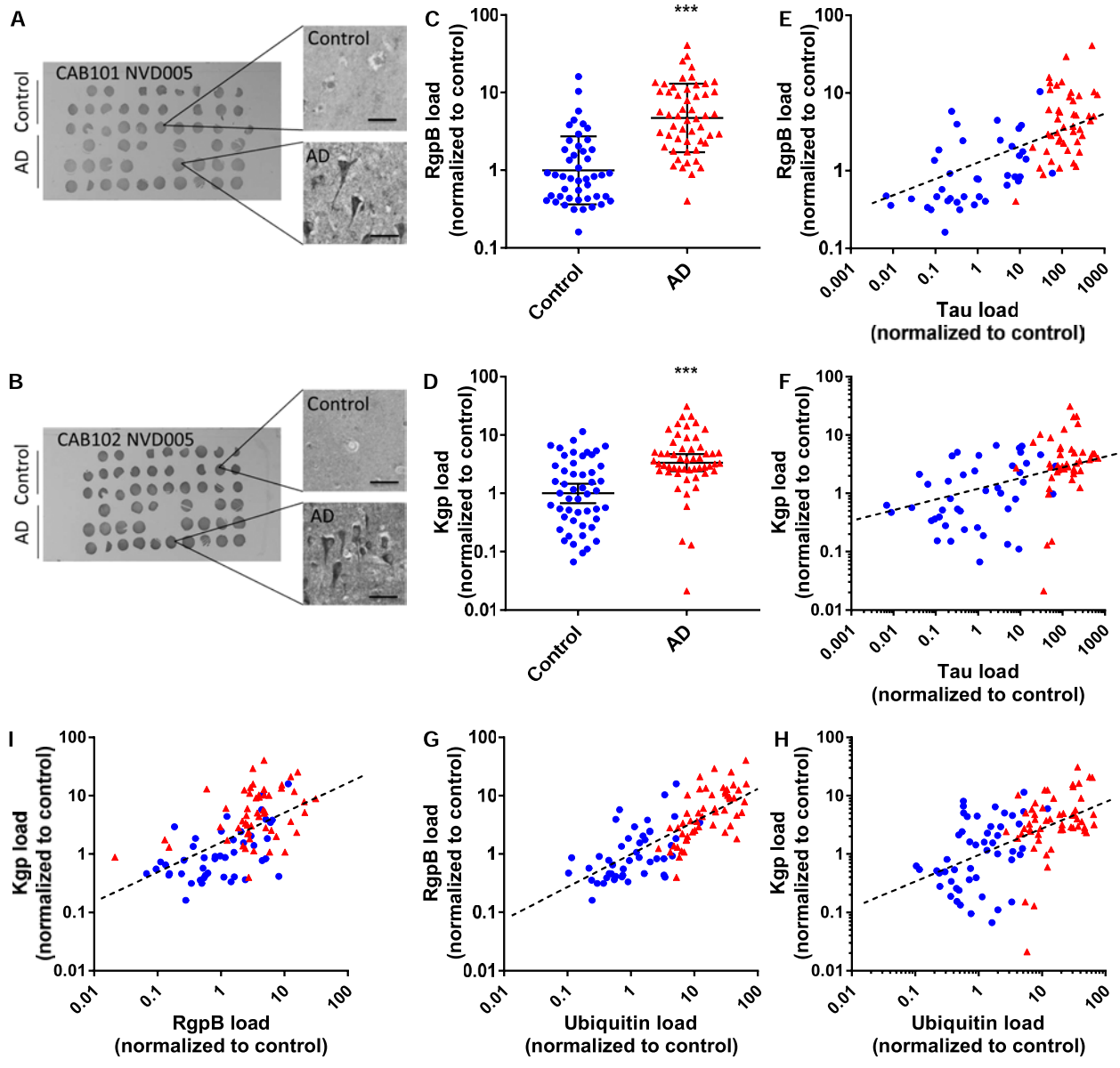

Fig. 1. Gingipain IR in brain correlates with AD diagnosis and pathology. (**A** and **B**) Representative TMA NVD005 containing brain tissue cores from the MTG of AD patients and controls probed for RgpB (A) and Kgp (B) with antibodies CAB101 and CAB102, respectively. Higher magnification of representative tissue cores reveals higher neuronal RgpB-IR and Kgp-IR in AD tissue cores than in control cores. (**C**) RgpB-IR and (**D**) Kgp-IR data from TMAs NVD005 and NVD003 show significantly higher load in AD brain compared to controls. Mann-Whitney test, ***$P < 0.0001$; presented as geometric mean ± 95% confidence interval, $n = 99$ (C) and $n = 104$ (D). (**E** and **F**) Tau load correlates to RgpB load (Spearman $r = 0.674$, $P < 0.0001$, $n = 84$) (E) and Kgp load (Spearman $r = 0.563$, $P < 0.0001$, $n = 89$) (F). Blue, control; red, AD. (**G** and **H**) Ubiquitin load, a marker of AD pathology, correlates to RgpB load (blue, control; red, AD; Spearman $r = 0.786$, $P < 0.0001$, $n = 99$) (G) and Kgp load (Spearman $r = 0.572$, $P < 0.0001$, $n = 104$) (H). (**I**) RgpB load correlates with Kgp load (Spearman $r = 0.610$, $P < 0.0001$, $n = 99$).

a highly sensitive PCR method to detect low copy numbers of *P. gingivalis* DNA (see Materials and Methods), we were concerned that nested amplification of a common Gram-negative bacterium such as *P. gingivalis* in the presence of brain DNA could be creating a false-positive signal. Therefore, as an additional negative control, we used the same nested primer method to attempt to detect another ubiquitous Gram-negative bacterium, *Helicobacter pylori* (see Materials and Methods) (*42*). We tested the three AD brain DNA samples and three of the *P. gingivalis*–positive nondemented brain DNA samples for *H. pylori*. All six brain samples were negative for *H. pylori* using validated qPCR primers and probe (fig. S3D) (*43*), indicating that our *P. gingivalis* PCR results are not likely due to a PCR artifact. In summary, the identification of *P. gingivalis* DNA in AD brains and Kgp-positive nondemented control brains further validates the identification of Kgp in the same brain tissue samples by IP and WB.

P. gingivalis DNA is present in the CSF of clinical AD patients

CSF is considered a "window" into brain infection, providing insight into the neuropathogenesis of infectious agents (*44*). Hence, we conducted a prospective pilot study using CSF collected from 10 patients diagnosed with probable AD who had mild to moderate cognitive impairment (Fig. 4D). CSF and matched saliva samples were collected and analyzed for *P. gingivalis* DNA by qPCR detection of the *hmuY* gene (*41*). Positive and negative controls, similar to the standard of care for detection of other brain infections in CSF, were used (*45*, *46*). We were able to detect and quantify

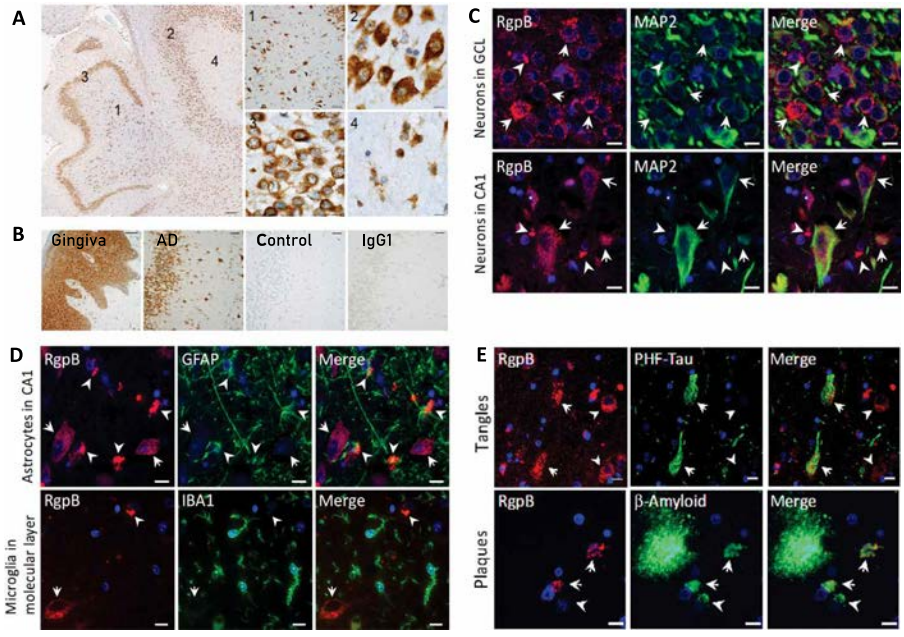

Fig. 2. RgpB colocalizes with neurons and pathology in AD hippocampus. (**A**) IHC using RgpB-specific monoclonal antibody 18E6 (representative images from a 63-year-old AD patient). The hippocampus shows abundant intracellular RgpB in the hilus (1), CA3 pyramidal layer (2), granular cell layer (3), and molecular layer (4). High-magnification images from the indicated areas (1 to 4) exhibit a granular staining pattern consistent with *P. gingivalis* intracellular infection. Scale bars, 200 μm (overview), 50 μm (1), and 10 μm (2 to 4). (**B**) AD hippocampus stained with 18E6 (AD) compared to gingival tissue (gingiva) from a patient with periodontal disease as well as a non-AD control and mouse IgG1 control (IgG1) in an adjacent hippocampal section. Scale bars, 50 μm. (**C**) Immunofluorescent colabeling with CAB101 reveals granular intraneuronal staining for RgpB (arrows) in MAP2-positive neurons in both the granular cell layer (GCL) and the pyramidal cell layer (CA1). Scale bars, 10 μm. (**D**) Dense extracellular RgpB-positive aggregates (arrowheads) were closely associated with astrocytes [glial fibrillary acidic protein (GFAP)]. There was no observed association of RgpB with microglia (IBA1). Scale bars, 10 μm. (**E**) RgpB was associated with paired helical filament Tau (PHF-Tau; arrows). RgpB-positive neurons negative for PHF-Tau (arrowheads) were also seen. Intracellular Aβ was often colocalized with RgpB (arrows). In some Aβ-positive cells, RgpB could not be detected (arrowheads). Scale bars, 10 μm.

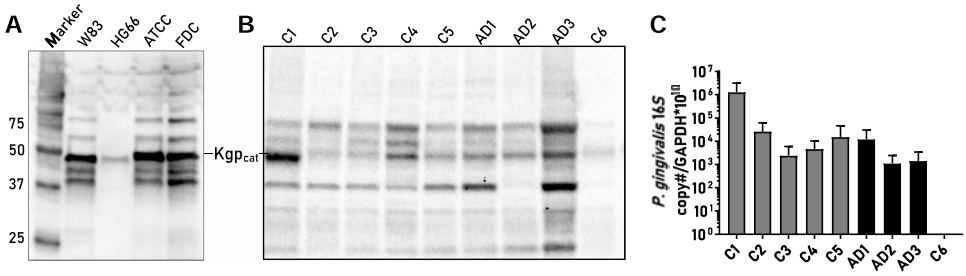

Fig. 3. Identification of *P. gingivalis*–specific protein and DNA in cortex from control and AD patients. (**A**) WB with four different strains of *P. gingivalis* and CAB102 detection of typical molecular weight bands for Kgp in bacterial lysates. (**B**) IP using brain lysates from nondemented controls (C1 to C6; ages 75, 54, 63, 45, 37, and 102 years, respectively) and AD patients (AD1 to AD3; ages 83, 90, and 80 years, respectively) using CAB102 with subsequent WB reveals the ~50-kDa Kgp catalytic subunit (Kgp$_{cat}$), along with higher– and lower–molecular weight Kgp species seen in (A). (**C**) qPCR from DNA isolated from the same brain lysates as the protein samples analyzed in (B) shows a positive signal in nondemented control (C1 to C5) and AD (AD1 to AD3) samples. Sample C6 from the 102-year-old nondemented control patient had no detectable qPCR signal in (C) and very faint bands indicating near absence of Kgp (B) (mean with SEM error bars of repeat qPCR runs).

copies of the *hmuY* gene by qPCR in CSF in 7 of the 10 clinically diagnosed AD patients, with *P. gingivalis* load ranging from 10 to 50 copies/μl of CSF (Fig. 4A), and the relative fluorescence intensity of the qPCR products on agarose gel was consistent with the qPCR data (Fig. 4C). Sequencing of the endpoint PCR products from CSF confirmed the presence of the *hmuY* gene (fig. S4). We then quantified the *P. gingivalis* load in the matching saliva samples from all 10 patients. All 10 matching saliva samples were positive for *P. gingivalis* by qPCR assay of the *hmuY* gene (Fig. 4B). As with the brain samples noted above, for a PCR-negative control, we analyzed CSF samples for the presence of *H. pylori* using methods with the same sensitivity as for *P. gingivalis*. All of the CSF samples were negative for *H. pylori* (Fig. 4C). The CSF data provide additional evidence for *P. gingivalis* infection in the brain of AD patients.

Tau is fragmented by gingipains

Because we identified colocalization of gingipain with tau tangles in AD brain (Fig. 2E), we were interested to see whether tau was a target for gingipain proteolysis. Tau truncation and fragmentation have been proposed to play a key role in inducing the formation of insoluble and hyperphosphorylated tau in AD (*47*–*49*). To determine whether gingipains cleave tau in a cell-based system, we used SH-SY5Y cells that express high–molecular weight forms of tau (*50*).

Using the Tau-5 antibody as a probe, SH-SY5Y cells infected with three different concentrations of *P. gingivalis* were examined at three different time points. The results showed a dose-dependent loss of soluble total tau within 1 hour of infection compared to uninfected cells, while cells infected with *P. gingivalis* gingipain–defective mutants showed soluble tau levels

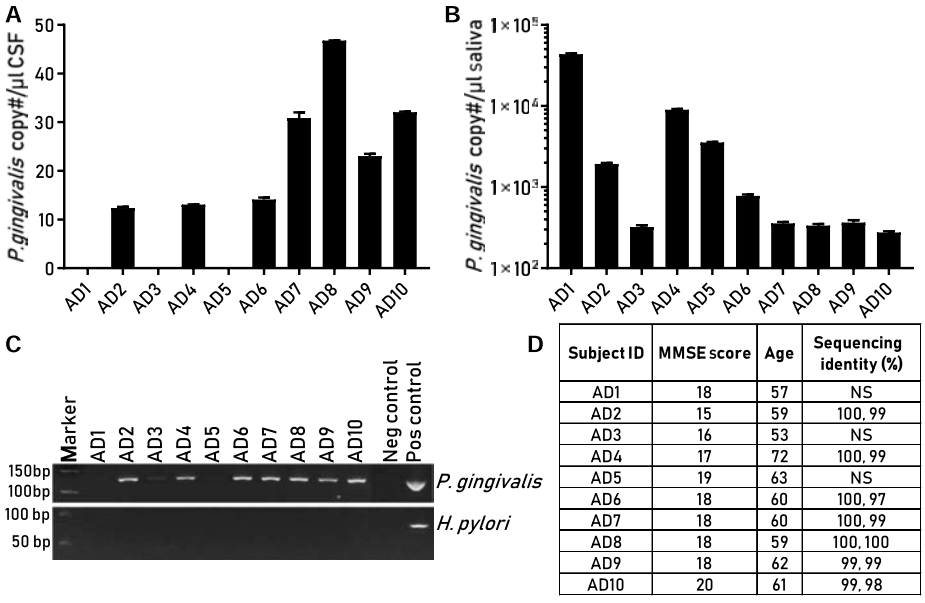

Subject ID	MMSE score	Age	Sequencing identity (%)
AD1	18	57	NS
AD2	15	59	100, 99
AD3	16	53	NS
AD4	17	72	100, 99
AD5	19	63	NS
AD6	18	60	100, 97
AD7	18	60	100, 99
AD8	18	59	100, 100
AD9	18	62	99, 99
AD10	20	61	99, 98

Fig. 4. Detection of *P. gingivalis* in CSF and oral biofluids from clinical AD subjects. (**A**) Detection and quantitation of *P. gingivalis* DNA by qPCR in CSF from subjects with probable AD. (**B**) Detection and quantitation of *P. gingivalis* DNA by qPCR from matching saliva samples. (**C**) Top: PCR products detecting *P. gingivalis* from CSF in (A) from all subjects run on agarose gel including negative and positive controls containing a synthetic DNA template. Faint or undetectable PCR products from subjects AD1, AD3, and AD5 were below the limit of quantitation for copy number and not of sufficient quantity for sequence analysis. Bottom: qPCR products from CSF from the same subjects for *H. pylori*. (**D**) Data table includes age and Mini Mental Status Exam (MMSE) score on subjects and sequence identity of PCR products to *P. gingivalis hmuY* DNA sequence. Sequence data are included in fig. S4. NS, not sequenced.

similar to uninfected cells, indicating that gingipains were responsible for the loss of the Tau-5 epitope (Fig. 5, A and B).

To characterize gingipain cleavage sites within tau, we incubated recombinant tau-441 with purified protein containing the catalytic domains of both Kgp and RgpB in combination and identified tau cleavage fragments by mass spectrometry (MS). Following exposure to 1 nM purified gingipains, we identified tau fragments covering 23% of the tau-441 amino acid sequence; at 10 nM gingipains, tau fragments were generated covering 85% of the tau sequence (Fig. 5D and table S3). From the identified tau fragments, we were able to deduce 14 RgpB cleavage sites and 30 Kgp cleavage sites within the tau-441 protein (Fig. 5D). Most of the Kgp cleavage sites (21 of 30) were located C-terminal to position 222 in the tau protein. For RgpB, the majority of cleavage sites (9 of 14) were located N-terminal to position 222. Within the Tau-5 antibody epitope, which spans residues 210 to 230 in tau-441, we identified two RgpB cleavage sites and two Kgp cleavage sites (Fig. 5D, b). Thus, gingipain cleavages within the Tau-5 antibody epitope were the likely cause of the loss of the Tau-5 antibody signal and therefore tau protein detection after SH-SY5Y cells were infected with *P. gingivalis*.

We identified a mid-domain, RgpB-generated tau peptide fragment, TPSLPTPPTR (residues 212 to 221), which is part of the Tau-5 epitope (Fig. 5D, g). This tau peptide is common to all tau isoforms and has been used as an analyte to measure tau levels in CSF (*51*) and determine the turnover rate of tau in the human central nervous system (CNS) (*52*). The TPSLPTPPTR fragment has been reported to be increased 1.7-fold in AD CSF compared to non-AD CSF (*51*).

Kgp generated four unique tau peptide fragments containing the hexapeptide sequence VQIVYK (Fig. 5D, e) and two unique tau peptide fragments containing the VQIINK sequence (Fig. 5D, f). Tau fragments containing these hexapeptide motifs have been shown to be involved in tau tangle formation by nucleating paired helical filaments (PHFs) from full-length tau (*53*, *54*).

Small-molecule gingipain inhibitors are neuroprotective

To determine whether gingipains are toxic to neurons in vitro, we exposed differentiated SH-SY5Y cells to either RgpB or Kgp for 24 hours. Combined application of RgpB and Kgp significantly increased cell aggregation (Fig. 6A). Pretreatment of gingipains with iodoacetamide, an irreversible cysteine protease inhibitor, prevented gingipain-induced aggregation, indicating that the proteolytic activity of the gingipains was responsible for the morphological changes (Fig. 6A).

On the basis of the cytotoxic activity of gingipains from *P. gingivalis*, their presence in AD brain, and their critical role in bacterial survival and virulence, we developed a library of potent and selective reversible and irreversible small-molecule gingipain inhibitors. COR286 and COR271 are irreversible inhibitors of arginine-specific (RgpA and RgpB) and lysine-specific (Kgp) gingipains, respectively, both with a median inhibitory concentration (IC_{50}) of <50 pM. COR119 is a reversible covalent Kgp inhibitor with an IC_{50} of 10 nM.

To quantify protective effects of gingipain inhibitors, we infected SH-SY5Y cells with the W83 strain of *P. gingivalis* at a multiplicity of infection (MOI) of 400 for 48 hours, producing approximately 50% cell death (Fig. 6B). COR286 and COR271 were both effective in blocking *P. gingivalis*–induced cell death in a concentration-dependent manner (Fig. 6B). Broad-spectrum antibiotics, moxifloxacin and doxycycline, even at concentrations that reduce bacterial survival in vitro (*55*), did not protect the cells. We also tested the γ-secretase inhibitor semagacestat (LY450139), which blocks the formation of $A\beta_{1-42}$ (*56*), to determine whether bacterial toxicity was mediated by *P. gingivalis*–induced Aβ production, but it had no protective effect (Fig. 6B).

We next assessed whether gingipains are neurotoxic in vivo and whether inhibitors can penetrate the brain and prevent gingipain neurotoxicity. Eight-week-old BALB/c mice were given a single administration of gingipain inhibitors via a combination of COR271 by oral gavage and COR286 subcutaneously, or both vehicles. Stereotactic injection of a combination of Kgp and RgpB into the hippocampus was performed 1.5 hours later. Seven days later, brains were analyzed for neurodegeneration. Mice injected with gingipains had a significantly greater number of degenerating neurons than saline-injected mice, but the neurodegeneration could be blocked by pretreatment with a combination of gingipain inhibitors COR286 and COR271 (Fig. 6, C and D).

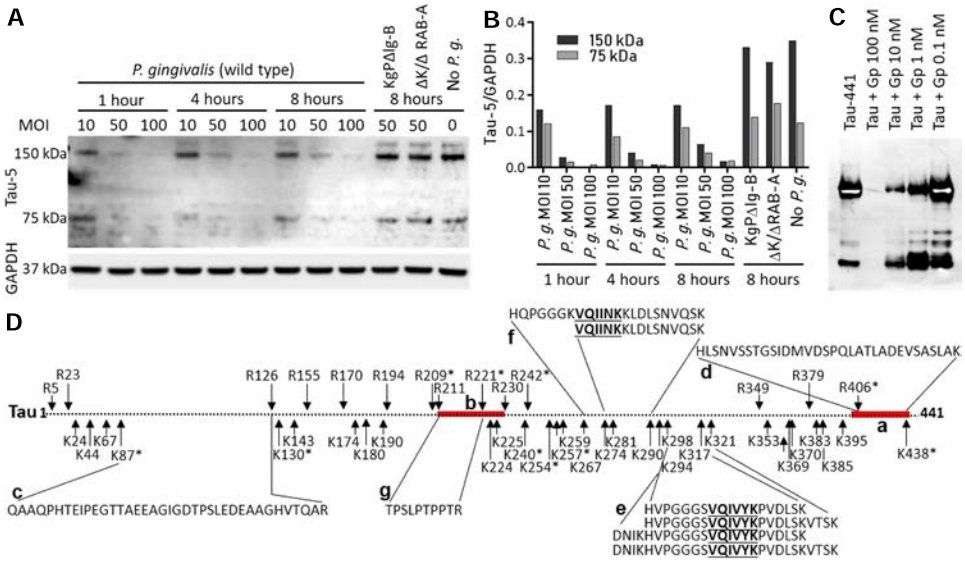

Fig. 5. *P. gingivalis* and gingipains fragment tau. (**A**) WB analysis of total soluble tau in SH-SY5Y cells infected with increasing concentrations of wild-type (WT) *P. gingivalis* strain W83 (*P.g.*) and *P. gingivalis* gingipain-deficient mutants either lacking Kgp activity (KgpΔIg-B) or lacking both Kgp and Rgp activity (ΔK/ΔRAB-A). Uninfected SH-SY5Y cells (No *P.g.*) were used as a negative control. Glyceraldehyde-phosphate dehydrogenase (GAPDH) was used as a loading control. Total tau was monitored with the monoclonal antibody Tau-5 at 1, 4, and 8 hours after infection. (**B**) Densitometry analysis of the total tau WB images. (**C**) WB analysis of rtau-441 incubated with purified Kgp and RgpB catalytic domains combined (Gp) at various concentrations for 1 hour at 37°C. The blot was probed with tau monoclonal antibody T46. (**D**) Gingipain cleavage sites in rtau-441 deduced from peptide fragments identified by MS for rtau-441 incubated with 1 or 10 nM gingipains. (a) T46 antibody epitope (red). (b) Tau-5 antibody epitope (red). (c) N-terminal tau fragment. (d) C-terminal tau fragment. (e) Kgp-generated tau fragments containing the VQIVYK sequence. (f) Kgp-generated fragments containing the VQIINK sequence. (g) An RgpB-generated tau fragment. *Cleavage sites identified at 1 nM gingipains.

Oral infection of mice with *P. gingivalis* results in brain infection and induction of $A\beta_{1-42}$

We next wanted to understand whether oral exposure to *P. gingivalis* would result in brain infiltration and induction of the stereotypical AD marker $A\beta_{1-42}$. Aged 44-week-old BALB/c mice were orally infected every other day over 6 weeks with *P. gingivalis* W83, Kgp knockout (ΔKgp) [Δ*kgp* (602–1732) Em^r] (*57*), or RgpA RgpB double knockout (ΔRgp) (Δ*rgpA rgpB*Δ495-B Cm^r, Em^r) (*58*) *P. gingivalis*. One W83-infected arm was administered the Kgp inhibitor COR119 three times per day subcutaneously over days 21 to 42. Endpoint PCR analysis of mouse brains for *P. gingivalis* revealed that the bacteria invaded the brain of all eight mice after oral infection for 6 weeks, and colonization was decreased by gingipain knockout strains or treatment with COR119 (Fig. 7A). Mouse brain $A\beta_{1-42}$ increased significantly after oral infection with *P. gingivalis* compared to mock-infected or COR119-treated mice (Fig. 7B). Mice infected with ΔRgp or ΔKgp strains of *P. gingivalis* had brain $A\beta_{1-42}$ levels no different than mock-infected, indicating that both gingipains were needed, either directly or indirectly, to induce an $A\beta_{1-42}$ response in vivo (Fig. 7B).

$A\beta_{1-42}$ has antibacterial effects against *P. gingivalis*

The significant $A\beta_{1-42}$ response in the mouse brain to *P. gingivalis* infection is consistent with reports demonstrating that $A\beta_{1-42}$ is an antimicrobial peptide (*4*, *6*). We therefore assayed whether $A\beta_{1-42}$ interacts with *P. gingivalis* and decreases its viability in vitro. After incubation of $A\beta_{1-42}$ with *P. gingivalis*, $A\beta_{1-42}$ colocalized with RgpB on the surface of the bacterium (Fig. 7C). Because $A\beta_{1-42}$ is known to disrupt cellular membranes, we hypothesized that Ab_{1-42} might disrupt the integrity of the *P. gingivalis* membrane to cause cell death. In a separate experiment, we used an assay that can detect damaged bacterial membranes and quantitate the amount of dead or dying bacterial cells as a result of membrane damage. We found that the proportion of dead and dying *P. gingivalis* bacterium significantly increased after incubation with $A\beta_{1-42}$ when compared to $A\beta_{1-40}$, $A\beta_{1-42}$ scrambled, and phosphate-buffered saline (PBS; Fig. 7D).

Oral administration of a Kgp inhibitor effectively treats *P. gingivalis* brain infection and prevents loss of hippocampal $Gad67^+$ interneurons in vivo

We next wanted to measure the effects of gingipain inhibitors on *P. gingivalis* load in the brain after oral infection of BALB/c mice. Eight-week-old mice were orally infected every other day for 42 days with *P. gingivalis* W83 [10^9 colony-forming units (CFU)] and were given 28 days of rest before study completion. Treatment, beginning after brain infection was established, was administered during days 36 to 70 (Fig. 7E). *P. gingivalis* DNA was identified by qPCR in the brain of all infected mice at day 35, and copies of the *P. gingivalis* genome significantly increased by day 70 (Fig. 7F). The Kgp inhibitor COR271, which has oral bioavailability and significant CNS penetration, administered orally twice a day significantly reduced bacterial load in the brain compared to the positive control infection arm and in comparison to baseline levels at 5 weeks (Fig. 7F). The RgpB inhibitor COR286, administered subcutaneously, was effective in reducing the brain bacterial load at 10 weeks, but was not as effective as COR271 in reducing the bacterial load below baseline at 5 weeks (Fig. 7F). The broad-spectrum antibiotic moxifloxacin was also beneficial in preventing the increase in brain colonization between day 35 and day 70 but was not effective in reducing the *P. gingivalis* load below the 5-week baseline (Fig. 7F). Combinations of COR271 with moxifloxacin or COR286 did not improve efficacy over COR271 alone (Fig. 7F).

Histological analysis of brains after the completion of the 10-week study revealed a significant loss of $Gad67^+$ GABAergic interneurons in the hippocampal dentate gyrus in the *P. gingivalis* infection group compared to mock infection (Fig. 7G). In AD, brain neuroimaging and postmortem studies have shown variable disruption of the hippocampal GABAergic system (*59*). Treatment with the Kgp inhibitor COR271 alone, the RgpB inhibitor COR286 alone, a combination of COR271 and COR286, COR271 plus moxifloxacin, and moxifloxacin alone, all beginning at day 36, reduced loss of the $Gad67^+$ interneurons, with moxifloxacin-treated arms trending to decreased protection (Fig. 7G).

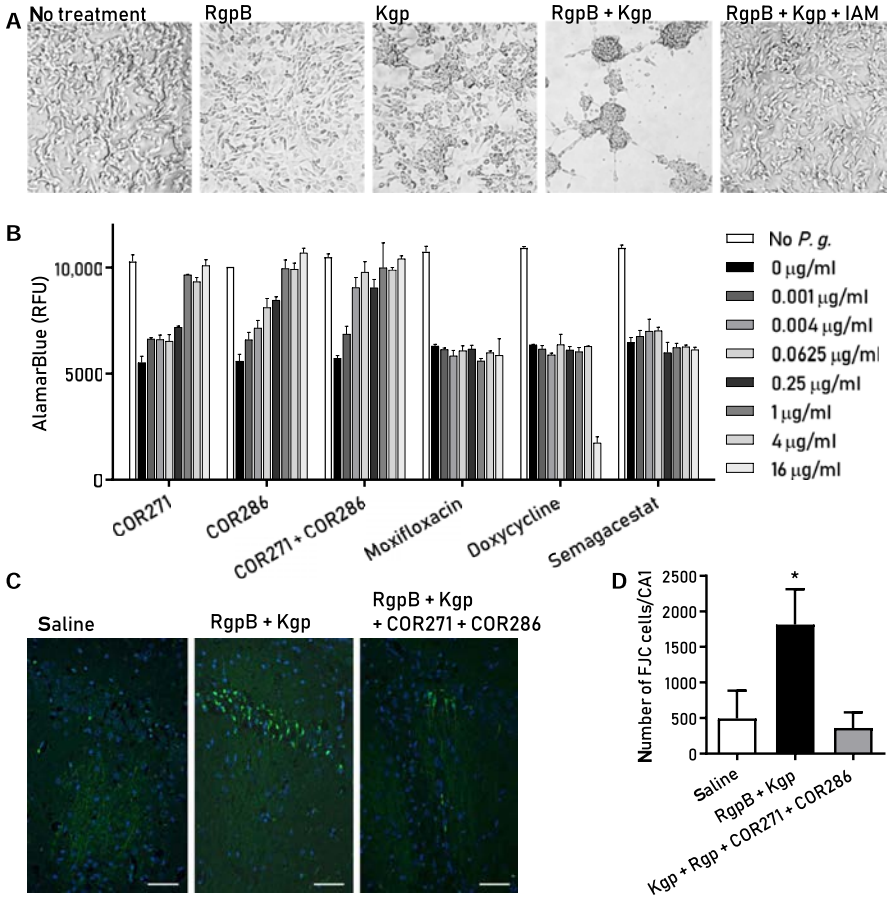

Fig. 6. Small-molecule gingipain inhibitors protect neuronal cells against *P. gingivalis*– and gingipain-induced toxicity in vitro and in vivo. (**A**) Differentiated SH-SY5Y neuroblastoma cells demonstrate cell aggregation after exposure to RgpB (10 μg/ml), Kgp (10 μg/ml), or both for 24 hours. The nonselective cysteine protease inhibitor iodoacetamide (IAM) blocks the gingipain-induced cell aggregation. (**B**) AlamarBlue viability assay shows that *P. gingivalis* (*P.g.*) is toxic to SH-SY5Y cells (MOI of 400) and that the small-molecule Kgp inhibitor COR271 and the RgpB inhibitor COR286 provide dose-dependent protection. The broad-spectrum antibiotics moxifloxacin and doxycycline and the γ-secretase inhibitor semagacestat did not inhibit the cytotoxic effect of *P. gingivalis*. (**C**) Fluoro-Jade C (FJC) staining (green) in pyramidal neurons of the CA1 region of the mouse hippocampus indicates neurodegeneration after stereotactic injection of gingipains. Counterstain with 4′,6-diamidino-2-phenylindole (DAPI) (blue). Scale bars, 50 μm. (**D**) The total number of FJC-positive cells was determined from serial section through the entire hippocampus. Results demonstrate a significant neuroprotective effect of gingipain inhibitors COR271 + COR286 after acute gingipain exposure in the hippocampus (*$P < 0.05$, $n = 14$). All graphs show the mean with SEM error bars.

COR388 treatment shows dose-dependent effects on brain *P. gingivalis* infection, $A\beta_{1-42}$, and tumor necrosis factor–α levels in mice

On the basis of the superior performance of the highly potent and specific Kgp inhibitor COR271 in the above in vivo mouse study in clearing *P. gingivalis* brain infection and protecting $Gad67^+$ neurons in the hippocampus compared to an Rgp inhibitor and a broad-spectrum antibiotic, we developed the COR271 analog COR388. Similar to COR271, COR388 is a highly potent (picomolar inhibition constant on Kgp) and selective irreversible small-molecule inhibitor of Kgp, with superior oral pharmacokinetic and drug-appropriate properties including significant CNS penetration.

In parallel, we also developed Kgp activity–based probes to characterize COR388 Kgp target engagement in intact *P. gingivalis* bacteria and biological tissue samples. We developed the fluorescent activity probe COR553 by combining a potent, small-molecule irreversible Kgp inhibitor with Cy5 (Fig. 8A) and validated its specificity and potency on Kgp in vitro (Fig. 8, B to D). COR553 bound Kgp present in bacterial cultures of *P. gingivalis* but did not bind a strain deficient in Kgp (Fig. 8B). Preincubation of bacterial lysate with Kgp antibody CAB102 depleted Kgp protein and COR553 binding from the lysate, while CAB102 antibody–bound complexes contain Kgp and COR553 binding, confirming the identity of the COR553 target (Fig. 8C). Preincubation of *P. gingivalis* with 100 nM COR388 before COR553 binding resulted in COR388 engagement with the Kgp active site and a block of COR553 activity probe binding (Fig. 8D). Using the COR553 probe, we demonstrated COR388 Kgp target engagement ex vivo in human oral subgingival plaque samples obtained from patients with periodontal disease (table S4). COR553 labeled Kgp present in plaque in four of the five subjects. Preincubation with COR388 blocked probe binding to the active site, while total Kgp protein was still detected by CAB102 (Fig. 8E). High levels of Kgp in these plaque samples mirrored detection of *P. gingivalis* DNA in the plaque samples (Fig. 8F). These same four subjects also had detectable levels of *P. gingivalis* in saliva (Fig. 8G).

Using a defined growth medium, we showed that COR388 inhibited the growth of *P. gingivalis*, demonstrating that an inhibitor of the Kgp virulence factor involved in generating nutrient amino acids for energy acts as a narrow-spectrum antibiotic (Fig. 8H). To test for the potential for resistance to COR388, *P. gingivalis* was passaged in the presence of COR388 or the broad-spectrum antibiotic moxifloxacin. As shown in Fig. 8I, *P. gingivalis* developed complete resistance to moxifloxacin, with the minimum inhibitory concentration (MIC) increasing over 1000-fold in 12 passages. Resis-

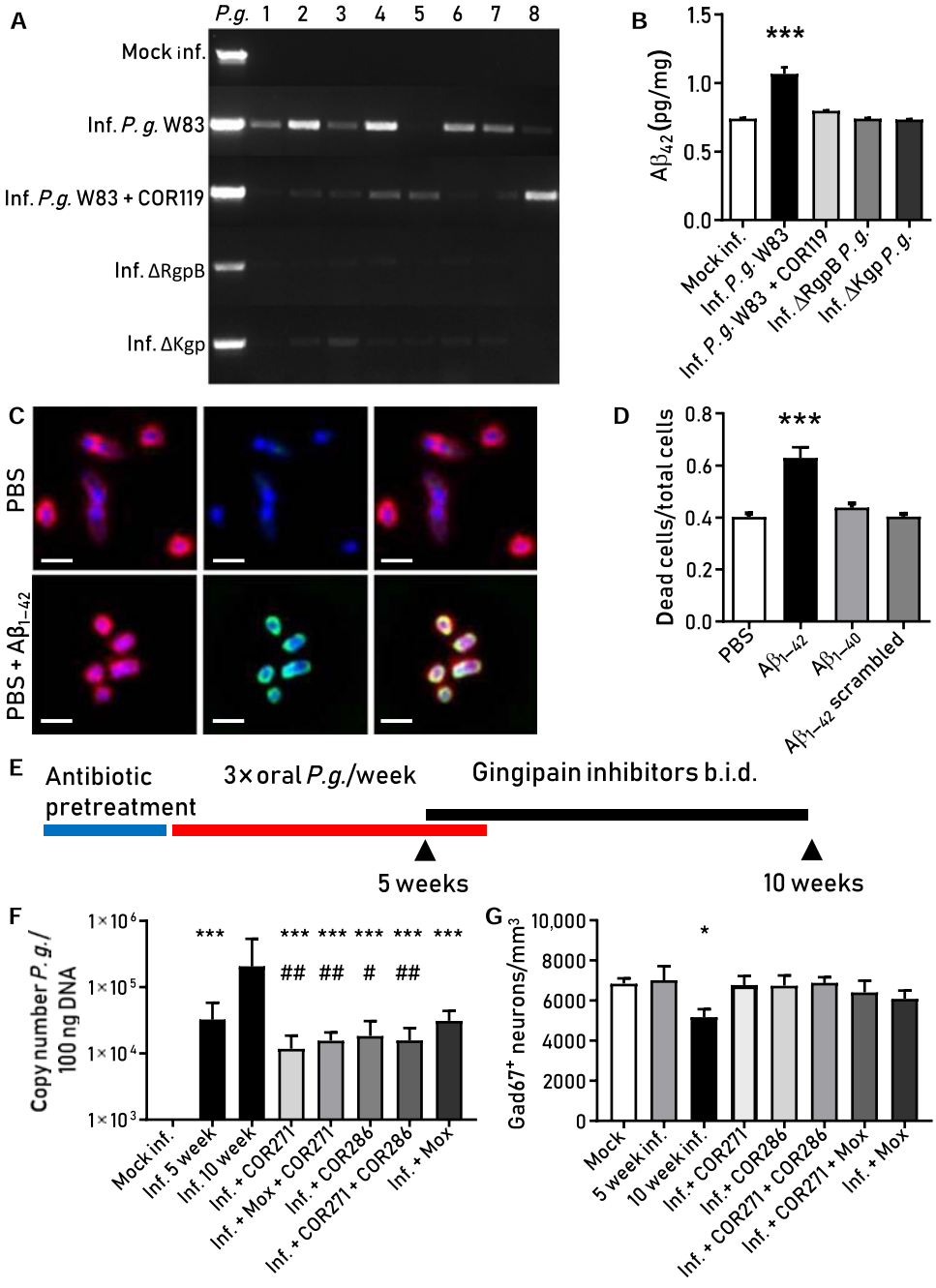

Fig. 7. *P. gingivalis* invasion of the brain induces an $A\beta_{1-42}$ response that is blocked by gingipain inhibition in mice. (**A**) *P. gingivalis* PCR product in mouse brains after oral infection with *P. gingivalis* W83, with or without treatment with the Kgp inhibitor COR119, or infection with gingipain knockout strain ΔRgpB or ΔKgp. Lanes 1 to 8 represent individual experimental animals. In the first lane (*P.g.*), *P. gingivalis* W83 was used as a positive control. (**B**) *P. gingivalis* W83–infected mice, but not COR119-treated mice or mice infected with gingipain knockouts, had significantly higher $A\beta_{1-42}$ levels compared to mock-infected mice (***$P < 0.001$, $n = 40$). (**C**) RgpB-IR (red) colocalized with $A\beta_{1-42}$-IR (green) on the surface of *P. gingivalis* (**D**) $A\beta_{1-42}$, but not $A\beta_{1-40}$ or $A\beta_{1-42}$ scrambled, decreased viability of *P. gingivalis* (***$P < 0.001$, $n = 12$). (**E**) Study design to quantitate the effect of gingipain inhibitors on brain *P. gingivalis* load. (**F**) qPCR results showed a substantial *P. gingivalis* copy number in the brain at 5 weeks, increasing 10-fold at 10 weeks (Inf. 10 week). All treatment groups showed a significant decrease in *P. gingivalis* load compared to vehicle-treated Inf. 10 week mice (***$P < 0.0001$, $n = 63$). Treatment with the Kgp inhibitor COR271 resulted in a 90% reduction of *P. gingivalis* copy number. Comparing treatment groups to baseline infection at the beginning of treatment (Inf. 5 week) showed a significant reduction with COR271 and COR286 ($^{\#\#}P < 0.01$, $^{\#}P < 0.05$) but not with moxifloxacin. (**G**) The number of $Gad67^+$ interneurons in the dentate gyrus of the hippocampus was significantly decreased in the Inf. 10 week group (*$P < 0.05$, $n = 120$). This decrease was reduced in all treatment groups, with COR271 and COR286 trending to better protection than moxifloxacin. (F) Geometric mean with 95% confidence interval. (B), (D), and (G) show the mean with SEM error bars.

tance to COR388 in two independent assays did not develop in this study. Efficacy of COR388 was tested in vivo to treat an established *P. gingivalis* brain infection in the mouse model described above for COR271 efficacy testing (Fig. 7E). Similar to COR271, oral dosing of COR388 twice daily resulted in dose-dependent efficacy when administered to an established *P. gingivalis* brain infection. Doses of 10 and 30 mg/kg reduced *P. gingivalis* load, $A\beta_{1-42}$, and tumor necrosis factor–α (TNFα) levels in brain tissue compared to those of infected animals treated with vehicle (Fig. 8, J to L). The lowest dose of COR388 at 3 mg/kg showed some reduction of brain *P. gingivalis* load but did not reduce levels of brain $A\beta_{1-42}$ or TNFα (Fig. 8, J to L). Investigational new drug application–enabling studies were completed with COR388, and the compound is currently in clinical studies (ClinicalTrials.gov NCT03331900).

DISCUSSION

The findings of this study offer evidence that *P. gingivalis* and gingipains in the brain play a central role in the pathogenesis of AD, providing a new conceptual framework for disease treatment. Accordingly, we demonstrate the presence of *P. gingivalis* DNA and gingipain antigens in AD brains and show in vivo that oral administration of small-molecule gingipain inhibitors blocks gingipain-induced neurodegeneration, significantly reduces *P. gingivalis* load in the mouse brain, and significantly decreases the host $A\beta_{1-42}$ response to *P. gingivalis* brain infection.

Our identification of gingipain antigens in the brains of individuals with AD and also with AD pathology but no diagnosis of dementia argues that brain infection with *P. gingivalis* is not a result of poor dental care following the onset of dementia or a consequence of late-stage disease, but is an early event that can explain the pathology found in middle-aged individuals before cognitive decline (*60*). We also demonstrate that *P. gingivalis* bacterial load can be detected in the CSF of clinical AD patients, providing further evidence of *P. gingivalis* infection of the CNS.

The PCR analysis of *P. gingivalis* in the brain and CSF reported here does not differentiate between *P. gingivalis* strains, and future studies are needed to determine what *P. gingivalis* strains are present in the brain and CSF and whether some strains might be more virulent than others in causing disease. In addition, there is one other species of *Porphyromonas* that is known to produce gingipains, *Porphyromonas gulae* (*61*). *P. gulae* is a natural inhabitant of the oral cavity of companion animals such as dogs, and a recent study demonstrated that dogs can transmit *P. gulae* to the oral cavity of their owners (*62*). Research is underway to determine whether *P. gulae* may be contributing to the gingipain load in AD brains.

Evidence from our work reported here lends support to the emerging concept that Aβ is an antimicrobial peptide (*4*–*6*), and mutations (*63*, *64*) contributing to loss of this function could allow more robust infection with *P. gingivalis* and higher risk for disease. In addition, sustained high levels of antimicrobial Ab driven by chronic *P. gingivalis* infection of the brain may

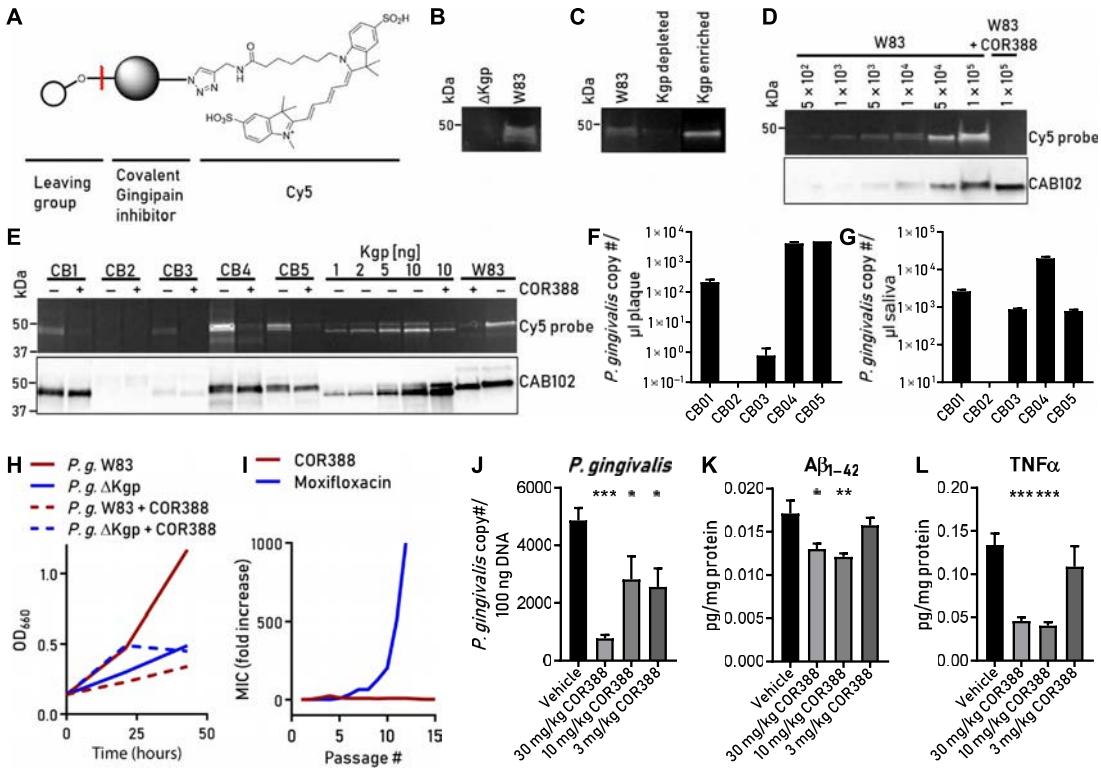

Fig. 8. COR388 target engagement and dose-dependent effects on brain *P. gingivalis*, $A\beta_{1-42}$, and TNFα in mice. (**A**) COR553 fluorescent activity probe for Kgp. (**B**) COR553 labeling of Kgp in *P. gingivalis* W83 strain and no labeling in mutant deficient in Kgp (ΔKgp). (**C**) W83 lysates labeled with COR553. Left lane, before immunodepletion; middle lane, after immunodepletion with anti-Kgp–conjugated beads; right lane, after elution from anti-Kgp–conjugated beads. (**D**) W83 strain titrated and labeled with COR553 to determine the limit of bacterial detection. See Results for details. (**E**) Oral plaque samples from human subjects (CB1-5) with periodontal disease were incubated ex vivo with COR553 probe with or without preincubation with COR388. COR553 probe and CAB102 detected Kgp strongly in three subjects (CB1, CB4, and CB5) and weakly in one subject (CB3). COR388 preincubation blocked COR553 probe binding to Kgp. (**F**) qPCR analysis of plaque samples using *hmuY* gene–specific primers identified *P. gingivalis* DNA in samples. (**G**) qPCR analysis of saliva samples. The bar graphs in (F) and (G) show the means and SEMs of three replicates. (**H**) COR388 treatment of W83 culture in defined growth medium reduced growth similarly to a Kgp-deficient strain (ΔKgp) over 43 hours. (**I**) Resistance developed rapidly to moxifloxacin but not COR388 with repeat passaging of bacterial culture. (**J** to **L**) Efficacy of COR388 at three oral doses of 3, 10, and 30 mg/kg twice daily in treating an established *P. gingivalis* brain infection in mice. Reduction of brain tissue levels of *P. gingivalis* (J), $A\beta_{1-42}$ (K), and TNFα (L). The bar graphs show the means with SEM error bars. ***$P < 0.001$, **$P < 0.01$, *$P < 0.05$, *t* test with Dunn's multiple comparison correction; $n = 39$.

be toxic to host cells, and therefore, reduction of Ab levels after treatment of the *P. gingivalis* infection should be beneficial. Furthermore, Down syndrome (DS), the most common genetic cause of mental disability, has been used to support Aβ as a therapeutic target because of the notably high prevalence of dementia with Alzheimer-type pathology in DS patients (greater than 50% after the age of 60) and the fact that the amyloid precursor protein gene, which gives rise to Aβ, is present on chromosome 21, which is triplicated in DS (*65*). However, in support of our hypothesis, an aggressive form of periodontitis with rapid progression and onset as early as 6 years of age is associated with DS, but not age-matched normal controls or other mentally handicapped patients of a similar age distribution (*66*). The occurrence of *P. gingivalis* has been found to be significant in the subgingival plaque of DS patients beginning around the age of 5 years when compared to age-matched controls, indicating that *P. gingivalis* abnormally colonizes DS patients in early childhood (*67*). The reason behind DS patients being susceptible to *P. gingivalis* infection at such an early age is unclear but may be due to the immunodeficiency that is associated with DS (*68*). Research is needed to determine whether *P. gingivalis* and gingipains are present in DS CSF and brain.

Although not specifically addressed in this report, once the oral cavity is infected, *P. gingivalis* may access the brain and spread via a number of pathways including (i) infection of monocytes followed by brain recruitment (*69, 70*), (ii) direct infection and damage to endothelial cells protecting the blood-brain barrier (*28*), and/or (iii) infection and spreading through cranial nerves [e.g., olfactory (*71*) or trigeminal] to the brain. After entering the brain, we suggest that *P. gingivalis* may spread slowly over many years from neuron to neuron along anatomically connected pathways, similar to what has been demonstrated for vascular cell-to-cell transmission of *P. gingivalis* (*72*).

Tau pathology has also been suggested to spread from neuron to neuron (*73*), with a pattern resembling an infectious process. Our data indicate that tau is a target of gingipain proteolysis, and we propose that tau pathology seen in AD brains may be due to the transneuronal spread of *P. gingivalis*, with direct damage of tau by gingipain proteolysis as well as gingipain activation of human proteases that act on tau. Gingipains have been shown to directly cleave procaspase-3 to activate caspase-3 (*74*), a caspase that has been implicated in both tau phosphorylation (*75*) and tau cleavage (*76*). Proteolysis of tau by gingipains would be predicted to increase the turnover rate of tau and trigger a compensatory increase in tau production rate to maintain homeostasis in neurons infected by *P. gingivalis*. Recent research on the kinetics of tau in the human CNS using the tau mid-domain TPSLPTPPTR fragment as a reporter found that the production rate of tau was increased in CSF of subjects with preclinical and clinical AD (*52*). Our data demonstrating that both Kgp and RgpB independently correlate with tau load in AD brains lend support to the hypothesis that gingipains may be a driver of a compensatory increase in tau production. Last, further research is needed to determine whether the gingipain-generated C-terminal tau fragments containing the hexapeptide microtubule-binding domains that we identified in vitro can drive tau filament formation in vivo.

Here, we have not addressed how *P. gingivalis* infection might relate to apolipoprotein E4 (*APOE4*), the greatest genetic risk factor for sporadic AD (*77*). Studies in mice deficient in APOE proteins demonstrated an impaired innate immune response to the bacterial pathogen *Listeria monocytogenes* (*78*), implicating APOE in normal innate immune function in vivo. It was recently reported that human APOE is a target of gingipain proteolysis, and the authors suggested that this mechanism could generate neurotoxic APOE fragments in the AD brain (*79*). We propose that APOE4 may be more susceptible to gingipain cleavage than APOE3 or APOE2 due to the presence of more arginine residues, resulting in decreased innate immune function and the generation of neurotoxic fragments (*80*). The distinct role of APOE in relation to *P. gingivalis* infection and targeting by gingipains remains a focus of future studies.

Our identification of *P. gingivalis* in the CNS underscores the importance of genetic findings linking innate immune response genes to AD susceptibility, including *TREM2* (*81*), *TLR4* (*82*), *CR1* (*83*), and *NLRP3* (*84*). For example, recent studies have highlighted the association between variants of triggering receptor expressed on myeloid cells 2 (*TREM2*) and AD (*81*). *TREM2* encodes a receptor expressed on immune cells such as macrophages and microglia, with heterozygous *TREM2* variants conferring a risk of developing AD similar to one copy of *APOE4* (*81*). TREM2 has been shown to regulate inflammatory responses (*85*) and serve as a phagocytic receptor for bacteria (*86*). TREM1, which shares homology with TREM2, has also been linked to AD amyloid pathology and cognitive decline (*87*). The risk-associated *TREM1* allele was shown to decrease TREM1 surface expression on monocytes (*87*). *P. gingivalis* has been shown to induce *TREM1* gene expression (*88*), and it is therefore possible that carriers of the *TREM1* AD–associated allele have a reduced ability to respond to infection by *P. gingivalis*. In addition, TREM1 is a target for gingipain proteolysis and degradation, with data showing that Rgp can cleave soluble TREM1 from the cell surface and that Kgp can degrade TREM1, actions that could induce chronic inflammation (*88*). Additional research is needed to determine whether TREM2 is involved in the innate immune response to *P. gingivalis* and whether *P. gingivalis* and gingipains have similar effects on the expression and degradation of TREM2 as they do for TREM1. In summary, we propose that genetic polymorphisms of innate immune system genes in essential immune pathways may result in defective clearance of *P. gingivalis* and gingipains from the brain, resulting in chronic, low-level infection and neuroinflammation in susceptible individuals.

With regard to infection-induced neuroinflammation, inflammasomes, multiprotein complexes that act as intracellular innate immune defense systems (*89*), have been shown to be activated in AD brains (*90*). *P. gingivalis* has been shown to modulate inflammasome activity (*91*). Recent research indicates that Aβ plaque formation in AD is connected to the innate immune response through activation of the NLRP3 inflammasome in microglia and release of ASC specks that drive Aβ assembly and deposition (*92*). Notably, *P. gingivalis* was the first microbial pathogen shown to induce ASC aggregation specks in *P. gingivalis*–infected primary human monocytes through activation of the NLRP3 inflammasome (*93*). Inflammasomes act in intracellular innate immune defense against intracellular pathogens by activating interleukin-1b (IL-1β) and IL-18, causing cell death through pyroptosis and thereby eliminating the intracellular niche for pathogen replication (*94*). Furthermore, recent reports have shown that *P. gingivalis* OMVs, nanoscale proteoliposomes that are enriched in gingipains and released into surrounding tissues, are rapidly internalized into mammalian cells (*95*), where they drive NLRP3 inflammasome activation and ASC speck formation and cause cell death through pyroptosis (*96, 97*). This research suggests that *P. gingivalis* in the human brain, through release of OMVs enriched in gingipains, could drive NLRP3 inflammasome activation, ASC speck aggregation, and subsequent Aβ plaque formation. In addition, recent evidence has shown that the NLRP1 inflammasome in neurons can detect bacterial virulence factors such as proteases by serving as a substrate for the pathogenic enzymes (*98*). We suggest that intraneuronal gingipains may therefore drive neuronal NLRP1 activation, resulting in pyroptosis of neurons and activation of caspase-1, leading to release of the neuroinflammatory interleukins IL-1β and IL-18.

Last, we have shown that broad-spectrum antibiotics do not protect against *P. gingivalis*–induced cell death in vitro, whereas gingipain inhibitors do. We also demonstrated in vivo that an orally administered Kgp inhibitor is more effective than a high-dose subcutaneous broad-spectrum antibiotic in clearing *P. gingivalis* from the brain. It was recently demonstrated that a small-molecule inhibitor of a *Clostridium difficile* cysteine protease virulence factor, TcdB, reduced disease pathology in a mouse model of *C. difficile*–induced colitis but did not reduce the *C. difficile* bacterial load (*99*). In contrast, we report here that small-molecule inhibition of the cysteine protease Kgp reduced not only disease pathology in mouse brain but also *P. gingivalis* bacterial load. The mechanisms underlying the decrease in *P. gingivalis* bacterial load in the brain by Kgp inhibitors are likely due to reduction of Kgp-generated peptide nutrients essential for the growth of this asaccharolytic bacterium (*100*) and blocking of Kgp-dependent heme acquisition that is critical for *P. gingivalis* energy production (*101, 102*). We have demonstrated that *P. gingivalis* develops rapid resistance to a broad-spectrum antibiotic, moxifloxacin, but not to the Kgp

inhibitor COR388. Therefore, with the growing concern about widespread antibiotic resistance (*103*), and severe side effects such as *C. difficile* colitis from broad-spectrum antibiotic use (*104*), an antivirulence factor inhibition approach to treatment of *P. gingivalis* is the most promising path while reducing pressures for resistance.

In conclusion, we have designed an orally bioavailable, brain-penetrant Kgp inhibitor currently being tested in human clinical studies for AD. The present data indicate that treatment with a potent and selective Kgp inhibitor will reduce *P. gingivalis* infection in the brain and slow or prevent further neurodegeneration and accumulation of pathology in AD patients.

MATERIALS AND METHODS

Study design

This study was conducted to investigate the prevalence of *P. gingivalis* in the AD brain and to elucidate possible *P. gingivalis*–dependent mechanisms of action for neurodegeneration and AD pathology. In addition, we performed a series of preclinical studies to enable the development of a therapeutic compound against *P. gingivalis*–induced AD. To demonstrate the presence of gingipain antigens in the AD brain, TMAs containing nondemented control and AD brain tissue were used for IHC. To avoid potential bias and subjective elements in assessing the results, stained TMAs were scanned and images were analyzed for gingipain IR using the MetaMorph image analysis program. Evidence for the presence of *P. gingivalis* in the AD brain was further verified by IP, WB, and PCR. To demonstrate the presence of *P. gingivalis* in the CNS of living patients prospectively diagnosed with probable AD, CSF was analyzed for *P. gingivalis* by PCR. The in vitro experiments to demonstrate *P. gingivalis* fragmentation of tau analyzed by WB and MS were designed after detecting the correlation of increased tau load with gingipains in the TMAs and the colocalization of gingipain with tau tangles in human AD brain. To study the efficacy of gingipain inhibitors and neurodegenerative effects of chronic *P. gingivalis* infection in vivo, we developed a mouse model for chronic infection with *P. gingivalis*. The sample size for the mouse model for brain infection with *P. gingivalis* was empirically determined on the basis of effect size and SD. A blinded observer performed quantification of the loss of hippocampal GABAergic neurons after *P. gingivalis* brain infection and the number of degenerating neurons after intrahippocampal injection of gingipains. The efficacy of the top lead compound, COR388, was determined in the brain by qPCR for *P. gingivalis*–specific genes and by enzyme-linked immunosorbent assay (ELISA) for $A\beta_{1-42}$ and TNFα. Animals were assigned to each experimental group with an equal probability of receiving vehicle or treatment.

Human tissue samples

The human postmortem brain tissue obtained from the Neurological Foundation of New Zealand Human Brain Bank at the University of Auckland was donated to the Brain Bank with family consent, and its use for this study was approved by the University of Auckland Human Participants Ethics Committee. The control cases had no history of neurological abnormalities, and cause of death was unrelated to any neurological condition. Independent pathological analysis confirmed that any amyloid pathology was deemed normal for age in the control cases selected for this study. Pathological analysis was carried out on all AD cases used in this study to determine pathological diagnosis and to assign pathological grades, which, together with a history of dementia, confirmed the diagnosis (tables S1 and S2).

Postmortem tissue samples collected under institutional review board (IRB)–approved protocols were obtained from the University of California Davis Alzheimer's Disease Center, the University of California San Francisco (UCSF) Neurosurgery Tissue Bank, ProteoGenex (Culver City, CA), and PrecisionMed (Solana Beach, CA). Gingival tissue samples were collected from human volunteers with chronic periodontal disease who provided signed informed consent after the nature and possible consequences of the studies were explained under a University of California at San Francisco IRB–approved protocol (approval no. 11-05608). CSF and saliva samples were collected from human volunteers with a diagnosis of probable AD who provided signed informed consent after the nature and possible consequences of the studies were explained under an IRB-approved protocol obtained from PrecisionMed (Solana Beach, CA). Oral plaque and saliva samples were collected from human volunteers with chronic periodontal disease who provided signed informed consent after the nature and possible consequences of the studies were explained under an IRB-approved protocol obtained from the Forsyth Institute (Cambridge, MA).

Animals

Specific pathogen–free (SPF) female BALB/c mice were purchased from Envigo (UK) for the oral infection experiments with *P. gingivalis*. Mice were maintained in individually ventilated cages and fed a standard laboratory diet and water ad libitum under SPF conditions within the animal care facility at Faculty of Biochemistry, Biophysics and Biotechnology, the Jagiellonian University, Krakow, Poland. Mice were kept under a 12-hour light/dark cycle at 22° ± 2°C and 60 ± 5 relative humidity. Control and bacterially infected mice were housed in separate cages. To study $A\beta_{1-42}$ levels in the brains of orally infected mice and the efficacy of gingipain inhibitors to decrease *P. gingivalis* infection of the brain, 40 (n = 8 per arm) 43- to 44-week-old female BALB/c mice or 100 (n = 10 per arm) 8-week-old female BALB/c mice were used, respectively. All the experiments were reviewed and approved by the I Regional Ethics Committee on Animal Experimentation, Krakow, Poland (approval nos. 164/2013 and 116/2016).

To study neurodegeneration after stereotactic injection of gingipains into mouse hippocampus, fifteen 8-week-old male BALB/c mice were purchased from Envigo (USA). Animals were group-housed (n = 2 to 4 per cage) in plastic cages. Animals were maintained on a 12/12-hour light/dark cycle with the room temperature (RT) maintained at 22° ± 2°C and approximately 50% humidity and received standard rodent chow and tap water ad libitum in the Brains On-Line, LLC Animal Facility (South San Francisco, CA). Experiments were conducted in accordance with the protocols approved by the Institutional Animal Care and Use Committee of Brains On-Line, LLC (approval no. US16003).

Antibody production

Polyclonal antibodies CAB101 and CAB102 were produced by GenScript USA Inc. (New Jersey) according to their express immunization protocol. Briefly, immunogens were expressed in a bacterial expression system and used for four consecutive immunizations of four rabbits each. The immunogen sequences expressed are 401 to 736 residues for CAB101 (RgpB; GenBank: BAG33985.1) and 22 to 400 residues for CAB102 (Kgp; GenBank: BAG34247.1). After the last immunization, sera were pooled and antigen affinity–purified. Specific binding was tested on WBs, and nonspecific binding on human histology sections was controlled by coincubation of polyclonal antibodies with their respective immunogens before IHC staining.

Human TMAs

Human brain TMAs comprised a total of 58 2-mm-diameter core samples, 29 from dementia-free control individuals and 29 from AD cases, each on two arrays (NVD003 and NVD005). Final sample sizes reflect the loss of several samples from the slide during processing (see tables S1 and S2).

IHC to detect gingipains, tau, and ubiquitin in human TMAs

TMAs were constructed from paraffin-embedded MTG blocks, as described in detail by Narayan *et al.* (*105*). TMA sections were cut at a thickness of 7 mm and were annealed to slides by heating at 60°C for 1 hour. Sections were then dewaxed using xylene immersion in xylene twice (1 hour and 10 min, respectively) and rehydrated using a standard graded ethanol series procedure. For IHC, slides were immersed in sodium citrate antigen retrieval buffer (pH 6), heated at 121°C for 2 hours in 2100 Antigen Retriever (Aptum, Pick Cell Laboratories), and then rinsed three times for 5 min in milliQH_2O. For tau (1:20,000; rabbit A0024, DAKO), IHC slides were immersed in 99% formic acid for 5 min, rinsed three times in milliQH_2O, and then treated as per other slides. Slides were then incubated with an endogenous peroxidase blocking solution (50% methanol, 1% H_2O_2, diluted in

mQH_2O) for 20 min at RT. This was followed by three washes in PBS, and then slides were incubated with blocking buffer (10% normal goat serum in PBS) for 1 hour at RT. Primary antibodies mouse anti-ubiquitin (1:2000; MAB1510, Chemicon), CAB101 (1:500), and CAB102 (1:500) were applied for incubation overnight at 4°C.

To detect antibody binding, slides were washed in PBS with Triton X-100 for 5 min and then twice in PBS for 5 min each and incubated with biotinylated goat anti-mouse or anti-rabbit antibodies (Sigma-Aldrich) for 3 hours at RT. After further washing, they were incubated for 1 hour at RT with Sigma Extravidin peroxidase at 1:1000 dilution and then washed and incubated with the peroxidase substrate [3,3′-diaminobenzidine with 0.04% $Ni(NH_4)_2(SO_4)_2$] to develop the color change. Following PBS-milliQH_2O washes (3 × 5 min each), the slides were dehydrated in a graded ethanol series followed by xylene and mounted under coverslips with DPX mounting medium.

Gingipain antibodies were optimized initially on formalin-fixed paraffin-embedded sections of gingival tissue collected from periodontal disease patients at the UCSF School of Dentistry under an IRB-approved protocol. Testing was then performed on MTG (from both postmortem control and AD human brains) and cerebellum (negative control). Specificity of antibody staining was demonstrated using positive and negative controls, secondary antibody only, isotype controls, and antigen pre-absorption. "No primary" antibody controls were negative for staining. Stained slides were scanned at 10× objective using a MetaSystems VSlide slide scanner, and brightfield images were analyzed for gingipain (and other markers) IR using the MetaMorph image analysis program. For each marker, the images were thresholded. Two thresholds for each core were determined: one to determine the total area of the core and the other to determine the total area of the thresholded region. To determine the load of staining per core, the thresholded area of staining was divided by the total core area. This analysis controlled for varying core sizes.

IHC of human AD brain sections for neurons, astrocytes, and RgpB-IR

For 18E6 analysis, which recognizes a unique epitope within the immunoglobulin (Ig)–like domain of Arg-gingipain (RgpB) (*58*), IHC was performed using the Ventana Benchmark XT automated slide preparation system at the UCSF Brain Tumor Research Center tissue core. For immunoperoxidase staining, after tissue sections (5 mm thickness) were deparaffinized (at 75°C; EZ-Prep, Ventana Medical Systems), antigen retrieval was performed for 30 min [Cell Conditioning 1 (pH 8.5), Ventana Medical Systems] at 95° to 100°C. H_2O_2 (3%) (Thermo Fisher Scientific) was applied for 8 min to reduce background staining. Antibody 18E6 (University of Georgia Monoclonal Antibody Facility) was incubated at RT for 32 min at 1:10 dilution. Staining was developed using the UltraView Universal DAB Detection System (Ventana Medical Systems), and slides were counterstained with hematoxylin.

For immunofluorescence, sections were deparaffinized in xylene and rehydrated in a graded alcohol series. Heat-mediated antigen retrieval was performed with citric buffer (pH 6.0) (H-3300, Vector Laboratories). After PBS washes, sections were incubated in blocking solution, 5% donkey serum, and 0.3% Triton X-100 in PBS for 1 hour at RT. Sections were then incubated overnight at 4°C in primary antibodies anti-MAP2 (1:500; ab5392, Abcam), CAB101 (1:500), anti-IBA1 (1:1000; ab97120, Abcam), anti–β-amyloid, 17–24 (1:500; SIG-39200; 4G8, BioLegend), and anti-AT8 (1:2000; MN1020B, Thermo Fisher Scientific) in 3% donkey serum and 0.3% Triton X-100 in PBS. After PBS washes, slides were incubated with secondary antibody solution, either Alexa Fluor 647 goat anti-chicken (1:200; A21449, Life Technologies) and Alexa Fluor 488 donkey anti-rabbit (1:200; Jackson ImmunoResearch) mixed with anti–GFAP-Cy3 (1:250; MAB3402C3, Millipore) or Cy3-donkey anti-rabbit (1:200; Jackson ImmunoResearch), Alexa Fluor 488 donkey anti-mouse (1:200; Jackson ImmunoResearch), and Alexa Fluor 647 donkey anti-goat (1:200; Jackson ImmunoResearch) in PBS with 0.3% Triton X-100 for 2 hours at RT. Sections were washed in PBS and counterstained with 4′,6-diamidino-2-phenylindole (DAPI) (Invitrogen; D1306). Autofluorescence was quenched with TrueBlack Lipofuscin Autofluorescence Quencher 1:20 in 70% ethanol (catalog no. 23007, Biotium), and slides were mounted with ProLong Gold Antifade (P36930, Thermo Fisher Scientific). Coimmunofluorescence on *P. gingivalis* was performed by drying bacteria on SuperFrost Plus microscope slides. Bacteria were immersed in 4% paraformaldehyde for 10 min, washed three times in PBS, and incubated in formic acid for 7 min, followed by another three washes with PBS. Cells were exposed to anti–β-amyloid, 17–24 (1:500; SIG-39200; 4G8, BioLegend) and CAB101 (1:500) in 3% donkey serum and 0.3% Triton X-100 in PBS for 30 min at RT, followed by 30-min incubation in Cy3-donkey anti-rabbit (1:200; Jackson ImmunoResearch) and Alexa Fluor 488 donkey anti-mouse (1:200; Jackson ImmunoResearch) in PBS, counterstained with DAPI, and coverslipped with ProLong Gold Antifade (Thermo Fisher Scientific; P36930).

Histological analysis was performed on an Olympus BX61 motorized microscope. Fluorescence images were taken with a sCMOS camera (Zyla-5.5-USB3, Andor), and brightfield images were taken on a color charge-coupled device camera (DP27, Olympus). Images were processed for brightness and contrast correction, cropping, and addition of scale bars with CellSens 1.14 Dimension software (Olympus).

Human brain Kgp IP and WB

Brain tissue from each subject sample (cortex, 100 mg) was homogenized on ice in 1 ml of B-PER lysis buffer (Thermo Fisher Scientific) with proteinase inhibitor cocktail (Millipore) and then kept on ice for 10 min. The bacteria control was prepared by pelleting 10^9 bacteria by centrifugation at 5000*g* for 10 min. Then, the pellet was lysed in 1 ml of the same lysis buffer on ice for 10 min. All samples were then centrifuged at 16,000*g* for 20 min at 4°C, and the supernatant was collected. Protein concentration was measured using a Pierce BCA assay kit (Thermo Fisher Scientific). One milligram of total protein from each sample was denatured at 95°C for 5 min, and then an equal volume of antibody binding and washing buffer from the Dynabeads Protein G Immunoprecipitation Kit (Thermo Fisher Scientific) was added. For the bacteria control, 10^7 bacteria were used. For the brain sample spiked with bacteria, 1 mg of total brain protein was mixed with bacterial lysate of 10^7 bacteria. The samples were incubated with 10 μg of rabbit polyclonal CAB102 antibody with rotation overnight at 4°C. The next day, prewashed Dynabeads Protein G beads were incubated with 1 mg of bovine serum albumin (BSA) in binding buffer for 30 min and then washed three times with washing buffer. Then, samples were incubated with Dynabeads with rotation for 30 min at RT. Samples were washed four times with 200 μl of washing buffer using magnetic rack. Beads were then dissolved with 20 μl of elution buffer and 10 μl of NuPAGE LDS sample buffer and 50 mM dithiothreitol (DTT) and heated at 70°C for 10 min. Then, IP proteins were eluted from the magnetic beads using magnetic rack. Each sample (15 μl) was then subjected to SDS–polyacrylamide gel electrophoresis (PAGE) electrophoresis. SDS-PAGE gel was subjected to WB analysis by using Trans-blot Turbo transfer system (Bio-Rad) to transfer proteins to polyvinylidene difluoride (PVDF) membrane. The membrane was then rinsed with tris-buffered saline (TBS) and then blocked with blocking buffer from the Clean-Blot IP Detection Kit (Thermo Fisher Scientific) for 1 hour. The blot was then incubated with 1:1000 primary antibody CAB102 overnight with rocking in blocking buffer at 4°C. The blot was then washed three times with TBST buffer, 5 min each, and then incubated with 1:250 dilution of Clean-Blot detection reagent [horseradish peroxidase (HRP)] in blocking buffer for 1 hour at RT. Blot was then washed four times with TBST and then subjected to Pierce ECL detection reagent and ChemiDoc imaging system.

qPCR analysis of *P. gingivalis* in human brain tissue

DNA was extracted and purified from postmortem cortex brain tissues following the protocol described in the Blood and Tissue Kit (Qiagen). Copy number of the *P. gingivalis* genome in brain DNA samples was determined by qPCR with *P. gingivalis*–specific *16S* primers [(ACCCTTTAAAC-CCAATAAATC (forward) and ACGAGTATTGCATTGAATG (reverse)] and fluorescent-labeled probe (CGCTCGCATCCTCCGTATTAC). The qPCR reaction mixture contained 100 ng of brain DNA, 0.5 μM primers/0.15 μM

probe, and Kapa Fast qPCR Mix (Kapa Biosystems). PCR amplification was performed using the following cycling parameters: 3 min at 95°C, 50 cycles of 3 s at 95°C, and 30 s at 60°C. Copy number was determined from the standard curve generated using a synthetic template.

Sequence analysis of *P. gingivalis* DNA amplified from human brain tissue

For sequencing, an approximately 1-kb region of the *P. gingivalis* genome encompassing the *hmuY* gene (except sequences corresponding to the first six amino acids) was amplified from 50 ng of brain DNA by PCR. PCR amplification (95°C/5 min; 95°C/20 s, 60°C/15 s, and 72°C/1 min for 35 cycles; 72°C/2 min) was performed using the KAPA HiFi HotStart ReadyMix PCR Kit (Kapa Biosystems) and primers [TTCTCCGCACTCTGTGCATT (forward) and AGCACTTCGATTCGCTCGAT(reverse)] designed to amplify the *hmuY* gene from the *P. gingivalis* genome. PCR products were run on 2% agarose gel, and DNA bands close to the expected size (based on the PCR product obtained from amplification of purified *P. gingivalis* DNA) were excised from the gel (Fig. 2F). DNA was extracted from the gel pieces following the protocol described in the Gel Extraction Kit (Qiagen). Approximately 5% of the eluted DNA was reamplified using the same *hmuY* PCR primers. Sequencing of reamplified PCR products was performed using nested primers (fig. S3).

qPCR analysis of *P. gingivalis* in human CSF and saliva

CSF and matching saliva samples were obtained from PrecisionMed (Solana Beach, CA). Ten volunteer subjects, who were diagnosed with probable AD and met the criteria of having a Mini Mental Status Exam (MMSE) score of 20 or below, were serially enrolled in PrecisionMed's IRB-approved protocol for CSF collection in November 2017 and donated CSF samples and matching saliva samples for *P. gingivalis* PCR analysis.

CSF PCR method

DNA was extracted from 50 ml of CSF using Puregene Core Kit A (Qiagen). The final DNA pellet was dissolved in 50 μl of DNA hydration buffer. A preamplification PCR assay (20 cycles) was performed with 5 μl of CSF DNA and *P. gingivalis hmuY* gene–specific H1.2 primers [GGTGAAGTCGTAAATGTTAC (H1.2 forward) and TTGACTGTAATACGGCCGAG (H1.2 reverse)]. A serial dilution of synthetic template DNA was also preamplified for the calculation of copy number. The preamplified PCR products were diluted, and a qPCR assay was performed with nested *hmuY* primers [GAACGATTTGAACTGGGACA (H1.1 forward) and AACGGTAGTAGCCTGATCCA (H1.1 reverse)] and a probe (/56-FAM/TTCTGTCTT/ ZEN/ GCCGGAGAATACGGC/3IABkFQ/). A serial dilution of the same synthetic template DNA was included in the qPCR assay to generate a standard curve and calculate starting copy number in CSF.

Saliva PCR method

DNA was extracted from 50 μl of saliva using Puregene Core Kit A (Qiagen). The final DNA pellet was dissolved in 50 ml of DNA hydration buffer. A qPCR assay was performed with 2 μl of saliva DNA and *hmuY* primers (H1.1) and the probe mentioned above. A serial dilution of synthetic template DNA was included in the qPCR assay to calculate starting copy number.

qPCR analysis of *H. pylori* in human brain and CSF

The preamplification and qPCR protocol used for detection of *H. pylori* copy number in brain, CSF, and saliva samples were the same as those used for detecting the *P. gingivalis hmuY* gene copy number noted above. The qPCR primers and probe used for detection of *H. pylori* copy number have previously been described (*43*). We designed two primers [GATTAGTGCCCATATTATGGA (Hpy_outer_For) and CTCACCAGGAACTAATTTAC (Hpy_outer_Rev)] for the preamplification step. These primers amplified a 217-bp fragment encompassing the region amplified by the qPCR primers. A synthetic DNA of 240 bases encompassing the region amplified by outer primers was used as a control for the preamplification step.

Effects of *P. gingivalis* infection on tau in SH-SY5Y cells

SH-SY5Y cells (~2.4 × 10^6) were spin-inoculated with MOIs of 10, 50, and 100 with each of the following: *P. gingivalis* [American Type Culture Collection (ATCC) BAA-308] [wild type (WT)], *P. gingivalis KgPDIg-B*, and *P. gingivalis* Δ*K*/Δ*RAB-A*. Uninfected SH-SY5Y cells were used as a control. SH-SY5Y cells and *P. gingivalis* strains were centrifuged at 1000*g* for 10 min at RT in Dulbecco's modified Eagle's medium (DMEM)/F12 supplemented with 2 mM L-glutamine and BSA (200 μg/ml), followed by incubation for 1, 4, and 8 hours, respectively, in a CO_2 incubator. After the indicated incubation times, cells were collected and cell pellets were lysed with 250 μl of radioimmunoprecipitation assay buffer supplemented with protease inhibitor cocktail for 10 to 15 min. Total protein (16 μg) was used for WB. WBs were probed with tau monoclonal antibody TAU-5 (Thermo-MA5-12808). Glyceraldehyde-phosphate dehydrogenase (GAPDH) was used as an internal reference.

Tau-441 incubation with gingipains and WB

Tau-441 (2N4R) (rPeptide, T-1001-1; molecular weight, 45.9 kDa) (2 μg) was reconstituted in 1% NH4OH and digested by 100, 10, 1, and 0.1 nM Kgp/RgpB in working buffer [20 nM sodium phosphate and 1 mM DTT (pH 7.5)]. Digestion reactions were performed for 1 hour at 37°C; reactions were stopped with protease inhibitor (P8340, Sigma-Aldrich). Proteins were separated by electrophoresis at 70 V for 15 min and then at 85 V for 1.5 hours on a 10% Criterion TGX precast gel (Bio-Rad, 5671033) (Bio-Rad, Criterion vertical electrophoresis cell) and electroblotted overnight onto a PVDF membrane at 10 V (Bio-Rad, Criterion Blotter). Blot was blocked with BLOTTO (87530, Thermo Fisher Scientific) for 1 hour and probed with primary antibody anti-Tau46 (13-6400, Thermo Fisher Scientific) at 1:1000 dilution in 3% BSA in TBS for 2 hours. Blot was then washed three times for 10 min each with TBST (28630, Thermo Fisher Scientific) and then incubated with secondary antibody HRP goat anti-mouse (1:50,000; 31439, Thermo Fisher Scientific) in 3% BSA in TBS for 30 min. After further washing, blot was washed three times for 10 min with TBST, and blot staining was visualized using chemiluminescence detection (34096; Super-Signal West Femto, Thermo Fisher Scientific).

Liquid chromatography–MS/MS analysis of gingipain-generated tau cleavage products

Tau samples treated with 1 nM Kgp/RgpB or 10 nM Kgp/RgpB were analyzed by 1D Nano LC-MS/MS (JadeBio, San Diego, CA). A reversed-phase column (200 μm × 20 cm C_{18} 2.5 μm 130 Å) was generated in-house and coupled online to a Q Exactive mass spectrometer (Thermo Fisher Scientific, Bremen, Germany). Peptides were separated by a linear gradient from 95% buffer A [0.1% formic acid (FA) in water]/5% buffer B [0.1% FA in acetonitrile (ACN)] to 60% buffer A/40% buffer B over 150 min at 500 nl/min. The mass spectrometer was operated in a data-dependent TOP20 mode with the following settings: mass range, 400 to 2000 mass/charge ratio (*m/z*); resolution for MS^1 scan, 70,000 full width at half maximum (FWHM); resolution for MS^2 scan, 17,500 FWHM; isolation width, 3 *m/z*; NCE, 27; underfill ratio, 1%; dynamic exclusion, 15 s. Raw MS/MS spectra were searched against UniProt Human + *P. gingivalis* + decoy sequence databases. False discovery rate was <0.1% at the peptide level.

Small-molecule gingipain inhibitor characterization

Structure-based design was used to develop a library of gingipain inhibitors, which were tested on purified Kgp and RgpB to assess potency and determine inhibition constants. The detailed chemical synthesis and structure of compounds in the relevant series of arginine gingipain inhibitors including COR286 can be found in International Patent Application PCT/US2015/054050 and PCT/US2016/061197. The detailed chemical synthesis and structure of compounds in the structural series for lysine gingipain inhibitors including COR119, COR271, and COR388 can be found in PCT/US2016/061197. The capacity of compounds to inhibit the activity of lysine or arginine gingipain was measured in a fluorogenic assay. The assay was performed in buffer [100 mM tris-HCl, 75 mM NaCl, 2.5 mM CaCl2, 10 mM cysteine, and 1% dimethyl sulfoxide (DMSO) (pH 7.5)] for 90 min

at 37°C. Kgp, RgpB, and RgpA were isolated from culture of *P. gingivalis*, as described by Potempa and Nguyen (*39*). The fluorogenic substrate for Kgp was 10 μM Z-His-Glu-Lys-MCA and for RgpA and RgpB was 10 μM Boc-Phe-Ser-Arg-MCA. Trypsin buffer was 10 mM tris and 10 mM $CaCl_2$ (pH 8.0), and the substrate was Z-Gly-Gly-Arg-AMC. COR286 has an IC_{50} of ≤20 pM on purified RgpB and an IC_{50} of 300 pM on structurally related RgpA but no significant inhibition of Kgp. COR119 has an IC_{50} of 10 nM on Kgp, with COR271 and COR388 having IC_{50} values of ≤50 pM on Kgp. All have no significant activity on RgpB. All compounds show negligible inhibition of trypsin with IC_{50} values of ≥10 μM. COR271 and COR388 were profiled more extensively on a series of cellular proteases, and no biologically meaningful activity (IC_{50} > 10 μM) was detected on these enzymes including cathepsin S, calpain, tryptase, thrombin, plasmin, FXa, FVIIa, BACE1, DPP4, proteasome, deubiquitinating peptidases, and caspase family enzymes.

A Morrison inhibition constant (K_i) was determined for COR271 and COR388, and both display a K_i of <0.01 nM. Enzyme kinetic studies were performed to determine the mode of inhibition of the compounds by monitoring recovery of enzyme activity following dilution of existing enzyme/inhibitor complexes. COR119 is a reversible inhibitor, and COR271 and COR388 display irreversible binding kinetics. COR286 contains an identical catalytic binding site mechanism as COR271. The enzyme progress curves from this study were used to estimate K_{off} and $T_{1/2}$ (half-life) of the reversible enzyme complex with COR119. Fitting the progress curve allows an estimate of $K_{off/obs}$ (min^{-1}) of 0.032 and $T_{1/2}$ of 22 min for COR119. A K_{off} value for COR271 and COR388 cannot be calculated, as their binding is irreversible.

The COR553 activity probe was prepared by the copper-catalyzed azide-alkyne cycloaddition reaction (*106*) between an azide derivative of the irreversible Kgp inhibitor COR553 and an alkyne amide derivative of the Cy5 fluorophore. The COR553 probe forms an irreversible covalent bond with a catalytic cysteine residue in the active site of Kgp by displacement of a phenol leaving group.

Effect of gingipain inhibitors on *P. gingivalis* toxicity in SH-SY5Y cells

Human neuroblastoma SH-SY5Y cells at 13 passages were cultured in complete medium [DMEM/F12 (Invitrogen) supplemented with 2 mM L-glutamine (Invitrogen), 10% heat-inactivated fetal bovine serum (10099141, Invitrogen), and 1% penicillin-streptomycin (Invitrogen)] in a 5% CO_2 incubator (Thermo Fisher Scientific). Cells were seeded at a density of 2×10^4 to 4×10^4 cells per well (200 μl of 1×10^5 to 2×10^5 cells/ml) in 96-well black/flat-bottom plates (Greiner) manually coated with collagen type I and then incubated in a CO_2 incubator at 37°C.

When cells reached 70 to 80% confluency (~6×10^4 cells per well), they were challenged with *P. gingivalis* with or without COR271, COR286, moxifloxacin (32477, Fluka), doxycycline (D9891-5G, Sigma-Aldrich), or semagacestat (S1594, SELLECK) at various concentrations.

On the day of testing, the stock solution was diluted by eight serials of twofold dilution in DMSO (Sigma-Aldrich) in a sterile V-bottom 96-well plate (WIPP0280, Axygen) from well 2 to well 10. Well 11 contained DMSO only. From well 2 to well 11, the concentrations were 12.8, 6.4, 3.2, 1.6, 0.8, 0.4, 0.2, 0.1, 0.05, and 0 mg/ml. This was the compound mother plate, with each well containing 200× testing concentrations of compound in DMSO. Then, 6 μl from the mother plate was transferred into a 96-deep-well plate filled with 594 μl of complete medium–penicillin/streptomycin (1:100 dilution) to 2× testing concentration (128, 64, 32, 16, 8, 4, 2, 1, 0.5, and 0 μg/ml). This was the working solution.

P. gingivalis (ATCC BAA-308) was inoculated from −80°C stock onto a brain heart infusion agar (BD-211065). The plate was incubated for 72 hours at 37°C in an anaerobic workstation (YQX-II, Shanghai Yuejin). The atmosphere was kept at 80% N_2, 10% CO_2, and 10% H_2.

On the day of testing, plates were processed in ambient atmosphere. Bacteria were harvested and suspended in complete medium–penicillin/streptomycin (without penicillin/streptomycin). Suspension was adjusted using a Siemens MicroScan turbidity meter (Siemens) to 0.5 turbidity, which is equivalent to ~6×10^8 CFU/ml. Bacterial suspension was diluted in complete medium–penicillin/streptomycin to a final bacterial density of 6×10^8 CFU/ml (for MOI of 1:1000) including one well with no bacteria as a negative control.

Cells in the testing plate were washed once with 200 μl of complete medium–penicillin/streptomycin. Then, 100 μl of working solution and 100 μl of bacterial suspension were added. The final testing concentrations were 64, 32, 16, 8, 4, 2, 1, 0.5, 0.025, and 0 μg/ml with 1% DMSO. The testing plates were incubated at 37°C in a 5% CO_2 incubator for 24 hours.

Cell viability was determined using AlamarBlue (Invitrogen). Cells in the testing plates were washed twice using complete medium–penicillin/streptomycin to remove bacteria in the suspension. Then, 220 μl of AlamarBlue/medium mix (consisting of 200 μl of complete medium–penicillin/streptomycin and 20 μl of AlamarBlue) was added to each well of the testing plates. The testing plates were then incubated in a 37°C CO_2 incubator for fluorescent reduced AlamarBlue to develop. The fluorescent signal from the reduced AlamarBlue (excitation, 530 nm/emission, 590 nm) was read after 6 hours, before saturation, on a SpectraMax M2e plate reader (Molecular Devices).

Stereotactic injection of gingipains in mouse hippocampus

A 7-day study was designed to detect gingipain-induced hippocampal neurodegeneration with Fluoro-Jade C (FJC), a fluorescent stain that has been shown to exhibit maximum staining of degenerating neurons 1 week after a neurotoxic insult (*107*). Fifteen 8-week-old male BALB/c mice (Envigo) were used in the study. Animals were group-housed (n = 2 to 4 per cage) in plastic cages. Animals were maintained on a 12/12-hour light/dark cycle, with the RT maintained at 22° + 2°C and approximately 50% humidity, and received standard rodent chow and tap water ad libitum.

Mice were anesthetized using isoflurane (2%, 800 ml/min O_2). Bupivacaine/epinephrine was used for local analgesia, and carprofen was used for perioperative/postoperative analgesia. A solution of RgpB (5 μg/ml) + Kgp (5 μg/ml) + 5 mM L-cysteine was prepared in sterile saline. Bilateral injections of 0.5 μl were made into coordinates from bregma: anteroposterior −2.0, lateral ±1.5, and ventral −1.4 mm from dura at a rate of 0.1 μl/min with a 5-min rest period using a Hamilton syringe (10-μl syringe with corresponding 30-gauge blunt tip needle; model no. 80308) and the stereotactic micromanipulator (Ultra Micro Pump III with Micro4 Controller, World Precision Instruments). When compound delivery was complete, the needle was left in place for 5 min and then withdrawn such that it took approximately 1 min to fully withdraw the needle.

Mice received a single administration of vehicle or drug 1.5 hours before stereotactic gingipain injection. Inhibitor-treated mice received COR271 (100 mg/kg) in PBS by oral gavage and COR286 (20 mg/kg) in 25% pluronic F127 subcutaneously at a dose volume of 5 and 10 ml/kg, respectively. Vehicle-treated mice received either PBS or pluronic.

Seven days later, mice were anesthetized with isoflurane (2%, 800 ml/min O_2) and perfused with PBS. Brains were harvested, fixed in 10% formalin, embedded in paraffin, and sectioned at 5 μm.

Serial sections 200 μm apart through the entire hippocampus were stained with the FJC Ready-to-Dilute Staining Kit (Biosensis) according to the manufacturer's protocol, and FJC-positive cells in the CA1 area were counted on an Olympus BX61 motorized microscope.

Growth of *P. gingivalis* W83

P. gingivalis [W83 (ATCC, Rockville, MD), ΔKgp (Δ*kgp*), and ΔRgp (Δ*rgpArgpBΔ495-B* Cm^r, Em^r] (*57*, *58*) was streaked on tryptic soy broth (TSB) agar plates [5% sheep blood, supplemented with L-cysteine (0.5 mg/ml), hemin (5 mg/ml), and vitamin K (0.5 μg/ml)] and grown under anaerobic conditions at 37°C for 5 to 7 days. Samples were then inoculated in TSB with hemin, vitamin K, and L-cysteine (TSB-HKC) until mid-log phase OD_{600} (optical density at 600 nm) of 0.5 to 0.7. Bacteria were washed in PBS and prepared at a final concentration of 1×10^{10} cells/ml in PBS + 2% methylcellulose.

P. gingivalis oral infection in mice

Experimental periodontitis was induced by ligature placement. During the procedure, mice were anesthetized with an intraperitoneal injection of ketamine (200 mg/kg; VetaKetam, Poland) and xylazine (10 mg/kg; Sedasin, Biowet, Poland), and the eyes were lubricated with ointment (Puralube Vet; PharmaDerm, Melville, NY). Next, a 5-0 silk ligature (Roboz Surgical Instrument Co., MD, USA) was tied around the upper maxillary left and right second molar. Suture was applied and tied gently to prevent damage to the periodontal tissue. The ligature was left in position for the entire experimental period so that inflammation could be constantly induced by colonization of bacteria inside of it.

Experiment 1

To study $A\beta_{1-42}$ levels in the brains of orally infected mice, 40 (n = 8 per arm) 43- to 44- week-old female BALB/c mice were infected for 6 weeks every other day. For infection, 100 μl of the bacterial solution was applied topically to the buccal surface of the maxillae. COR119 in 2% DMSO/PBS was administered three times a day by subcutaneous injection starting on day 21 and continuing through day 42. Vehicle-treated animals received DMSO only. To further define the role of gingipains in the induction of brain $A\beta_{1-42}$, mice were infected with *P. gingivalis* W83 (WT) or *P. gingivalis* lacking Kgp (Δ*kgp*) or the Rgp-null *P. gingivalis* mutant strain (ΔRgp) (*58*). After 6 weeks, the mice were euthanized and perfused with PBS, and brains were harvested and frozen in liquid nitrogen.

Experiment 2

To study the efficacy of gingipain inhibitors to decrease *P. gingivalis* infection of the brain, 100 (n = 10 per arm) 8-week-old female BALB/c mice were infected for 6 weeks every other day as described above. The mice received gingipain inhibitors or moxifloxacin for 5 weeks (days 36 to 70). COR271 was administered orally twice daily in PBS at 10 mg/kg; COR286 was administered subcutaneously twice daily in 25% pluronic F127 (10 mg/kg; Sigma-Aldrich, USA). Moxifloxacin (Sigma-Aldrich, USA) was administered subcutaneously twice daily in PBS at 10 mg/kg. Vehicle-treated animals received PBS or pluronic only. A group of mock-infected and *P. gingivalis* W83 (WT)–infected mice were euthanized on day 35 to gather baseline measurements before the start of treatment. After 10 weeks, *P. gingivalis* W83 (WT)–infected mice and mice infected with bacteria ± gingipain inhibitors or moxifloxacin were euthanized, and the brain and serum were harvested and frozen in liquid nitrogen.

Experiment 3

To study the efficacy of gingipain inhibitors to decrease *P. gingivalis* infection of the brain, 70 (n = 10 per arm) 8-week-old female BALB/c mice were infected for 6 weeks every other day as described above. The mice received COR388 (3, 10, or 30 mg/kg) or COR271 (10 mg/kg) twice daily in PBS for 5 weeks (days 36 to 70) by oral administration. Vehicle-treated animals received PBS only. Mice were euthanized on day 35 or day 70, and one brain hemisphere and serum were frozen in liquid nitrogen, while one brain hemisphere was fixed in 10% formalin.

Aβ ELISA

Brain samples (posterior half of the left hemisphere) were homogenized in radioimmunoprecipitation assay buffer (VWR), and $A\beta_{1-42}$ was quantified with a Novex Mouse Beta Amyloid 1-42 (Aβ42) ELISA kit (Thermo Fisher Scientific, USA) according to the manufacturer's specifications.

ELISA assays for TNFα

Brain lysate was quantified for TNFα with ProcartaPlex Chemokine Convenience Panel 1 (Thermo Fisher Scientific) on a Luminex platform following the manufacturer's protocol and with a V-PLEX Proinflammatory Panel 1 Mouse kit (Meso Scale Diagnostics, Rockville, MD). Results from both assays were corrected for protein content and normalized to the mock group, and the means of both assays were analyzed as a combined dataset.

Endpoint PCR analysis of *P. gingivalis* in mice brain tissue

Bacterial DNA was extracted from mouse brains using DNeasy Blood & Tissue Kits (Qiagen, Germany) according to the manufacturer's protocols. The concentration of DNA was measured using a NanoDrop 2000 (Thermo Fisher Scientific, USA). Bacterial DNA was amplified with 16*S* ribosomal RNA (rRNA) primers for the W83 strain of *P. gingivalis* [AGGCAGCTTGCCATACTGCG (forward) and ACTGTTAGCAACTACCGATGT (reverse)]. PCR amplification was conducted in a 12-μl reaction volume including 3 μl of brain DNA (80 ng of DNA), 6 μl of EconoTaq PLUS Green 2× Master Mix (Lucigen, USA), 0.6 μl (10 μM) of each primer (GenoMed, Poland), and 1.8 μl of H_2O (Thermo Fisher Scientific, USA). Forty cycles of amplification were performed in a DNA thermal cycler (TProfessional TRIO, Biometra, Germany) consisting of 3 min for 95°C, 20 s for 95°C, 30 s for 57°C, 30 s for 72 °C, and 5 min for 72°C. The amplified product was identified by electrophoresis in a 1.5% agarose gel (BioShop, Canada). The DNA was stained with ethidium bromide, visualized under short wavelength transilluminator, and photographed in runVIEW imager (BIOCOMdirect, UK).

$A\beta_{1-42}$ binds to the surface of *P. gingivalis*

Recombinant Aβ (1-42) Ultra-Pure, Ammonium Hydroxide (rProtein) was prepared as stock solutions (1 mg/ml) in 1% $NaNH_4$. *P. gingivalis* was washed in PBS and incubated at 10^8 CFU/ml in Aβ (10, 30, and 100 μg/ml) for 1 hour at RT and ambient oxygen. For IHC, a 10-μl solution was dried on a SuperFrost Plus glass slide (VWR) fixed in 4% paraformaldehyde for 10 min. Slide was then rinsed with PBS and dH_2O, exposed to formic acid, and, after washing with PBS, incubated for 2 hours in PBS, 0.3% Triton X-100, and primary antibodies CAB102 (1:1000) and 4G8 (1:1000; BioLegend). Fluorescence labeling was performed with Alexa Fluor 488 donkey anti-rabbit (1:200; Jackson ImmunoResearch) and Cy3 donkey anti-goat (1:200; Jackson ImmunoResearch) in PBS. Slides were mounted with ProLong Gold Antifade (Thermo Fisher Scientific). Images were taken on an Olympus BX61 microscope with a Zyla 5.5 sCMOS camera (Andor).

Antimicrobial effects of Aβ on *P. gingivalis*

Recombinant Aβ (1-40, 1-42, 1-42 scrambled) Ultra-Pure, Ammonium Hydroxide (rProtein) was prepared as 0.2 mM stock solutions in 1% $NaNH_4$. Aβ peptides were added to *P. gingivalis* cultures at a final concentration of 20 mM and kept at 37°C under anaerobic conditions for 24 hours. Cells were washed in PBS and stained with the LIVE/DEAD BacLight Bacterial Viability Kit (Thermo Fisher Scientific) according to the manufacturer's protocol. Fluorescence intensity was quantified on a PerkinElmer Envision Plate reader.

qPCR analysis of *P. gingivalis* in mouse brain tissue

DNA was extracted from brain tissue using the DNeasy Blood & Tissue Kit (Qiagen, Germany) according to the manufacturer's protocol. TaqMan qPCR was performed with Kapa Probe fast qPCR Mix (Rox Low) on a Bio-Rad CFX96 Real-Time System C1000 Touch ThermalCycler with the forward (5′-AGCAACCAGCTACCGTTTAT-3′) and reverse (5′-GTACCTGTCGGTTTACCATCTT-3′) primers and 6-FAM-TACCATGTTTCGCAGAAGCCCTGA-TAMRA as the detection probe. The primers were based on single copy of *P. gingivalis* arginine–specific cysteine-proteinase gene (*108*). Duplicate samples were assayed in a total volume of 10 μl, containing 100 ng of template brain genomic DNA solution, TaqMan Universal PCR Master Mix (2×) (Kapa Biosystems, USA), and the specific set of primers (final concentration, 5 μM) and probe (final concentration, 4 μM) (GenoMed, Poland), corresponding to 562.5 nM of forward and reverse primers and 100 nM of the probe. After an initial incubation step of 2 min at 50°C and denaturation for 95°C for 20 s, 40 PCR cycles (95°C for 20 s and 60°C for 30 s) were performed. The number of copies of the *P. gingivalis* genome was calculated by matching C_q values with a standard curve prepared from serial dilutions of cultured *P. gingivalis* W83 (WT).

Quantification of hippocampal Gad67$^+$ interneurons

Anti-GAD67 antibody, clone 1G10.2 (MAB5406, MilliporeSigma), was used at a dilution of 1:2000 for IHC. Quantification of Gad67$^+$ interneurons was performed with CellSens 1.5 Software. The area of the hilus was

defined as the area between the blades of the dentate gyrus connected by a straight line on the open side. The number of cells on every 40th section through the hippocampus was counted. The results are presented as the number of cells per volume of tissue.

Preparation of *P. gingivalis* lysates for gel electrophoresis

Bacteria (10^8) were collected and centrifuged at 5000*g* for 10 min at 4°C. The supernatant was discarded. Bacterial cell pellet was lysed with 1 ml of B-PER lysis buffer (Thermo Fisher Scientific) on ice for 10 min and then centrifuged for 10 min at 14,000*g* at 4°C. The supernatant containing protein lysate was collected.

COR553 activity probe labeling of Kgp

P. gingivalis lysate, purified Kgp, or human subgingival plaque samples were incubated with 1 μM of Cy5 probe COR553 for 1 hour at 37°C with shaking. For COR388-treated samples, 1 μM COR388 was added for 30 min at 37°C before the addition of COR553. Then, samples were denatured with NuPAGE LDS sample buffer (Thermo Fisher Scientific) containing 50 mM DTT at 95°C for 10 min and subjected to SDS-PAGE with Criterion 4 to 15% precast gel (Bio-Rad) and tris/glycine/SDS running buffer (Bio-Rad). Gel was run at 75 V for 10 min and then at 125 V for 1.5 hours, followed by Cy5 visualization with ChemiDoc imaging system (Bio-Rad).

IP of Kgp labeled with COR553

For IP of Cy5-labeled Kgp, the samples were incubated with 10 mg of rabbit polyclonal CAB102 antibody with rotation overnight at 4°C, incubated with prewashed Dynabeads Protein G beads with rotation for 20 min at RT, washed, and magnetically separated. Beads were then dissolved with 20 μl of elution buffer and 10 μl of NuPAGE LDS sample buffer and 50 mM DTT and heated at 70°C for 10 min, eluting the IP proteins. Samples were then subjected to SDS-PAGE, and Cy5 probe signals were visualized with a ChemiDoc imaging system (Bio-Rad).

WB analysis of COR553-labeled samples

After imaging with Cy5 detection, the same gels were transferred to PVDF membranes and immunoblotted with anti-Kgp antibody CAB102. Membranes were blocked with 3% BSA TBST buffer for at least 1 hour, incubated with 1:1000 CAB102 for 2 hours at RT or overnight at 4°C in blocking buffer, and visualized with goat anti-rabbit IgG HRP-conjugated antibody (#31462, Thermo Fisher Scientific) and chemiluminescent detection using SuperSignal West Femto (Thermo Fisher Scientific) and a ChemiDoc imaging system.

Collection and processing of human saliva and subgingival plaque samples

Oral subgingival plaque and saliva samples were obtained from five human subjects with periodontal disease under an IRB-approved clinical protocol. An unstimulated saliva sample (about 1 ml) was obtained by collection into a sterile 15-ml falcon tube following a 2-min water rinse. Samples were collected at a consistent time of day to avoid diurnal effects and were kept cold during and following collection. After collection was complete, the cap of the tube was tightly screwed and transferred to −80°C.

Two subgingival plaque samples per site were collected from periodontal sites of four periodontal teeth with ≥6 mm pocket depth using Endodontic absorbent paper points (size, 40). The sampling sites were gently air-dried and isolated with cotton pellets to avoid saliva contamination. The paper points were inserted in the pockets for 30 s until resistance was felt. Paper points were held with pliers, removed from the site, and placed into prelabeled 1.5-ml microcentrifuge tubes. Samples were eluted from the paper points by placing them in 100 μl of B-PER lysis buffer in a low-bind 1.5-ml tube, flicking the tube at one flick per second for 30 s, discarding the paper point, and snap-freezing the samples in liquid nitrogen. Each plaque sample was processed in this manner separately but combined for analysis. Twenty microliters of the eluate was used for COR553 probe labeling, 5 μl was used for BCA protein determination, and 2 μl was used for qPCR.

qPCR detection of *P. gingivalis* copy number in saliva and subgingival plaque of human subjects

DNA was extracted from 50 μl of Saliva using Puregene Core Kit A (Qiagen). The final DNA pellet was dissolved in 50 μl of DNA hydration buffer. A qPCR assay was performed with 2 μl of saliva DNA and *hmuY* primers [GAACGATTTGAACTGGGACA (H1.1 forward) and AACGGTAGTAGCCTGATCCA (H1.1 reverse)] and a probe (/56-FAM/TTCTGTCTT/ZEN/GCCGGAGAATACGGC/3IABkFQ/). A serial dilution of synthetic template DNA was included in the qPCR assay to calculate the copy number of *P. gingivalis* in saliva. qPCR was performed on 2 μl of neat eluate of subgingival plaque (no DNA extraction). The primers and methods were the same as those used for saliva above.

Determination of Kgp-dependent growth of *P. gingivalis*

P. gingivalis [WT (ATCCBAA-308) and KgPΔIg-B] was inoculated from stocks into 20 ml of prereduced modified TSB medium [TSB + yeast extract (5 mg/ml), L-cysteine (0.5 mg/ml), hemin (5 μg/ml), and vitamin K1 (1 μg/ml)] and incubated at 37°C for 48 hours anaerobically in a Coy type C vinyl chamber. Prereduction of all solutions used was done by transferring the liquids to an anaerobic chamber for >16 hours immediately after autoclaving. On the day of the experiment, the primary culture was diluted to obtain OD of 0.2 to 0.25 using a Siemens MicroScan turbidity meter in the prereduced modified TSB medium and incubated for 6 hours to reach log phase (OD of approximately 0.5 to 0.6) at 37°C. Then, the bacteria were collected by centrifuging at 4000 rpm for 10 min and washed. Pellets were diluted to 3×10^8 to 5×10^8 CFU/ml, and 10 ml of these diluted cultures was transferred into conical tubes and centrifuged. The resultant pellet was resuspended using 10 ml of defined medium to assess growth. The defined medium consists of the following: salt base supplement [10.0 mM NaH_2PO_4, 10.0 mM KCI, 2 mM citric acid, 1.25 mM $MgCl_2$, 20.0 μM $CaCl_2$, 0.1 μM Na_2MoO_4, 25.0 μM $ZnCl_2$, 50.0 μM $MnCl_2$, 5.0 μM $CuCl_2$, 10.0 μM $CoCl_2$, and 5.0 μM H_3BO_3 (pH 7.0)] with 20 mM α-ketoglutarate, 3% BSA, hemin (5 μg/ml), and vitamin K (1 μg/ml). Fifty microliters of 100× COR388 stock prepared in DMSO was added to the bacterial suspension (3×10^8 to 5×10^8 CFU/ml) for each strain with a final concentration of 500 nM. Vehicle cultures were treated with 0.1% DMSO. The bacteria were incubated at 37°C in the anaerobic chamber, and OD was measured at 0, 21, and 43 hours to generate a time course of culture growth.

Assessment of in vitro resistance of *P. gingivalis*

P. gingivalis (ATCC BAA-308) and *P. gingivalis* Kgp knockout were thawed, and a culture of $OD_{600} = 1.2$ (equals 3×10^9 to 5×10^9 CFU/ml) was prepared as described above. Resistance was assessed by incubation of 16 serial passages of *P. gingivalis* in the defined medium listed previously, and resistance to COR388 was performed simultaneously with cultures incubated with the broad-spectrum antibiotic moxifloxacin. Because COR388 does not completely inhibit *P. gingivalis* growth in vitro, we defined MIC as the minimum COR388 concentration that produced a partial inhibition cutoff, specifically >50% inhibition compared to nontreated cultures. Resistance was assessed in two standard methods, with the final data reported as an average of both methods. Cultures were first prepared with drug and moxifloxacin in a range of doses passaging each time for 17 passages and monitoring MIC with each passage. In a separate study, drug concentrations were gradually increased between passages. The lowest drug concentration that inhibited >50% growth was recorded as the MIC, inoculum from this passage used for the next passage, and assessed at a new drug concentration using the highest drug concentration that was sublethal and raising the concentrations throughout the test as needed.

Statistical analysis

Data were analyzed with GraphPad Prism version 7.02 for Windows (GraphPad Software, La Jolla, CA, USA; www.graphpad.com). Outliers were detected with the ROUT method ($Q = 0.2\%$) and removed from further analysis. Outliers were not removed from data presented in Fig. 1. To determine whether the data were normally distributed, we performed a

Shapiro-Wilk test. If P values were below 0.05, then the data were considered nonparametric and analyzed by Mann-Whitney test or Kruskal-Wallis one-way analysis of variance (ANOVA) followed by Dunn's post hoc test. Parametric data were analyzed by unpaired t test or by one-way ANOVA followed by Dunnett's multiple comparisons test. Correlations were analyzed with Spearman's correlation coefficient.

SUPPLEMENTARY MATERIALS

Supplementary material for this article is available at http://advances.sciencemag.org/cgi/content/full/5/1/eaau3333/DC1

Fig. S1. CAB101 analysis of non-AD neurological disease brain microarrays.

Fig. S2. RgpB IHC in hippocampal samples from nondemented and AD patients.

Fig. S3. Sequencing of *P. gingivalis hmuY* PCR products from AD brains.

Fig. S4. Sequencing of *P. gingivalis hmuY* PCR products from clinical AD CSF.

Table S1. NVD003 AD and control TMA patient data.

Table S2. NVD005 AD and control TMA patient data.

Table S3. Tau fragments identified by MS after gingipain exposure.

Table S4. Demographic information of patients with CP who donated saliva and subgingival plaque samples.

REFERENCES AND NOTES

1. T. Wyss-Coray, J. Rogers, Inflammation in Alzheimer disease—A brief review of the basic science and clinical literature. *Cold Spring Harb. Perspect. Med.* **2**, a006346 (2012).
2. V. Kaushal, R. Dye, P. Pakavathkumar, B. Foveau, J. Flores, B. Hyman, B. Ghetti, B. H. Koller, A. C. LeBlanc, Neuronal NLRP1 inflammasome activation of Caspase-1 coordinately regulates inflammatory interleukin-1-beta production and axonal degeneration-associated Caspase-6 activation. *Cell Death Differ.* **22**, 1676–1686 (2015).
3. F. Mawanda, R. Wallace, Can infections cause Alzheimer's disease? *Epidemiol. Rev.* **35**, 161–180 (2013).
4. D. K. V. Kumar, S. H. Choi, K. J. Washicosky, W. A. Eimer, S. Tucker, J. Ghofrani, A. Lefkowitz, G. McColl, L. E. Goldstein, R. E. Tanzi, R. D. Moir, Amyloid-β peptide protects against microbial infection in mouse and worm models of Alzheimer's disease. *Sci. Transl. Med.* **8**, 340ra72 (2016).
5. S. J. Soscia, J. E. Kirby, K. J. Washicosky, S. M. Tucker, M. Ingelsson, B. Hyman, M. A. Burton, L. E. Goldstein, S. Duong, R. E. Tanzi, R. D. Moir, The Alzheimer's disease-associated amyloid β-protein is an antimicrobial peptide. *PLOS ONE* **5**, e9505 (2010).
6. P. Spitzer, M. Condic, M. Herrmann, T. J. Oberstein, M. Scharin-Mehlmann, D. F. Gilbert, O. Friedrich, T. Grömer, J. Kornhuber, R. Lang, J. M. Maler, Amyloidogenic amyloid-β-peptide variants induce microbial agglutination and exert antimicrobial activity. *Sci. Rep.* **6**, 32228 (2016).
7. R. P. Darveau, G. Hajishengallis, M. A. Curtis, *Porphyromonas gingivalis* as a potential community activist for disease. *J. Dent. Res.* **91**, 816–820 (2012).
8. E. K. Kaye, A. Valencia, N. Baba, A. Spiro III, T. Dietrich, R. I. Garcia, Tooth loss and periodontal disease predict poor cognitive function in older men. *J. Am. Geriatr. Soc.* **58**, 713–718 (2010).
9. M. Gatz, J. A. Mortimer, L. Fratiglioni, B. Johansson, S. Berg, C. A. Reynolds, N. L. Pedersen, Potentially modifiable risk factors for dementia in identical twins. *Alzheimers Dement.* **2**, 110–117 (2006).
10. P. S. Stein, M. Desrosiers, S. J. Donegan, J. F. Yepes, R. J. Kryscio, Tooth loss, dementia and neuropathology in the Nun study. *J. Am. Dent. Assoc.* **138**, 1314–1322; quiz 1381–2 (2007).
11. A. R. Kamer, E. Pirraglia, W. Tsui, H. Rusinek, S. Vallabhajosula, L. Mosconi, L. Yi, P. McHugh, R. G. Craig, S. Svetcov, R. Linker, C. Shi, L. Glodzik, S. Williams, P. Corby, D. Saxena, M. J. de Leon, Periodontal disease associates with higher brain amyloid load in normal elderly. *Neurobiol. Aging* **36**, 627–633 (2015).
12. J. M. Noble, L. N. Borrell, P. N. Papapanou, M. S. V. Elkind, N. Scarmeas, C. B. Wright, Periodontitis is associated with cognitive impairment among older adults: Analysis of NHANES-III. *J. Neurol. Neurosurg. Psychiatry* **80**, 1206–1211 (2009).
13. M. Ide, M. Harris, A. Stevens, R. Sussams, V. Hopkins, D. Culliford, J. Fuller, P. Ibbett, R. Raybould, R. Thomas, U. Puenter, J. Teeling, V. H. Perry, C. Holmes, Periodontitis and cognitive decline in Alzheimer's disease. *PLOS ONE* **11**, e0151081 (2016).
14. S. Poole, S. K. Singhrao, S. Chukkapalli, M. Rivera, I. Velsko, L. Kesavalu, S. Crean, Active invasion of *porphyromonas gingivalis* and infection-induced complement activation in ApoE$^{-/-}$ mice brains. *J. Alzheimers Dis.* **43**, 67–80 (2015).
15. N. Ishida, Y. Ishihara, K. Ishida, H. Tada, Y. Funaki-Kato, M. Hagiwara, T. Ferdous, M. Abdullah, A. Mitani, M. Michikawa, K. Matsushita, Periodontitis induced by bacterial infection exacerbates features of Alzheimer's disease in transgenic mice. *NPJ Aging Mech. Dis.* **3**, 15 (2017).
16. S. Poole, S. K. Singhrao, L. Kesavalu, M. A. Curtis, S. Crean, Determining the presence of periodontopathic virulence factors in short-term postmortem Alzheimer's disease brain tissue. *J. Alzheimers Dis.* **36**, 665–677 (2013).
17. S. K. Singhrao, A. Harding, S. Poole, L. Kesavalu, S. Crean, *Porphyromonas gingivalis* periodontal infection and its putative links with Alzheimer's disease. *Mediators Inflamm.* **2015**, 137357 (2015).
18. A. L. Griffen, M. R. Becker, S. R. Lyons, M. L. Moeschberger, E. J. Leys, Prevalence of *Porphyromonas gingivalis* and periodontal health status. *J. Clin. Microbiol.* **36**, 3239–3242 (1998).
19. L. Forner, T. Larsen, M. Kilian, P. Holmstrup, Incidence of bacteremia after chewing, tooth brushing and scaling in individuals with periodontal inflammation. *J. Clin. Periodontol.* **33**, 401–407 (2006).
20. J. Mahendra, L. Mahendra, V. M. Kurian, K. Jaishankar, R. Mythilli, Prevalence of periodontal pathogens in coronary atherosclerotic plaque of patients undergoing coronary artery bypass graft surgery. *J. Maxillofac. Oral Surg.* **8**, 108–113 (2009).
21. J. Katz, N. Chegini, K. T. Shiverick, R. J. Lamont, Localization of *P. gingivalis* in preterm delivery placenta. *J. Dent. Res.* **88**, 575–578 (2009).
22. M. Ishikawa, K. Yoshida, H. Okamura, K. Ochiai, H. Takamura, N. Fujiwara, K. Ozaki, Oral *Porphyromonas gingivalis* translocates to the liver and regulates hepatic glycogen synthesis through the Akt/GSK-3β signaling pathway. *Biochim. Biophys. Acta* **1832**, 2035–2043 (2013).
23. J.-L. C. Mougeot, C. B. Stevens, B. J. Paster, M. T. Brennan, P. B. Lockhart, F. K. B. Mougeot, *Porphyromonas gingivalis* is the most abundant species detected in coronary and femoral arteries. *J. Oral Microbiol.* **9**, 1281562 (2017).
24. Y. Guo, K.-A. Nguyen, J. Potempa, Dichotomy of gingipains action as virulence factors: From cleaving substrates with the precision of a surgeon's knife to a meat chopper-like brutal degradation of proteins. *Periodontol. 2000* **54**, 15–44 (2010).
25. M. J. Gui, S. G. Dashper, N. Slakeski, Y.-Y. Chen, E. C. Reynolds, Spheres of influence: *Porphyromonas gingivalis* outer membrane vesicles. *Mol. Oral Microbiol.* **31**, 365–378 (2016).
26. D. Grenier, S. Roy, F. Chandad, P. Plamondon, M. Yoshioka, K. Nakayama, D. Mayrand, Effect of inactivation of the Arg- and/or Lys-gingipain gene on selected virulence and physiological properties of *Porphyromonas gingivalis*. *Infect. Immun.* **71**, 4742–4748 (2003).
27. P. G. Stathopoulou, J. C. Galicia, M. R. Benakanakere, C. A. Garcia, J. Potempa, D. F. Kinane, *Porphyromonas gingivalis* induce apoptosis in human gingival epithelial cells through a gingipain-dependent mechanism. *BMC Microbiol.* **9**, 107 (2009).
28. S. M. Sheets, J. Potempa, J. Travis, C. A. Casiano, H. M. Fletcher, Gingipains from *Porphyromonas gingivalis* W83 induce cell adhesion molecule cleavage and apoptosis in endothelial cells. *Infect. Immun.* **73**, 1543–1552 (2005).
29. J. A. Kinane, M. R. Benakanakere, J. Zhao, K. B. Hosur, D. F. Kinane, *Porphyromonas gingivalis* influences actin degradation within epithelial cells during invasion and apoptosis. *Cell. Microbiol.* **14**, 1085–1096 (2012).
30. T. F. Flemmig, E. Milián, H. Karch, B. Klaiber, Differential clinical treatment outcome after systemic metronidazole and amoxicillin in patients harboring *Actinobacillus actinomycetemcomitans* and/or *Porphyromonas gingivalis*. *J. Clin. Periodontol.* **25**, 380–387 (1998).
31. J. Travis, J. Potempa, Bacterial proteinases as targets for the development of second-generation antibiotics. *Biochim. Biophys. Acta* **1477**, 35–50 (2000).
32. A. E. Clatworthy, E. Pierson, D. T. Hung, Targeting virulence: A new paradigm for antimicrobial therapy. *Nat. Chem. Biol.* **3**, 541–548 (2007).
33. C. T. Supuran, A. Scozzafava, A. Mastrolorenzo, Bacterial proteases: Current therapeutic use and future prospects for the development of new antibiotics. *Expert Opin. Ther. Pat.* **11**, 221–259 (2001).
34. T. Kadowaki, A. Baba, N. Abe, R. Takii, M. Hashimoto, T. Tsukuba, S. Okazaki, Y. Suda, T. Asao, K. Yamamoto, Suppression of pathogenicity of *Porphyromonas gingivalis* by newly developed gingipain inhibitors. *Mol. Pharmacol.* **66**, 1599–1606 (2004).
35. P. T. Nelson, I. Alafuzoff, E. H. Bigio, C. Bouras, H. Braak, N. J. Cairns, R. J. Castellani, B. J. Crain, P. Davies, K. Del Tredici, C. Duyckaerts, M. P. Frosch, V. Haroutunian, P. R. Hof, C. M. Hulette, B. T. Hyman, T. Iwatsubo, K. A. Jellinger, G. A. Jicha, E. Kovari, W. A. Kukull, J. B. Leverenz, S. Love, I. R. Mackenzie, D. M. Mann, E. Masliah, A. C. McKee, T. J. Montine, J. C. Morris, J. A. Schneider, J. A. Sonnen, D. R. Thal, J. Q. Trojanowski, J. C. Troncoso, T. Wisniewski, R. L. Woltjer, T. G. Beach, Correlation of Alzheimer disease neuropathologic changes with cognitive status: A review of the literature. *J. Neuropathol. Exp. Neurol.* **71**, 362–381 (2012).
36. A. Hershko, A. Ciechanover, The ubiquitin system. *Annu. Rev. Biochem.* **67**, 425–479 (1998).
37. C. T. Chu, J. L. Caruso, T. J. Cummings, J. Ervin, C. Rosenberg, C. M. Hulette, Ubiquitin immunochemistry as a diagnostic aid for community pathologists evaluating patients who have dementia. *Mod. Pathol.* **13**, 420–426 (2000).
38. R. Sperling, E. Mormino, K. Johnson, The evolution of preclinical Alzheimer's disease: Implications for prevention trials. *Neuron* **84**, 608–622 (2014).
39. J. Potempa, K.-A. Nguyen, Purification and characterization of gingipains. *Curr. Protoc. Protein Sci.* **Chapter 21**, Unit 21.20 (2007).

40. J. Potempa, R. Pike, J. Travis, The multiple forms of trypsin-like activity present in various strains of *Porphyromonas gingivalis* are due to the presence of either Arg-gingipain or Lys-gingipain. *Infect. Immun.* **63**, 1176–1182 (1995).
41. A. Gmiterek, H. Wójtowicz, P. Mackiewicz, M. Radwan-Oczko, M. Kantorowicz, M. Chomyszyn-Gajewska, M. Frączczak, M. Bielecki, M. Olczak, T. Olczak, The unique *hmuY* gene sequence as a specific marker of *Porphyromonas gingivalis*. *PLOS ONE* **8**, e67719 (2013).
42. B. Linz, F. Balloux, Y. Moodley, A. Manica, H. Liu, P. Roumagnac, D. Falush, C. Stamer, F. Prugnolle, S. W. van der Merwe, Y. Yamaoka, D. Y. Graham, E. Perez-Trallero, T. Wadstrom, S. Suerbaum, M. Achtman, An African origin for the intimate association between humans and *Helicobacter pylori*. *Nature* **445**, 915–918 (2007).
43. C. Schabereiter-Gurtner, A. M. Hirschl, B. Dragosics, P. Hufnagl, S. Puz, Z. Kovách, M. Rotter, A. Makristathis, Novel real-time PCR assay for detection of *Helicobacter pylori* infection and simultaneous clarithromycin susceptibility testing of stool and biopsy specimens. *J. Clin. Microbiol.* **42**, 4512–4518 (2004).
44. S. S. Spudich, A. C. Nilsson, N. D. Lollo, T. J. Liegler, C. J. Petropoulos, S. G. Deeks, E. E. Paxinos, R. W. Price, Cerebrospinal fluid HIV infection and pleocytosis: Relation to systemic infection and antiretroviral treatment. *BMC Infect. Dis.* **5**, 98 (2005).
45. Y. Yamamoto, PCR in diagnosis of infection: Detection of bacteria in cerebrospinal fluids. *Clin. Diagn. Lab. Immunol.* **9**, 508–514 (2002).
46. M. J. Espy, J. R. Uhl, L. M. Sloan, S. P. Buckwalter, M. F. Jones, E. A. Vetter, J. D. C. Yao, N. L. Wengenack, J. E. Rosenblatt, F. R. Cockerill III, T. F. Smith, Real-time PCR in clinical microbiology: Applications for routine laboratory testing. *Clin. Microbiol. Rev.* **19**, 165–256 (2006).
47. H. Yin, J. Kuret, C-terminal truncation modulates both nucleation and extension phases of τ fibrillization. *FEBS Lett.* **580**, 211–215 (2006).
48. B. Kovacech, M. Novak, Tau truncation is a productive posttranslational modification of neurofibrillary degeneration in Alzheimer's disease. *Curr. Alzheimer Res.* **7**, 708–716 (2010).
49. S. Taniguchi-Watanabe, T. Arai, F. Kametani, T. Nonaka, M. Masuda-Suzukake, A. Tarutani, S. Murayama, Y. Saito, K. Arima, M. Yoshida, H. Akiyama, A. Robinson, D. M. A. Mann, T. Iwatsubo, M. Hasegawa, Biochemical classification of tauopathies by immunoblot, protein sequence and mass spectrometric analyses of sarkosyl-insoluble and trypsin-resistant tau. *Acta Neuropathol.* **131**, 267–280 (2016).
50. D. Uberti, C. Rizzini, P. F. Spano, M. Memo, Characterization of tau proteins in human neuroblastoma SH-SY5Y cell line. *Neurosci. Lett.* **235**, 149–153 (1997).
51. T. McAvoy, M. E. Lassman, D. S. Spellman, Z. Ke, B. J. Howell, O. Wong, L. Zhu, M. Tanen, A. Struyk, O. F. Laterza, Quantification of tau in cerebrospinal fluid by immunoaffinity enrichment and tandem mass spectrometry. *Clin. Chem.* **60**, 683–689 (2014).
52. C. Sato, N. R. Barthélemy, K. G. Mawuenyega, B. W. Patterson, B. A. Gordon, J. Jockel-Balsarotti, M. Sullivan, M. J. Crisp, T. Kasten, K. M. Kirmess, N. M. Kanaan, K. E. Yarasheski, A. Baker-Nigh, T. L. S. Benzinger, T. M. Miller, C. M. Karch, R. J. Bateman, Tau kinetics in neurons and the human central nervous system. *Neuron* **97**, 1284–1298.e7 (2018).
53. M. von Bergen, P. Friedhoff, J. Biernat, J. Heberle, E.-M. Mandelkow, E. Mandelkow, Assembly of τ protein into Alzheimer paired helical filaments depends on a local sequence motif (^{306}VQIVYK^{311}) forming β structure. *Proc. Natl. Acad. Sci. U.S.A.* **97**, 5129–5134 (2000).
54. J. Stöhr, H. Wu, M. Nick, Y. Wu, M. Bhate, C. Condello, N. Johnson, J. Rodgers, T. Lemmin, S. Acharya, J. Becker, K. Robinson, M. J. S. Kelly, F. Gai, G. Stubbs, S. B. Prusiner, W. F. DeGrado, A 31-residue peptide induces aggregation of tau's microtubule-binding region in cells. *Nat. Chem.* **9**, 874–881 (2017).
55. S. Eick, W. Pfister, Efficacy of antibiotics against periodontopathogenic bacteria within epithelial cells: An in vitro study. *J. Periodontol.* **75**, 1327–1334 (2004).
56. E. Portelius, H. Zetterberg, R. A. Dean, A. Marcil, P. Bourgeois, M. Nutu, U. Andreasson, E. Siemers, K. G. Mawuenyega, W. C. Sigurdson, P. C. May, S. M. Paul, D. M. Holtzman, K. Blennow, R. J. Bateman, Amyloid-$\beta_{1-15/16}$ as a marker for γ-secretase inhibition in Alzheimer's disease. *J. Alzheimers Dis.* **31**, 335–341 (2012).
57. M. Sztukowska, A. Sroka, M. Bugno, A. Banbula, Y. Takahashi, R. N. Pike, C. A. Genco, J. Travis, J. Potempa, The C-terminal domains of the gingipain K polyprotein are necessary for assembly of the active enzyme and expression of associated activities. *Mol. Microbiol.* **54**, 1393–1408 (2004).
58. K.-A. Nguyen, J. Travis, J. Potempa, Does the importance of the C-terminal residues in the maturation of RgpB from *Porphyromonas gingivalis* reveal a novel mechanism for protein export in a subgroup of Gram-Negative bacteria? *J. Bacteriol.* **189**, 833–843 (2007).
59. K. Govindpani, B. Calvo-Flores Guzman, C. Vinnakota, H. J. Waldvogel, R. L. Faull, A. Kwakowsky, Towards a better understanding of GABAergic remodeling in Alzheimer's disease. *Int. J. Mol. Sci.* **18**, E1813 (2017).
60. W. Fornicola, A. Pelcovits, B.-X. Li, J. Heath, G. Perry, R. J. Castellani, Alzheimer disease pathology in middle age reveals a spatial-temporal disconnect between amyloid-β and phosphorylated tau. *Open Neurol. J.* **8**, 22–26 (2014).
61. J. C. Lenzo, N. M. O'Brien-Simpson, R. K. Orth, H. L. Mitchell, S. G. Dashper, E. C. Reynolds, *Porphyromonas gulae* has virulence and immunological characteristics similar to those of the human periodontal pathogen *Porphyromonas gingivalis*. *Infect. Immun.* **84**, 2575–2585 (2016).
62. Y. Yamasaki, R. Nomura, K. Nakano, S. Naka, M. Matsumoto-Nakano, F. Asai, T. Ooshima, Distribution of periodontopathic bacterial species in dogs and their owners. *Arch. Oral Biol.* **57**, 1183–1188 (2012).
63. L. Sun, R. Zhou, G. Yang, Y. Shi, Analysis of 138 pathogenic mutations in presenilin-1 on the in vitro production of Aβ42 and Aβ40 peptides by γ-secretase. *Proc. Natl. Acad. Sci. U.S.A.* **114**, E476–E485 (2017).
64. R. Zhou, G. Yang, Y. Shi, Dominant negative effect of the loss-of-function γ-secretase mutants on the wild-type enzyme through heterooligomerization. *Proc. Natl. Acad. Sci. U.S.A.* **114**, 12731–12736 (2017).
65. W. B. Zigman, D. A. Devenny, S. J. Krinsky-McHale, E. C. Jenkins, T. K. Urv, J. Wegiel, N. Schupf, W. Silverman, Alzheimer's disease in adults with Down syndrome. *Int. Rev. Res. Ment. Retard.* **36**, 103–145 (2008).
66. P. J. Cichon, L. B. Crawford, W. D. Grimm, Early-onset periodontitis associated with Down's syndrome—Clinical interventional study. *Ann. Periodontol.* **3**, 370–380 (1998).
67. A. Amano, T. Kishima, S. Kimura, M. Takiguchi, T. Ooshima, S. Hamada, I. Morisaki, Periodontopathic bacteria in children with Down syndrome. *J. Periodontol.* **71**, 249–255 (2000).
68. G. Ram, J. Chinen, Infections and immunodeficiency in Down syndrome. *Clin. Exp. Immunol.* **164**, 9–16 (2011).
69. M. B. Giacona, P. N. Papapanou, I. B. Lamster, L. L. Rong, V. D. D'Agati, A. M. Schmidt, E. Lalla, *Porphyromonas gingivalis* induces its uptake by human macrophages and promotes foam cell formation in vitro. *FEMS Microbiol. Lett.* **241**, 95–101 (2004).
70. M. Coureuil, H. Lécuyer, S. Bourdoulous, X. Nassif, A journey into the brain: Insight into how bacterial pathogens cross blood-brain barriers. *Nat. Rev. Microbiol.* **15**, 149–159 (2017).
71. B. R. Talamo, W.-H. Feng, M. Perez-Cruet, L. Adelman, K. Kosik, V. M.-Y. Lee, L. C. Cork, J. S. Kauer, Pathologic changes in olfactory neurons in Alzheimer's disease. *Ann. N. Y. Acad. Sci.* **640**, 1–7 (1991).
72. L. Li, R. Michel, J. Cohen, A. DeCarlo, E. Kozarov, Intracellular survival and vascular cell-to-cell transmission of *Porphyromonas gingivalis*. *BMC Microbiol.* **8**, 26 (2008).
73. T. E. Cope, T. Rittman, R. J. Borchert, P. S. Jones, D. Vatansever, K. Allinson, L. Passamonti, P. Vazquez Rodriguez, W. R. Bevan-Jones, J. T. O'Brien, J. B. Rowe, Tau burden and the functional connectome in Alzheimer's disease and progressive supranuclear palsy. *Brain* **141**, 550–567 (2018).
74. S. Urnowey, T. Ansai, V. Bitko, K. Nakayama, T. Takehara, S. Barik, Temporal activation of anti- and pro-apoptotic factors in human gingival fibroblasts infected with the periodontal pathogen, *Porphyromonas gingivalis*: Potential role of bacterial proteases in host signalling. *BMC Microbiol.* **6**, 26 (2006).
75. J. Chu, E. Lauretti, D. Praticò, Caspase-3-dependent cleavage of Akt modulates tau phosphorylation via GSK3β kinase: Implications for Alzheimer's disease. *Mol. Psychiatry* **22**, 1002–1008 (2017).
76. P. Sandhu, M. M. Naeem, C. Lu, P. Kumarathasan, J. Gomes, A. Basak, Ser^{422} phosphorylation blocks human Tau cleavage by caspase-3: Biochemical implications to Alzheimer's Disease. *Bioorg. Med. Chem. Lett.* **27**, 642–652 (2017).
77. E. H. Corder, A. M. Saunders, W. J. Strittmatter, D. E. Schmechel, P. C. Gaskell, G. W. Small, A. D. Roses, J. L. Haines, M. A. Pericak-Vance, Gene dose of apolipoprotein E type 4 allele and the risk of Alzheimer's disease in late onset families. *Science* **261**, 921–923 (1993).
78. S. E. Roselaar, A. Daugherty, Apolipoprotein E-deficient mice have impaired innate immune responses to *Listeria monocytogenes* in vivo. *J. Lipid Res.* **39**, 1740–1743 (1998).
79. J. Lönn, S. Ljunggren, K. Klarström-Engström, I. Demirel, T. Bengtsson, H. Karlsson, Lipoprotein modifications by gingipains of *Porphyromonas gingivalis*. *J. Periodontal Res.* **53**, 403–413 (2018).
80. F. M. Harris, W. J. Brecht, Q. Xu, I. Tesseur, L. Kekonius, T. Wyss-Coray, J. D. Fish, E. Masliah, P. C. Hopkins, K. Scearce-Levie, K. H. Weisgraber, L. Mucke, R. W. Mahley, Y. Huang, Carboxyl-terminal-truncated apolipoprotein E4 causes Alzheimer's disease-like neurodegeneration and behavioral deficits in transgenic mice. *Proc. Natl. Acad. Sci. U.S.A.* **100**, 10966–10971 (2003).
81. T. R. Jay, V. E. von Saucken, G. E. Landreth, TREM2 in neurodegenerative diseases. *Mol. Neurodegener.* **12**, 56 (2017).
82. P. Minoretti, C. Gazzaruso, C. D. Vito, E. Emanuele, M. P. Bianchi, E. Coen, M. Reino, D. Geroldi, Effect of the functional toll-like receptor 4 Asp299Gly polymorphism on susceptibility to late-onset Alzheimer's disease. *Neurosci. Lett.* **391**, 147–149 (2006).
83. N. Brouwers, C. Van Cauwenberghe, S. Engelborghs, J.-C. Lambert, K. Bettens, N. Le Bastard, F. Pasquier, A. G. Montoya, K. Peeters, M. Mattheijssens, R. Vandenberghe, P. P. Deyn, M. Cruts, P. Amouyel, K. Sleegers, C. Van Broeckhoven, Alzheimer risk associated with a copy number variation in the complement receptor 1 increasing C3b/C4b binding sites. *Mol. Psychiatry* **17**, 223–233 (2012).
84. M.-S. Tan, J.-T. Yu, T. Jiang, X.-C. Zhu, H.-F. Wang, W. Zhang, Y.-L. Wang, W. Jiang, L. Tan, NLRP3 polymorphisms are associated with late-onset Alzheimer's disease in Han Chinese. *J. Neuroimmunol.* **265**, 91–95 (2013).

85. X. Gao, Y. Dong, Z. Liu, B. Niu, Silencing of triggering receptor expressed on myeloid cells-2 enhances the inflammatory responses of alveolar macrophages to lipopolysaccharide. *Mol. Med. Rep.* **7**, 921–926 (2013).

86. E.-N. N'Diaye, C. S. Branda, S. S. Branda, L. Nevarez, M. Colonna, C. Lowell, J. A. Hamerman, W. E. Seaman, TREM-2 (triggering receptor expressed on myeloid cells 2) is a phagocytic receptor for bacteria. *J. Cell Biol.* **184**, 215–223 (2009).

87. J. M. Replogle, G. Chan, C. C. White, T. Raj, P. A. Winn, D. A. Evans, R. A. Sperling, L. B. Chibnik, E. M. Bradshaw, J. A. Schneider, D. A. Bennett, P. L. De Jager, A TREM1 variant alters the accumulation of Alzheimer-related amyloid pathology. *Ann. Neurol.* **77**, 469–477 (2015).

88. N. Bostanci, T. Thurnheer, J. Aduse-Opoku, M. A. Curtis, A. S. Zinkernagel, G. N. Belibasakis, *Porphyromonas gingivalis* regulates TREM-1 in human polymorphonuclear neutrophils via its gingipains. *PLOS ONE* **8**, e75784 (2013).

89. F. Martinon, J. Tschopp, Inflammatory caspases: Linking an intracellular innate immune system to autoinflammatory diseases. *Cell* **117**, 561–574 (2004).

90. M. Saresella, F. La Rosa, F. Piancone, M. Zoppis, I. Marventano, E. Calabrese, V. Rainone, R. Nemni, R. Mancuso, M. Clerici, The NLRP3 and NLRP1 inflammasomes are activated in Alzheimer's disease. *Mol. Neurodegener.* **11**, 23 (2016).

91. I. Olsen, Ö. Yilmaz, Modulation of inflammasome activity by *Porphyromonas gingivalis* in periodontitis and associated systemic diseases. *J. Oral Microbiol.* **8**, 30385 (2016).

92. C. Venegas, S. Kumar, B. S. Franklin, T. Dierkes, R. Brinkschulte, D. Tejera, A. Vieira-Saecker, S. Schwartz, F. Santarelli, M. P. Kummer, A. Griep, E. Gelpi, M. Beilharz, D. Riedel, D. T. Golenbock, M. Geyer, J. Walter, E. Latz, M. T. Heneka, Microglia-derived ASC specks cross-seed amyloid-β in Alzheimer's disease. *Nature* **552**, 355–361 (2017).

93. M. T.-H. Huang, D. J. Taxman, E. A. Holley-Guthrie, C. B. Moore, S. B. Willingham, V. Madden, R. K. Parsons, G. L. Featherstone, R. R. Arnold, B. P. O'Connor, J. P.-Y. Ting, Critical role of apoptotic speck protein containing a caspase recruitment domain (ASC) and NLRP3 in causing necrosis and ASC speck formation induced by *Porphyromonas gingivalis* in human cells. *J. Immunol.* **182**, 2395–2404 (2009).

94. S. Mariathasan, D. S. Weiss, V. M. Dixit, D. M. Monack, Innate immunity against *Francisella tularensis* is dependent on the ASC/caspase-1 axis. *J. Exp. Med.* **202**, 1043–1049 (2005).

95. T. N. Ellis, M. J. Kuehn, Virulence and immunomodulatory roles of bacterial outer membrane vesicles. *Microbiol. Mol. Biol. Rev.* **74**, 81–94 (2010).

96. J. D. Cecil, N. M. O'Brien-Simpson, J. C. Lenzo, J. A. Holden, W. Singleton, A. Perez-Gonzalez, A. Mansell, E. C. Reynolds, Outer membrane vesicles prime and activate macrophage inflammasomes and cytokine secretion in vitro and in vivo. *Front. Immunol.* **8**, 1017 (2017).

97. A. J. Fleetwood, M. K. S. Lee, W. Singleton, A. Achuthan, M.-C. Lee, N. M. O'Brien-Simpson, A. D. Cook, A. J. Murphy, S. G. Dashper, E. C. Reynolds, J. A. Hamilton, Metabolic remodeling, inflammasome activation, and pyroptosis in macrophages stimulated by *Porphyromonas gingivalis* and its outer membrane vesicles. *Front. Cell. Infect. Microbiol.* **7**, 351 (2017).

98. Y. Zhao, F. Shao, Diverse mechanisms for inflammasome sensing of cytosolic bacteria and bacterial virulence. *Curr. Opin. Microbiol.* **29**, 37–42 (2016).

99. K. O. Bender, M. Garland, J. A. Ferreyra, A. J. Hryckowian, M. A. Child, A. W. Puri, D. E. Solow-Cordero, S. K. Higginbottom, E. Segal, N. Banaei, A. Shen, J. L. Sonnenburg, M. Bogyo, A small-molecule antivirulence agent for treating *Clostridium difficile* infection. *Sci. Transl. Med.* **7**, 306ra148 (2015).

100. Y. Shi, D. B. Ratnayake, K. Okamoto, N. Abe, K. Yamamoto, K. Nakayama, Genetic analyses of proteolysis, hemoglobin binding, and hemagglutination of *Porphyromonas gingivalis*. Construction of mutants with a combination of rgpA, rgpB, kgp, and hagA. *J. Biol. Chem.* **274**, 17955–17960 (1999).

101. J. W. Smalley, A. J. Birss, B. Szmigielski, J. Potempa, Sequential action of R- and K-specific gingipains of *Porphyromonas gingivalis* in the generation of the haem-containing pigment from oxyhaemoglobin. *Arch. Biochem. Biophys.* **465**, 44–49 (2007).

102. R. D. Pathirana, N. M. O'Brien-Simpson, G. C. Brammar, N. Slakeski, E. C. Reynolds, Kgp and RgpB, but not RgpA, are important for *Porphyromonas gingivalis* virulence in the murine periodontitis model. *Infect. Immun.* **75**, 1436–1442 (2007).

103. C. L. Ventola, The antibiotic resistance crisis: Part 1: Causes and threats. *P. T.* **40**, 277–283 (2015).

104. J. H. Kwon, M. A. Olsen, E. R. Dubberke, The morbidity, mortality, and costs associated with *Clostridium difficile* infection. *Infect. Dis. Clin. North Am.* **29**, 123–134 (2015).

105. P. J. Narayan, S.-L. Kim, C. Lill, S. Feng, R. L. M. Faull, M. A. Curtis, M. Dragunow, Assessing fibrinogen extravasation into Alzheimer's disease brain using high-content screening of brain tissue microarrays. *J. Neurosci. Methods* **247**, 41–49 (2015).

106. H. C. Kolb, M. G. Finn, K. B. Sharpless, Click chemistry: Diverse chemical function from a few good reactions. *Angew. Chem. Int. Ed.* **40**, 2004–2021 (2001).

107. J. L. Poirier, R. Čapek, Y. De Koninck, Differential progression of Dark Neuron and Fluoro-Jade labelling in the rat hippocampus following pilocarpine-induced status epilepticus. *Neuroscience* **97**, 59–68 (2000).

108. J. M. Morillo, L. Lau, M. Sanz, D. Herrera, A. Silva, Quantitative real-time PCR based on single copy gene sequence for detection of *Actinobacillus actinomycetemcomitans* and *Porphyromonas gingivalis*. *J. Periodontal Res.* **38**, 518–524 (2003).

Acknowledgments: We are enormously grateful to the brain tissue donors and their families. We are also very grateful to N. Mehrabi, M. Singh-Bains, and S. Feng (Centre for Brain Research, University of Auckland) for their expert assistance with TMA construction, IHC, and MetaMorph analyses and to M. Eszes, the Human Brain Bank manager. **Funding:** P.M. was supported by National Science Center 2016/23/B/NZ5/011469, Poland. J.P. was supported by NIH/NIDCR grant R01DE022597. This work was funded by Cortexyme Inc. **Author contributions:** S.S.D. and C.L. developed and coordinated the project, designed experiments, evaluated the data, and drafted the manuscript. F.E. designed, performed, and analyzed IHC and immunofluorescent experiments on human brain tissues; designed, performed, and analyzed experiments on stereotactic injection of gingipains into mouse brain; designed, performed, and analyzed experiments on the antibacterial effects of Aβ on *P. gingivalis*; and analyzed brain samples from all animal experiments. M.B. and A.M. designed, performed, and analyzed experiments using a mouse model of *P. gingivalis*–induced periodontal disease and brain infection. A.K. designed and oversaw the development of small-molecule gingipain inhibitors. M.N. performed IP and WB of Kgp from human brain tissues. U.H. analyzed brain samples from all animal experiments. D.R. designed, performed, and analyzed PCR experiments of *P. gingivalis* DNA load in human CSF. C.G. performed in vitro digestion of recombinant tau-441 by gingipains and developed the WB of tau proteolytic fragments. L.J.H. and S.A.-K. designed and evaluated experiments and edited the manuscript. S.K. evaluated experiments and edited the manuscript. A.L. assisted in biochemical aspects of the experiments. M.I.R. evaluated experiments and edited the manuscript. B.P. provided purified gingipains. P.M., A.H., and K.A. assisted in performing mouse experiments and analyzing animal specimens. H.H. provided saliva and subgingival plaque samples from periodontal subjects at The Forsyth Institute. G.D.W. and E.C.R. analyzed gingipain-IR in AD brain tissue at the University of Melbourne and provided gingipain antibodies. R.L.M.F., M.A.C., and M.D. coordinated experiments and analyzed brain TMAs using anti-gingipain antibodies at NeuroValida, the University of Auckland. J.P. developed and coordinated the project, designed experiments, evaluated the data, and helped draft the manuscript. **Competing interests:** S.S.D. and C.L. are co-founders of Cortexyme, are employees of the company, and own Cortexyme stock. F.E., M.N., U.H., D.R., C.G., L.J.H., S.A.-K., S.K., and A.L. are Cortexyme employees with stock options. A.K. is a paid consultant of Cortexyme and owns Cortexyme stock. M.I.R. and J.P. are scientific advisors to Cortexyme and have options to purchase Cortexyme stock. A.K., S.S.D., and C.L. are inventors on two issued patents both entitled "Inhibitors of lysine gingipain" (US/9,975,473 and US/9.988,375) as well as two pending patent applications entitled "Inhibitors of arginine gingipain" (PCT/US2016/061197, filed on 9 November 2016) and "Ketone inhibitors of lysine gingipain" (PCT/US2017/051912, filed on 15 September 2017). S.S.D. and C.L. are inventors on a patent application entitled "Methods of use for therapeutics targeting the pathogen *P. gingivalis*" (US2017/ 0014468, filed on 29 April 2015). A.K. and L.J.H. are inventors on a patent application entitled "Gingipain activity probes" (62/459,456; filed on 15 February 2017). Cortexyme is the assignee of these patents and applications. The other authors declare that they have no competing interests. **Data and materials availability:** All data needed to evaluate the conclusions in the paper are present in the paper and/or the Supplementary Materials. Additional data related to this paper may be requested from the authors.

Submitted 30 May 2018
Accepted 11 December 2018
Published 23 January 2019
10.1126/sciadv.aau3333

Citation: S. S. Dominy, C. Lynch, F. Ermini, M. Benedyk, A. Marczyk, A. Konradi, M. Nguyen, U. Haditsch, D. Raha, C. Griffin, L. J. Holsinger, S. Arastu-Kapur, S. Kaba, A. Lee, M. I. Ryder, B. Potempa, P. Mydel, A. Hellvard, K. Adamowicz, H. Hasturk, G. D. Walker, E. C. Reynolds, R. L. M. Faull, M. A. Curtis, M. Dragunow, J. Potempa, *Porphyromonas gingivalis* in Alzheimer's disease brains: Evidence for disease causation and treatment with small-molecule inhibitors. *Sci. Adv.* **5**, eaau3333 (2019).

WHITE PAPER

Quantitative live-cell analysis characterizing morphology and function of iPSC-derived neurons and support cells

John N. Rauch, Susana Alcantara, Daniel Appledorn, Tim Dale, Gillian Lovell, Libuse Oupicka, Aaron Overland, Cicely L. Schramm
Essen BioScience, Ann Arbor, MI, 48108, USA

Summary & Impact

- The ability to simultaneously monitor morphology and functional readouts over time is critical for thorough characterization of human induced pluripotent stem cell (hiPSC)-derived models.
- Here we present live-cell imaging data used to quantify functional readouts of hiPSC-derived neurons and microglia and qualitatively assess morphology using the IncuCyte®.
- Development of spontaneous activity and patterns of coordinated network bursting varied between iPSC-derived neuronal models.
- hiPSC-derived microglia exhibited morphological changes during differentiation.
- hiPSC-derived microglia demonstrated phagocytic potential and chemotactic migration toward C5a.
- These data illustrate the ability for long-term monitoring and functional characterization of hiPSC-derived neuronal cultures and support cells using live-cell analysis techniques.

IncuCyte® System for continuous live-cell analysis

IncuCyte® Live-Cell Analysis System

A fully automated phase contrast and two-color fluorescence system that resides within a standard cell incubator for optimal cell viability. Designed to scan plates and flasks repeatedly over time.

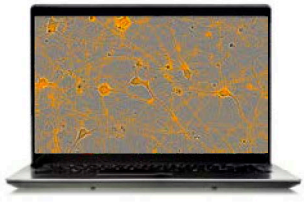

IncuCyte® Software

Fast, flexible and powerful control hub for continuous live-cell analysis comprising image acquisition, processing and data visualization

IncuCyte® Reagents and Consumables

A suite of non-perturbing cell labeling and reporter reagents

Quantification of neuronal activity

Intensity Range Image

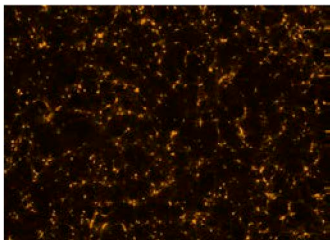

Masked Active Objects

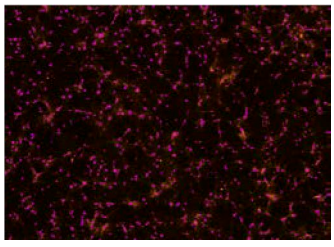

All Object Traces

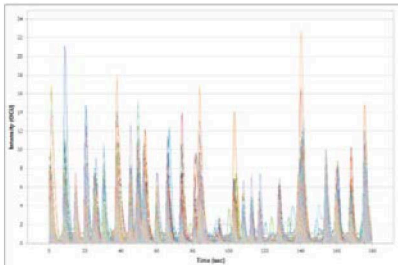

Fully Automated Analysis Metrics

Neuronal Activity

- Active Object #
- Mean Intensity
- Mean Burst Strength
- Mean Burst Rate
- Mean Burst Duration

Network Connectivity

- Mean Correlation

The IncuCyte® neuronal activity assay uses a genetically encoded calcium indicator to measure calcium fluctuations in neuronal cells by taking 180-second scans at 3 frames per second. The orange fluorescent image represents activity range (maximum–minimum fluorescence) over a complete scan. Automated segmentation defines active objects and allows display of all active object temporal traces within an image. Built-in analytical tools facilitate data analysis with metrics that define neuronal activity. The assay is performed using the IncuCyte® S3 Live-Cell Analysis System for Neuroscience.

Long-term analysis of network development in iPSC-derived neurons

Neuronal Activity

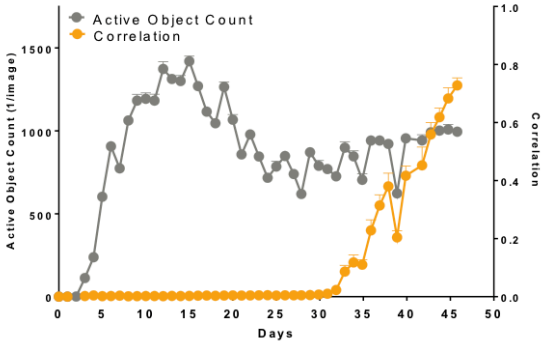

Day 15

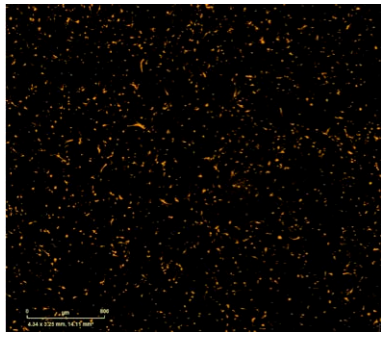

Day 44

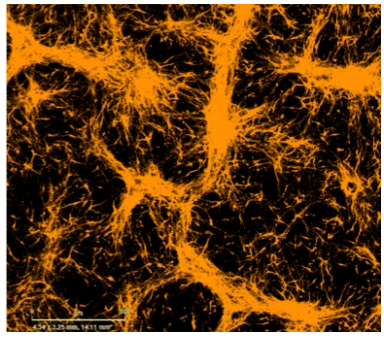

CNS.4U iPSC-derived neuronal cells (Ncardia) seeded at 20,000 cells/well in a 96-well microplate were infected with IncuCyte® NeuroBurst Orange Reagent to monitor neuronal activity over time. Quantification of the orange fluorescent signal kinetics shows an increase in active object count over the course of the experiment along with a corresponding increase in mean correlation (connectivity) starting at Day 30 (n = 8 +/– SEM), signifying development of a functional, mature network. Fluorescent range images at day 15 and 44 show morphological changes and an increase in fluorescent intensity, indicative of enhanced calcium flux.

Functional evaluation of excitatory and inhibitory iPSC-derived neurons

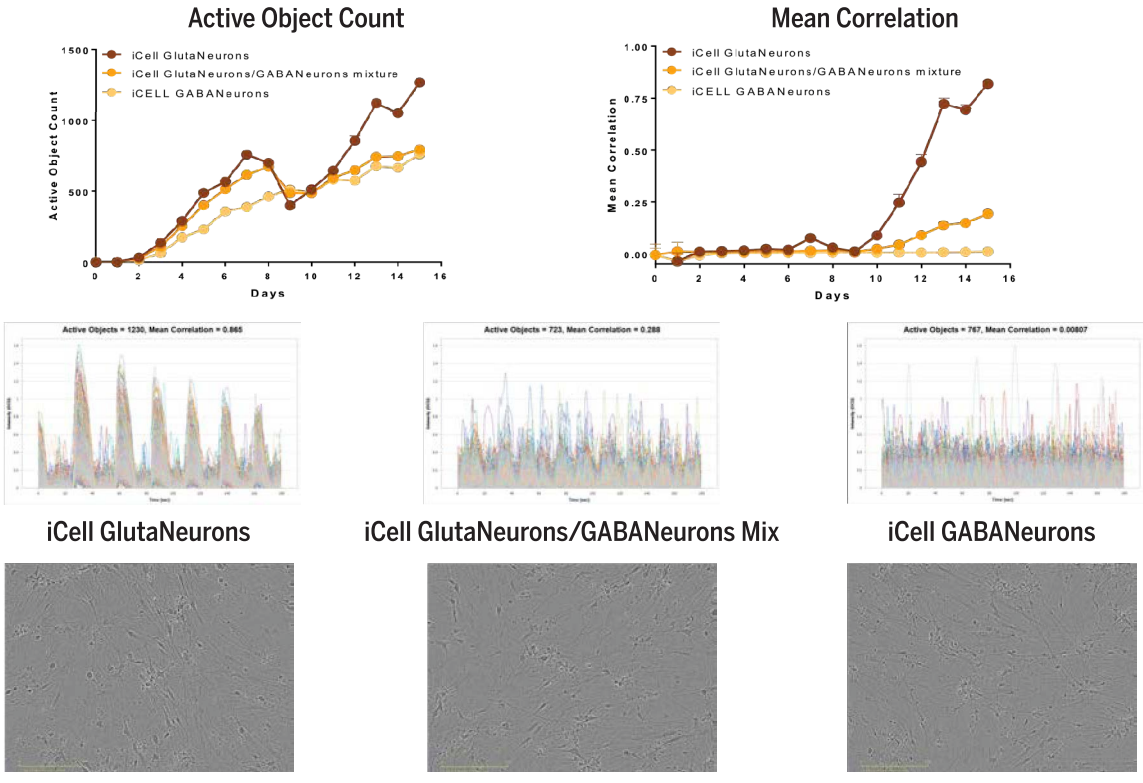

iCell GlutaNeurons and iCell GABANeurons from Cellular Dynamics International (CDI) were seeded independently at 20,000 cells/well or mixed at 10,000 cells each/well. All neurons were plated with a coculture of rat astrocytes seeded at 15,000 cells/well on PEI/laminin coated 96-well plates. Spontaneous neuronal activity was monitored over a period of 15 days beginning at DIV 3. Automated analysis was used to quantify active object # and mean correlation. All wells displayed spontaneous neuronal activity with increasing active objects over time. GlutaNeurons had a rapid increase in correlated activity starting at Day 10. The mixture of Gluta and GABANeurons had lower levels of correlated activity, while GABANeurons showed no correlated activity. Phase images show similar morphology of Gluta and GABANeurons.

Monitoring differentiation of neural progenitor cells over time

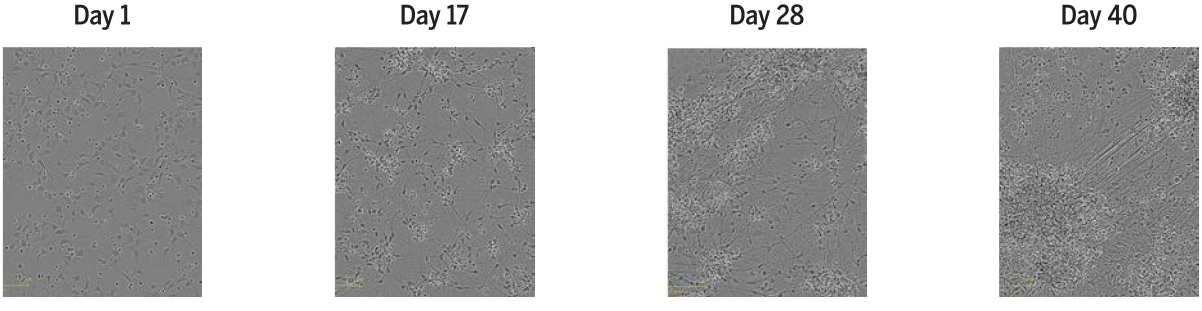

Neural Progenitor Cells from Axol Bioscience were plated after differentiation in a coculture with hiPSC-derived astrocytes and monitored for >40 days in culture. Distinct morphological changes were observed over this time course as the cells adopted a more neuronal phenotype.

Differentiation of iPSC-derived microglia

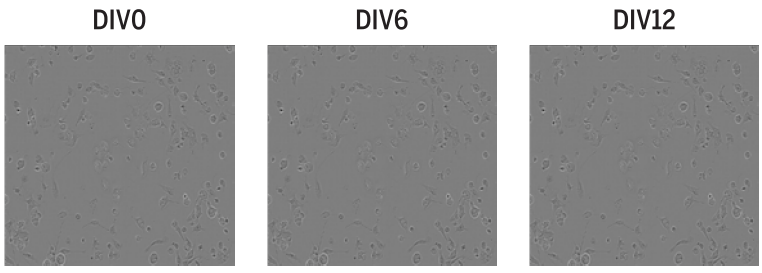

- iPSC-derived monocytes from Axol Bioscience were differentiated into microglia over the course of a 12-day induction period.
- Distinct morphological changes were observed over the course of differentiation: cells became larger and more elongated, consistent with a microglial phenotype.

Kinetic quantification of phagocytosis by microglia

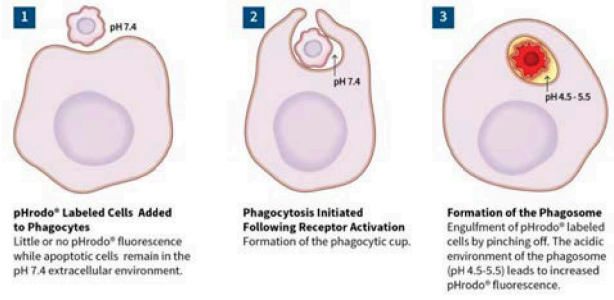

pHrodo® Labeled Cells Added to Phagocytes
Little or no pHrodo® fluorescence while apoptotic cells remain in the pH 7.4 extracellular environment.

Phagocytosis Initiated Following Receptor Activation
Formation of the phagocytic cup.

Formation of the Phagosome
Engulfment of pHrodo® labeled cells by pinching off. The acidic environment of the phagosome (pH 4.5-5.5) leads to increased pHrodo® fluorescence.

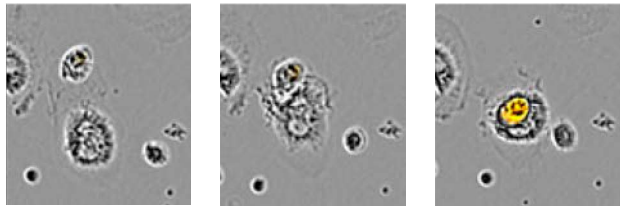

Time-lapse visualization of iPSC-derived microglia (Axol Bioscience) engulfing pHrodo® Orange-labeled apoptotic Neuro-2A cells. Images verify the entry of an apoptotic target cell into the cytoplasm of microglia.

Microglial phagocytosis of neurodegenerative disease-related peptides

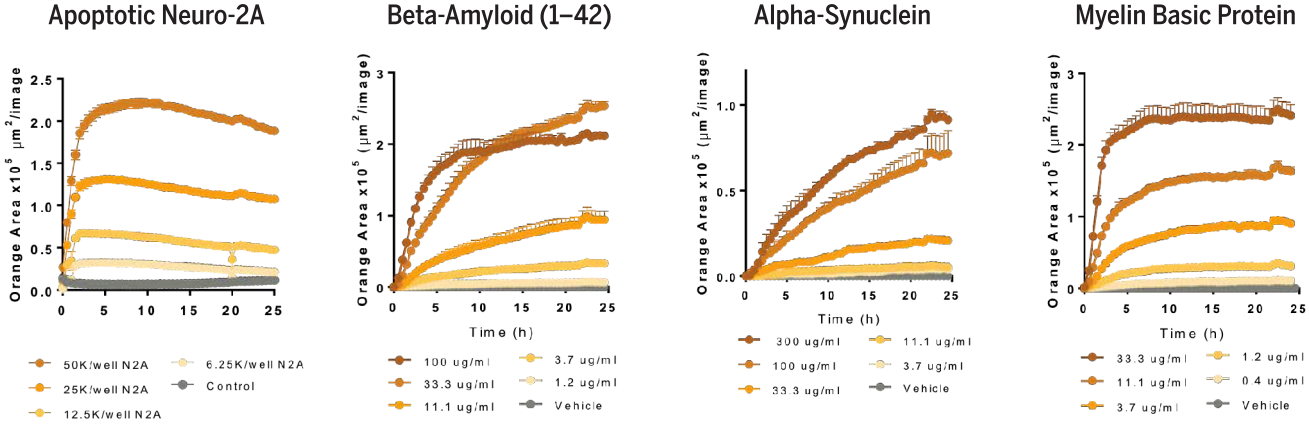

iPSC-derived microglia (Axol Bioscience, 30,000 cells/well) phagocytose physiologically relevant target material. Kinetic graphs display the concentration-dependent response to pHrodo® labeled apoptotic Neuro-2A cells, Beta-Amyloid (1–42), Alpha-Synuclein, and Myelin Basic Protein.

Chemotactic migration of iPSC-derived microglia

Chemotaxis Assay Plate

Concentration-dependent movement toward complement component 5a

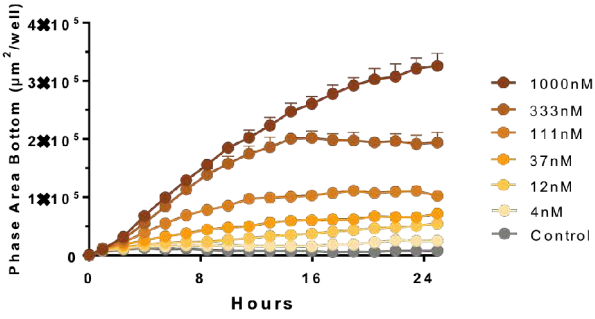

Top of Membrane with Mask

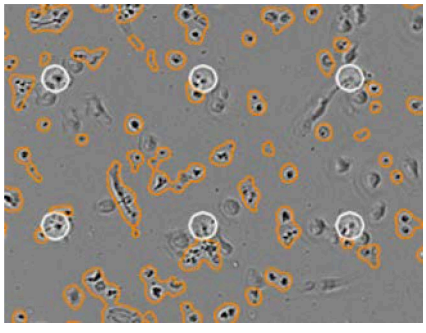

Bottom of Membrane with Mask

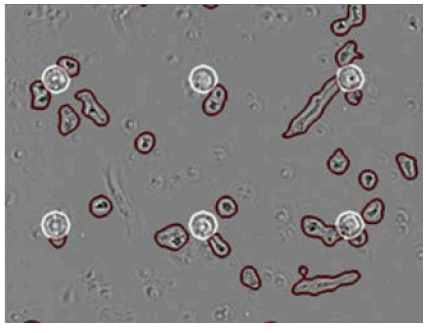

The IncuCyte® ClearView Chemotaxis Plate provides an optically clear surface for label-free imaging and analysis of chemotactic cell migration using the IncuCyte® Live-Cell Analysis System. iPSC-derived microglia from CDI show concentration-dependent directional migration toward the chemoattractant C5a. Images display the top side and bottom side of the membrane along with automated segmentation of cells (orange or brown mask respectively). Pores in the membrane are circled in white. Microglia move from the top side of the membrane through the pores to the bottom side where the chemoattractant C5a is located.

WHITE PAPER

Live-cell analysis of uptake of neuropathology-associated peptides by human iPSC-derived microglia

G. Lovell, M. Bowe, S. Lopez Alcantara, J. Rauch, L. Oupicka, A. Overland, C. Schramm, T. Dale, D. Trezise
Essen BioScience, Welwyn Garden City, AL7 3AX UK & Ann Arbor, MI, 48108, USA

Summary & Impact

- The presence of aggregated peptides such as Amyloid β (1–42) and α-Synuclein are associated with disease phenotypes (Alzheimer's disease and Parkinson's disease, respectively).
- Microglia, as the resident macrophage of the brain, have several functions, including clearance of peptide aggregates (phagocytosis) and apoptotic cells (efferocytosis).
- Here we describe characterization of the activation and function of microglia using IncuCyte® live-cell analysis.
- Phase and fluorescence images were captured with IncuCyte® and segmented fluorescence was quantified.
- In all cases robust, time-dependent signal changes were observed, consistent with known microglia function.
- We conclude that live-cell analysis is a flexible and powerful method for analysing microglia activity, where morphological and functional parameters can be readily quantified and integrated over time.

IncuCyte® System for continuous live-cell analysis

IncuCyte® Live-Cell Analysis System

A fully automated phase contrast and two-color fluorescence system that resides within a standard cell incubator for optimal cell viability. Designed to scan plates and flasks repeatedly over time.

IncuCyte® Software

Fast, flexible and powerful control hub for continuous live-cell analysis comprising image acquisition, processing and data visualization

IncuCyte® Reagents and Consumables

A suite of non-perturbing cell labeling and reporter reagents

Kinetic quantification of phagocytosis by microglia

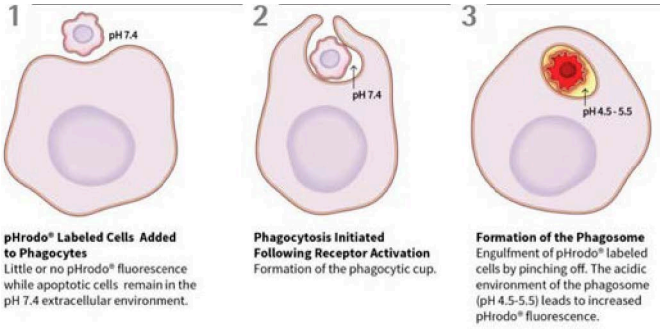

pHrodo® Labeled Cells Added to Phagocytes
Little or no pHrodo® fluorescence while apoptotic cells remain in the pH 7.4 extracellular environment.

Phagocytosis Initiated Following Receptor Activation
Formation of the phagocytic cup.

Formation of the Phagosome
Engulfment of pHrodo® labeled cells by pinching off. The acidic environment of the phagosome (pH 4.5-5.5) leads to increased pHrodo® fluorescence.

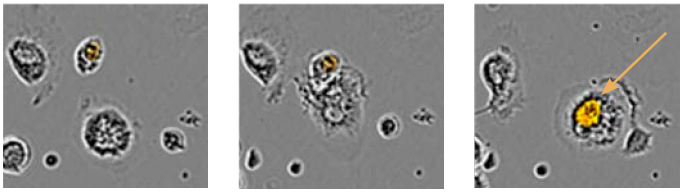

Phagocytosis Assay Principle

- Microglial precursors (Axol Bioscience) were seeded into a 96-well plate (30K/well) & differentiated to mature microglia for 2 weeks before assay
- Target apoptotic cells were labeled with a pH-sensitive fluorophore (IncuCyte® pHrodo® Orange Cell Labeling Kit). Non-engulfed labeled target cells (white arrow) have low fluorescence.
- Labeled target cells were added to mature microglia (30K/well) and placed into the IncuCyte® system where phase and fluorescence images were acquired every 30 minutes for 24h.
- Target cells were engulfed into the acidic phagolysosome of the microglia (cytoplasmic, orange arrow) where the fluorescence increases in intensity.
- The response was quantified as an increase in fluorescence area and shows a rapid phagocytosis of the target cells.

Live-cell analysis and quantification of microglia function

Phagocytosis of IncuCyte® bioparticles

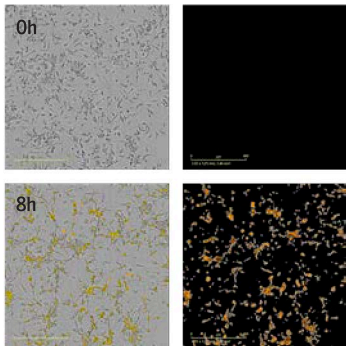

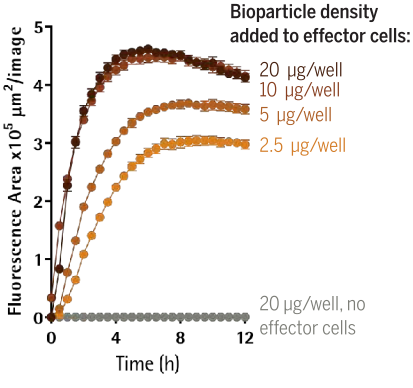

- IncuCyte® pHrodo® E. coli Bioparticles were added to iPSC microglia (Axol Bioscience).
- Phase and fluorescence images show an increase in cytoplasmic fluorescence (grey mask indicates segmented fluorescence) within the microglia between 0 and 8h.
- Bioparticles were engulfed within 8 h with a density-dependent increase in rate and total fluorescence area until 10 µg/ml.

Phagocytosis of apoptotic Neuro-2A cells

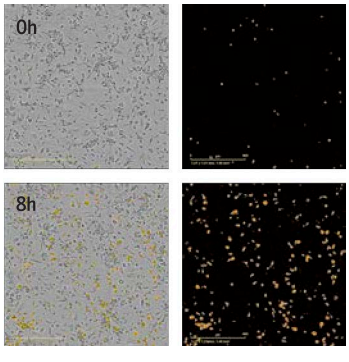

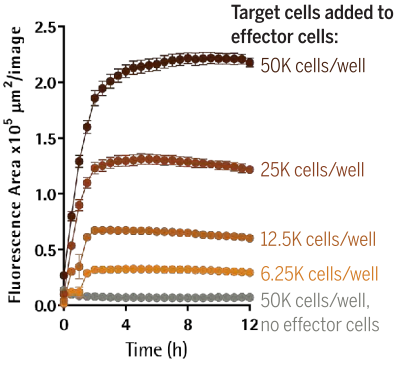

- Apoptotic target cells labeled with IncuCyte® pHrodo® Orange Cell Labeling kit were added to iPSC microglia (Axol Bioscience).
- Both cell types are visible in Phase HD images, however at 8h the number of target cells has reduced, and fluorescence within the cytoplasm of microglia has increased.
- Target cells were rapidly engulfed within 2h in a density-dependent manner.

Activation state of microglia affects phagocytic function

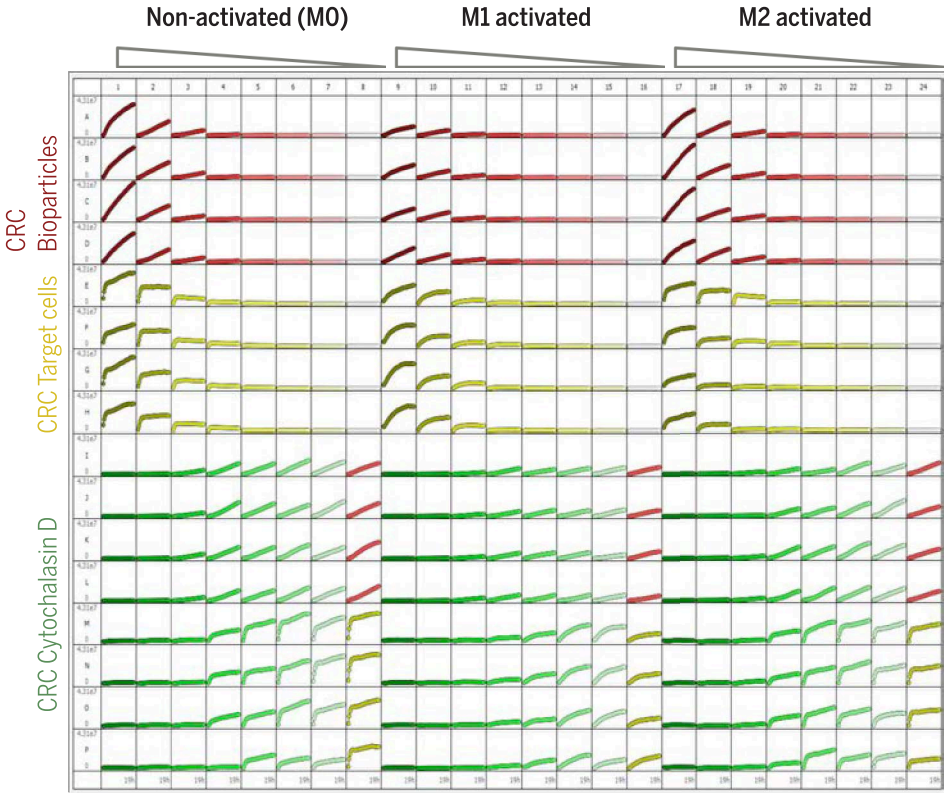

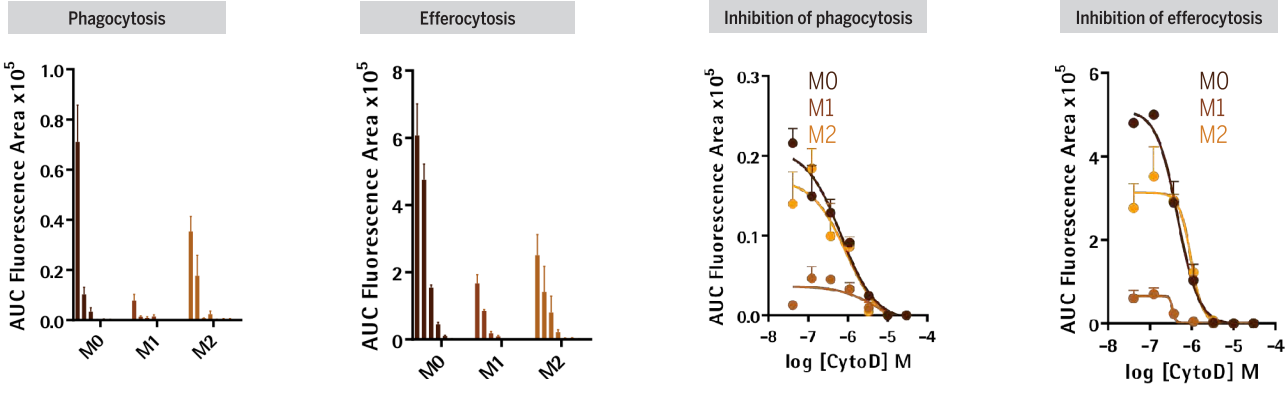

- iPSC Microglia (Axol Bioscience) were left unactivated (M0, col 1–8) or treated with LPS and IFN γ (M1, col 9–16) or IL-4 and IL–13 (M2, col 17–24) to induce polarization of the cells. Half of these cells (rows I–P) were then treated with a concentration range of cytochalasin D, an inhibitor of phagocytosis.
- Target material (IncuCyte® pHrodo® E. coli Bioparticles or apoptotic Neuro-2A cells labeled with IncuCyte® pHrodo® Orange Cell Labeling Kit) was added at increasing concentrations (rows A–H) or at a single density (rows I–P).
- The plate view shows an overview of phagocytosis, plotting fluorescence area over time per well of the 384-well plate.
- In both cases microglia activated to M1 phenotype had the lowest phagocytic function with unactivated cells (M0) showing the highest rate of both phagocytosis and efferocytosis. CytoD inhibits both phagocytosis and efferocytosis in a concentration-dependent manner.

iPSC microglia engulf aggregated Amyloid β, Myelin and α-synuclein

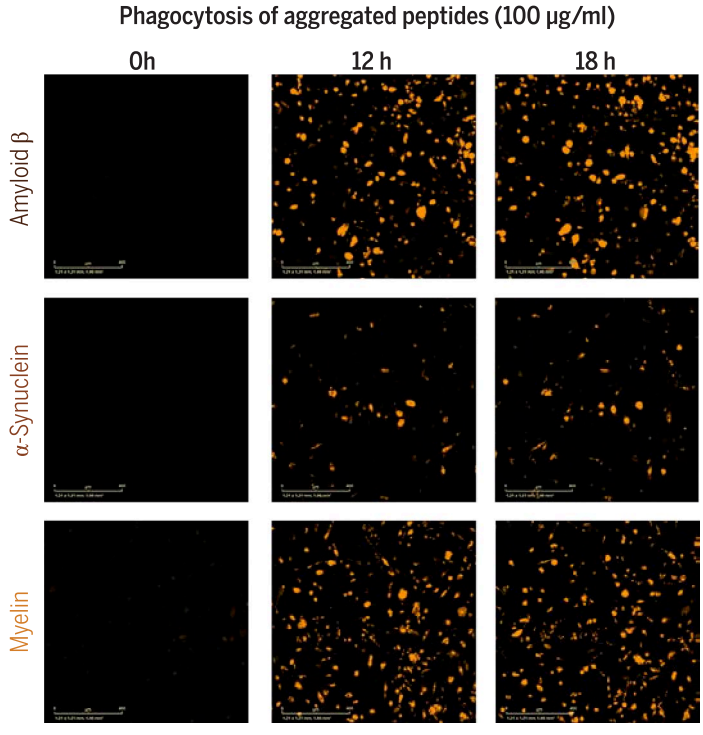

- Axol Bioscience iPSC microglial precursor cells were seeded into a 96-well plate at 30k cells/well and differentiated to mature microglia for 2 weeks. Peptides were labeled using IncuCyte® pHrodo® Orange Cell Labeling Kit, and aggregates were formed at 37 ˚C for 48h prior to assay. The peptides were added to cells at 0.4–300 µg/ml, and phase and fluorescent images were acquired in IncuCyte® for 36h.

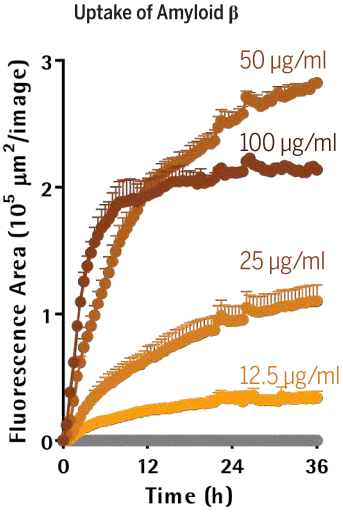

- Uptake of Amyloid β is concentration-dependent. 0.4 µg/ml is engulfed at a low rate, with fluorescence reaching a plateau at 0.3 x10^5 µm^2/image at 24h; 100 µg/ml, shows the highest rate of engulfment, with fluorescence area reaching plateau at 2.0 x10^5 µm^2/image by 12h.

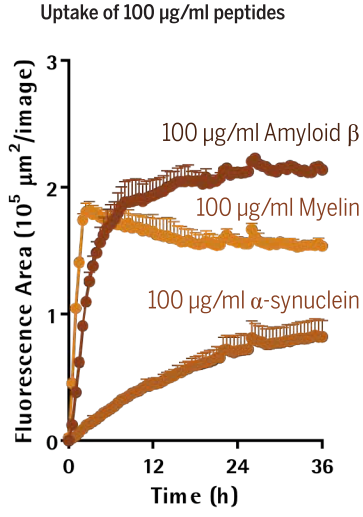

- Rate of phagocytosis varies between peptides. Myelin is taken up most rapidly by microglia (fully engulfed within 2h), while phagocytosis of Amyloid β is less rapid, and begins to slow after 12h. α-synuclein uptake is more gradual and at 24h, the fluorescence area is approximately 30% that of Amyloid β.
- This variance may be due to differential size or aggregation form of each peptide.

Engulfment of Aβ is dependent on cell type and peptide aggregation

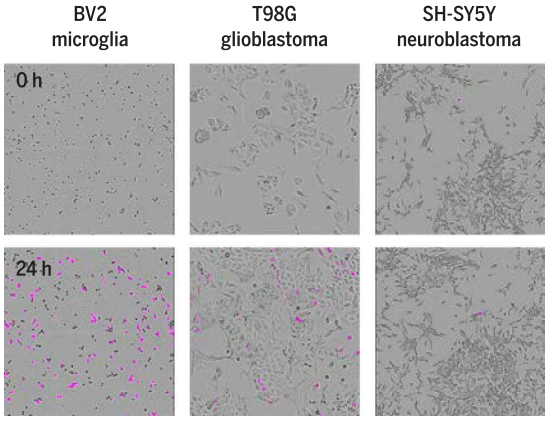

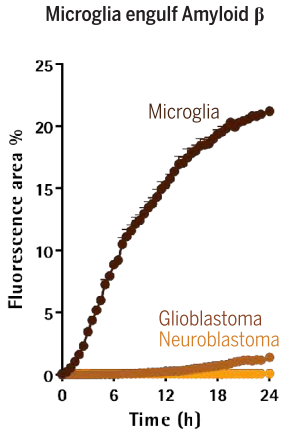

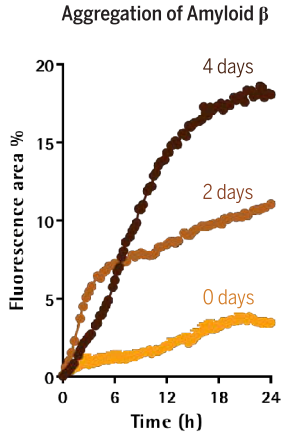

- Internalization of aggregated, labeled Amyloid β by three cell lines was compared. Phase HD images show differences in morphology between cell lines and the increase in fluorescence area (pink mask) at 24h. Data indicates the change in normalized fluorescence area over time (fluorescence area was normalized to phase area per well to account for proliferation and variations in cell morphology).
- BV2 microglia cells are phagocytic and rapidly engulf aggregated peptide with concomitant increase in fluorescence area over 24h, while glioblastoma and neuroblastoma cells show minimal peptide internalization.
- The phagocytosis of labeled Amyloid β, which was aggregated for 0, 2, or 4 days, was compared. Increasing the aggregation of the peptide changes the kinetic profile of uptake by BV2 cells, and longer aggregation times resulted in greater engulfment over a 24h period.

Blockade of scavenger receptors inhibits engulfment of Aβ

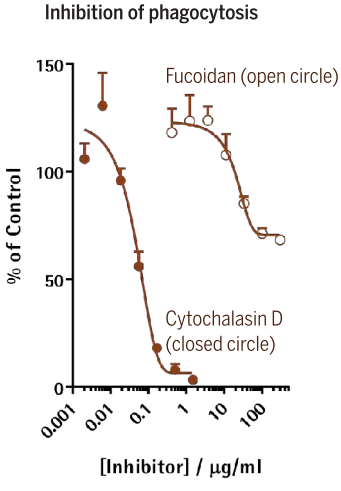

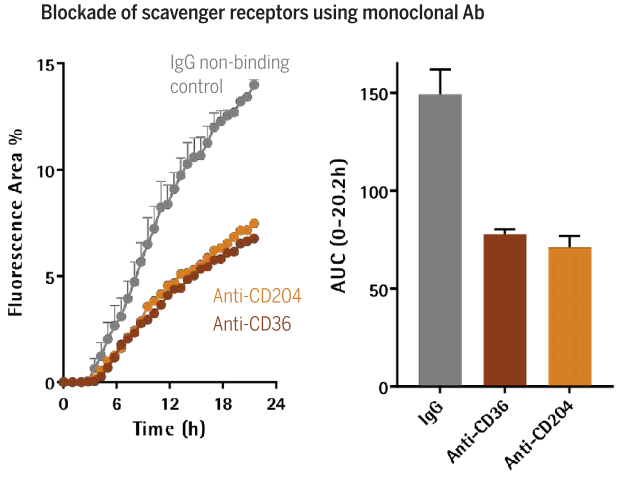

Inhibitor	Target
Fucoidan	Scavenger receptors - nonspecific
Cyto D	Actin (inhibits polymerization)
Anti-CD204	Scavenger receptor A
Anti-CD36	Scavenger receptor B

- Cytochalasin D and fucoidan inhibit phagocytosis of aggregates in a concentration-dependent manner. CytoD inhibits cytoskeletal rearrangement, a key process in phagocytosis. Treatment of BV2 microglia cells with 0.5 µg/ml CytoD completely inhibits engulfment of Amyloid β aggregates in a concentration-dependent manner. Fucoidan is a polysaccharide known to bind scavenger receptors. Treatment of the cells with 300 µg/ml fucoidan achieves partial (~35%) inhibition.
- Binding scavenger receptors A and B with monoclonal antibodies (anti-CD204 and anti-CD36 respectively) prevents the cell from engaging with target material. Inhibition of phagocytosis is observed in the presence of 10 µg/ml of both antibodies, achieving approximately 50% inhibition compared to IgG (non-binding antibody control).

Dissecting the role of microglia in Alzheimer's disease: An interview with Dr. Beth Stevens

Q&A

Beth Stevens began her career in 2004 as a graduate student interested in brain development and the role of non-neuronal (glial) cells found in the brain. In those days, little attention was paid to microglia, the brain's resident immune cells. However, as a postdoc in the late Ben Barres' lab at Stanford University, a serendipitous discovery led to her fascination with microglia as active, dynamic shapers of the brain. Her laboratory, which is split between Boston Children's Hospital and the Broad Institute of MIT and Harvard in Cambridge, Massachusetts, went on to discover that microglia play a crucial role in the normal development of synaptic connections and also in neurodegenerative disorders, such as Alzheimer's disease.

Stevens, a Howard Hughes Medical Institute investigator, spoke with *Science* about why Alzheimer's researchers have turned their focus toward microglia, how these cells remodel synapses, and the promise these findings hold for developing disease-modifying therapeutics.

How has the Alzheimer's field changed its view of microglia in recent years?

Microglia represent just 7%–10% of the cells in the brain and were long thought to be the brain's immune defenders. Pathology samples from human brains showed microglial cells often surrounding the amyloid plaques—classic hallmarks of Alzheimer's disease. These phagocytic cells were thought to be reactive and involved in plaque clearance—a secondary response to a primary problem.

Over the last decade, we have discovered that microglial cells in particular are doing a lot more than just responding: They are active players in normal brain development and normal brain homeostasis. Alzheimer's researchers who have been focused on amyloid or tau proteins are now sitting up and taking notice.

When did you suspect that microglia were more than just the mop-up crew of the brain?

When I started in the Barres lab in 2004, the lab was investigating how secreted signals from glial cells regulate synapse development in neurons.

Unexpectedly, an unbiased screen identified a role for C1q and other proteins of the innate immune system's complement cascade in synaptic pruning, a normal process necessary for precise brain wiring. Ben Barres had a hunch this was going to be important, so I followed this clue.

In the immune system, when blood-borne complement proteins encounter a pathogen or an apoptotic cell, they glom on to it and tag it; that signals the circulating macrophage "pacmen" to eat the problem cells.

We found that several of these complement "eat me" signals were expressed in the normal developing brain and that they mediate pruning of extra synapses during development of the visual system (*1*). We hypothesized that microglia, which are macrophage-like cells in the brain, could be using this complement mechanism to recognize and "eat" excess or unwanted synapses.

Are microglial cells pruning synapses in the healthy, developing brain?

When I started my lab at Boston Children's Hospital in 2008, the first question we asked is whether and how microglia prune developing synapses. Around that same time, exciting in vivo imaging studies revealed that microglia in the normal brain are incredibly dynamic, motile, and constantly surveying the brain.

My first postdoc, Dorothy Schafer, led the project using the well-defined mouse visual system. She labeled the retinal axons with different colors and traced the synaptic endings of the axons to the visual thalamus in transgenic mice that expressed green-fluorescent protein in microglia. In her 3D reconstructions, she found the labeled axon terminals inside the lysosomes of the microglia during this period of synaptic remodeling (2).

Additionally, Schafer showed that microglia were indeed using the complement mechanism. If we genetically knock out the complement proteins or the complement receptor, CR3, on the microglial cells, there is a ~50% reduction in synaptic pruning.

How does a microglial cell eat a synapse?

Our data suggest that complement proteins bind to the weaker synaptic connections and instruct microglia to nibble away the endings of the axons. Blocking this pathway results in too many synapses and abnormal connectivity. Most interesting of all, it is not a random cleanup job. Rather, the synapses eaten by the microglia tend to be the less active ones.

Of course, just as in the immune system, in the brain there is a milieu of other molecules that regulate this process, including "don't eat me" signals that protect cells, and so microglia must read a whole repertoire of cues to decide.

How do synapse-eating microglia come into play in Alzheimer's disease?

We hypothesized that maybe this normal pruning mechanism of development becomes aberrantly activated in the aged brain and in neurodegenerative disorders. Pathological synapse loss is an early hallmark of Alzheimer's that happens years before there are cognitive and clinical symptoms.

Synapse loss is the strongest correlate of cognitive decline, yet remarkably little is known about why certain synapses and brain regions are vulnerable. Could this developmental pruning mechanism be happening in the preclinical Alzheimer's brain? My lab took a leap into the Alzheimer's field to test this idea.

What did that leap reveal?

I was lucky to recruit Soyon Hong as a talented postdoc to test the idea that microglia might be involved in the synapse loss in Alzheimer's, in collaboration with the labs of Dennis Selkoe and Cynthia Lemere.

We looked at regions such as the hippocampus, where synapse loss happens early, and found that the complement proteins C1q and C3 are highly upregulated and are both bound to subsets of synapses in that area. We went on to show that microglia and complement proteins contribute to the early synapse loss in amyloid mouse models of Alzheimer's (*3*, *4*). Very recent work from Morgan Sheng's group showed a similar mechanism in a tau model of Alzheimer's (*5*).

The microglia we studied were called into action and overeating—but was this overeating good or bad? When we genetically blocked either the complement proteins or the CR3 receptors on the mice microglia, we could protect the synapse loss. In other words, the microglial overeating appears detrimental in the context of disease.

It's very exciting to me that this mechanism has also been shown in several other neurodegenerative models, including frontal temporal dementia, glaucoma, and other Alzheimer's models, suggesting a common mechanism of pathological synapse loss.

Have microglia been implicated in Alzheimer's in other ways?

Over the last decade, genome-wide association studies have looked at the genetics of late-onset Alzheimer's. More than 50% of those Alzheimer's risk genes or variants identified are expressed in or enriched in myeloid cells, which include the resident microglia in the brain (*6*). Some of those are genes and receptors known to be involved in phagocytosis and lysosomal function. For example, TREM2, a clear Alzheimer's risk gene, plays a role in the ability of microglia to respond to beta amyloid and other challenges.

Personally, I think pruning synapses is just the tip of the iceberg. Using single-cell sequencing and emerging new tools, we are well positioned to deeply characterize microglia and neuroimmune interactions to ascertain what human genetics is telling us about microglia biology. We can now ask about the various microglial states and what they mean—are those states beneficial or detrimental to brain function (*7*)?

What does this mean for finding effective treatments for Alzheimer's?

Making progress toward new therapies will require a collaborative and multidisciplinary effort—sharing new tools, protocols, and data. I believe a focused effort across many labs, institutions, and industry partnerships will get us closer to pathways and potential drug targets. There are likely several ways to modulate microglia states to push them to a more beneficial condition, maybe to clear amyloid or cellular debris more quickly.

Of course, that could represent a double-edged sword. If you turn on a phagocytosis pathway that instructs microglia to "eat more," you have to do it in a way that doesn't cause them to eat the wrong things, such as functional synapses. You can't just "blanket-boost" phagocytosis—you need specificity.

Can we tune our immune system to fight Alzheimer's as we've seen it used for cancer treatments?

It isn't too early to be thinking about immunoneurology for Alzheimer's in the way we think of immuno-oncology treatments for cancer. Can we shift the immune system to a defensive, protective mode, and at the same time dial down the detrimental states of immune cells within the brain? Both of these things will probably have to happen for successful treatment to occur.

References

1. B. Stevens *et al., Cell* **131**, 1164–1178 (2007).
2. D. P. Schafer *et al., Neuron* **74**, 691–705 (2012).
3. S. Hong *et al., Science* **352**, 712–716 (2016).
4. Q. Shi *et al., J. Neurosci.* **35**, 13029–13042 (2015).
5. T. Wu *et al., Cell Rep.* **28**, 2111–2123 (2019).
6. A. G. Efthymiou, A. M. Goate, *Molec. Neurodegen.* **12**, 43 (2017).
7. M. W. Salter, B. Stevens, *Nat. Med.* **23**, 1018–1027 (2017).

sartorius

Feel empowered with IncuCyte® Live-Cell Analysis

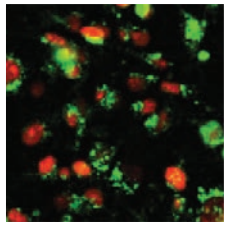

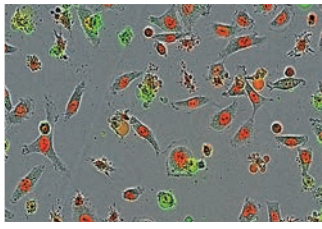

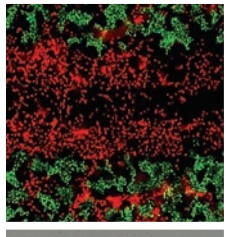

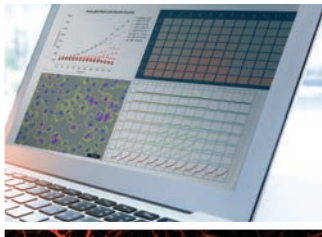

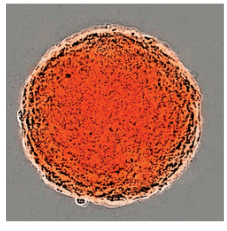

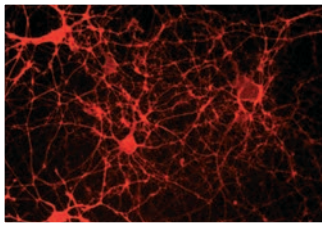

IncuCyte speeds scientific discovery by combining lab-tested protocols and reagents with powerful, automated image acquisition and analysis. With IncuCyte's user friendly interface and robust instrument portfolio, any cell biologist can gain dynamic insights into the health, morphology, movement and function of their cell models, all from the stable environment of a tissue culture incubator.

With a rapidly growing collection of over 2,200 peer reviewed articles, new applications using the IncuCyte are being published continuously in therapeutic areas such as Immunology, Oncology, Immuno-oncology and Neuroscience.

Select an IncuCyte for your research at **www.sartorius.com/incucyte**

Get new answers

Protect your cells

Ask new questions

Improve productivity

sartorius

A New Era of Discovery Awaits. IncuCyte® S3 Live-Cell Analysis System for Neuroscience

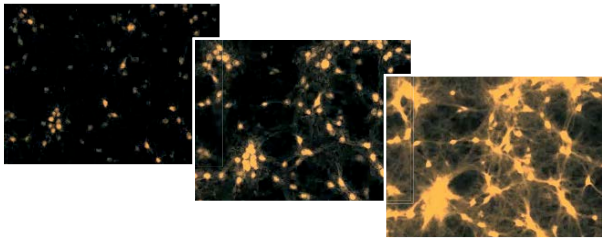

With brand new assays that speed cell-based research and discovery, IncuCyte gives you the power to study a range of biological processes in real time and at microplate throughput. Explore this groundbreaking, turnkey solution – including a suite of non-perturbing reagents, live-cell protocols and purpose-built software.

Evaluate Networks and Function

Quantitatively evaluate **dynamic** neuronal networks and neuro-immune function with continuous, automated analysis.

Visually Verify Changes

Visually verify morphological changes and validate measurements with images and movies.

Conduct Long-term Studies

Conduct week- or month-long studies on sensitive cells while they sit undisturbed in your incubator.

Discover more at
www.essenbioscience.com/neuroscience